CHAIN-LENGTH PROPERTIES OF CONJUGATED SYSTEMS: STRUCTURE, CONFORMATION, AND REDOX CHEMISTRY

by

Saadia Chaudhry

A Dissertation

Submitted to the Faculty of Purdue University

In Partial Fulfillment of the Requirements for the degree of

Doctor of Philosophy

Department of Chemistry

West Lafayette, Indiana

May 2021

THE PURDUE UNIVERSITY GRADUATE SCHOOL

STATEMENT OF COMMITTEE APPROVAL

Prof. Jianguo Mei, Chair

Department of Chemistry

Prof. Chris Uyeda

Department of Chemistry

Prof. Mark Lipton

Department of Chemistry

Prof. Suzanne Bart

Department of Chemistry

Approved by:

Dr. Christine Hrycyna

In the name of Allah, the Most Gracious, the Most Merciful.

Whosoever knows himself, knows his Creator.

The Maker of matter, space, and time.

The Arranger of forms and colors.

The Shaper of beauty.

ACKNOWLEDGMENTS

My graduate career has completely transformed me not only as a scientist but as a human. I had absolutely no intention of letting this process touch me so deeply, but I'm glad it did. I have spent the last six years in a state of metamorphosis, and I owe this to my advisor, Prof. Jianguo Mei. His patience, kindness, and altruistic approach to mentoring his students have given me space and time to nurture my strengths and tend to my weaknesses as a scientist. His stoic work ethic, passion for science, and delightful humor have been a continuous source of inspiration. Even through my shenanigans and periods of stagnation, he has encouraged and supported me. Looking back at the countless discussions we have had about science and philosophy, I am deeply grateful for the time, energy, and resources he has invested into mentoring me. Because of him, I am confident in continuing my path as a chemist. Thank you for lighting this fire in me, Prof. Mei.

I would also like to thank my collaborators Prof. David McMillian, Prof. Chad Risko, and Prof. Xiaodan Gu, for their contributions to my projects and for the stimulating discussions over the years. To my committee members, Prof. Chris Uyeda, Prof. Mark Lipton, and Prof. Suzanne Bart, thank you for contributing your valuable time and expertise to my education. To Purdue's talented instrument staff, including Dr. John Harwood, Donna Bertram, Dr. Hauping Mo, Jerry Hirschinger, Arlene Rothwell, Dr. Pat Bishop, Dr. Mike Everly, and Dr. Matthias Zeller, thank you for your time and advice on how to plan, troubleshoot, and analyze my experiments. Whether our interactions were brief or lengthy, I gained valuable insight into conducting careful scientific research from you all.

As an undergraduate at William Paterson University of NJ, I had the opportunity to run with a talented group of scientists. Thank you to Prof. Bhanu Chauhan and Prof. David Snyder for taking a chance on me and for supporting me. To Qiaxian and Aarti, not only did you teach me the basic skills to work in a chemistry lab, but you also provided me with an environment where I could comfortably reveal my naivety for chemistry. Qiaxian, your intelligence, sarcasm, and wit has taught me how to sharpen my communication and debate skills. You are the greatest worst friend I could ever ask for. Thank you for your loyalty throughout all these years.

I joined the Mei group in 2015 with Aristide, Jiazhi, and William as the first batch of graduate students. Our experience was unique to say the least, but it gave us grounds to play and learn on untainted territory. I have experienced moments of wisdom, frustration, and excitement

with each one of them; *"Do a Ph.D., they said. It will be fun, they said. You won't be poor, they said."* Well, "*they"* were right about the fun part and that was because of you guys. Next, I would like to thank Dr. Liyan You, one of the most intelligent and compassionate scientists with whom I have ever had the pleasure of working. Dr. You helped me get my chemistry off the ground when I came to Purdue as an inexperienced student. His calm demeanor and intricate knowledge of organic chemistry showed me how to think independently and critically in the lab. I would also like to thank past and present Mei group members: Kuluni, Vani, Dung, Kenny, Yukun, Natalie, Jiayingzi, Yan, Hanning, John, Atheena, Ke, Zhifan, Zhiyang, Mustafa, and Xuefei. I look forward to following your careers and hopefully working with all of you in the future.

On a more personal note, I want to thank my close friends and family who have given me a tremendous amount of energy throughout my graduate tenure. To my roommate of three years, Monita, thank you for your friendship. I feel truly blessed to have shared my time with such a wonderful and caring person. To my Purdue crew, including Elissia, Yan, Moises, Mavreen, and Brianna, thank you for the memories and support. Those heated, late-night debates and that Kanye West concert will forever be lit. To my friends around the country, including All'a, Monsurat, Femi, Anya, Jagoda, and Mama Cassandra, thank you all for your love and support. To my family, words could never quantify my love for you. But hear me out anyway. To my father, you have sacrificed a great deal for me to have this opportunity. You taught me that that this world will take away everything I love one day, but it can never take away my education. Thank you for keeping me grounded and teaching me how to fight in this world. You gave me top-notch DNA. To my brother, your brilliance, gentle soul, and go-getter attitude motivate me like no other. I am ready to kick off Golden Age Pt. 2 with you, Hamza. To my mother, thank you for bringing me into this world. Without you, none of this could have been possible.

Ultimately, all praise is due to the Most High. I was steered onto this path by my Creator. His subtle, yet ingenious maneuvering of my graduate career has been a great blessing. I am deeply grateful for His mercy. Alhamdullilah.

TABLE OF CONTENTS

LIST OF TABLES

LIST OF FIGURES

ABSTRACT

The development of solution-processable semiconducting polymers has brought mankind's long-sought dream of plastic electronics to fruition. Their potential in the manufacturing of lightweight, flexible yet robust, and biocompatible electronics has spurred their use in organic transistors, photovoltaics, electrochromic devices, batteries, and sensors for wearable electronics. Yet, despite the successful engineering of semiconducting polymers, we do not fully understand their molecular behavior and how it influences their doping (oxidation/reduction) properties. This is especially true for donor-acceptor π-systems which have proven to be very efficient at tuning the electronic properties of organic semiconductors. Historically, chain-length dependent studies have been essential in uncovering the relationship between the molecular structure and physical properties of a polymer. Discussed here is the investigation of a complete donor-acceptor molecular series composed of monodispersed and well-defined donor-acceptor conjugated molecules ranging from oligomer to polymer scale lengths. We used these molecules to form a relationship between the molecular structure, chain conformation, and doping properties of a widely used donor-acceptor structure. We found that the π-conjugated backbone begins to transform from a planar, rigid-rod to a flexible, coil-like conformation at approximately 15 repeat units, or 4500 Da, in solution. We investigate the influence of this convergence limit on the optical and electronic properties of the π-system, giving insight into the nature of their redox states and properties. This research aids in understanding the solution behavior of π-conjugated organic materials.

CHAPTER 1. GENERAL INTRODUCTION

1.1 Brief Intro

The late stand-up comedian and philosopher George Carlin once performed a passionate monologue called "Saving the Planet" that addresses the purpose of humanity on earth:[1]

> "The Earth doesn't share our prejudice towards plastic. Plastic came out of the Earth! The Earth probably sees plastic as just another one of its children. Could be the only reason the Earth allowed us to be spawned from it in the first place: it wanted plastic for itself, didn't know how to make it, needed us. Could be the answer to our age-old philosophical question: "Why are we here?" PLASTIC!!! So the plastic is here, our job is done, we can be phased out now, and I think that's really started already, don't you?"

The earth began the 'age of plastics' at the outset of the 20th century when, when Leo Baekeland synthesized the first fully synthetic plastic using phenol and formaldehyde under heat and pressure.[2] World War II encouraged the "plastic innovation period" and necessitated the use of cellophane, polyvinyl chloride (PVC), neoprene, polystyrene, polyethylene, nylon, polytetrafluoroethylene, polyethylene terephthalate (PET), polyester, poly-paraphenylene terephthalamide (Kevlar), and polypropylene. In total, plastic production in the USA increased by 300% during World War II and continues to rise to this day, despite its significant impact on the environment.[3] Could Carlin be right? Is humanity's sole purpose to synthesize plastic? Possibly. And if you are in the field, even better.

Scientists have moved swiftly in their pursuit of plastic materials, otherwise known as *synthetic metals*. One of these pursuits includes the development of plastic electronics, or flexible organic metals otherwise known as conjugated polymers (CPs). CPs have brought to fruition mankind's long-sought goal of plastic electronics. This dream was first manifested in the 1970s upon the discovery of iodine-doped, conducting polyacetylene (PA) by Heeger, MacDiarmid, and Shirakawa, earning them the 2000 Noble Prize in Chemistry.[4] Their invention initiated the field of conducting polymers, a class of materials that has gained tremendous attention for a multitude of applications. Their solution processability into thin-films, flexibility, and lightweight properties make them attractive for applications in optoelectronic devices, such as light emitting diodes, solar cells, field-effect transistors, organic lasers, electrochromics, batteries, and sensors. CPs have also facilitated new applications like indoor light harvesting, wearable electronics, inexpensive

thermoelectrics, and high-temperature electronics.[5,6] Water-soluble CPs have proven to be biocompatible for biological and medical applications like imaging, diagnostics, and therapy. Therefore, I would disagree with Carlin. Our purpose is not yet complete. There is much more plastic still to be made.

1.2 Electronic structure of π-conjugated polymers

The single most important feature of organic CPs is the nature of their π-conjugated system. The π-conjugated framework is a continuous array of overlapping π-orbitals supported by a σ-bond backbone. The π-orbitals are composed of alternating single and double bonds between carbon (or hetero) atoms employing sp^2 and sp hybridization. The lobes of the π-orbitals align perpendicular to the plane of the σ-bonds, so the interaction between π-orbitals (a π-bond) leads to electron density above and below the plane. As such, the atoms and π-electrons are so closely spaced that they behave as one continuous system with electronic or chemical gradients. While electrons in a σ-bond are tightly held by the nuclei, electrons in π-bonds are only *loosely* held, allowing delocalization of π-electrons across all adjacent aligned π-orbitals. This behavior of π-electrons in CPs forms the foundation for the useful optical and electronic properties of π-conjugated materials.

Insight into the electronic energy level structures of CPs can be gained by examining the frontier molecular orbitals of a conjugated system. Band theory classifies materials into three categories based on the band gap energy (Eg) between the valence band (VB) and conduction band (CB): i) metals: zero Eg where electrons can move freely across the VB and CB, making the material conductive; ii) semiconductors: low Eg (<3.0 eV) where thermal excitation of electrons or charge injection is needed to promote conductivity; iii) insulating (non-conducting): large Eg (>3 eV) where electrons remain localized in the VB and the material cannot be made conductive. CPs are classified as semiconductors.

A carbon atom has four valence electrons, two in the 2s orbitals and two in the 2p orbitals. Hybridization between the σ-orbitals of sp^2 and sp carbon (or hetero) atoms forms a localized σ-framework composed of bonding and nonbonding orbitals. These localized orbitals are in the plane of the molecule. Interaction between unhybridized π-orbitals that are adjacent to one another in the σ-framework occurs above and below the plane of the molecule. A π-orbital can contribute

one electron, two electrons, or zero electrons into a π-system, which respectively corresponds to half of a double bond, a lone pair, or an empty orbital. The π-bond energy level is slightly stabilized, whereas the antibonding π*-orbital is slightly destabilized. In the case of 1,3-butadiene, three π-orbitals are adjacent to one another and interact to form alternating single and double bonds. Delocalization of electron density across all π-orbitals results in four resonance structures, thereby increasing stability through conjugational effects. Naturally, as the number of overlapping π-orbitals, or conjugation length, increases, the energy gap between the HOMO and LUMO levels decrease. Stretching of C-C bonds creates an alternating structure of long and short bonds, breaking the symmetry of the π-bonds and stabilizing the π-system, also known as bond length alternation. In Figure 1.1a, the highest occupied molecular orbital (HOMO) and lowest unoccupied molecule orbital (LUMO) of thiophene are shown, respectively analogous to the top of the VB and the bottom of the CB as described by band theory.[7]

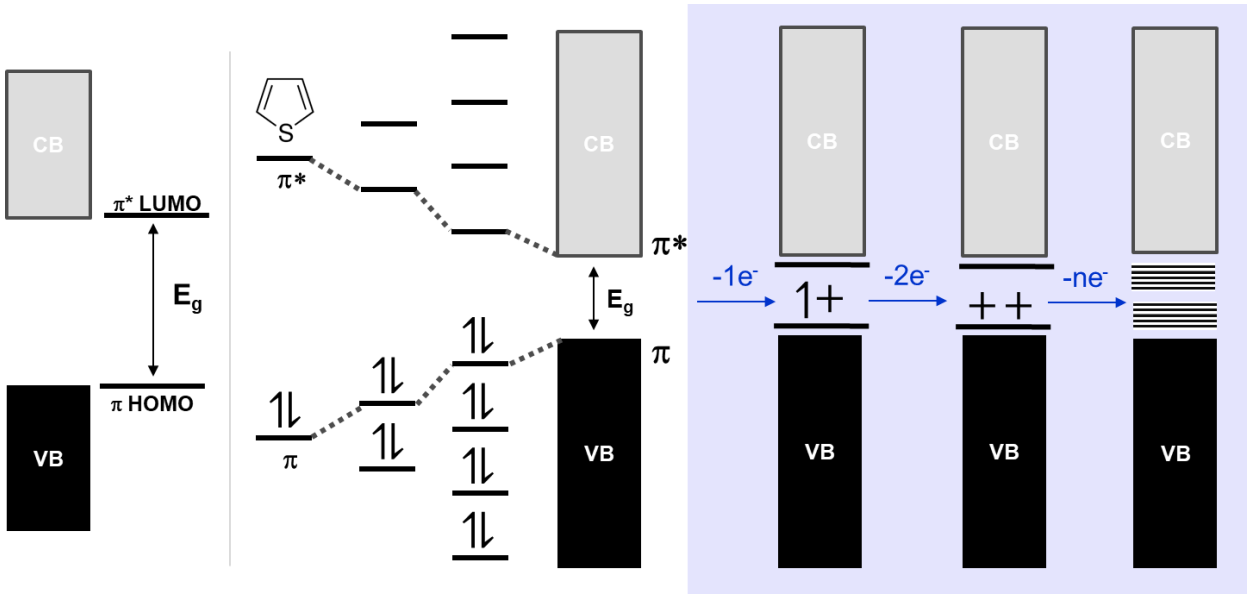

Figure 1.1 Electronic properties of Conjugated Polymers. a) Conceptual model of the buildup of electronic energy bands using thiophene (Th) to represent conjugated polymers. Band diagrams showing the differences in energy for metals, semiconductors, and insulators.

1.3 Doping of conjugated polymers

The doping of CPs has a long history in the study of organic electronics. They were uninteresting from the point of view of electronic materials until the 1970s when the metallic

conductivity in halogen-doped polyacetylene was discovered.[4] Currently (2021), the most popular doped CP is PEDOT:PSS, composed of partially π-doped (oxidized) poly(3,4-ethylene dioxythiophene) and charge compensated by anionic polystyrene sulfonate.[8] The ability of π-electron polymers to be reversibly doped at room temperature makes them fundamentally different from conventional inorganic semiconductors. The term "doping" does not merely imply an oxidation or reduction reaction. The doping of CPs implies i) charge transfer by oxidation (π-doping) or reduction (n-doping), ii) insertion of counterions to maintain charge neutrality, and iii) the simultaneous change in chemical potential of the π-system. The oxidation of π-conjugated backbones generates positive charge carriers (holes) and increases their π-type character. As the π-doped product is polycationic, anions must be incorporated into the polymer to maintain charge neutrality. Doping of CP can be achieved by five techniques: electrochemical doping, chemical doping, in-situ doping, photo/radiation-induced doping, or charge-injection doping. This thesis focuses on the electrochemical and chemical/molecular doping of CPs, which are discussed in detail below.[9]

Electrochemical doping. The reversible and controlled nature of electrochemical doping and dedoping makes it more advantageous than chemical doping. In electrochemical doping, the electrode supplies the redox charge (by donating or withdrawing electrons) to the CP's redox-active units. If the polymer is dissolved in solution, counterions are already surrounding the polymer in solvent and the redox charge is instantaneously compensated. However, in thin films the ions have to diffuse into and out of the polymer matrix to compensate for the charge, leading to morphological changes, swelling-shrinking, of the polymer film. Electrochemical doping is the most elegant doping method because it allows fine control of the redox-state or doping level of the CP via the cell voltage with respect to a reference electrode, also known as the applied voltage potential.

Chemical doping. In contrast, chemical doping, also known as molecular doping, involves electron transfer between the CP and a chemical reactant, the so-called dopant or impurity. In the case of π-doping, a difference between the electron affinity (EA) of the dopant and the ionization energy (IE) of the CP is beneficial ($EA_{dopant}>IE_{polymer}$). The dopant level, or charge carrier concentration, affects many electrical properties and can be high or low depending on application needs. Chemical doping can be efficient by a gaseous or solution pathway, but may lead to inhomogeneous doping if performed in the solid state.[10] The performance of CPs depends on their

doping properties and directly impact their application in optoelectronic organic devices ranging from transistors, light-emitting diodes, non-linear optics, photovoltaics, sensors, capacitors, and electrochromic devices.

1.4 Alkylenedioxythiophenes for Organic Electronics

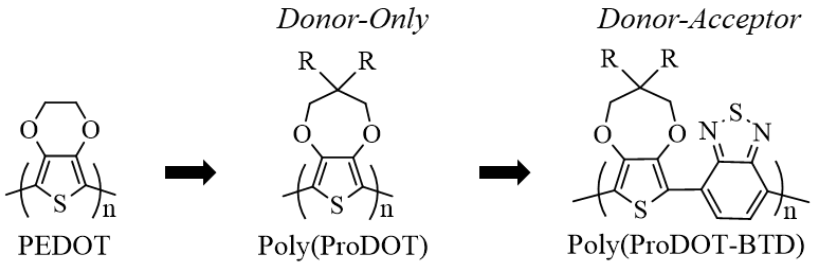

Scheme 1. Evolution of alkylenedioxythiophenes.

The advancement of organic CP based electrochromic devices is based in the development of alkylenedioxyhetereocycles. By introducing an alkyelenedioxy bridge of a heterocycle, (i) we incorporate electron-donating oxygen atoms on the β-β' positions of the heterocycle that increases the electron density in the conjugated system by raising the HOMO level and minimally affecting the LUMO level, allowing for easy oxidation and redox reversibility, (ii) we block the β positions from participating in unwanted α-β and β-β couplings during polymerization and enhance the reactivity of the α positions for substitution or carbon-carbon cross coupling, and (iii) we can introduce various solubilizing side chains on the alkylene bridge which is away from the conjugated backbone, allowing for solubility in common organic solvents without drastically altering the effective conjugation length and change in steric hinderance between π-conjugated monomer units. This approach has been successfully used to functionalize thiophenes, pyrroles, furans and selenophenes. Polymers composed of alkylenedioxythiophenes (ADOT), particularly PEDOT, have rapidly gained notoriety among conducting polymers since the beginning of the 1990s. The conducting form of ADOTs are valuable for their high degree of visible light transmissivity, low oxidation potential, moderate band gap, and concurrent environment stability. For electrochromics, high color contrast between the neutral, visible state and the doped, transparent state is achievable with ADOT-based systems. Even more, extending the ethylene

bridge of PEDOT to a propylene bridge allows introduction of solubilizing side chains onto the polymer by substitution of the central carbon atom. The 3,4-propylenedioxythiophene (ProDOT) monomer has become a popular choice for electrochromic polymers because introduction of alkyl side chains on the propylene bridge endows it with good solution processibility and thin-film properties, while still maintaining the electrical properties of the ADOTs.[11–15]

1.5 Donor-Acceptor Structures

One of the simplest ways to take advantage of the strong electron rich properties of ProDOT is to couple it with electron poor monomers, formally known as donor-acceptor (D-A) type structures. Combining electron-releasing (push) and electron-withdrawing (pull) units to modulate the HOMO-LUMO gap of a polymer, also referred to as a 'push-pull' CPs, can effectively regulate the magnitude of the band gap and therefore allow fine tuning of the absorption wavelength from colored to transmissive states, ranging from the ultraviolet, through the entire visible region of the spectrum, and well into the near-infrared. This strategy relies upon the fact that each moiety contributes to lowering the bandgap of the π-system by either decreasing the ionization potential via choice of donor unit or by increasing electronic affinity via choice of acceptor unit. Relatively small band gaps ranging between 1.0 and 1.9 eV are achievable with D-A structures. As such, interesting opto-electronic properties are accessible through the D-A strategy, including access to the entire color palate through careful selection of the D-A units for electrochromics. This alternating structure results in two strong absorption bands in the UV-vis-NIR consisting of a low energy D-A charge transfer (CT) and a high energy π-π* transition that is delocalized along the polymer backbone (Figure 1.3.1). This absorption spectrum provides two advantages in that the CT absorption can be below 1.0 eV, while the higher energy transition provides relatively broad spectral coverage. The D-A CT creates a 'push-pull' effect between the D-A units, resulting in greater double bond character between and causing planarization of the conjugated backbone and a decrease in the HOMO–LUMO gap. Control of the monomers' electron donor and acceptor strength, monomer ratio, and sequence allows fine regulation of the polymer's band gap energy, and thereby control of the material's optical and electronic properties. Additionally, D-A structure generally exhibit pronounced ambipolar charge transport (electron and hole conductance) in OFETs, approaching the performance of small molecular semiconductors. This is surprising because D-A type polymers are significantly less crystalline than donor-only polymers, such as

polythiophenes. This makes understanding their intrinsic D-A molecular properties important to the organic electronics community.

Among the D-A combinations, the PB benzothiadiazole combination has been a successful candidate for electrochromism. Extensive work by the Reynold's group has proven the PB system can achieve broad absorption with easily tunable coloring properties as a function of polymer doping level, conjugation length, and the ration between the D-A units. However, understanding of the molecular structures that define its redox active properties is lacking. Important features such as stability of the doped state and its reactivity in the ambient have rarely been considered at the molecular level, but nonetheless, are fundamental prerequisites for achieving longevity of electrochromic devices. These issues can become disastrous during device operation and result in materials with subpar performance or limited lifetimes.

1.6 Scope of this thesis

In this dissertation, we aim to understand the fundamental nature of π-conjugated charge carriers in a D-A system. This will be done by finding the answer to the following question: what is the convergence limit – *or the relationship between increasing π-conjugation and change in physical properties* – of a D-A conjugated system. This research highlights the following properties: change in molecular structure, chain conformation, and redox-active optical and electronic properties. Motivated by earlier investigations conducted via the oligomer approach, we will focus on the design, rigorous characterization, and in-depth structure-property analysis from small molecule to polymer scale lengths. Ultimately, this strategy reveals a distinction between oligomers and polymers lengths for the select π-system.

Firstly, we discuss the basic redox structure and properties of a D-A-D three unit small molecule to understand the essential nature of the conjugated system before investigating longer lengths. The design of a series of trimer molecules with varying functional groups are discussed, followed by electrochemical analysis of their radical cation and dication states. The trimer structure is chemically doped, isolated as ionic salts in its oxidized states, and thoroughly characterized in the solution and solid states. Secondly, we will demonstrate the synthesis and molecular structure of a complete D-A oligomer series ranging from n=3 to 21, and its polymer homologs. With this model series, we will show how the chain conformation changes with increasing conjugation length in solution, to reveal a conformational transition point. Thirdly, we

will discuss the accessible oxidation states of each chain length, analyze their specific optical and electronic properties, and present theoretical concepts which explain the nature of the charge carriers. We will close our discussion with an answer to the scientific question posed by this thesis and an outlook on the overarching vision that this research will propel.

CHAPTER 2. REDOX PROPERTIES OF A D-A-D OLIGOMER

2.1 Introduction

Despite the wide variety of D-A structures found in the literature, the nature of charge carrier species in small molecule oligomers containing acceptor units remains ambiguous and requires exploration. Recently, Teran and Reynolds[11] studied the neutral and oxidized states of two BTD containing D-A-D oligomers based on EDOT and ProDOT donors. This study presents evidence that π-dimerization of radical cations can lead to irreversibility of the redox reaction in CP thin films. Cao and Curtis[16] studied the charge carriers in EDOT-bithiazole oligomers of A-D-A and D-A-D sequences. In this study, the radical cation state of the electron poor oligomer undergoes π-dimerization while the radical cation state of the electron rich oligomer undergoes disproportionation into the neutral and dication states. A study by Polander *et al.*[17] determined that the D-A-D sequence of a BTD-dithienopyrrole based oligomer has a higher oscillator strength in the radical cation state versus the A-D-A sequence. They attribute this effect to the greater electron density in the D-A-D oligomer and the higher number of double bonds. Karsten *et al.*[18] studied the trimers of cyclopentadithiophene coupled with different acceptors in a D-A-D sequence to find out how their strength would impact the electronic properties of the oxidized species. They found that the electronic properties did not vary greatly for different acceptor units. This brief review shows that investigation of the oxidative properties of D-A π-systems requires further efforts.

In this chapter, we present our investigation into the oxidation pathways and products of a D-A-D molecule, composed of sulfide endcapped ProDOT-BTD-ProDOT (PBP), by electrochemical oxidation and chemical oxidation-isolation. Electrochemistry is used to extract information about the oxidation potential, valence band energy level, reversibility of the redox species, and the extent of interaction between the two electroactive ProDOT groups. Chemical oxidation is used to complement the electrochemical analysis by allowing investigation of the molecular structures of the isolated radical cation and dication states. This is achieved by oxidation of the D-A-D molecule with antimony (V) chloride ($SbCl_5$) and isolation of the oxidation states as $SbCl_6$ salts. Five derivatives of the D-A-D structure are also used to uncover the impact of long vs. short side chain, D-A-D vs. D-D-D sequence, and endcapping group on the electrochemical properties of the central PBP system. These results are presented in Appendix A.

2.2 Results and Discussion

2.2.1 Design and Synthesis

A discrete D-A-D molecule composed of PBP and sulfide endcapping groups was synthesized, as shown in Scheme 1 and described in Appendix A. In this study, two derivatives of the D-A-D molecule (3A-1 and 3A-2) are prepared. The long solubilizing side chain derivative, 3A-1, was used for electrochemical and variable temperature spectroscopic studies. The short side chain derivative, 3A-2, was chosen for x-ray crystallography, mass spectrometry, and density functional theory (DFT) calculations.

ProDOT (R=ethylhexyloxy) was purchased commercially and ProDOT (R=H) was synthesized according to previous reports.[19,20] As shown in Scheme 1, initial end capping of the ProDOT unit was achieved by monolithiation with n-Butyllithium (n-BuLi) in tetrahydrofuran (THF) and subsequent reaction with dimethyldisulfide to give ProDOT-SCH3 in 80% yield. Palladium catalyzed direct arylation cross-coupling of ProDOT-SCH3 and dibromo-BTD was conducted to produce the tri-heterocyclic molecule, 3A-1, in 41% yield.

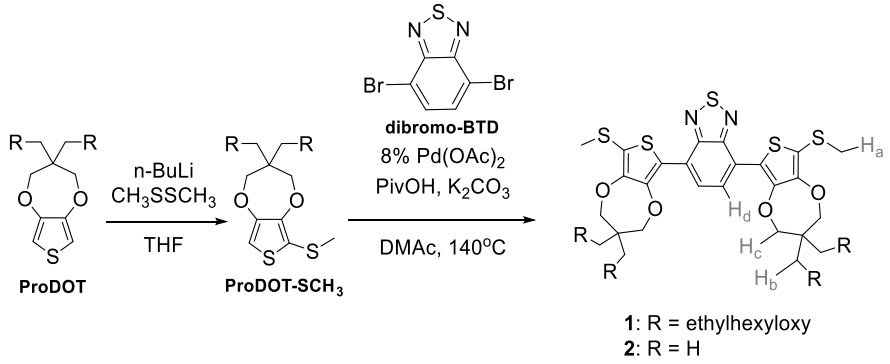

Scheme 1. Synthesis of the sulfide endcapped ProDOT-BTD-ProDOT molecules 1 and 2. Hydrogen atom labels on 1 correspond to the ^{1}H NMR spectra in Figure 2.6. (Abbreviations: Pivalic Acid (PivOH), Dimethylacetamide (DMAc)).

2.2.2 Electrochemistry

Initial CV of 3A-1 showed a single and fully reversible oxidation step at an $E_{1/2}$ potential of 0.405 V (vs. Fc^+/Fc). Scan rate-dependent experiments showed no change in anodic voltage and net chemical reversibility, indicating Nernstian type behavior and a diffusion coefficient of 2.67 ×

10^{-5} cm^2/s. However, a closer investigation revealed two overlapping redox waves. The difference in the two standard potentials was not quantifiable by CV due to the broadening effect of the charging current on the faradaic process, and thereby required higher sensitivity of the faradaic current by DPV, revealing a 2e oxidation process with a 117 mV difference between the consecutive $E_{1/2}$ potentials at $E_{1/2}^1$=305 mV and $E_{1/2}^2$=422 mV, and a comproportionation constant of K_c=95. A potential difference above 100 mV between consecutive oxidative states in a π-conjugated molecule typically shows that interaction between the two electroactive centers is involved, in this case the (ProDOT-SCH_3 donor units).[21–23] The first single electron transfer process initially led us down a different investigative path in which we suspected the molecular structure to be the cause of the seemingly single-electron oxidation event. We explored the influence of the molecular structure on the electrochemical behavior of a 3-unit conjugated oligomer. The following sections describe the journey we undertook to understand the influence of the D-A monomer sequence, side chain, and endcapping group on the electrochemical behavior of a three-unit conjugated oligomer. In hindsight, we took the scenic route.

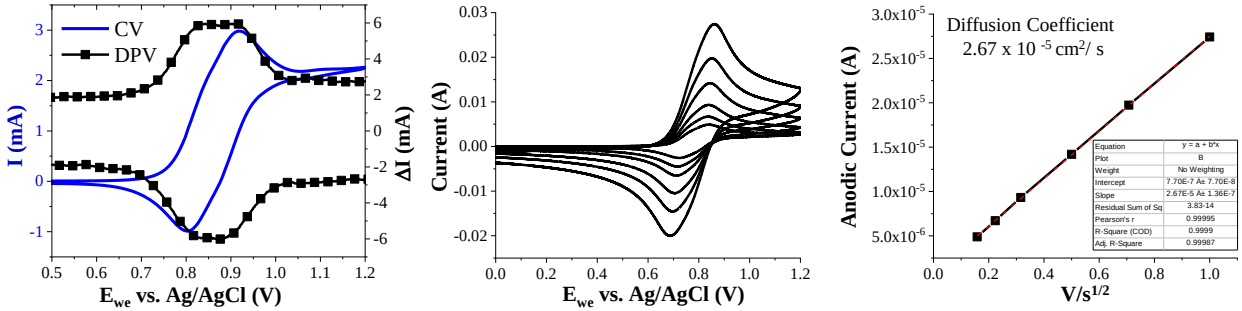

Figure 2.1. A) CV and DPV of a 1 mM solution of 3A-1 in 0.2 M $TBAPF_6/CH_2Cl_2$ at a platinum button working electrode vs. Ag/AgCl (Ferrocene $E_{1/2}$ = 0.51V vs. Ag/AgCl). B) Scan rate dependence of 3A-1, and C) Current vs. square root of scan rate and diffusion coeffcient.

2.2.3 Spectroelectrochemistry

After investigation of the molecular structure was exhausted, the electronic properties of the radical cation and dication states of the D-A-D structure were probed. The two oxidation states of 3A-1 are expected to have distinct absorption properties in the ultraviolet-visible-near infrared (UV-vis-NIR) region and thus 3A-1 was subjected to spectroelectrochemistry in solution. To induce formation of the one-electron and two-electron oxidized species, 3A-1 was treated with

increasingly positive potentials in increments of 25 mV (Figure 2.1B). Initially, electrochemical oxidation gives rise to a pair of absorption bands at 808 and 1295 nm that corresponds to the mid-gap transitions of the radical cation (3A-$1^{\bullet+}$). Further increasing the potential resulted in depletion and hypsochromic shifting of the neutral D-A charge transfer band at 490 nm, whereas 3A-$1^{\bullet+}$ continued to increase in absorbance. Absorption by the dication (3A-1) at 620 nm began to grow before consumption of 1 was complete, presumably because diffusion was slow in the unstirred solution.[24] At later stages in the oxidation, the transformation of 3A-$1^{\bullet+}$ to 3A-1 became isosbestic with an isosbestic point at 734 nm. It should be noted that conjugated structures like 3A-1 undergo intermolecular interactions in solution and so concentration effects must be excluded. At a higher concentration of 2×10^{-3} M, the oxidation of 3A-1 showed a similar progression and indicated that the electron-transfer processes are sequential and independent of the initial molecule concentration.

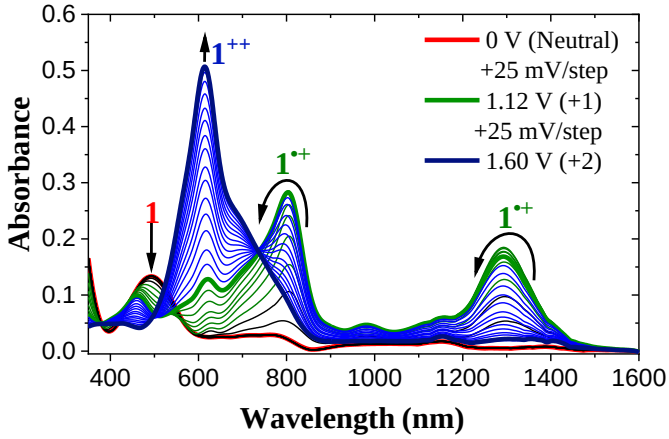

Figure 2.2. Spectroelectrochemistry of a 40 μM solution of 1 in 0.2 M $TBAPF_6/CH_2Cl_2$, conducted in an optically transparent thin layer quartz cuvette equipped with a platinum honeycomb electrode vs. Ag/AgCl.

2.2.4 Chemical Oxidation

In the following section, we describe the chemical oxidation of the D-A-D molecules 3A-1 and 3A-2 by $SbCl_5$ in solution. Chemical isolation of the radical cation and dication states allowed for further structural and mechanistic characterizations well beyond the limits of electrochemical techniques, such as x-ray crystallography, UV-vis-NIR, EPR, and NMR methods. $SbCl_5$ was chosen after weaker oxidants such as $FeCl_3$, $AgPF_6$, BF_3, and H_2O_2 were unable to achieve

stoichiometric control of the oxidation reactions and failed to produce high yields of the desired products. Oxidation by $SbCl_5$ typically proceeds with the following stoichiometry[25]:

$$3SbCl_5 + 2e^- \rightarrow 2[SbCl_6]^- + SbCl_3 \text{ (Pathway 1)}$$

In addition to its strong Lewis acidity, $SbCl_5$ is also a powerful chlorinating reagent for aromatic hydrocarbons.[25–27] This dual oxidation-chlorination reactivity can be problematic in certain cases, such as the oxidation of electron rich molecules, where competition between one-electron transfer and electrophilic chlorination can take place. Ligand-disproportionation of $SbCl_5$ is known to generate the electrophilic complex $SbCl_4^+$, a reactive source of chloronium ions (Cl^+) that are two-electron oxidants.[26,28–30]

$$2\ SbCl_5 \rightleftarrows SbCl_4{-}Cl_2{-}SbCl_4 \rightleftarrows SbCl_6^- + SbCl_4^+ \text{ (Pathway 2)}$$

When present in solution, chloronium ions can cause undesired chlorination reactions and lead to impure radical cation solids. During our investigation of 3A-1, we observed that $SbCl_5$ is able to perform chloronium ion transfer oxidation is a function of its concentration, where the quantity of the two-electron oxidation product increases linearly as a function of $SbCl_5$ molarity, irrespective of a constant one-electron oxidation stoichiometry. Due to the difficulty of directly observing the reactive $SbCl_4^+$ complex, we set out to quantify the chlorinated cations that form by reaction with $SbCl_4^+$.[28,29,31,32] This section also discusses the concentration dependent reactivity of $SbCl_5$ as a chemical oxidant.

Radical Cation. Chemical oxidation of 3A-1 by $SbCl_5$ successfully generated the radical cation as a hexachloroantimonate salt. Consistent with Pathway 1, reaction with one equivalent of a 0.1 M stock solution of $SbCl_5$ in CH_2Cl_2 formed the one-electron oxidation state, which was isolated in 47% yield by precipitation with *n*-hexane at -18°C. Dissolution of the purified 3A-$1^{\bullet+}(SbCl_6)$ in dichloromethane (CH_2Cl_2) showed UV-vis-NIR absorption peaks consistent with those obtained for 3A-$1^{\bullet+}$ by spectroelectrochemistry (Figure 2.3).

Dication. 3A-1 was discovered to be generated through strikingly different mechanisms by oxidation with $SbCl_5$. In contrast to the mechanism of 3A-$1^{\bullet+}$, the one-electron oxidation reaction of 3A-1 with 1.0 M $SbCl_5$ yielded a mixture containing all three states (3A-1, 3A-$1^{\bullet+}$, and 3A-1), whereas one-electron oxidation with 0.02 M $SbCl_5$ solely produced 3A-$1^{\bullet+}$. The different reactivity of $SbCl_5$ at low and high concentrations indicates that two different species are responsible for the electron transfer reaction. Moreover, the reaction mixture remained stable in the presence of the neutral molecule at high concentrations without any signs of the dication peak decreasing in

absorbance intensity. To explore the concentration dependence of the oxidant further, one-electron oxidation of a 30 mM solution of 3A-1 was carried out at varying concentrations of $SbCl_5$, ranging from 0.02 – 1.0 M. The absorbance intensity of 3A-1 increased linearly as a function of the $SbCl_5$ molarity while keeping the stoichiometric ratio constant for one-electron oxidation. Treatment of 3A-1 with 1.0 M $SbCl_5$ generates the dication in 18% yield by precipitation with *n*-hexane at -78°C. The rest of the reaction products is a mixture of unreacted 3A-1 and 3A-1$^{\bullet+}$. Dissolution of 3A-1$(SbCl_6)_2$ shows UV-vis-NIR absorption peaks consistent with those obtained for 3A-1 by spectroelectrochemistry.

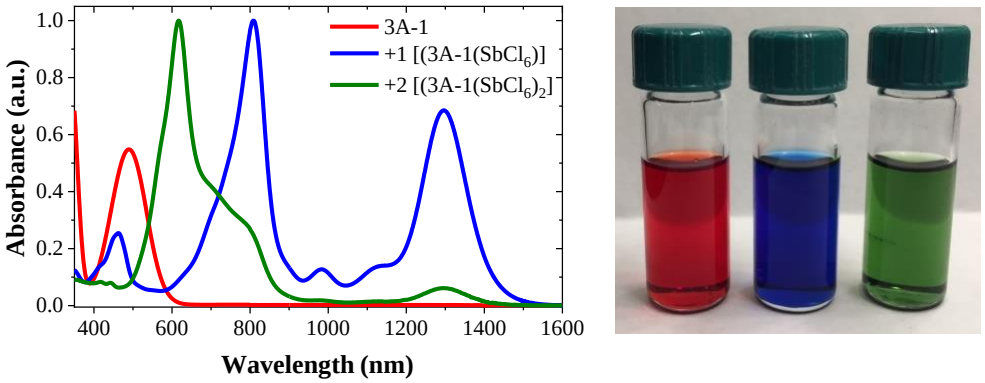

Figure 2.3. UV-vis-NIR absorption spectra of 3A-1, 3A-1$^{\bullet+}$ and 3A-1 as $SbCl_6$ salts redissolved in CH_2Cl_2. (Inset: color of 1 (red), 1•+ (green) and 1 (blue) in solution).

At higher concentrations of $SbCl_5$, oxidation of 3A-1 occurs by an unanticipated two-electron transfer pathway. The concentration dependence of the reaction suggests that $SbCl_5$ must undergo ligand-disproportionation at higher concentrations in solution to produce the positively charged antimony tetrachloride ($SbCl_4^+$) complex, a reactive source of electrophilic chloronium ions (Cl^+). The kinetic stability of the dication in the presence of neutral 3A-1 in the reaction mixture implies that the two-electron oxidized product must be a modified form of 3A-1. Otherwise, isolated 3A-1 reacts with 3A-1 in solution to undergo radical comproportionation and yields 3A-1$^{\bullet+}$(Appendix A). The modified form of the dication is apt to be a chloride-adduct, Cl-1$^+$, which can form as a result of chloronium ion transfer, a two-electron oxidation route (Pathway 2).[33–35]

Electrophilic chlorination of 3A-1 is most likely to occur at the sulfur atom of the sulfide terminal groups as each is an electron rich site amenable to halonium ion transfer. The formation

of sulfur-halides by treatment of sulfides with halogenating agents has also been well documented in the literature.[33–35] Meerwein *et al*. first prepared a stable salt of dimethyl chlorosulfonium hexachloroantimonate by reaction of dimethyl sulfide with 2–4 M excess of $SbCl_5$.[36] A similar study by Partridge corroborates the concentration dependent reactivity of $SbCl_5$ for the oxidation of diethyldicarbazole, for which the organic molecule was oxidized only when the $SbCl_5$ solution reached a critical concentration of 0.1 M or higher in CH_2Cl_2.[37] Yet, the concentration dependent reactivity of $SbCl_5$ still remains unrecognized. Chloronium ion transfer would give the sulfur halide and result in a net $2e^-$ electron oxidation, yielding Cl-1^+, which is formally a chloride adduct of 3A-1 (Scheme 2).[38]

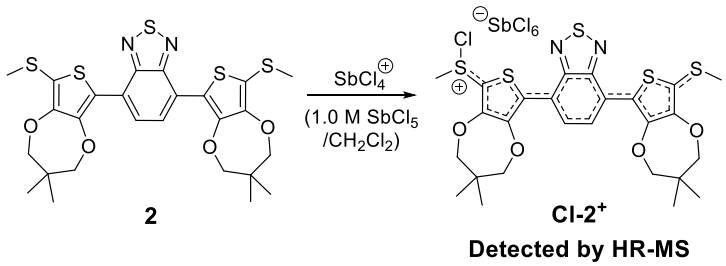

Scheme 2. Proposed mechanism for the atom transfer oxidation ($-2e^-$) of 3A-2 to Cl-2^+, an adduct of 3A-2.

Attempts to isolate Cl-1^+ failed, so high resolution mass spectrometry (HR-MS) studies were conducted with 3A-2, which has a lower mass and fewer carbon atoms than 3A-1. A reaction solution of 3A-2 with one equivalent of 1.0 M $SbCl_5$ in CH_2Cl_2 was used to successfully detect the chlorine 35 and 37 isotope peaks of Cl-2^+ at 627 and 629 m/z (Appendix A). The presence of methanol in the vaporization chamber at high temperatures (100°C) caused solvolysis of Cl-2^+ to the methoxide adduct, exposing the labile nature of Cl-2^+. Furthermore, the chlorine isotope peaks were only measurable for a few minutes after ionization of the reaction solution.

2.2.5 X-Ray Crystallography

Attempts to crystallize 3A-1, 3A-$1^{\bullet+}$, and 3A-1 failed, presumably due to the bulky solubilizing side chains present on the propylene bridge of the ProDOT units. As a result, 3A-2 served as a proxy for 3A-1. Chemical oxidation of 3A-2 by $SbCl_5$ generates the radical cation and dication as hexachloroantimonate salts. The redissolved solutions of 3A-$2^{\bullet+}$ and 3A-2 gave

absorption spectra that matched 3A-1$^{\bullet+}$ and 3A-1 without any discrepancy in their absorption wavelengths (Appendix A). Single crystals of 3A-2$^{\bullet+}$ were obtained by slow diffusion of *n*-hexane into *o*-dichlorobenzene under air at room temperature for one week. Two black crystals with distinct morphologies were selected and subjected to single crystal analysis. A rod shaped crystal of 3A-2$^{\bullet+}$($SbCl_6^-$) was confirmed to possess a 1:1 organic radical to hexachloroantimonate anion ratio (Figure 2.4). Another block shaped crystal was resolved to be a two-electron oxidized decomposition product of the cation, 3A-2'.

Although a single crystal of 3A-2 was not obtained, a two-electron oxidized decomposition product with a partial quinoidal character was detected. Remarkably, one of the sulfide endcapping groups of the parent structure proved to have been substituted by an oxygen atom, generating the two-electron oxidized, asymmetrically terminated 3A-2' molecule (Figure 2.4). Theoretical calculations of the absorption spectrum of 3A-2', derived via time-dependent DFT (TDDFT) calculations (see below, Figure 2.4), exhibits a maximum absorption peak at λ_{TDDFT}=601 nm. This absorption spectrum is similar to the experimental and theoretical absorption spectra of 3A-2 (λ_{exp}=620 nm/ λ_{TDDFT}=626 nm). This analysis implies that 3A-2' and 3A-2 have similar character. Furthermore, comparison among the DFT geometries and TDDFT-derived spectra of 3A-2$^{\bullet+}$, 3A-2, and 3A-2' shows that 3A-2' has mixed radical cation and dication character, as suggested by the crystal structure: π-bond lengths closer to the ketone group are similar to the theoretical bond lengths of quinoidal 3A-2, while the π-bond lengths closer to the sulfide group are similar to experimental and theoretical bond lengths of cyanine-like 3A-2$^{\bullet+}$ (Figure 2.5, Table S1 in Appendix A); further details of the DFT and TDDFT calculations are provided below. A 1.241(7) Å bond length of the new C=O bond agrees with reported literature values of similar structures.[39–41] Additionally, there is an increase in the adjacent C-S bond of the thiophene ring from 1.726(3) to 1.784(6) Å on going from 3A-2$^{\bullet+}$ to 3A-2', which confirms the electron withdrawing nature of the ketone functional group.[41] Nonetheless, CHN-Cl analysis of 3A-2($SbCl_6^-$)$_2$ confirmed a 1:2 cation to anion ratio in the solid state.

Based on the evidence given, we propose the formation of 3A-2' is plausible because upon oxidation of 3A-2, the terminal sulfide substituents can take on a sulfonium ion character and become conjugated with the D-A-D π-backbone. Nucleophilic attack by adventitious water molecules from ambient air then becomes feasible at the sp^2 carbon* atom of thiophene, followed by the elimination of CH_3SH to yield a ketone (Figure 2.5B). In other words, delocalization of the

positive charge onto the thiophene ring makes it more susceptible to nucleophilic attack.[42,43] Oxidation of the alcohol intermediate by O_2 or another 3A-2$^{\bullet+}$ ion in solution becomes possible because formation of a carbon-oxygen double bond ultimately stabilizes the quinoidal form, indicating a two-electron oxidation decomposition route.

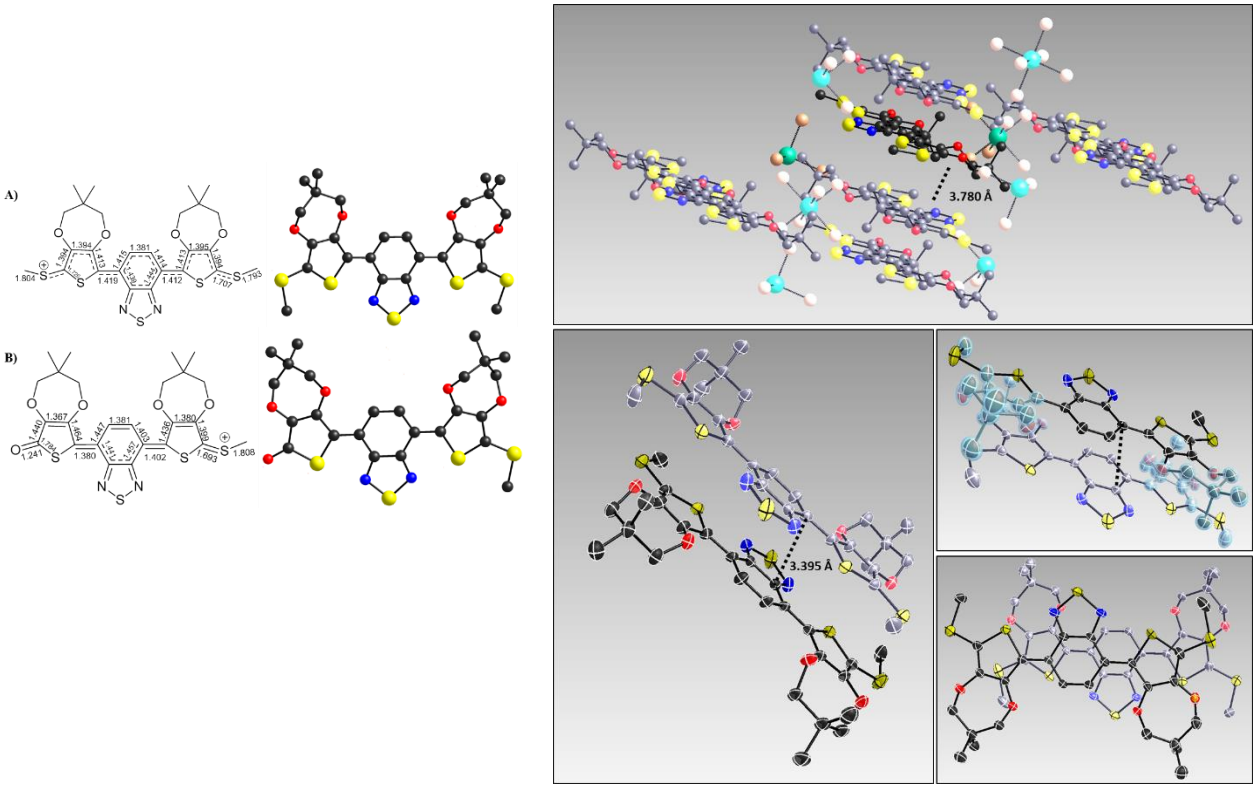

Figure 2.4. A) Molecular structure of 3A-2$^{\bullet+}$ as an isolated monomer (moiety $C_{26}H_{28}N_2O_4S_5 \cdot Cl_6Sb$) derived from x-ray crystallography, showing the bond lengths and chemical structure. The unit cell for 3A-2$^{\bullet+}$ contains 0.5 of 2($SbCl_6$) counter anions on inversion centers per 1 organic cation and 0.5($C_6H_4Cl_2$) solvent molecule. B) Molecular structure of 3A-2' (moiety $C_{25}H_{25}N_2O_5S_4 \cdot Cl_6Sb$) derived from x-ray crystallography, showing the bond lengths and chemical structure. The unit cell for 3A-2' contains 1 $SbCl_6$ counter anion per 1 organic cation and 3A-2($C_6H_4Cl_2$) solvent molecules. Complete unit cells of the crystal structures are shown in Figure S13 in Appendix A.

2.2.6 Density Functional Theory (DFT) Calculations.

To examine the oxidation of PBP in more detail, we carried out DFT calculations on 3A-2, which was chosen to reduce the computational cost (by limiting the number of atoms in the alkyl chains). All calculations were carried out at the OT-ωB97X-D/6-31+G(d,p) [OT = optimally tuned] level of theory,[44–46] where the range-separation parameter ω for 3A-2 was tuned via the ionization

potential (IP)-tuning procedure[44–50]; importantly, non-empirically tuned long-range corrected density functionals have been suggested to be beneficial in the investigation of molecular systems that may possess either localized or delocalized charges (i.e., have mixed-valence character).[51] The influence of the solvent environment (CH_2Cl_2; ε=8.93) was modeled through the polarizable continuum model (PCM); overall, the analyses do not change if results from isolated (gas phase) calculations are used. Each optimized geometry was confirmed as a minimum on the potential energy surface through normal mode analysis. The Gaussian09 software suite was used for all DFT calculations.[52]

Bond Length as a Function of State. Three oxidation states were considered – 3A-2, 3A-$2^{\bullet+}$, and 3A-2^{++}. Starting with 3A-2, the geometry of the D-A-D π-conjugated backbone has an aromatic-like bond alternation pattern. The thiophene moieties of the ProDOT units are twisted by ≈24° with respect to the central BTD unit, while the methyl group of the methylthio moiety is nearly orthogonal (≈83°) with respect to the thiophene ring. Upon oxidation to form 3A-$2^{\bullet+}$, there is a notable change in the dihedral angles, with both moving to a more planar conformation (each on the order of ≈2°), and the bond lengths along both moving to a more planar conformation (each on the order of ≈2°), and the bond lengths along the π-conjugated pathway take on a cyanine-like form. The planarization is even further enhanced upon going to 3A-2, where the dihedral becomes less than 1°. The bond lengths along the primary π-conjugated pathway also undergo considerable change, with the double-bond–single-bond alternating/aromatic character of the neutral species being replaced by more cyanine-like character in the radical cation, and then quinoid character for the dication. Importantly, both the bond length changes and the charge distributions (Figure S8) are symmetric; here we used charge model 5 (CM5) charges as they are basis set independent, have less conformational dependence compared to many other population analyses, and have been shown to reproduce molecular dipoles. This means that the monocation and dication charges are equally delocalized in each case across the entire structure. We do note that: (i) attempts to break the molecular symmetry of 3A-$2^{\bullet+}$ via Hartree-Fock geometry optimization followed by DFT calculations resulted in delocalized charges, providing some confidence that the charge is delocalized in this system; (ii) for 3A-2, we evaluated the possibility that the system could form either a closed-shell singlet or open-shell triplet state, but, generally, the two states showed similar geometric patterns and charge distributions (see SI for further details). For 3A-2', the situation does differ. When compared to the closed-shell singlet state of 3A-2 and 3A-$2^{\bullet+}$, the bond lengths

of 3A-2’ show a mixed bond character with quinoidic bond properties in the thiophene ring where the ketone substitution occurs and cyanine-like bond properties in the remainder of the molecule. Overall, the molecular geometries determined by x-ray crystallography and the DFT calculations agree reasonably well.

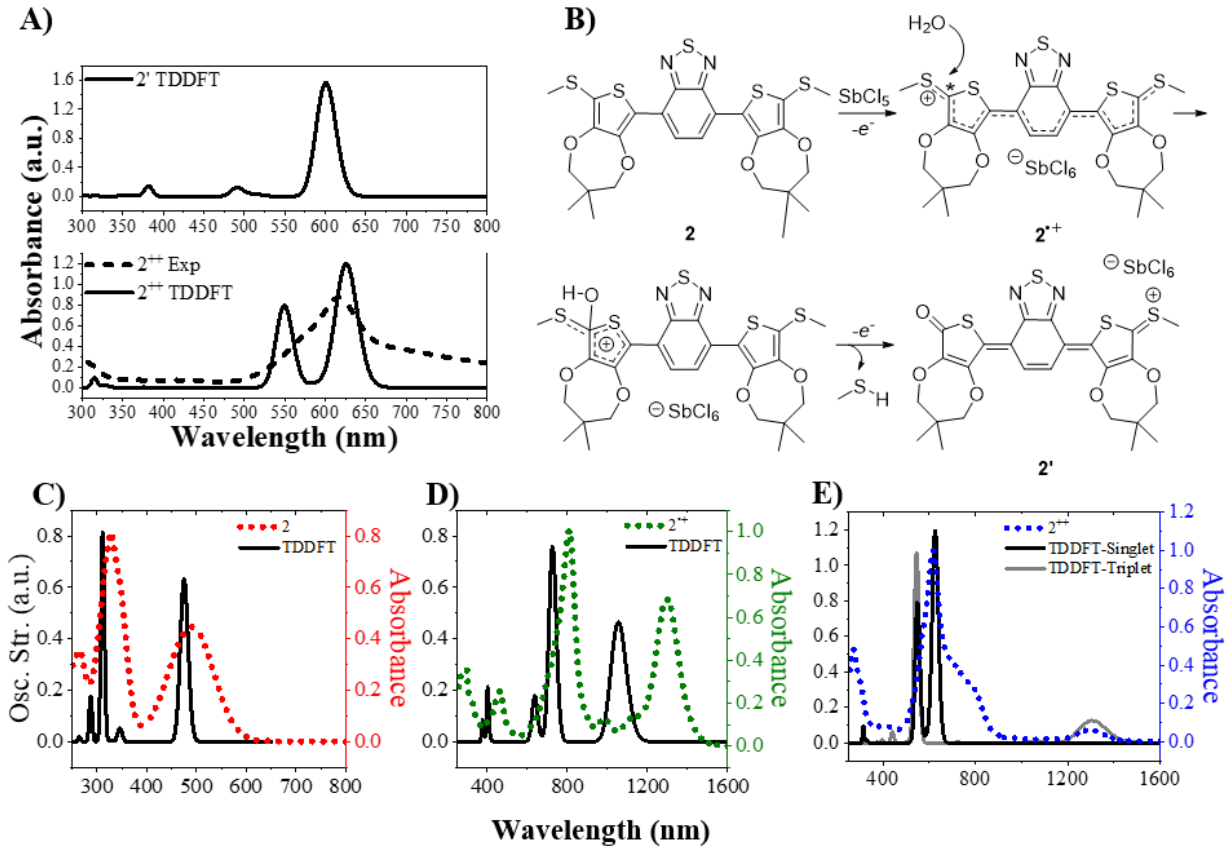

Figure 2.5. A) Comparison between the UV-vis-NIR absorption spectrum of 3A-2 and the TDDFT derived spectra of 3A-2’ and 3A-2(singlet) at the TD-OT-ωB97X-D/6-31+G(d,p)level of theory. B) Proposed mechanism for the degradation of 3A-2$^{\bullet+}$ to 3A-2’. Comparison between the experimental (dotted line) and TDDFT spectra (solid line) for C) 3A-2, D) 3A-2$^{\bullet+}$ and E) 3A-2 in the singlet and triplet states.

Optoelectronic Properties. To explore the excited state characteristics of 3A-2, 3A-2$^{\bullet+}$, and 3A-2 in more detail, TDDFT calculations were carried out at the TD-OT-ωB97X-D/6-31+G(d,p) level of theory. There is good agreement between the experimental and TDDFT-derived spectra (Figure 2.5C-E), with the major experimental peaks accounted by the TDDFT calculations; note that the TDDFT-based spectra were created through Gaussian convolutions of the calculated transitions with a full-width-at-half-maximum (fwhm) of 0.1 eV. Starting with 3A-2, the low-lying

$S_0 \rightarrow S_1$ vertical transition occurs at 2.61 eV (475 nm; *f* [oscillator strength] = 0.63), and is predominantly a HOMO (highest-occupied molecular orbital) → LUMO (lowest-unoccupied MO) transition. The lowest-lying transition of 3A-2$^{\bullet+}$ lies at 1.18 eV (1054 nm; *f* = 0.46) and, as expected, occurs between the HOMO–1 (nomenclature used in reference to the neutral molecule) → SOMO (singly-occupied MO). In the case of 3A-2, the spectrum does depend on whether the singlet (closed-shell) or triplet (open-shell) forms are used. In the case of the singlet, the lowest lying transition is at 1.98 eV (626 nm; *f* = 1.19) and is a HOMO → LUMO transition (in the parlance of the neutral molecule, these are the HOMO-1 and HOMO, respectively). However, when the triplet, open-shell case is considered, a very low energy 0.95 eV (1305 nm; *f* = 0.13) transition, consistent with the low-energy peak observed experimentally, and a strong transition at 2.27 eV (546 nm; *f* = 1.07) are present. These results suggest that there could be some open-shell character to 3A-2. Finally, for 3A-2' (Figure 2.5A), the first transition lies at 2.06 eV (601 nm; *f* = 1.57) and is predominantly at HOMO → LUMO excitation, which is comparable to 3A-2.

2.2.7 Electron Paramagnetic Resonance (EPR) Spectroscopy.

EPR spectroscopy of 3A-1$^{\bullet+}$ confirmed its paramagnetic nature with a well resolved hyperfine structure and a g-value of 2.007 (Figure 2.6A). A nine-line splitting pattern, including the two weak, broad signals on the outskirts of the hyperfine structure, correspond to radical hyperfine coupling from the acceptor domain of the D-A-D molecule. Simulation of the spectrum was accomplished with two nitrogen (I=1) and two hydrogen atoms (I=1/2) of the BTD moiety, yielding hyper-fine coupling constants of A_N = 1.37 G and A_H = 2.74 G. These values suggest a stronger radical interaction with the hydro-gen atoms than the nitrogen atoms of the acceptor. Lowering the temperature to 170 K caused a drastic decrease in the radical intensity signal to almost zero, consistent with the formation of diamagnetic, spin coupled dimers (Figure 2.6B), discussed in detail below. [53–57]

A solution of 3A-1 shows an extremely weak EPR signal and a slightly higher g-value, which is absent at low temperatures. This result is presumably due to a partial open-shell character of 3A-1 or due to the formation of paramagnetic complexes between residual radical cation and dication species in solution.[53] Further investigation is necessary to make a definitive conclusion.

2.2.8 Nuclear Magnetic Resonance (NMR) Spectroscopy.

To further study the molecular structures of 3A-1$^{\bullet+}$ and 3A-1^{++}, variable temperature ^{1}H NMR was conducted by tracking the three proton environments in the conjugated backbone of 3A-1; benzothiadiazole ('Hd', 2H), propylene bridge ('Hc', 4H) and sulfide terminal groups ('Ha', s, 6H). At room temperature the unpaired radical of 3A-1$^{\bullet+}$ caused paramagnetic line broadening of the ^{1}H peaks, severely hampering the spectrum's resolution. Only the alkyl side chain protons, which did not experience radical delocalization, were observable at room temperature (δ 0.5-1.5 ppm, δ 3.0-3.6 ppm; shown in SI). This prompted variable temperature NMR analysis of 3A-1$^{\bullet+}$, in keeping with its low temperature diamagnetism observed by EPR. A CD_2Cl_2 solution of 3A-1$^{\bullet+}$($SbCl_6$) was decreased from room temperature down to ~200 K. This led to a decrease in the chemical shift of 'Ha' and 'Hd' in relation to the neutral state. All 1H environments were accounted for and consistent with the coupling of free radical species to form NMR active π-dimers in solution (Figure 2.6C). The splitting of the singlet 'Ha' and 'Hd' protons indicated loss in symmetry of the D-A-D molecule upon π-dimerization. Warming the solution back to room temperature led to broadening of the peak signals again, indicating that the low temperature species were reversible and non-covalent dimers. The crystal structure of 3A-1$^{\bullet+}SbCl_6$ showed that it adopts a π-dimer form in the solid state, with a π-π stacking distance of 3.395 Å (Figure S9), which is less than the sum of carbon-carbon van Dar Waals radii. In conjunction, low temperature UV-vis-NIR of 3A-1$^{\bullet+}$ showed a hypsochromic shift of the radical cation absorption bands and formation of new absorption peaks at 624 and 938 nm (Figure S10). Solid thin films of 3A-1$^{\bullet+}$ confirmed the hypsochromic shift and π-dimer peaks to absorb at 638, 938, and 1458 nm (Figure S10). These results verify that two 3A-1$^{\bullet+}$ monomers can undergo π-dimerization at low temperature in solution. Overall, it is likely that this H-aggregated, π-dimer is composed of two radical cations in an asymmetrically stacked configuration.[53–56] This is a common phenomenon observed for the bridging of two paramagnetic radical complexes at low temperatures so that their unpaired spins interact.[58]

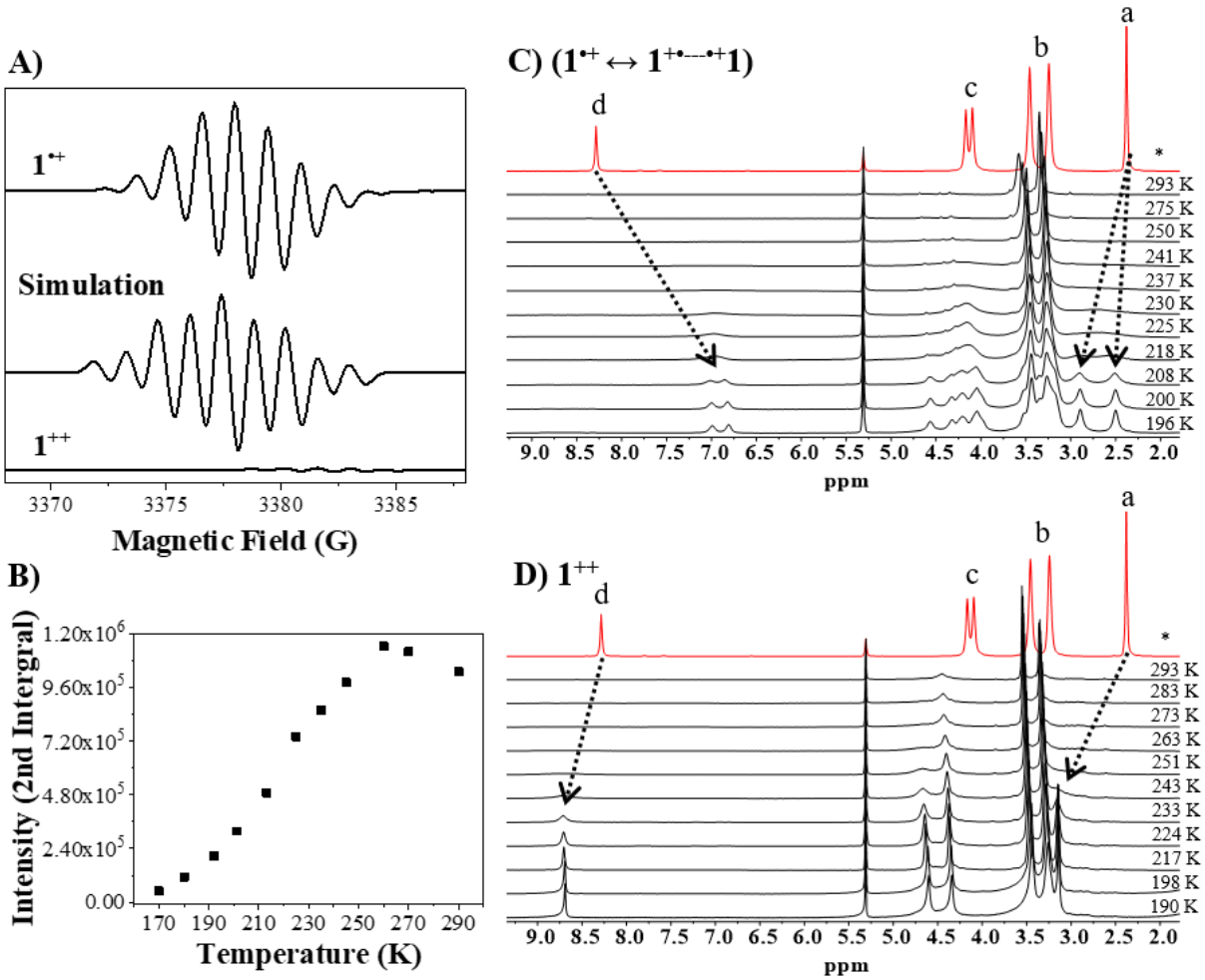

Figure 2.6. A) EPR spectra of 3A-$1^{\bullet+}$ and 3A-1 at 283 μM in CH_2Cl_2. WinEPR Simulation of 3A-$1^{\bullet+}$ was conducted with two ^{14}N atoms (A_N=1.37) and two ^{1}H atoms (A_H=2.74). B) Change in EPR intensity of 3A-$1^{\bullet+}$ in a 1:1 $CHCl_3$:CH_2Cl_2 solution at 283 μM from 290 K to 170 K. Variable temperature ^{1}H NMR of C) $1^{\bullet+}$ and D) 1 at 30mg/mL in CD_2Cl_2 from 293 K to ~200 K. Red line* corresponds to 1 at 200 K for comparison. Dotted arrows show the change in proton environments between neutral and oxidized states. Labels (a-d) correspond to proton environments of 1 as depicted in Scheme 1.

The room temperature NMR of 3A-1$(SbCl_6)_2$ (Figure 2.6D) exhibited the paramagnetic line broadening effect similar to 3A-$1^{\bullet+}$, in line with its extremely low EPR signal. Again, this may be due to either a partial open-shell, singlet state or residual radical species in the sample. It should be noted that oxidation of 3A-1 with excess $SbCl_5$ did not produce a diamagnetic species observable at room temperature. If the presence of residual 3A-$1^{\bullet+}$ is causing NMR peak broadening, then π-dimer peaks should be observed in the dication sample at low temperatures. In this case, no π-dimers were observed by low temperature NMR or UV-vis-NIR (Figure S10).

Lowering the NMR temperature from 290 K to 200 K led to a downfield shift of all the proton peaks. This downfield shift of the conjugated backbone proton signals is evidence of the aromatic to quinoidal transformation that 3A-1 undergoes upon two-electron oxidation. Unlike the dimerization of 3A-$1^{\bullet+}$ at low temperatures, the ^{1}H NMR spectrum of 3A-1 does not undergo peak splitting and is interpreted to retain its symmetry. All low temperature UV-vis-NIR and NMR results are summarized in Table S2.

2.3 Conclusion

The molecular consequences of electron transfer reactions in organic π-conjugated systems directly influence their redox functionality as electrochromic materials. Accordingly, it is important to understand the unique structure and reactivity of individual redox states. In this study, we have examined the molecular structures and mechanisms of four different electron oxidation products generated by the chemical reaction of a sulfide endcapped PBP molecule with $SbCl_5$. We confirmed the structures and reaction pathways of:

(i) the one-electron oxidation state

(ii) a decomposition product of the $1e^-$ oxidation state; via $2e^-$ oxidation and oxygen atom substitution at terminal position

(iii) the two-electron oxidation state

(iv) a chloride-adduct of the two-electron oxidation intermediate state; via chloronium ion transfer by $SbCl_4^+$

Using x-ray crystallography and DFT calculations, we confirmed that the D-A-D π-conjugated backbone changes from an aromatic to cyanine-like to quinoidal configuration from the neutral to radical cation to dication state. The EPR spectrum of the radical cation exhibited a well-resolved hyperfine structure with coupling constants of A_N = 1.37 G and A_H = 2.74 G due to electron delocalization across the acceptor domain. Low temperature conditions drove formation of spin coupled π-dimers in solution, with an apparent H-aggregated, asymmetric configuration as interpreted by NMR and UV-vis-NIR spectroscopy. Single crystals of the radical cation and its decomposition to a mono-ketone terminated product confirmed the instability of 3A-$1^{\bullet+}$ in the ambient due to increased lability of the sulfide terminal groups. We propose that this decomposition occurs because delocalization of a positive charge to the terminal sulfide groups upon oxidation transforms it into a sulfonium ion which can readily undergo nucleophilic

substitution in the presence of water. More notably, because the dication state (λ_{exp}=620 nm) could not be crystallized, the single crystal of the two-electron oxidized decomposition product (λ_{TDDFT}=600 nm) served as a comparable surrogate with partial quinoidal bond character.

Separate from the redox properties of the D-A-D molecule, we also uncovered new insight into the reactivity of $SbCl_5$ as a two-electron oxidant when present at high concentrations in dichloromethane. In contrast to the sequential electrochemical oxidation of 3A-1, chemical oxidation by $SbCl_5$ was not sequential nor stoichiometry based. Dication formation was observed to be a function of increasing $SbCl_5$ concentration, via a chloronium ion transfer ($SbCl_4^+$), whereas radical cation formation was observed to follow stoichiometric oxidation at dilute concentrations. HR-MS confirmed the formation of a chloride-adduct intermediate to justify a chloronium ion oxidation pathway as an alternative way to generate the dication state by $SbCl_5$ oxidation. This work provides new understanding of redox active organic D-A materials which can be beneficial for the development of, but not limited to, organic electronics such as electrochromic devices, redox flow batteries, and electrochemical transistors. Future work will focus on exploring the redox properties of conjugated molecules as a function of π-conjugation length and D-A sequence.

CHAPTER 3. CHAIN STRUCTURES AND CONFORMATIONS OF A π-CONJUGATED DONOR-ACCEPTOR OLIGOMER SERIES

3.1 Introduction

The rich optical, electrical, and mechanical properties of CPs are directly governed by their physical chain conformation and how chains are ordered in the solution and solid state. At first glance, the photophysics of CPs seem simple: strong electronic correlations and formation of tightly bonded excitons.[59] The occasional structural or chemical defect is believed to the perturb the delocalization pathway of π-electrons, leading to formation of distinct conjugated segments on the polymer chain. However, this picture is overall misleading. In fact, defects along a polymer chain can maintain conjugation while distorting the shape of the chain, one of the key features that endows CPs with flexibility while maintaining conductivity. The deception in trying to depict the shape of the conjugated backbone arises when the transition from the chemical to the physical perspective is made. What is the connection between the chemical structure of a polymer to the real physical essence of the polymer chain in solution or in thin film?

For simple and flexible polyolefins, such as polyethylene and polystyrene, the random-coil model is used to describe chain conformations as a function of monomer units in the form of a coiled-hydrodynamic sphere. For semiflexible π-conjugated systems which undergo specific intrachain and interchain interactions, the Kratky-Porod chain model is used to describe their flexibility by quantifying backbone stiffness, or persistence length (L_p), a characteristic length scale at which the backbone bends on average by 90 degrees; where at short length scales they behave as rigid rods (L_p=Lc) and at long length scales they behave as flexible coils (L_p<L_c). However, for high molecular weight polymers, if L_p is significantly shorter than L_c, the chain is a flexible coil. Based on freely rotating chains, the Kratky-Porod chain model describes worm-like polymers based on the relationships between average end-to-end distance through space ($\langle h^2 \rangle$), L_p, and the polymer chain-length (or contour length) (L_c). A continuous transition between the rod-like regime at small L_c/L_p and the coil like regime at large L_c/L_p captures both conformations for worm-like chains as a function of chain length, also referred to as the 'rod-to-coil' (order-to-disorder) transition. CPs are rod-like at low molecular weights and large persistence lengths; otherwise they are semiflexible.[59–65] Only a few polymers are extremely stiff, such as DNA

(persistence lengths, 50−70 nm).[66] Despite the stiffness of DNA, it could behave as a flexible coil if it is long enough. CPs typically do not achieve a comparable persistence length with DNA due to the existence of a significant amount of backbone torsion. To the best of our knowledge, no other study has measured the rigidity of a D-A conjugated polymer composed of P and B via the oligomer approach. Therefore, it is of great interest to systematically investigate backbone rigidity and the rod-to-coil transition of D-A CPs experimentally.

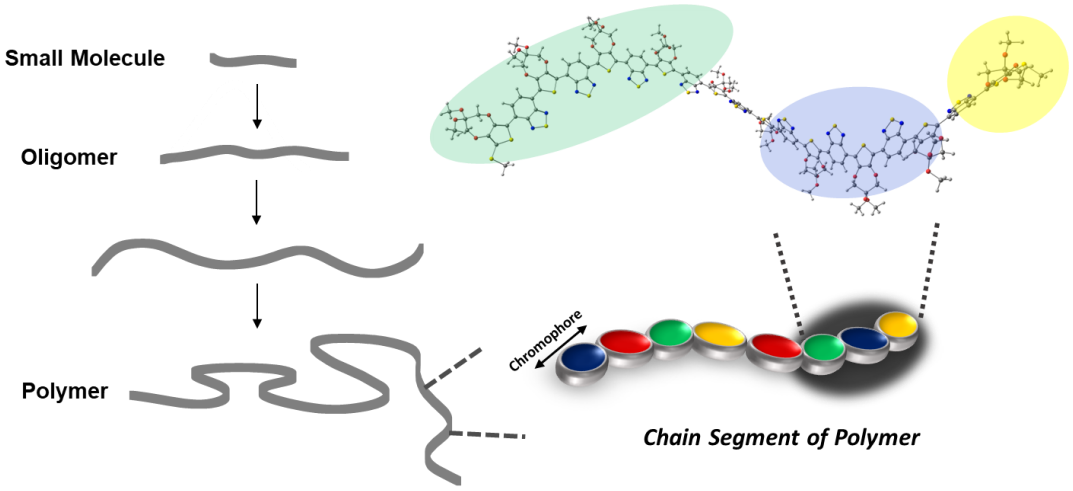

Figure 3.1. Evolution of chain structure as a function of increasing chain-length from oligomer to polymer length scales and the segmentation of the conjugated backbone.

The transition from the low molecular weight, rod-like conformation regime to the high molecular weight, coil-like regime is experimentally explored through the oligomer approach in this chapter. Before we head in molecular model used to explore CP chain conformation, we have to understand the importance of using oligomeric species for polymer research. Due to the statistical nature of polymerization reactions, most synthetic techniques that afford polymeric compounds generate polydisperse material, or mixtures of polymer chains of varying molecular weights, batch-to-batch variations, and encounter solubility issues. These challenges make it difficult to decipher the structure-property relationships of CPs. Alternatively, monodisperse oligomers with well-defined molecular structures and chain lengths serves as excellent surrogates for interpreting the structural and conformational properties of their corresponding polydisperse analogs. These precise models can further provide specific information concerning the solution, electronic, and morphological properties of their higher homologs. For example, at what length does a conjugated system begin to behave like a polymer? By building a series of oligomers and

determining their linear or nonlinear optical, electronic, and structural trends, we can assess the π-systems' convergence limits - the relationship between increasing oligomer size and change in physical properties. In fact the detailed characterization of well-defined materials is often easier than their polydisperse homologs. In addition to their use as models for higher homologs, conjugated oligomers offer distinct advantages of precisely controlled length, size, and shaped compounds for applications where material homogeneities can be detrimental for performance. These include catalysis, molecular recognition processes, nanoelectronics or nanophotonics, and the construction of self-assembled organic frameworks.

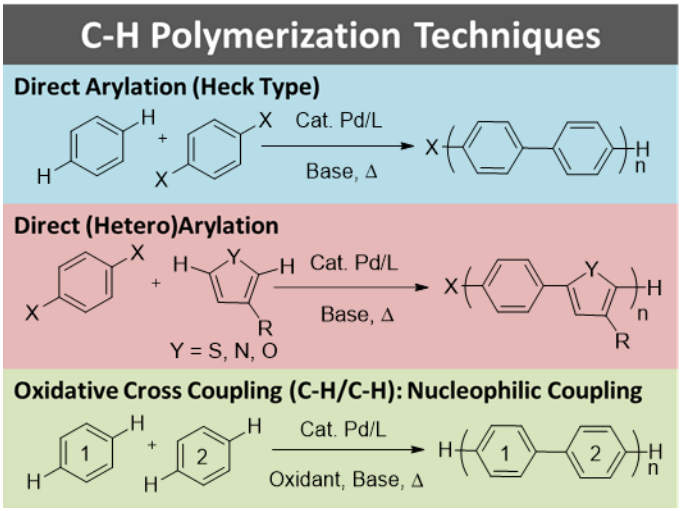

Figure 3.2. Differences between the 3 main C-H polymerization techniques.

Historically, the oligomer approach has been limited to the study of short chains in solution or thin films of electrosynthesized species on electrodes. The emergence of side chain engineering and new carbon-carbon cross coupling techniques have made tangible the synthesis of soluble conjugated oligomers with long chain lengths, close to polymer scales. Although widely employed, traditional metal cross-coupling techniques, such as Stille (C-Br/C-Sn) and Suzuki (C-Br/ C-B) couplings, are plagued with major shortcomings, including: 1) pre-functionalization of monomers at the carbon position, severely limiting the monomer scope, 2) production of large amounts of toxic metal and waste, as is the case for organo-tin compounds in Stille coupling, 3) poor atom economy, and 4) high cost effectiveness.[67–70] These shortcomings can be decreased with palladium catalyzed C-H activated cross-coupling. C-H activation (C-Br/C-H) can be achieved by four

distinct routes: 1) direct arylation, 2) direct heteroarylation, 3) oxidative cross-coupling, and 4) reductive crosσ-coupling.[71]

The C-H bond is activated and cleaved by a catalyst to form a C(sp^2)-M-H species to cross couple with another C-X or C-H bond. Palladium metal is commonly used, although Cu, Ni, Rd, and Ru have also been reported. C-H bond activation is essentially dictated by the intrinsic properties of the C-H bond, where the presence of a hetero-atom, a directing/ functional group, or a solubilizing group can assist in distinguishing the Gibbs free energy of activation of multiple C-H bonds with similar dissociation energies. Cross coupling proceeds via a typical three step process, in which an Ar-X goes through 1) oxidative addition to form an Ar-Pd-X species, followed by 2) transmetalation with another activated carbon bond to form Ar-Pd-Ar', and finally 3) reductive elimination to form Ar-Ar'. C-H activation does not require a transmetalation step and is similar to a heck type reaction, where after oxidative addition, a C(sp^2) bond undergoes migratory insertion followed by a β-H elimination to form the cross coupled product. Usually, the C-H bond activation/ cleavage step is considered to be the rate determining step in the catalytic cycle. It can proceed via an electrophilic aromatic substitution (S_EAr) or a concerted metalation deprotonation (CMD) pathway under the common Pd/L-RCO_2 conditions. Consider the arylation of an arene species in the presence of a palladium catalyst for the following discussion of small molecule C-H activation. S_EAr proceeds via a two-step process in which a Wheland intermediate is initially formed by the palladium covalently bonding to the carbon position to form Pd-C(arene), disrupting the π-conjugation and the C-C bond orders. The Pd-C(arene)-H intermediate is followed by proton abstraction by a carboxylate ligand, producing the Pd-C(arene) species needed for cross coupling to occur. On the other hand, CMD undergoes a single step metalation-deprotonation simultaneously. A carboxylate ligand serves as the proton shuttle while the metal coordinates to the arene in a concerted fashion, preserving the π-conjugation of the arene species. Most studies provide evidence that CMD is in fact the intermediary process.[72]

In this chapter, we use C-H activated carbon-carbon cross coupling to synthesize a discrete D-A conjugated model series (nPB)and explore its molecular structure and physical chain conformations in solution. Composed of the D unit ProDOT (P) and the A unit BTD (B), monodisperse oligomers (n=3, 5, 7, 9, 15, 21) and their higher polymer homologs are synthesized. First, we investigate their molecular structure via extensive characterization by NMR spectroscopy and mass spectrometry. Next, we characterize the chain conformation of each oligomer and

polymer by small angle neutron scattering (SANS) in solution. Finally, we explore the rod-to-coil transition point of the nPB series. The influence of these molecular and conformational properties on the opto- properties of nPB materials are discussed in chapter 4.

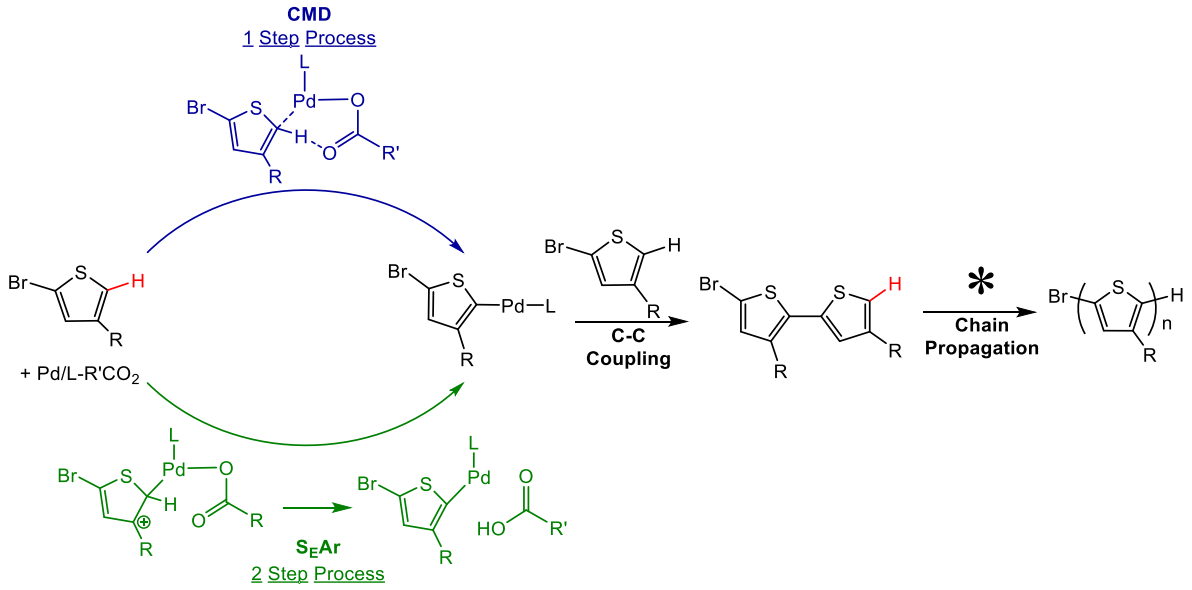

Figure 3.3.Direct (hetero) arylation homopolymerization of 5-bromoalkylthiophene illustrating the difference between concerted metalation deprotonation (CMD) and electrophilic aromatic substitution (S_EAr) cleavage processes.

3.2 Results and Discussion

Firstly, we begin by verifying the molecular structure and dispersity of each molecule in the nPB series via NMR, APCI/MALDI and GPC. Secondly, we use SANS to quantity the relationship between chain length and conformation through which we identify a 'rod-to-coil' conformational transition point at a certain length.

3.2.1 Synthesis of the alternating nPB oligomer series

The direct acquisition of various oligomer lengths by stepwise and iterative palladium catalyzed C-H activated C-C coupling allowed us to construct a complete series of monodisperse conjugated oligomers and their polymer homologues with increasing chain length. A segmented synthetic procedure was used where oligomers of known lengths are added to the end(s) of another oligomer chain with subsequent purification and chain end functionalization. This allowed the

oligomer chains to grow by several units per iteration, in contrast to one-unit growth per iteration. In addition, C-H/C-Br cross-coupling decreases the number of refunctionalization steps by approximately half, making the synthesis less tedious. Difference in molecular size between the reacted segments and the unreacted or polymerized segments were often several units in length different and thereby allowed simple purification of desired chain lengths. Synthesis of the nPB oligomer series is shown in scheme 1.

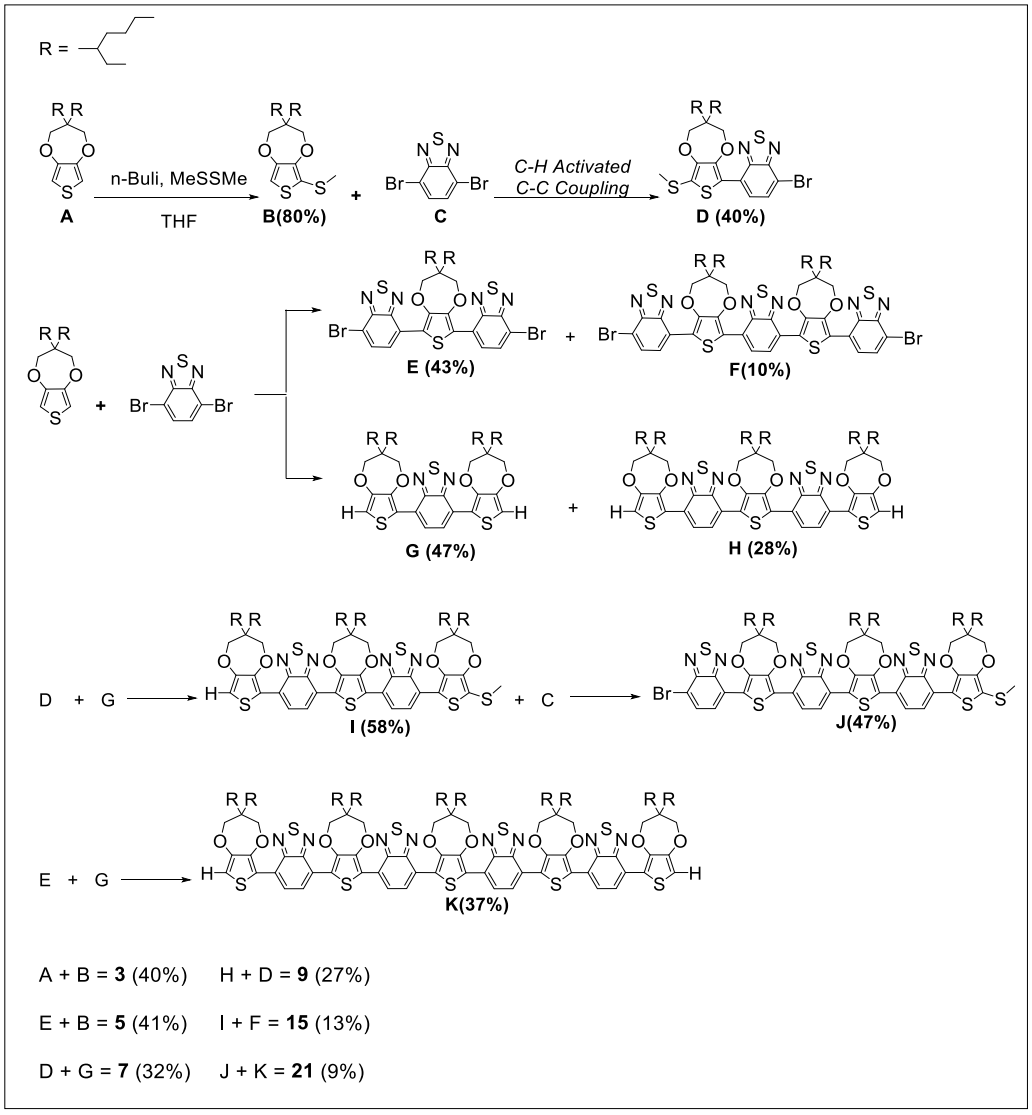

Scheme 1. Synthesis of the nPB oligomers. a) n-BuLi, CH_3SSCH_3, b) C-H Activation Conditions: $Pd(OAc)_2$, $(o\text{-}MeOPh)_3P$, pivalic acid, Cs_2CO_3.

3.2.2 Structural Characterization

NMR

Representative ^{1}H NMR spectra of nPB are shown in Figure 3.3. The ratio between the endcapping methyl thio protons (Ha) and the BTD protons on the chain backbone (He) were used to determine the molecular structure of the oligomers. Hb, Hc, and Hd represent the chemical shifts of the propylene bridge and solubilizing alkyl chain protons, as shown in the labeled inset of Figure 3.3. The transformation of each proton environment with increasing chain length is described below. In the following text, the prefix "end-" and "mid-" will be used to distinguish between the different sites of the oligomer chain.

Aromatic Protons (Ha, He): As the oligomer chain grows, the ratio of Ha: He increases from 6:2 (3), 6:4 (5), 6:6 (7), 6:8 (9), 6:14 (15), and 6:20 (21). He shows as a singlet in 3 and doublet-of-doublet (dd) in 5, indicating the nonequivalence of the BTD protons adjacent to methylthio groups vs. away from the methylthio groups, or towards the middle of the chain. As the chain length increases from 5 to 7 to 9, two different He environments emerge composed of a singlet overlapping with the dd peak. The dd peak is representative of the end-BTD protons and the singlet peak is representative of the mid-BTD protons. With continuing increase in chain length to 15, a new proton environment for the mid-BTD He protons are observed. This peak broadens and is no

longer resolvable at n=21, as is typically observed for polymers at room temperature NMR time scales. Furthermore, the steady downfield chemical shift of the He mid-chain protons saturates at 21, indicating an increase in aromaticity in the conjugated backbone from 3 to 21 units.

The ^{1}H NMR spectra of the polymer samples exhibit similar features to n=21, although with broader peaks. End group analysis of the He:Ha peak ratio was used to calculate the molecular weight of the P1, P2 and P3 as 32, 54, and 50 units respectively (deconvoluted and integrated NMR spectra shown in SI). This result was verified by GPC, as discussed in the following section. As the molecular weight increases, peak broadening diminishes the resolution difference between end-chain and mid-chain proton environments, although the difference is still observable at room temperature NMR. This result shows that difference between the mid-chain and end-chain protons of the conjugated backbone or end-capping groups can both be used to determine the molecular weight of the polymer.

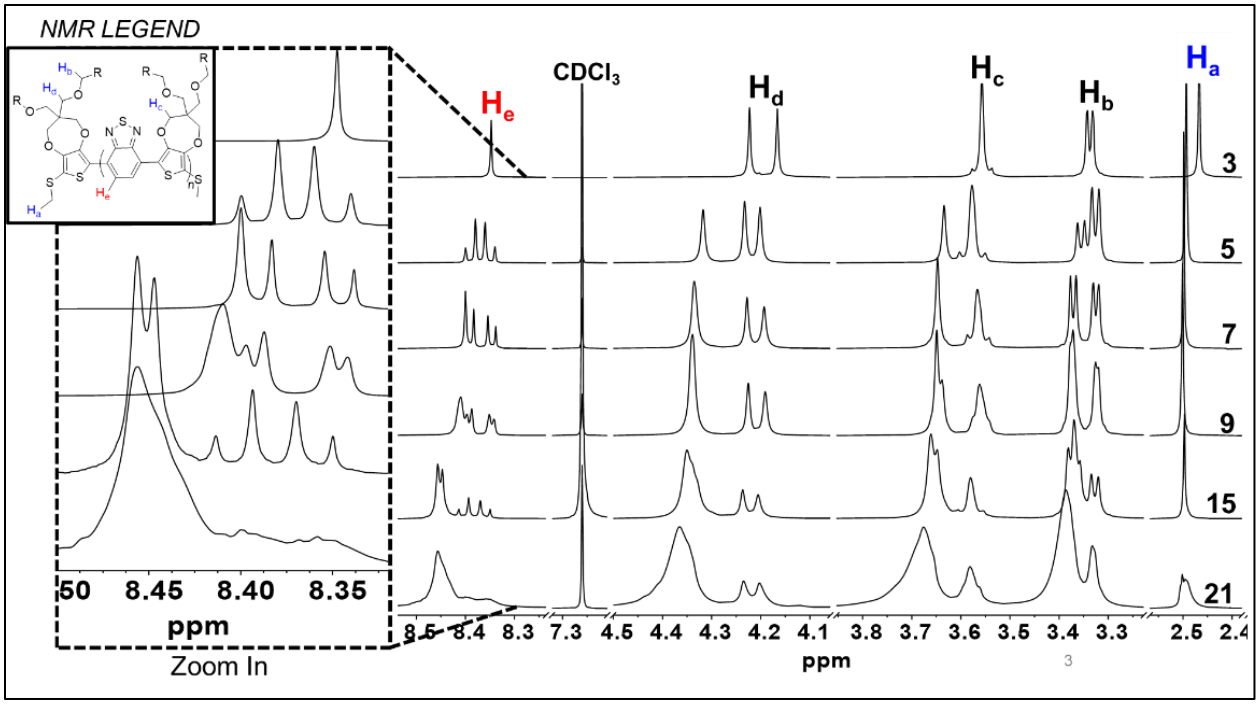

Figure 3.4. ^{1}H NMR spectra of the nPB series in $CDCl_3$ (7.26 ppm) (Inset figure: protons peak legend.)

Alkyl Protons(Hb, Hc, Hd): These peaks represent the propylene bridge protons and the chiral alkyl chain. The presence of the alkyl solubilizing chain creates a center of chirality at the C2 position of the propylene bridge, giving rise to two distinct stereoisomers of the monomer. The Hb peak of the alkyl chain is split into a doublet due to its presence near a chiral center. As the chain grows larger than 3, this single doublet is split into double doublets, with an upfield doublet representing the end-ProDOT units and retaining a constant integral value and chemical shift with increasing chain length. The downfield doublet is characteristic of the mid-ProDOT units in the chain, and hence increase in ratio as the chain length grows. The same trend is seen for the Hc and Hd proton environments, where the end-ProDOT monomers are detected to have a distinct chemical shift from the rest of the D units in the oligomer chains. Eventually, resolution is lost at 21 units as was the case for the aromatic protons. Nonetheless, the two environments of the end-ProDOTs versus the mid-ProDOTs can be differentiated, even for the polymers. The rest of the alkyl chain protons are detected between 1.8 – 0.8 ppm and are shown in the SI.

Mass Spectrometry

The nPB series was evaluated by GPC, APCI and MALDI to confirm molecular weight and dispersity. The GPC chromatograms of sample refractive index vs. time are shown in Figure 2. The series follows a linear trend where 3 has the lowest molecular weight and highest elution time and 21 has the highest molecular weight and lowest elution time. More importantly, all oligomers possess close to perfect monodispersity at a PDI value of 1.01(±0.01). As the oligomer chain grew from n=3 to 21 units, the accuracy of the Mn values determined by GPC increased. HRMS was conducted to verify the molecular weight of each oligomer and the accuracy of the GPC results. Although the GPC analysis overestimated the molecular weight of the oligomer series in all cases, the accuracy increased as the chain length became longer. These results are further supported by NMR characterization, giving us confidence in the monodispersity and molecular structure of each species in the series. The calculated and experimental mass analyses are summarized in Table 1.

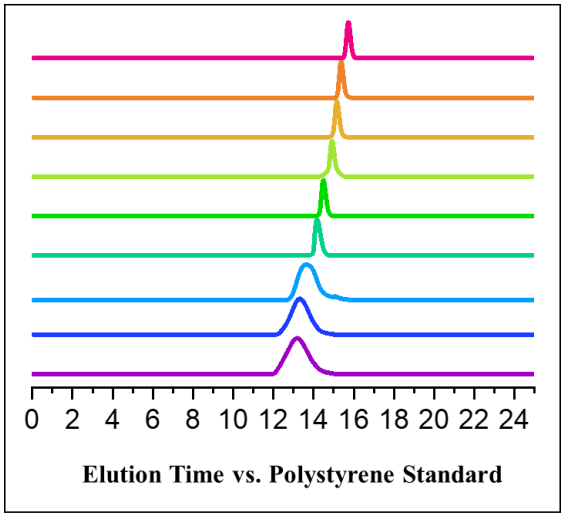

n	Calc $[M+H]^+$	Exp	GPC Mn (Da)	Dispersity Index
Oligomers				
3	1104	1104	1516	1.01
5	1677	1677	2172	1.01
7	2251	2251	2711	1.02
9	2822	2822	3447	1.01
15	4540	4540[(a)]	5387	1.02
21	6261	6261[(a)]	7131	1.02
Polymers				
P1	28 units		9,396	1.37
P2	43 units		14,470	1.34
P3	48 units		15,892	1.26
[(a)]MALDI				

Figure 3.5. Summary of the mass analysis for nPB by GPC and HRMS.

Chain Conformation: SANS characterization

SANS is a well-established method to measure the backbone rigidity of CPs in a dilute solution. Extensive work has been done to probe the planarity of P3HT chains and geometrical information concerning their aggregation behavior in solution.[73] SANS

characterization typically occurs in the range of $0.009 < q(A^{-1}) < 0.07$. The scattering intensity in this region can be modeled using:

$$I(q) = \Phi_v \Phi_{FF} (\Delta\rho_{FF})^2 P_{FF}(q) + \Phi_v (1 - \Phi_{FF}) (\Delta\rho_{Amor}) 2P_{Amor}(q)$$

I=scattering intensity, q=scattering vector,

Φ_v=volume fraction of material in solution, $\Delta\rho_{FF}$=scattering length density contrast,

Φ_{FF}=fraction of the sample that is assembled in a specified form factor,

P_{FF}=form factors of the aggregate, P_{Amor}=amorphous domains

To define the chain-length properties for the nPB series and its rod-to-coil transition, each oligomer and polymer was systematically characterized in equilibrium at the mesoscale (~1-1000nm) by SANS in solution.[61-62,71–74] The neutron scattering contrast arises from the scattering length density difference between the hydrogenous D-A CPs and the deuterated solvent. Representative SANS curves of the nPB oligomers and polymers are shown in Appendix B. The scattering profiles show drastic increases in low q intensity as the molecular weight increases, as low q scattering is very sensitive to large particles. The polymer backbone rigidity is described by Lp, which is the characteristic length scale it takes for the chain to bend more than 90 degrees.[78] In the present work, to acquire the quantitative comparison of conformational characteristics, the SANS data was fitted using a flexible cylinder model in SasView to extract the contour length, persistence length, and radius for each sample. As shown in Figure 2, the contour length increases from 2.1 nm for 3 to 24.9 nm for P3, which is in a reasonable agreement with the molecular weight. Remarkably, Lp only increases from 1.28 nm to 3.12 nm. It is worth noting that Lp quickly increases from n=3 to 7, then plateaus until it stabilizes at about 3 nm for the polymers. This feature arises as the persistence length is independent of molecular weight above a critical molecular weight. Furthermore, the acquired persistence length of the entire polymer is close to the chain rigidity for poly(3-alkylthiophenes) (P3ATs) with thiophene backbones determined by Segalman et. al.[79] It was observed that poly(3-hexylthiophene) (P3HT) also has a persistence length of 3 nm. This similarity between the backbone rigidity of homopolymer P3HT and D-A polymers, P1-P3, suggests that the co-contained thiophene units in the backbone brings a similar amount of backbone torsion in the chain.

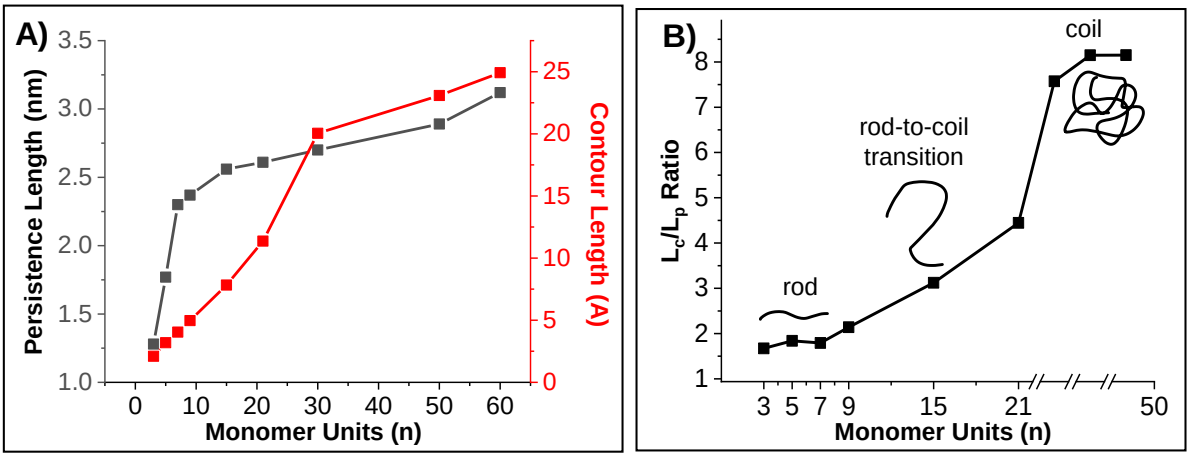

Figure 3.6. A) The persistence length of oligomers and polymers with different numbers of repeating units fitted by a flexible cylinder model in SasView. B) Lc/Lp changes with the number of repeat units.

To explore the shape of CP chains, the ratio between Lc to Lp was calculated and plotted with molecular weight, as shown in Figure 2. Overall, three regions can be identified in the curve. For low molecular weight oligomers (at below 9-unit chain), the ratio of Lc to Lp is around 2, corresponding to a semiflexible chain. This means that even shorter oligomer chains are not entirely rigid, which can be attributed to the backbone torsion from the alternating D-A backbone. For high molecular weight polymers (P2 and P3), the ratio of Lc to Lp increases to 8, meaning the polymer chain behaves like a flexible coil-shape. which is reasonable for a long chain. Concurrently, an apparent rod-to-coil transition is observed at n=15, marking a distinction between oligomer and polymer chain properties. The implications of this chain length dependent transition on the electronic properties is explored via electrochemistry and UV/vis spectroscopy in chapter 4.

3.3 Conclusion

In summary, we have described here the chain structure of the nPB oligomers (n=3-21) and their polymer homologs. These results reflect the impact of the chain-length on the chain structure of weakly interacting, D-A oligomers and polymers in the solution state, which is important for soluble and solution processed thin-film of CPs. We have thoroughly characterized the molecular structure of the conjugated backbone and provided deep insight into how the structure changes as the conjugation length increases. We have also discovered that the backbone conformation

undergoes a rod-to-coil transition at approximately 15 units in good solution. These results reveal that short nPB chain (n=3-9) possess rod-like conformations with persistence lengths up to 2.5 nm, whereas the longer chains (n=15-21) begin to kink and eventually coil at polymer length scales in solution. These results show that our current understanding of CP chain conformations and dynamics in solution is at its infancy. The current knowledge gap includes what configurations of CP chains adopt in solution, how these shapes impact film formation during solution casting, and ultimately whether these configurations can be predicted, designed, and manipulated for specific applications. Quantum chemistry alone is of limited utility in addressing these gaps, since calculations are carried out in vacuum or screened media. Therefore, to make true progress in this field, a truly microscopic theory to account for local anisotropic environments and intermolecular aggregation effects is needed. These gaps in our knowledge directly bear the significance of the structure-property relationships that contribute to the ultimate performance of CPs.

CHAPTER 4. OXIDATION CHEMISTRY AND OPTICAL PROPERTIES OF A DONOR-ACCEPTOR π-CONJUGATED OLIGOMER SERIES

4.1 Introduction

The reversible oxidation or reduction of CPs is the fundamental mechanism that grants them application in electronics such as organic electrochemical transistors (OECT), electrochromic devices, and photovoltaics.[80] Although the conductive properties of CPs have been studied for over 30 years,[81] the fundamental nature of charged specie in CPs are still not well understand. This is because many experimental studies yield general information about bulk materials or device performance rather than molecular properties. Additionally, the theories and models we have borrowed from solid-state physics and inorganic semiconductors, including adaptation of the polaron-bipolaron model, does not completely explain the behavior of charged species in organic CPs. The properties of doped CPs depend on the chemical composition of the π-system, the chain dynamics and conformations, structural reorganization upon electron-transfer, counterion balancing, and influence of experimental conditions. A promising way to explore the molecular properties of CPs is through studying their corresponding monodisperse oligomers with well-defined chemical structures.[82] This chapter discusses the changes in structural, electronic, and optical properties of neutral and oxidized D-A PB oligomers (n=3-21) and polymers, as previously introduced in chapter 3. Specifically, the impact of chain conformation on the charge generation process as a function of chain length, charge behavior, and changes in electronic states and optical properties. This study is presented by way of theoretical modeling, electrochemistry, and spectroelectrochemistry of the nPB series in solution.

To investigate how charge generation and behavior governs the physical properties of conjugated π-systems, the electron-transfer process must be understood in conjunction with the optical, electronic, and geometric changes that occur with it. Electron oxidation of a π-system results in the generation of radical cations (polarons), dications (bipolarons, di-polarons, dimers), and other charge carriers. Most CPs have non-degenerate ground states, meaning when a charge (electron or hole) forms in its lattice, the resulting displacement of atoms and orbitals reduces the charge's energy so that a potential well containing the charge is formed. This charge is called a

polaron and it is a paramagnetic species. Strong coupling between the electronic and geometric structures (electron-phonon coupling) gives rise to non-equivalent forms of the conjugated backbone: aromatic and quinoidal resonance structures. For example, oxidation of polythiophene, one of the most well-studied CPs, causes destabilization of the system via a vertical (Frank-Condon) ionization.[83–86] Distortion of the lattice around a polaron, or relaxation to the quinoidal geometry, creates mid-electronic states within the energy band gap: a singly occupied molecular orbital (SOMO) above the valence band and an antibonding SOMO* below the conductance band. It should be noted, however, that the energetic level of the mid-gap states relative to the valence and conductance bands are intimately dependent on the structural features of the conjugated system, including the chain length, heteroatoms, and substituents. Commonly, two main electronic transitions are observed for a polaron in CPs: HOMO→SOMO and SOMO→SOMO*. The HOMO→SOMO transition is typically weaker in short oligothiophenes, but its molar absorptivity strength increases as the chain length increases.[87] Thus, the process of removing or adding electrons from a conjugated backbone can be followed by the concomitant changes in its optical spectra.

Two-electron oxidation to the dication state leads to geometric distortion in two sites and Columbic repulsion between two charges. If the energetic cost of geometric reorganization is lower than the repulsion between two positive cations, then the two charges will come together to form a bipolaron with a stronger lattice deformation than two separate polarons. The bipolaron is a diamagnetic charge whose mid-gap states are not occupied and all spins in the system are paired. One main electronic transition is observed for bipolarons in CPs: Valence band → new HOMO. In another case, if the energetic cost of the geometric deformation is too low, the two separate polarons will remain apart and repel each other. This is the case for long conjugated oligomers. Additionally, radical spin-spin coupling or π-dimer formation between two interacting chains is a common occurrence in π-systems that are prone to aggregation effects, as was previously discussed in Chapter 2. Thus, the absorption properties of conjugated materials can be tuned from colored-to-transmissive states within the UV-vis-NIR region, the basis for electrochromism in organic materials.

In contrast to polydisperse polymers, monodisperse oligomer with well-defined molecular structure and chain lengths serve as excellent surrogates for deciphering the behavior of polymers as a function of chain length. Important features of charge behavior in CPs have been revealed by

this approach including charge delocalization, interaction of radical spins, exciton dynamics, and effective conjugation lengths for electron rich homo-oligomers such as oligo -thiophenes,[88–90] -phenylenes, -phenylvinylenes, and -fluorenes. This is because the chain structure, conformation, and properties of oligomers are easier to characterize by conventional techniques and can be reliably used to extrapolate polymer properties. Systematic studies from the Heinze,[91–93] Mullen,[82] and Moore[94] groups have revealed important redox characteristics of CPs in the solution and solid state. Their investigation of oligo- thiophenes and arylvinylenes in solution have revealed several trends general to redox-active conjugated oligomers and polymers as a function of increasing chain length, including i) increase in number of redox states, ii) a decrease in oxidation potential, iii) a decrease in the potential difference between subsequent redox states, iv) separation of multiple charges across the chain due to Coulombic repulsion, and v) an increase in chemical stability of the charged species. Other studies stemming from these works have shown how the size of the aromatic subunit, the number of π-electrons in the conjugated system, chain conformation, and steric effects from functional or solubilizing groups can influence the electrochemistry of the conjugated oligomers in solution.[91] These patterns have allowed partial elucidation of charge generation, transfer, and storage mechanisms in CPs. However, these types of studies are limited to short π-type homo-oligomer lengths due to solubility issued or tedious syntheses of long chains that reach polymer length scales.

In this chapter, we uncover the correlation between increasing chain length, chain conformation, and the redox-active opto-electronic properties of a conjugated D-A oligomer series ranging from n=3 to 21 and polymers (nPB). The discrete and monodisperse nPB oligomer series introduced in chapter 3, composed of the methylthio endcapping groups and alternating PB units, is used. The oxidation states of nPB are explored via cyclic voltammetry (CV), differential pulse voltammetry (DPV), spectroelectrochemistry and density functional theory (DFT) calculations. The electrochemical potential vs. $1/n$ begins to follow a negative linear trend at 5 units. Oligomers 3 to 9 units undergo successive one-electron oxidation steps, while 15 units and higher begin to undergo multi-electron oxidations per step in CH_2Cl_2 – $TBAPF_6$ at a Pt ultramicroelectrode in solution. The electron transitions of each oxidation state (1+, 2+, 3+, etc.) are tracked by their UV-vis-NIR signatures, revealing a “bipolaron to di-polaron” transition point at 7 units, indicating that oligomers shorter than 7 units prefer bipolaron formation and oligomers longer than 7 units prefer formation of two polarons upon two-electron oxidations. The 15-unit oligomer absorbs furthest

into the NIR region (lowest energy electronic transition) compared to the longer doped chains, revealing the importance of synergy between chain length and oxidation state. This entire study shoe cases the n=15 chain length as the physical convergence limit for the nPB series. **T**his study demonstrates the chain-length dependent transitions concerning the chain conformation and the oxidation states of a model D-A π-conjugated system.

4.2 Results and Discussion

4.2.1 Alternating vs. non-alternating series

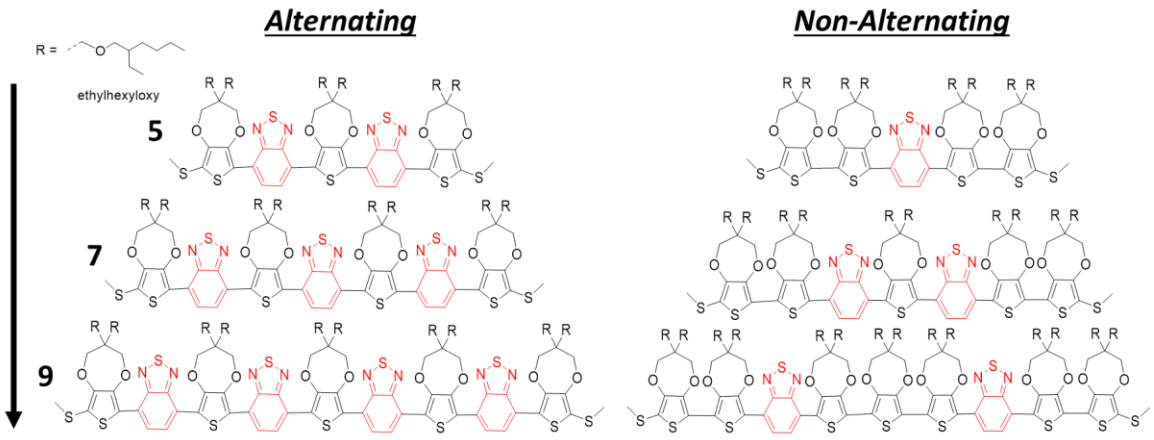

Scheme 1. Molecular structure of nPB Alternating vs. Non-alternating D-A sequence series for n=5, 7, 9 oligomer chain lengths.

Monomer sequence definition in macromolecules is essential to their molecular function. The sequence definition of biological molecules such as nucleic acids and proteins have a precise order than encodes genetic for cellular functions. In synthetic materials, it is important for self-assembly, catalysis, opto-electronics, molecular encoding and recognition of information, and phase behavior of blended materials.[95] Relating the primary monomer sequence to the physical, chemical, and electronic properties of organic materials remains a standing challenge due to the scarce synthetic availability of sequence-defined oligomers. Similar to the synthesis of the alternating nPB series described previously in chapter 3, a non-alternating oligomer series was designed and synthesized by C-H activated carbon-carbon cross coupling to explore the impact of monomer sequence on the redox properties of D-A conjugated molecules. Scheme 1 shows the

molecular structures of the alternating and non-alternating oligomers series. For n=5 and 7, the center of symmetry and number of donor units differ, whereas for n=9 the center of symmetry remains the same but the number of donor units differ between the alternating and non-alternating series.

Electrochemistry of Alternating and Non-Alternating Oligomers (n=5, 7, 9).

In sequence-defined oligomers, each monomer plays a role in the conjugated backbone's electronic structure and hence their redox properties. Solution voltammetry of the alternating and non-alternating series was conducted at ~1 mM in 0.2 M $TBAPF_6$ – CH_2Cl_2 at a Pt button electrode vs. Ag/AgCl. Figures 4.1-4.3 show the CV and DPV for the 5, 7, and 9 chain lengths. For 5-NA, the first and second oxidations occur simultaneously (one-step two-electron transfer process) whereas the alternating 5-A undergoes a stepwise oxidation to get to the dication state. Because 5-A has one more donor unit than 5-NA, it has a higher electron donating character and forms its radical cation at a lower anodic potential of 0.643 V, whereas 5-NA oxidizes to the radical cation state at 0.766 V vs. Ag/AgCl. The oxidation of all donor units are accounted for, where 5-NA fully oxidizes to the 4+ state and 5-A fully oxidizes to the 3+ state.

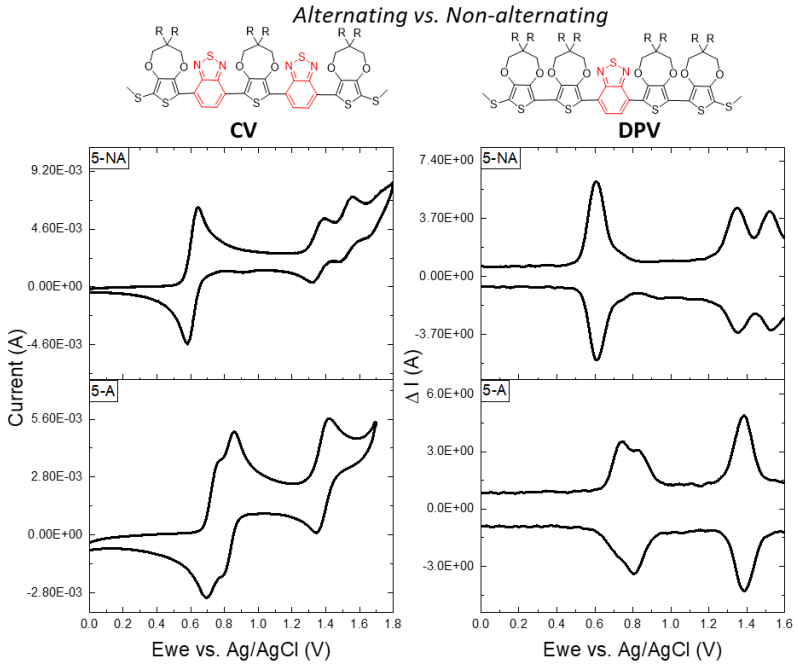

Figure 4.1. CV and DPV of 5-A and 5-NA at ~1 mM in 0.2 M $TBAPF_6$ – CH_2Cl_2 at a Pt button electrode vs. Ag/AgCl.

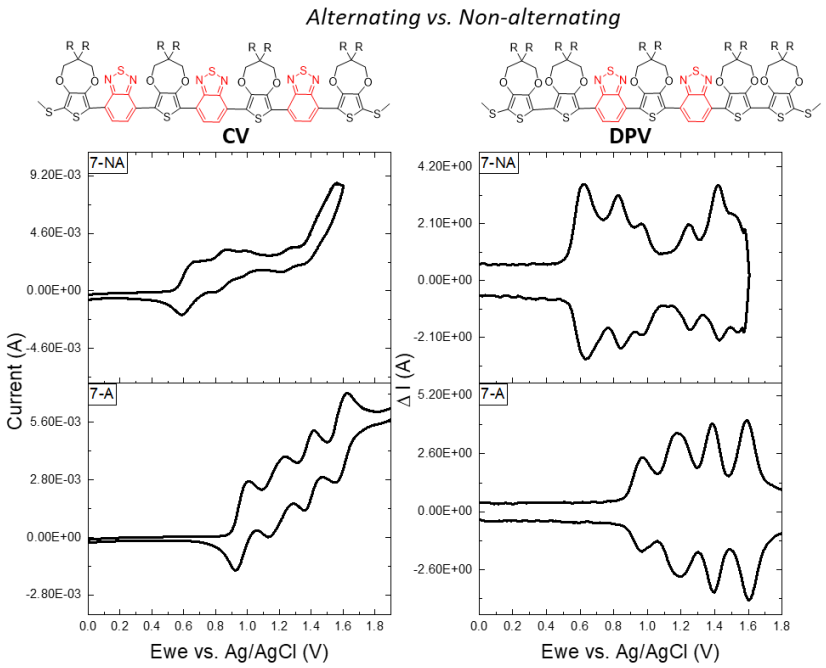

Figure 4.2. CV and DPV of 7-A and 7-NA at ~1 mM in 0.2 M $TBAPF_6$ – CH_2Cl_2 at a Pt button electrode vs. Ag/AgCl.

At the 7-unit chain length, both oligomers undergo stepwise oxidation. 7-NA reaches the 5+ state at full oxidation, representative of the five donor units in the molecule. The currents for each anodic peak vary causing doubt whether these waves in fact represent one-electron transfer processes. Attempts to quantify the number of electrons in each anodic wave were unsuccessful presumably due to changes in capacitance and non-faradaic effects at each step. 7-A reaches full oxidation at 4+, representative of the four donor units in the molecule. With increase in oxidation state, the current increases, and plateaus at the third wave, showing a clean and discrete four electron oxidation process. As expected for the NA series which has a higher content of donor units, the radical cation for 7-NA forms at 0.619 V and 0.970 V vs. Ag/AgCl for 7-A.

At the 9-unit chain length, voltammetric peaks begin to coalesce together as the chain gets longer. 9-NA shows five anodic peaks for a total of 7 donor units in the chain. 9-A shows four anodic peaks for a total of five door units. Radical cation formation for 9-NA is a little bit lower than 9-A, exhibiting anodic potentials of 0.490 and 0.550 V vs. Ag/AgCl respectively. In accordance with the systematic trend observed for all the alternating and non-alternating oligomer series, the electron-rich non-alternating oligomer oligomers oxidize at lower potentials than the alternating oligomer. The ratio of donor-to-acceptor units relative to random or alternating

monomer sequences shows to have an impact on the electrochemical oxidation of these molecules. It would be interesting to see how a block co-oligomer of D-A units behaves as a function of chain length.

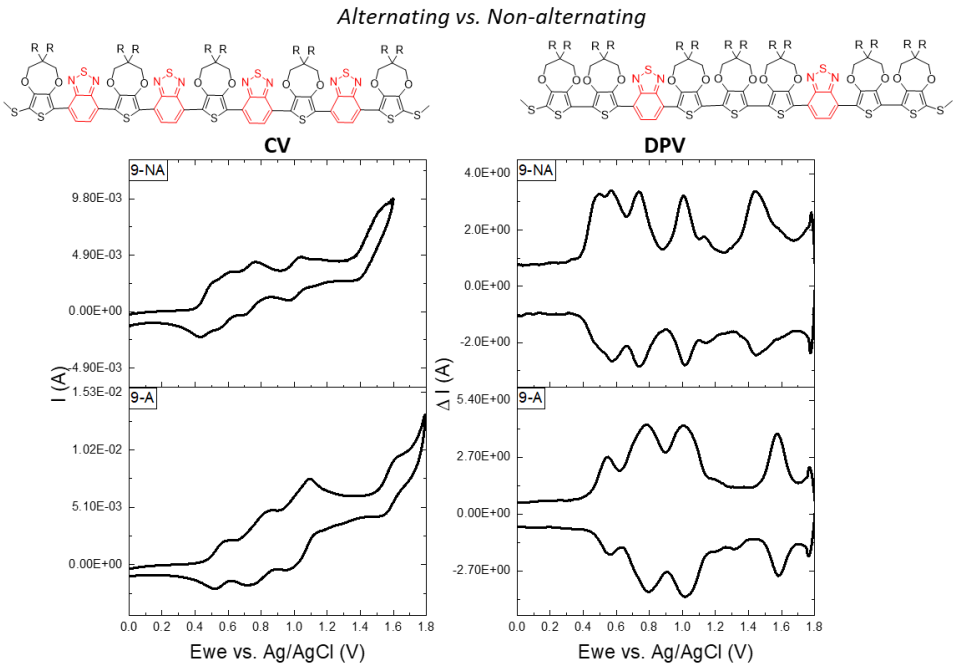

Figure 4.3. CV and DPV of 9-A and 9-NA at ~1 mM in 0.2 M $TBAPF_6$ – CH_2Cl_2 at a Pt button electrode vs. Ag/AgCl.

Table 1. Summary of Anodic Potentials of alternating and non-alternating nPB (n=3, 5, 7, 9) via DPV in 0.2 M $TBPAF_6$ – CH_2Cl_2 at ~1.0 Mm

n	Donor n	E^1_{pa}	E^2_{pa}	E^3_{pa}	E^4_{pa}	E^5_{pa}	E^6_{pa}
5-A	*3*	0.766	0.860	1.419			
5-NA	*4*	0.643(2e)		1.387	1.553		
7-A	*4*	0.970	1.180	1.390	1.594		
7-NA	*5*	0.619	0.824	0.965	1.250	1.424	
9-A	*5*	0.550	0.784	1.015	1.575		
9-NA	*7*	0.490	0.575	0.739	1.009	1.134	1.444
Experimental Conditions: ~1 mM analyte in 0.2 M TBAPF6 – CH2Cl2 at a Pt button electrode vs. Ag/AgCl.							

4.2.2 Theoretical Characterization

Density functional theory (DFT) calculations. In this section we turn our attention towards understanding how elongation from oligomer to polymer length scales impacts the redox and optical properties of the alternating D-A system. We begin this analysis with DFT calculations of

varied charged states of n=3, 5, 7, 9, 15, and 19; in addition to the neutral electronic state, the +1 (doublet; n=3-19), +2 (singlet & triplet n=3-9), +3 (doublet & quartet n=5-9), and +4 (singlet, triplet, quintet n=5-9) charged (spin) states were considered. We note that we were not able to achieve a converged radical-cation state for 21, and so this structure is not included in the computational analyses. The calculations were performed at the OT-ωB97X-D/6-31G(d,p) [OT = optimally tuned] level of theory[96–98], where the range-separation parameter ω for each molecule was tuned via the ionization potential-tuning procedure.[99–101] All alkyl chains were truncated to methyl groups to reduce computational cost, and each optimized geometry was confirmed as a minimum on the potential energy surface through normal mode analysis. The influence of the solvent environment (CH_2Cl_2; ε = 8.93) was modeled through the polarizable continuum model. The Gaussian09 software suite was used for all DFT calculations.[52] The relative energies of each spin state for each charge and plots of the bond-length alternation patterns are located in the SI.

The computed adiabatic ionization potential (AIP) for n=3-19 follows 5.23eV (3), 5.00 eV (5), 4.88 eV (7), 4.84 eV (9), 4.82 eV (15), and 4.82 eV (19). These trends suggest that the effective conjugation length[102–107] for this donor-acceptor system is reached at approximately 9 repeat units. For 3, 5, 7, and 9, a broken symmetry radical-cation state is the most stable conformation by 96 meV, 70 meV, 34 meV, and 12 meV, respectively; this broken symmetry state is achieved by rotation of one of the end-cap methyl thiol moieties with the charge localizing on one end of the molecular structure. The situation is reminiscent of a Robin and Day Class II mixed-valence systems.[108] For 15 (and 19), the symmetric state is the most favorable, with the charge localized in the center of the molecular structure; in both instances, the symmetric structure is energetically favorable by ~40 meV. Plots showcasing the bond-length alternation patterns of these varied states versus the respective neutral states are given in the SI.

Moving to the +2 charge in n = 3-9, the singlet state is more energetically stable in 3 and 5, which suggests that bipolaron (*i.e.*, spin-paired dication) formation is preferred. This is because the energy gained by forming only one deformation in a bipolaron may outweigh the increased Coulomb repulsion energy from two separate charges.[101] However, for the longer systems 7 and 9, it is the triplet state that is more energetically favorable, suggesting that two independent polarons (i.e., spin-unpaired dication) are present. These results demonstrate the length dependence concerning the preferred formation of a bipolaron or two polarons,[101] and an interplay between energy (de)stabilization due to electron pairing and Coulombic effects. For the +3 charge, the

doublet state is more energetically stable in every case examined. The +4 charge is somewhat more complicated in terms of the preferred spin state: In 5 and 9, the order follows singlet, triplet, and quintet, while in 7 it follows triplet, singlet, and quintet. We note that we treat the results of these higher charged states with caution because several effects could potentially stabilize one state (*e.g.*, polaron vs. bipolaron formation) over another in experiment – including explicit interactions with solvent molecules and/or counterions – are not accounted in the DFT calculations. Plots of the relative energies of these different charged states are provided in the SI.

4.2.3 Redox Characterization

Voltammetry at Ultramicroelectrode

With this understanding of, albeit isolated, oligomers in hand, we turn to their electrochemical studies. The voltammetry of CPs, typically conducted in the solid state, is plagued with nonfaradaic effects such as capacitance, film resistivity, and lattice expansion and contraction effects, resulting in broad and ill-resolved voltammetric waves. Additionally, CV experiments of CPs contain both kinetic (scan rate) and thermodynamic data ($E_{1/2}$ potential), making it difficult to separate the energetic effects. Thereby, the redox potential and shape of voltametric waves determined as a function of length for conjugated oligomers provide insight into understanding electron-transfer, structural changes, and charge interactions that may not be observable for CPs. To figure out the fundamental electron oxidation processes for the nPB series, solution electrochemistry via CV and differential pulse voltammetry (DPV) were conducted in 0.2 M $TBAPF_6$ - CH_2Cl_2 at a 25 μm Pt ultramicroelectrode (UME) surface. The use of an UME for macromolecular electrochemistry is advantageous for rapid mass transport, small double-layer capacitance, and small ohmic loss.[109,110] The voltammograms are shown in Figure 3A-B and the electrochemical data is summarized in Table 2.

As previously reported,[111] 3 exhibits one anodic peak appearing at $E_{1/2}$ = 1.044 V vs Ag/AgCl with net chemical reversibility. However, this single peak hides two oxidation processes, where a potential difference of 76 mV between the first and second oxidation waves ($\Delta E^{1\text{-}2}$) results in the seemingly single, broad anodic wave by CV which can be resolved in the 1st order derivative of the DPV (Appendix C). Similar to the oxidation of triphenylamine-tetracyanobutadiene based D-A-D oliogmers,[112,113] the anodic waves of 3 is assigned to the simultaneous oxidation of the two

methylthio-ProDOT monomers. This result suggests that they are electronically independent, and the central BTD unit interrupts the conjugation between the two. This result is also confirmed by the ≈24° twist between the PB unit as previously reported by crystallography and DFT.[114]

The first anodic potential for 5 occurs at $E_{1/2}$ = 1.064 V vs Ag/AgCl, 20 mV higher than 3. An increase in oxidation potential with increase in conjugation length is in stark contrast to expectations, as similar π-conjugated systems undergo a decrease in oxidation potential with increasing chain length [ref]. This deviation from a well-established redox trend is hypothesized to be a cause of aggregation or solvation effects because crystallite formation was observed for 5 in solution. 5 shows three reversible oxidation states, with the ΔE^{1-2} equal to 80 mV. Similar to 3, the singlet state is more energetically stable for the dication state and thus bipolaron formation is preferred. Further oxidation of 5 to the trication state requires a great deal of energy, with ΔE^{2-3} equal to 562 mV.

The oxidation potential of conjugated oligomers and polymers decrease with increase in chain length until the effective conjugation length is reached. In contrast to 5, 7 and 9 follow this trend and exhibit their one-electron oxidation $E_{1/2}$ values at 1.032 V and 0.924 V vs. Ag/AgCl respectively. For 7, four consecutive one-electron oxidation peaks with potential differences of ~200 mV between each state were detected by CV and DPV. This substantial increase in ΔE^{1-2} indicates Coulombic repulsion between two charges in the dication state. In agreement with the DFT calculations, the triplet state is more energetically favorable for 7, suggesting the formation of two polarons confined to a single chain instead of a bipolaron. Notably, this significant result shows that at a 7 unit chain length, there is a fundamental change in the way the electrons are being populated across the conjugated system for the nPB series. Further oxidation to the 3+ and 4+ states also requires ~200 mV per oxidation step. For 9, five consecutive one-electron oxidation peaks are detected with regard to the five donor units in the chain. Similar to 7, the ΔE^{1-2} for 9 is equal to 192 mV and indicates that the triplet state is more energetically favorable than the singlet state for 9^{2+}. Further oxidation of 9 to the 4+, and 5+ states is summarized in Table 2.

One-electron oxidation of 15 occurs at 0.800 V vs Ag/AgCl. As the conjugation length increases, successive oxidation peaks begin to coalesce and separation between two standard potentials decreases producing broad CV waves with the overall shape of one-electron reactions. Merging of separate voltammetric peaks with increasing chain length implies that the Coulombic repulsion between consecutive redox steps is decreasing, or their ionization energies are becoming

similar. Additionally, this voltammetric response may also be attributed to changes in the electron-transfer dynamics of larger chains an electrode's surface. Because the relationship between oligomer chain conformation and voltammetric response (faradaic and nonfaradaic) is complex, further studies would be required to make a definitive statement. Nonetheless, multiple anodic waves were detectable by DPV showing six oxidation states for 15, a molecule with eight donor units. The area beneath the last, broad oxidation peak of 15 is indicative of multiple electron transfers. This deviation from the 'one-electron oxidation per donor unit' trend is an impact of increase in chain length and can also be correlated to its coil-like backbone. All oxidation steps show to be reversible or quasi-reversible.

Similar to 15, the CV of 21 is broadly shaped with a drastic decrease of 296 mV in the onset of oxidation occurring at 0.504 V vs. Ag/AgCl. The redox potentials of other systems, such as oligofluorene and oligothiophenes, have also shown to change at scales longer than their maximum conjugation lengths. Typically, a linear relationship between the redox potential and 1/n is justified by particles in one-dimensional boxes, which does not seem to be the case in this study. In contrast, we hypothesize that the odd CV behavior of 21 may be a result of change in free energy caused by increase in positional entropy, as the positive charge can reside at varied positions along the chain. Additionally, backbone conformational changes caused by chain coiling in solution at lengths longer than 15 may affect the electron transfer dynamics and adsorption effects at the electrode's surfaces. Solvent and counter anion effects cannot be excluded, and may have a cumulative impact on the drastic lowering of the oxidation potential after the maximum conjugation length has been reached. Improved resolution of 21 was obtained with differential normal pulse voltammetry (DNPV), showing a clearly asymmetric voltammogram indicating that the dedoping process is not the same as the doping process and may be accompanied by different structural transformations or chemical changes within the oligomer chain that were not observed for the shorter oligomers chains. Furthermore, seven anodic peaks were detected for 21 by DNPV after deconvolution (Appendix C) and a final multielectron transfer step from 1.6 - 1.9 V. This increase in peak area of the final oxidation steps is also seen in P1, whose DNPV voltammogram shows numerous small peaks followed by one major peak at 1.9 V. For a polymer of ~25 units with 1.2 PDI (P1), it was pleasing to see multiple small peaks with the same anodic wave patterns as 9, 15, and 21, albeit with lower anodic potentials.

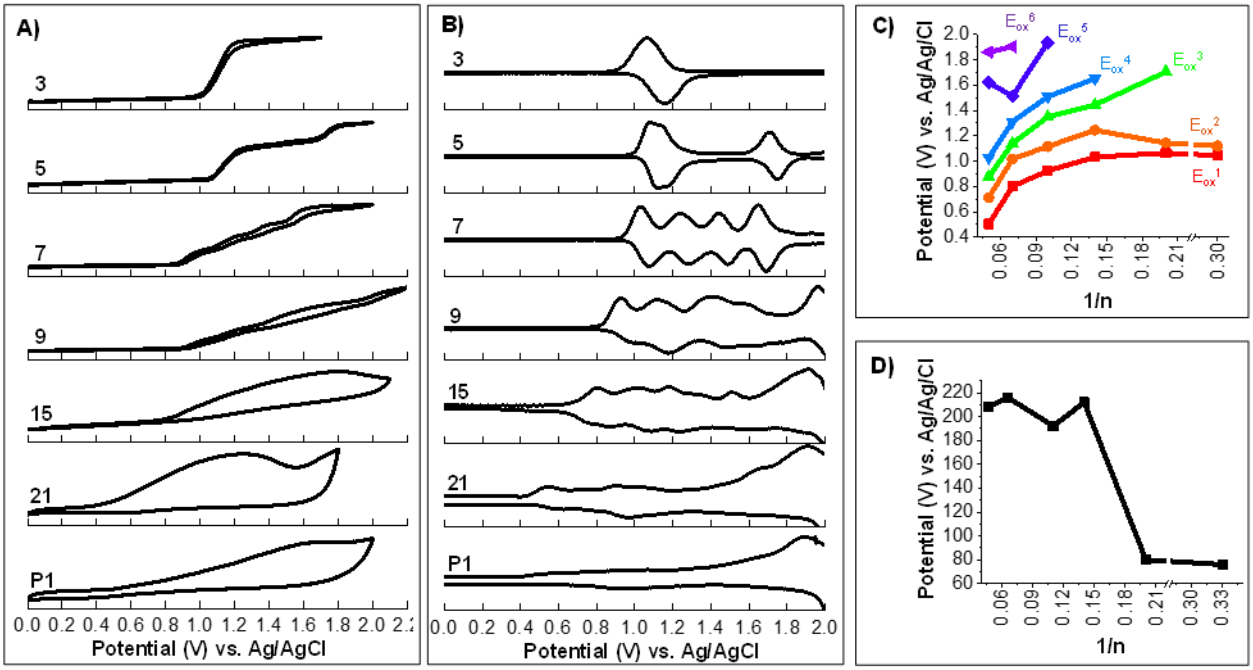

Figure 4.4. Electrochemistry of oligomer series at 1mM analyte concentration in 0.2 M $TBAPF_6$ /CH_2Cl_2 at a 25 μm Pt ultramicroelectrode vs. Ag/AgCl. (Voltammetry of oligomer series at a Pt Button electrode are given in the SI). A) Cyclic Voltammetry (CV) at 10 mV/s and B) Differential Pulse Voltammetry (DPV), C) Anodic potentials of all oxidation states as a function of chain length, and D) Anodic potential difference between the first and second oxidation peaks.

Table 2. Summary of Anodic Potentials of nPB (n=3 to 21 and P1) via DPV in 0.2 M $TBPAF_6$ – CH_2Cl_2 at ~1.0 mM.

n	E_{pa}^1	E_{pa}^2	E_{pa}^3	E_{pa}^4	E_{pa}^5	E_{pa}^6
3	1.044 (1e) [(a)]	1.120 (1e) [(a)]	-	-	-	-
5	1.064 (1e) [(a)]	1.144 (1e) [(a)]	1.704 (1e)	-	-	-
7	1.032 (1e)	1.244 (1e)	1.444 (1e)	1.652 (1e)	-	-
9	0.924 (1e)	1.116 (1e)	1.348 (1e)	1.508 (1e)	1.936 (1e)	
15	0.800 (1e)	1.016 (1e)	1.140 (1e)	1.311 [(a)]	1.512	1.904 (*ne*)
21	0.504	0.712	0.876	1.028	1.620	1.860 (*ne*)
P1	*0.408 onset of oxidation*					

[(a)] Calculated from deconvoluted data.

Optical Properties: Spectroelectrochemistry

Neutral States. The absorption spectra of neutral *n*(PB) in dichloromethane at room temperature are shown in Figure 4A. All oligomers exhibit the dual absorption bands characteristic of D-A systems, consisting of the π-to-p* band and the D-A charge transfer band. Both peaks bathochromically shift with increasing π-conjugation. A steep initial increase of +55 nm of the D-

A band was observed when increasing chain length from n=3 (489 nm) to 5. This inclination decreases to +24 nm from n=5 to 7, +15nm from n=7 to 9, and so forth. The D-A λ_{max} increases with increasing chain length and saturates at P1(~25 units) with a value of 636 nm.

Assessment of the optical properties of the neutral UV-vis spectra is confirmed by TDDFT calculations at the OT-ωB97X-D/6-31G(d,p) level of theory. The $S_0 \rightarrow S_1$ (π-to-p*) excitation, described in each system as predominately a HOMO→LUMO transition (though additional one-electron transitions become important as the oligomer length increases), increases from 3 (2.82 eV, 440 nm), 5 (2.28 eV, 543 nm), 7 (2.11 eV, 588 nm), 9 (2.03 eV, 612 nm), 15 (1.89 eV, 440 nm), and 19 (1.90 eV, 651 nm). We note that, like the ionization potential, the $S_0 \rightarrow S_1$ excitation converges at n≈15-19, suggesting that the effective π-conjugation length has been achieved.

Radical Cation (+1) States. One-electron oxidation of a conjugated oligomer leads to the formation of a radical cation, otherwise known as a polaron, considered to be a localized charged species with quinoidal geometrical changes confined to a limited number of monomeric units. Coupling of the charge with the geometric structure for π-conjugated materials causes new electronic states to appear within the band gap of the molecule. For a radical cation, a singly occupied level is generated above the valence band and an empty one appear below the conduction band. This leads to three electronic absorptions, associated with HOMO to SOMO, SOMO to SOMO*, and SOMO to LUMO. In this case, the +1 states of the nPB oligomer series show the two main electronic transitions at longer wavelengths (lower energies) relative to their neutral states. Two high intensity peaks for 3^+ can be found at 808 and 1295 nm, with weaker mid-gap transitions in between. The two transitions for 5^+ were observed as a broad and a weak low-energy state transition. From n=7-21 to P1, the higher energy transition, (SOMO to LUMO) underwent a continuous bathochromic shift with increase in conjugation length from 900 nm (7), 913 nm (9), 914 nm (15), 930 nm (21) to 1008 nm (P1). In contrast, the lower energy transition trend reached saturation at n=15, starting from 1295 nm (3), 1400-1600 nm (5), 1780 nm (7), 1976 nm (9), to 1500-2800 nm (15), with an trend inversion at 21+ and P1+, with hypsochromically shifted peaks located at λ_{max} values of 2032 nm (21) and 1696 nm (P1) respectively. For the radical cations, the TDDFT calculations show a red-shift and increase in the oscillator strength of the lowest-lying excitation, which predominantly consist of a SOMO→LUMO one-electron transition.

Dication (+2) States. The +2 states of the nPB series is represented by a single electronic transition absorbing at a lower wavelength compared to the +1 states. Similar to the trend observed for the +1 states, the main transition for the +2 state undergoes bathochromic shifting, with respect to the +1 state electronic transitions, till it reaches optical saturation at 15 and reverses to hypsochromic shifting at higher chain lengths of 21 and P1. Starting at 620 nm for 3, the wavelength continuously increases to 1052/1191 nm (5), 1533 nm (7), 952/1729 nm (9), and 900/1722/2400-2800 nm (15). At chain lengths higher than 15 units, the dication absorption blue shifts to 980/1620 nm (21) and 1450 nm (P1).

The spectroelectrochemistry of polymers typically show two transitions representing the polaron to bipolaron transition. Interestingly, P1 does not have the lowest energy transition of the nPB series and its highest oxidation level is blue shifted to its polaron transition. This hypsochromic shift of the bipolaron species can be rationalized by stronger lattice deformation of two positive charges in comparison to one positive charge, thereby causing the mid-gap transition to be further away from the band edge and requiring a higher energy electronic transitions.[83] However, the DNPV of P1 shows six small peaks before the large peak at 1.9 V (Figure S# in SI) in a voltammetry pattern similar to the voltammograms of 9, 15, and 21. Even though the same rich optical transitions are not observed for P1, its voltammogram reveals more than two electron oxidation steps occurring. As a matter of fact, there are approximately seven anodic peaks, making it reasonable to assume that the very broad absorption bands of doped P1 are due to the formation of diverse species within the chain and not just mere polaron-bipolaron charges. Indeed, TDDFT calculations for the polaron, bipolaron, and di-polaron states of 5, 7, and 9 reveal that the these bands have several peaks in the same energetic area, suggesting that deconvolution of the spectra could be difficult. This mismatch between the voltammetry and optical properties reveals the fundamental barriers in the interpretation of electrochemical data of CPs and the need for well-defined oligomer models to study fundamental electron-transfer steps at polymer length scales.

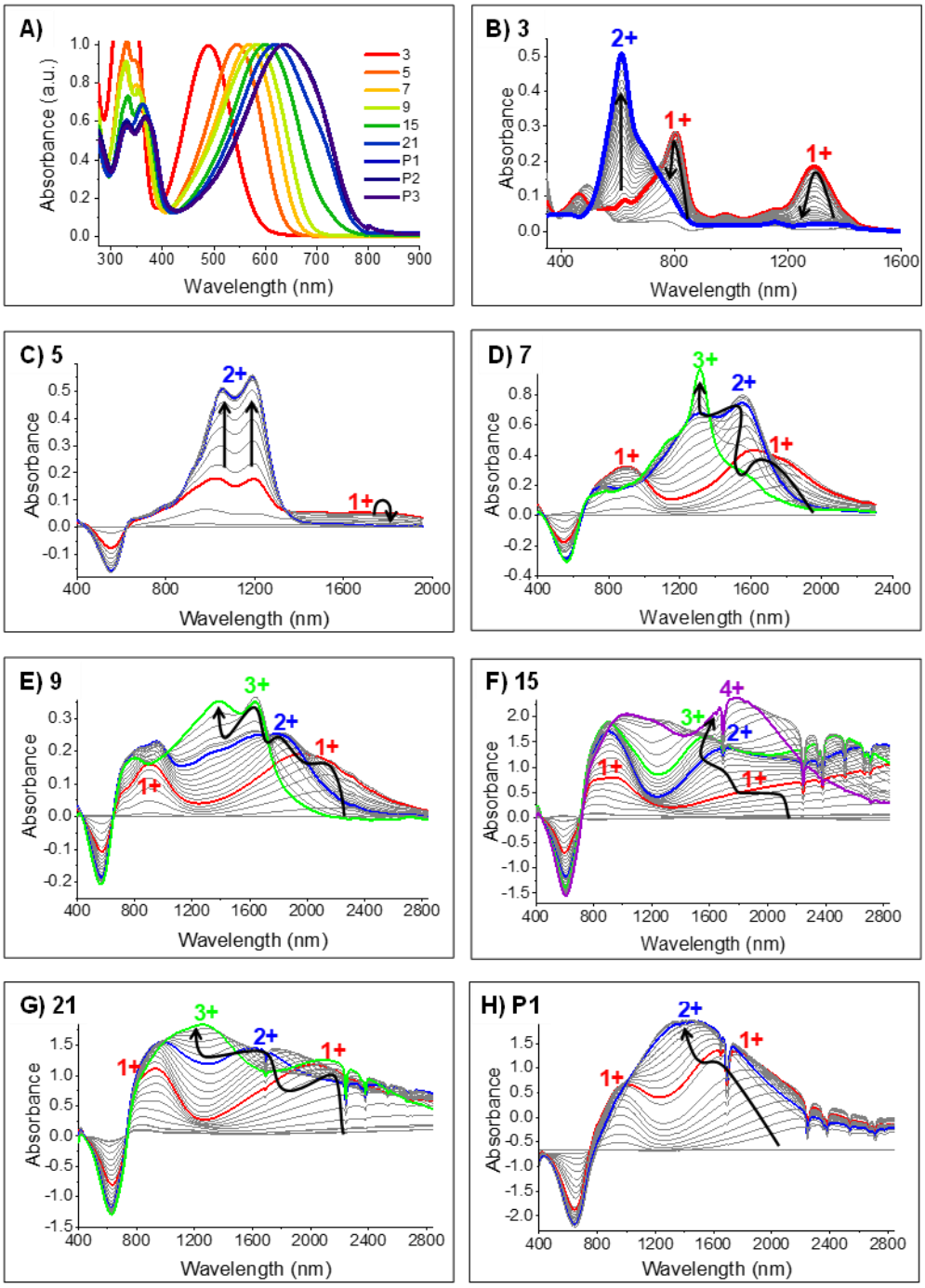

Figure 4.5. A) Neutral absorption spectra of nPB. Spectroelectrochemistry of nPB in 0.2 M $TBAPF_6$ /CH_2Cl_2. B) n=3 C) n=5 D) n=7 E) n=7 F) n=15 G) 21, and H) P1. Experiment was conducted in an air-tight optically transparent thin-layer quartz cuvette equipped with a Pt honeycomb electrode under nitrogen.

Table 3. Photophsycial properties of the oxidation states of the nPB series by spectroelectrochemistry in solution.

n	0 (nm)	+1 (nm)		+2 (nm)	+3 (nm)	+4 (nm)
3	489	808	1295	620	--	--
5	513	U	1400-1600	1052/1191	U	--
7	528	900	1780	1553	1314	U
9		913	1976	952/1729	1636/1375	1375
15		914 (b)	1500-2800	900/1722/2400-2800 (b)	940/1465/2000-2800 (b)	1010/1778
21		930 (b)	2032	980/1620	1260/2140	U
P1	636	1008	1696	1450	U	U
(b) = broad, U = unobservable						

4.3 Conclusion

In summary, we have described here the oxidation states of six nPB oligomers (n=3-21) and their polymer homologs. These results reflect the impact of the chain-length on the oxidation processes of π-conjugated, weakly interacting, donor-acceptor oligomers and polymers in the solution state, which is important for soluble and solution processed thin-film of CPs. We have demonstrated the following points in this study:

1. *Electron-Transfer Process:* The rod-to-coil transition is emulated during electrochemical oxidation because the voltammetric response changes from a single-electron transfer per step to multi-electron transfers per step at n=15. The polymer voltammogram reveals similar anodic wave patterns as observed for n=9-21, implying that there are multi-oxidation states in CPs instead of just ‘polarons and bipolarons’. Additionally, in contrast to the linear trend between increasing chain length and decreasing oxidation potential, the oxidation potential continues to decrease even after maximum conjugation length, or the physical convergence limit, has been reached. This conclusion highlights the gaps in understanding the role of chain conformation, solution interactions, and ions in the redox reaction of CPs.
2. *Charge Behavior:* In their radical cation states, the charge prefers to localize at one end of the chain making the chain asymmetric. In their dication states, the short rod-like oligomers prefer bipolaron formation, whereas the long coil-like oligomers prefer di-polaron formation. This result is clearly due to the chain length and is also experimentally proven

by voltammetry, as the ΔE (Columbic repulsion) between the first and second oxidation steps increases from 3 to 9, and decreases at longer lengths due to chain coiling effects.

3. *Optical Properties:* The lowest energy electronic transition of the +1 state reaches undergoes bathochromic shifting from 3 to 15 units, and reverse to hypsochromic shifting at 21 and polymer scale lengths. This is the same trend observed for the +2 state. In contrast to general belief, the dication state of 15 absorbs further into the NIR region than the polymer in solution, with no major change or enhancement in optical properties with increase in doping level/ oxidation state. This reveals that the chain length and the oxidation state have to be carefully synched up. After a certain length, increase in conjugation may begin to have an adverse effect on optical properties depending on applicational needs.

CHAPTER 5. CLOSING REMARKS AND OUTLOOK

In this dissertation, we demonstrate the convergence behavior of the chain structure, chain conformation, and redox properties of a D-A π-system as a function of increasing conjugation length. The oligomer approach was used to study a model system of monodisperse, discrete π-conjugated oligomers (n=3-21) and their polymer homologs. Their structure and physical properties were thoroughly investigated to reveal a distinction between the structure-property relationships of oligomers and polymers. This distinction is proven by a conformational transition , at a chain length of approximately 15 units, or 4540 Da, for the PB system in solution. At this specific chain length in the series, we begin to see a deviation from a rigid, planar conjugated system to a flexible, coil-like conjugated system.

In chapter 2, the basic redox properties of a D-A-D small molecule is revealed. Electrochemistry and isolation of the radical cation and dication states by chemical oxidation allowed structure-property analysis of the charged species in the solution and solid states. This study has revealed the molecular structures and redox mechanisms of four different oxidation products generated by the chemical reaction of a sulfide endcapped PBP molecule with SbCl5. This includes: (i) the radical cation state, (ii) a decomposition product of the $1e^-$ oxidation state via $2e^-$ oxidation and oxygen atom substitution at terminal position, (iii) the dication state, and (iv) a chloride-adduct of the $2e^-$ oxidation intermediate state via chloronium ion transfer by $SbCl_4^+$. Low temperature conditions and thin-film analysis show that the radical cations undergo intermolecular spin coupling to form an H-aggregated, asymmetric π-dimer. Furthermore, delocalization of the positive charge on the radical cation to the terminal sulfide groups gives it a sulfonium ion character, making it readily susceptible to decompose into a mono-ketone terminated product in the presence of water via nucleophilic substitution. The dication state shows to be stable and its change from an aromatic to a quinoidal backbone is thoroughly characterized. Separate from the redox properties of the D-A-D molecule, we also uncovered new insight into the reactivity of $SbCl_5$ as a $2e^-$ oxidant when present at high concentrations in dichloromethane. Ligand dissociation at high concentrations of $SbCl_5$ induces the formation of $SbCl_4^+$, an active source of the chloronium ions ($2e^-$ oxidant). We confirm this mechanism by proving the formation

of a chloride-adduct of the D-A-D molecule as an alternative way to generate the dication state by $SbCl_5$ oxidation.

After establishing the basic redox properties of the smallest D-A-D system in the PB series, we demonstrate the synthesis and characterization of the longer oligomers with chain lengths of n=5, 7, 9, 15, 21. In chapter 3, the successful synthesis of the monodisperse and discrete PB oligomer series is proven by NMR and mass spectrometry. The NMR shows how the molecular structure changes with increasing conjugation length, revealing a distinction between the monomer units at the end of the chain and the monomer units in the middle of the chain. SANS characterization allowed the reveal of a rod-to-coil conformational change at n=15 in solution. This result reveals that short nPB chain (n=3-9) possess rod-like conformations with persistence lengths up to 2.5 nm, whereas the longer chains (n=15-21) begin to kink and eventually coil at polymer length scales in solution. This result is further verified in the electrochemical properties of the model series.

In chapter 4, the oxidation states of the longer PB oligomers and their polymer homologs are explored. This study takes a look into how the chain-length and chain-conformation play a role in the oxidation processes of D-A π-systems. Firstly, we show that the voltammetric response changes from a single-electron transfer per step to multi-electron transfers per step at n=15, corresponding to the rod-to-coil transition from chapter 3. The polymer voltammogram reveals similar anodic wave patterns as observed for n=9-21, implying that there are multi-oxidation states in CPs instead of just polarons and bipolarons. Secondly, the radical cations prefer to localize at one end of the chain making the chain asymmetric. In the dication states, the short rod-like oligomers prefer bipolaron formation, whereas the long coil-like oligomers prefer di-polaron formation. This is due to the chain length and is also experimentally proven by voltammetry, as the $\Delta E^{1\text{-}2}$ (Columbic repulsion) increases from 3 to 9, and decreases at longer lengths. Thirdly, the lowest energy electronic transition of the radical cation state undergoes bathochromic shifting from 3 to 15 units and reverses to hypsochromic shifting at 21 units and polymer scale lengths. This is also observed for the dication states. In contrast to expectations, the dication state of 15 absorbs further into the NIR region than the polymer in solution, with no major change or enhancement in optical properties with an increase in doping level/ oxidation state. This reveals that the chain length and the oxidation state have to be carefully synced. After a certain length, an increase in

conjugation may begin to have an adverse effect on optical properties depending on the application constraints.

The development of solution-processable donor-acceptor type conjugated polymers in the 1990s has spurred three decades (and counting) of activity towards developing optoelectronic organic devices ranging from transistors and light-emitting diodes to photovoltaics and biosensors. Much progress has been propelled by the realization of highly general and modular side-chain substitutions that can render otherwise insoluble conjugated macromolecules soluble in solvents ranging from low dielectric organics to water. Following this strategy, soluble conjugated polymers exhibit a great deal of chemical structure diversity. Yet, despite the stunning success of engineering high-performance conjugated polymers for electronic applications, much remains to be learned about the chain-conformations and solution-phase behaviors (thermodynamics and hydrodynamics) of conjugated polymers. This knowledge gap inhibits our ability to rationally design deposition processes and control the condensed phase morphologies which directly govern polymer properties and performance in electronic devices. Thereby, the establishment of connections among chain conformations, solution-phase behaviors, and physical properties of conjugated polymers (optical, electronic, redox, and mechanical) is of vital importance to the polymer electronics community. To control structure-property relationships of conjugated polymers, the impact of their chain conformations and solution-phase behaviors on thin film formation, morphologies, and physical properties must be understood.

Our research has established an understanding of the solution behaviors of a series of well-defined molecular species by experimental and theoretical characterization. This insight is valuable for scientists across several fields including materials, polymers, and organic chemistry as it gives both experimental and theoretical insight into the basic nature of a popular class of materials across organic electronics, D-A conjugated polymers. This study entails the chain-length dependent properties of the D-A π-system as a function of increasing conjugation length from the small molecule to the polymer scale length. This insight can aid in understanding solution thin-film casting procedures, giving insight into the solution behavior of D-A polymers in solvent. Furthermore, it can assist in the development of a model which systematically explains how solution behaviors arise from molecular length extension, molecular weight distribution, as well as polymer chain interaction and composition. Ultimately, the goal is to build a theoretical framework for the universal description of chain conformations and phase behaviors of conjugated

polymers in solutions. The development of such a predictive modeling framework will in turn lead to rational design and processing of semiconducting polymers, one of the most fundamental goals of polymer science.

APPENDIX A: SUPPORTING INFORMATION FOR CHAPTER 2

A. General Information

All reagents purchased from commercial suppliers were used without further purification. The antimony(V) chloride reagent was purchased from Acros Organics as a 1.0 M solution in dichloromethane. All reactions were carried out under a N_2 atmosphere, unless otherwise noted. ^{1}H- and ^{13}C-NMR spectra were recorded using a Bruker ARX 400 MHz spectrometer in deuterated chloroform at 293 K and a Bruker ARX 500 MHz spectrometer in deuterated dichloromethane from a temperature range of 200 K to 293 K. High resolution electrospray ionization mass spectrometry was recorded on an Agilent 6320 LC-MS/MS. UV-vis-NIR absorption spectra were measured with an Agilent Technologies Cary 6000i spectrophotometer (350-1600 nm). All the electrochemistry related experiments (CV, DPV) were performed using BioLogic SΠ-150. Electron Paramagnetic Resonance (EPR) spectra were recorded on a Bruker EMX EPR spectrometer.

B. Synthetic Protocols

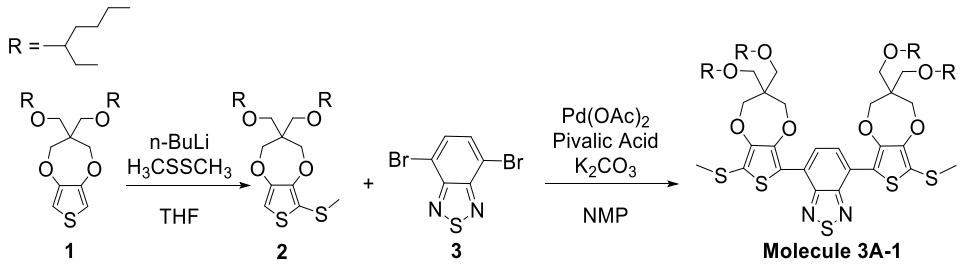

Scheme S1. Synthesis of molecule 3A-1.

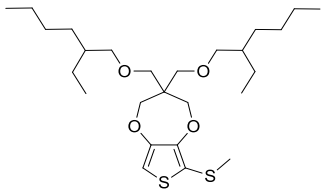

To a THF solution (75 mL) of 1 (2.00 g, 4.54 mmol) was added n-butyllithium (2.5 M, 5.0 mmol) in hexane at -78°C under N_2. After stirring for 120 min at 0°C, dimethyldisulfide (471 mg, 5.0 mmol) was added dropwise to the reaction mixture and then allowed to warm to room temperature. After stirring overnight, the reaction mixture was quenched with water and extracted with hexane and dried over Na_2SO_4. The crude product was concentrated under vacuum and passed through a short alumina column using hexanes:ethyl acetate (75:1). After solvent evaporation, the residue was separated by preparative HPLC (polystyrene/divinylbenzene stationary phase) with $CHCl_3$ to give 2 as a light yellow oil (1.77g, 80% yield). ^{1}H NMR (300 MHz, $CDCl_3$, ppm) δ: 6.44 (s, 1H), 4.09 (s, 2H), 4.00 (s, 2H), 3.47 (s, 4H), 3.27 (d, J = 5.7 Hz, 4H), 2.37(s, 3H), 1.35 – 1.23 (m, 20H), 0.90 – 0.84 (m, 13H). ^{13}C NMR (101 MHz, $CDCl_3$, ppm) δ 150.63, 149.15, 106.15, 74.18, 73.93, 73.61, 69.73, 47.83, 39.51, 30.57, 29.03, 23.89, 23.00, 21.12, 14.02, 11.06. HRMS (ESI), $[M+H]^+$ *m/z* calcd. for $C_{26}H_{47}O_4S_2$: 487.2910; found 487.2902

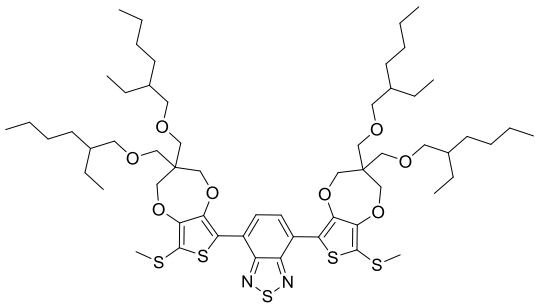

Molecule 3A-1: Compound 2 (3.63 mmol, 1.77 g), 3 (0.73 mmol, 214 mg), $Pd(OAc)_2$ (2.0 mol %), pivalic acid (1.10 mmol, 111 mg) and (1.90 mmol, 263 mg) were all added to a 25 mL schlenk tube and vacuumed for 30 minutes, and then purged with N_2 three times. Anhydrous N-methyl-2-pyrrolidone (5 mL) was added to the mixture and the reaction was heated at 110°C in an oil bath for 2 h, or until benzothiadiazole was completed consumed per TLC analysis. Upon completion, the reaction mixture was quenched with water and extracted with hexane. The organic layer was washed with water twice, then once with brine. The organic layer was separated and dried over $MgSO_4$, then filtered and concentrated. The desired product was purified via SiO_2 column

chromatography using hexanes:CH_2Cl_2 (3:1) to give molecule 3A-1 as an orange viscous oil (331 mg, 41% yield). ^{1}H NMR (500 MHz, CD_2Cl_2, ppm) δ 8.33 (s, 2H), 4.21 (s, 4H), 4.15 (s, 4H), 3.54 (s, 8H), 3.32 (dd, *J* = 5.0 Hz, 8H), 2.45 (s, 6H), 1.43 – 1.27 (m, 34H), 0.87 (m, 22H). ^{13}C NMR (126 MHz, CD_2Cl_2) δ 151.92, 149.69, 147.47, 126.69, 122.98, 117.32, 115.89, 109.21, 73.48, 73.38, 73.20, 69.04, 54.33, 54.11, 53.89, 53.68, 53.46, 47.58, 39.24, 30.32, 28.91, 23.60, 23.55, 23.26, 20.32, 14.23, 10.94. HRMS (ESI), $[M+H]^+$ *m/z* calcd. for $C_{58}H_{92}N_2O_8S_5$: 1104.5458; found 1104.5441. Elem. Anal. calcd. C, 63.01; H, 8.39; N, 2.53; found C, 63.25; H, 8.33; N, 2.60. Molar Absorption Coefficient: $\varepsilon_{490nm} = 2.4 \times 10^4$ $cm^{-1}M^{-1}$.

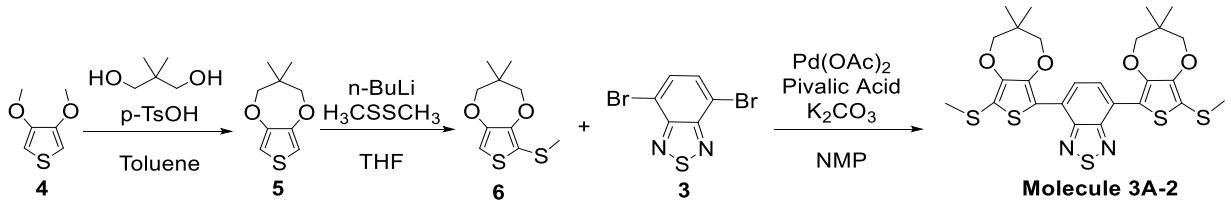

Scheme S2: Synthesis of Molecule 2.

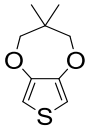

Compound 4 (0.023 mmol, 3.30 g), 2,2-dimethyl-1,3-propanediol (0.027 mmol, 2.86 g) and π-toluene sulfonic acid monohydrate (0.002 mmol, 435 mg) were added to a three-neck round bottom flask and purged with N_2. Toluene (60 mL) was added and the solution was refluxed overnight. The resulting mixture was filtered and the toluene soluble fraction was washed with water and concentrated under vacuum to yield a green viscous oil. The crude product was purified by SiO_2 column chromatography using hexanes:CH_2Cl_2 (2:1) to give 5 as a white solid product (2.36 g, 47% yield). ^{1}H NMR (400 MHz, $CDCl_3$, ppm) δ: 6.47 (s, 2H), 3.73 (s, 4H), 1.03 (s, 6H). ^{13}C NMR (101 MHz, $CDCl_3$, ppm) δ 149.90, 105.41, 79.99, 38.79, 21.58. HRMS (ESI), $[M+H]^+$ *m/z* calcd. for $C_9H_{13}O_2S$: 185.0631; found 185.0635.

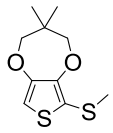

To a THF solution (150 mL) of 5 (2.36 g, 12.8 mmol) was added n-butyllithium (14.1 mmol, 2.5 M) in hexane at -78°C under N_2. After stirring for 120 min at 0°C, dimethyldisulfide (14.1 mmol, 1.33 g) as added dropwise to the reaction mixture and then allowed to warm to room temperature. After stirring overnight, the reaction mixture was quenched with water and extracted with hexane and dried over Na_2SO_4. The crude product was concentrated under vacuum and passed through a short alumina column using hexanes:ethyl acetate (75:1). After solvent evaporation, the residue was separated by preparative HPLC (polystyrene/divinylbenzene stationary phase) with $CHCl_3$ to give 6 as a light yellow oil (1.04 g, 35% yeild). ^{1}H NMR (400 MHz, $CDCl_3$, ppm) δ 6.48 (s, 1H), 3.81 (s, 2H), 3.72 (s, 2H), 2.36 (s, 3H), 1.03 (s, 6H). 13C NMR (101 MHz, $CDCl_3$, ppm) δ 150.92, 149.44, 114.69, 106.72, 80.03, 79.90, 38.88, 21.65, 21.19. HRMS (ESI), $[M+H]^+$ *m/z* calcd. for $C_{10}H_{15}O_2S_2$: 231.0508; found 231.0505

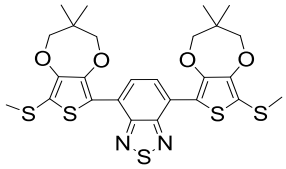

<u>Molecule 3A-2:</u> Compound 6 (4.52 mmol, 1.04 g), 3 (0.90 mmol, 265 mg), $Pd(OAc)_2$ (2.0 mol %), pivalic acid (1.35 mmol, 138 mg) and (1.80 mmol, 249 mg) were all added to a 25 mL schlenk tube and vacuumed for 30 minutes, and then purged with N_2 three times. Anhydrous N-methyl-2-pyrrolidone (3 mL) was added to the mixture and the reaction was heated at 110°C in an oil bath for 2 h, or until benzothiadiazole was completed consumed per TLC analysis. Upon completion, the reaction mixture was quenched with water and extracted with hexane. The organic layer was washed with water twice, then once with brine. The organic layer was separated and dried over $MgSO_4$, then filtered and concentrated. The desired product was purified via SiO_2 column chromatography using hexanes:CH_2Cl_2 (3:1) to give molecule 3A-2 as an orange solid (197 mg, 37% yield). ^{1}H NMR (400 MHz, $CDCl_3$, ppm) δ 8.28 (s, 2H), 3.93 (s, 8H), 2.48 (s, 6H), 1.11 (s, 12H). ^{13}C NMR (101 MHz, $CDCl_3$, ppm) δ 152.45, 150.43, 147.74, 127.45, 123.73, 118.64, 116.95, 80.02, 79.87, 38.87, 21.81, 20.61. HRMS (ESI), $[M+H]^+$ *m/z* calcd. for $C_{26}H_{29}N_2O_4S_5$: 592.0647; found 592.0629

C. Chemical Oxidation of 3A-1 and 3A-2 with Antimony(V) Pentachloride

Radical Cation (3A-1$^{\bullet+}$): A 50 ml solution of molecule **1** at 5.4 x 10^{-4}M (0.027 mmol, 30.0 mg) concentration was prepared in a schlenk tube equipped with a stir bar. From a *0.1 M stock solution of $SbCl_5$* in CH_2Cl_2, 1.5 eq. of $SbCl_5$ (0.041 mmol, 0.410 mL) was transferred to the reaction mixture via a needle and syringe, causing an immediate red to green color change. The solution was allowed to stir for 30 minutes. A 0.120 mL aliquot of the reaction was removed and diluted to 2 x 10^{-5} M for UV-vis-NIR analysis to confirm formation of NIR absorbing radical cation. The crude material was concentrated under vacuum, put under N_2 again, dissolved in 1 mL of CH_2Cl_2 and treated with 2 mL of anhydrous *n*-hexane. The solution was allowed to precipitate at -18^{o}C for 72 hours, centrifuged and washed with *n*-hexane twice. The solid was dried in vacuo to give **1**$^{\bullet+}$($SbCl_6$) as a dark green viscous solid (18.4 mg, 47% yield). Elem. Anal. 1$^{\bullet+}SbCl_6$ (+ ½$SbCl_5$): cald. C, 43.82; H, 5.83; N, 1.76; Cl, 18.96. found C, 44.13; H, 5.80; N, 1.74; Cl, 18.32. ^{1}H NMR (500 MHz, 196 K, CD_2Cl_2, ppm): δ 6.90 (d, *J* = 89.9 Hz, 2H), 4.57 (s, 1H), 4.33 (s, 1H), 4.21 (s, 2H), 4.03 (s, 3H), 3.44 (s, 7H), 3.26 (s, 6H), 2.89 (s, 3H), 2.50 (s, 3H), 1.17 (s, 42H), 0.79 (s, 32H).

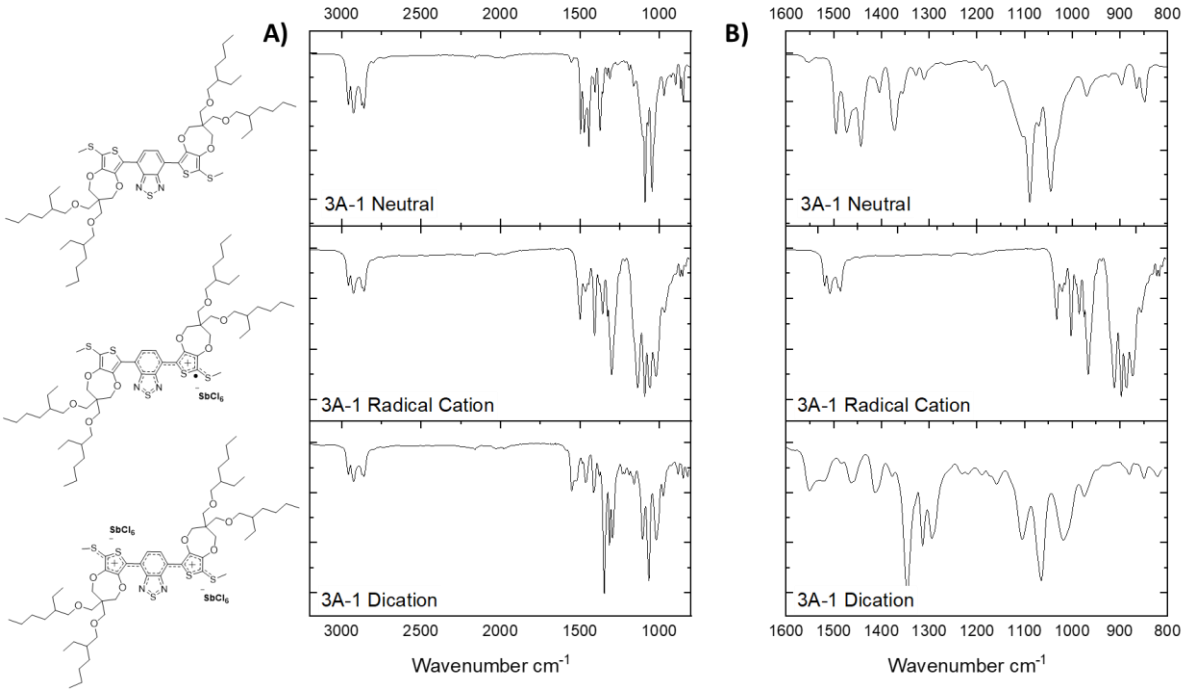

Figure S1. FT-IR of 3A-1 in the neutral, radical cation and dication states. A) 3000 – 800 cm^{-1} and B) Zoom in of 1600-800 cm^{-1} fingerprint region.

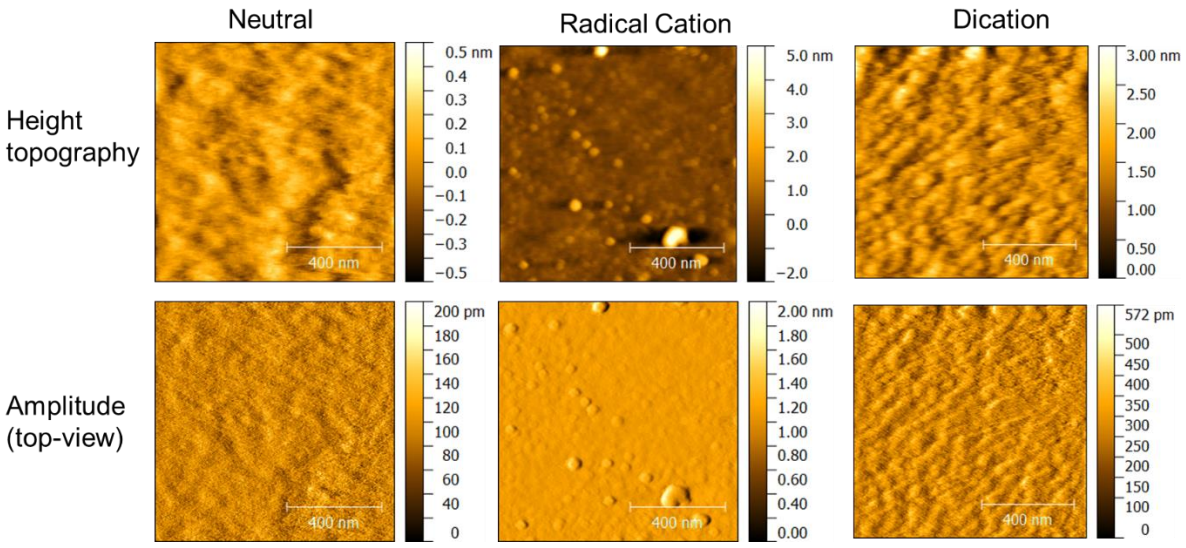

Figure S2. AFM imaging of 3A-1 in the neutral, radical cation, and dication states as thin-films.

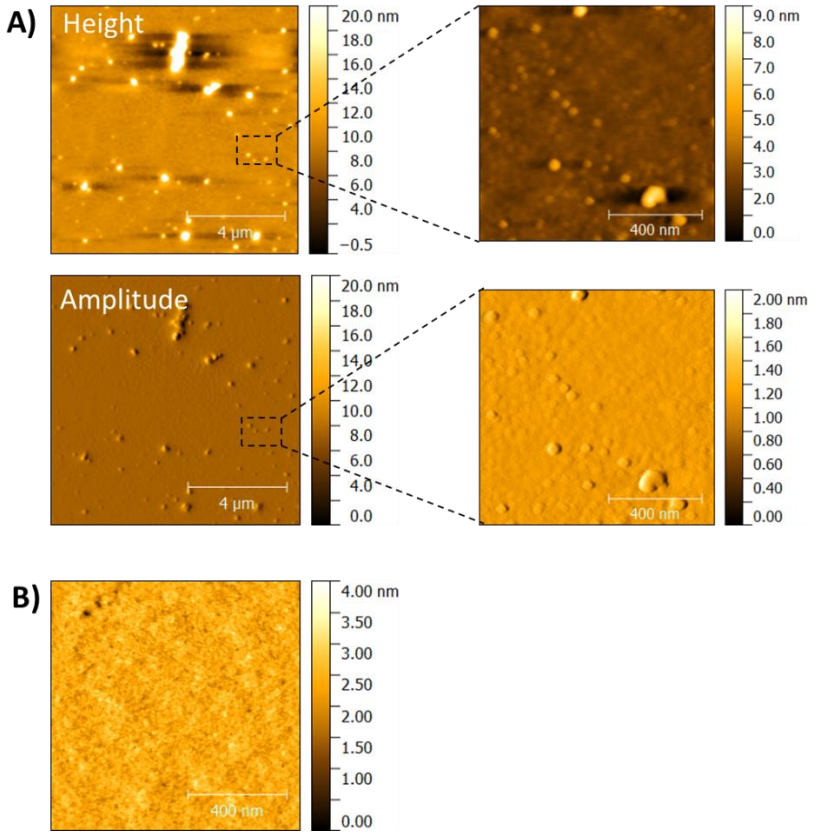

Figure S3. AFM imaging of A) 3A-1 radical cation in thin-film, B) $SbCl_5$.

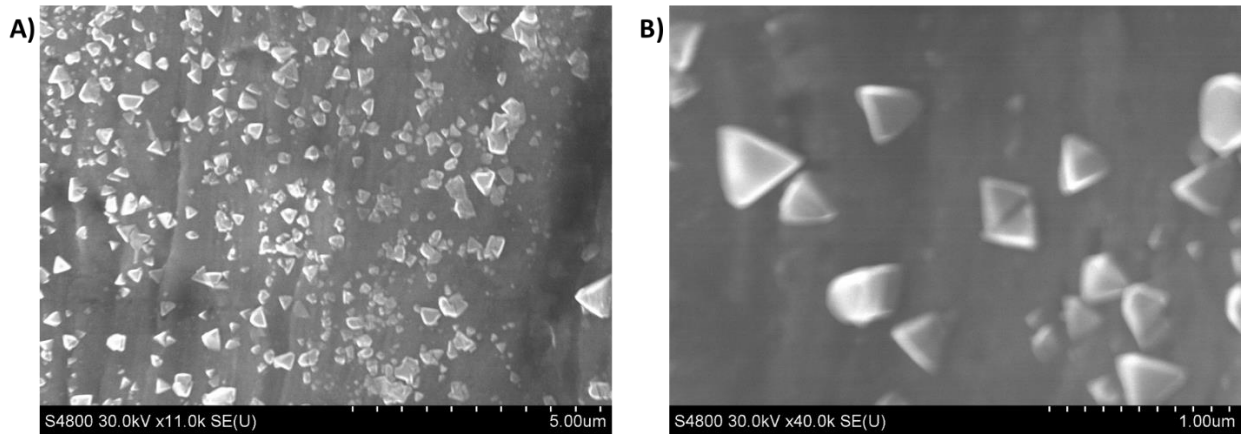

Figure S4. SEM image of 3A-1 radical cation morphology in solid state. A) at 5.00 μm and B) at 1 μm.

Dication (3A-1): A 0.5 mL solution of molecule 1 at 0.54 M (0.270 mmol, 300 mg) concentration was prepared in a schlenk tube equipped with a stir bar. From a *1.0 M stock solution of* $SbCl_5$ in CH_2Cl_2, 1.5 eq. of $SbCl_5$ (0.410mmol, 0.410 mL) was transferred to the reaction mixture via a needle and syringe, causing an immediate red to blue color change. The solution was allowed to stir for 30 minutes. A 0.10 mL aliquot of the reaction was removed, diluted to 2 x 10^{-5} M for UV-vis-NIR analysis to confirm formation of a visible absorbing dication (λ_{exp}=620 nm). The schlenk tube was submerged in an acetone-dry ice bath (-78^{o}C) and 5 mL of prechilled anhydrous *n*-hexane was added to the reaction to immediately precipitate gold-blue colored solid. The solid was filtered under nitrogen, washed with prechilled anhydrous *n*-hexane, and dried in vacuo to give microcrystals of $1(SbCl_6)_2$ as a gold olid (86 mg, 18% yield). Elem. Anal. $1(SbCl_6)_{2:}$ calcd. C, 39.26; H, 5.23; N, 1.58; Cl, 23.97. found C, 40.04; H, 5.05; N, 1.63; Cl, 23.08. ^{1}H NMR (500 MHz, 190 K, CD_2Cl_2, ppm): δ 8.69 (s, 2H), 4.60 (s, 4H), 4.34 (s, 4H), 3.44 (s, 8H), 3.26 (s, 8H), 3.14 (s, 6H), 1.18 (s, 22H), 0.83 – 0.75 (m, 34H).

D. Functional Group Derivatives:

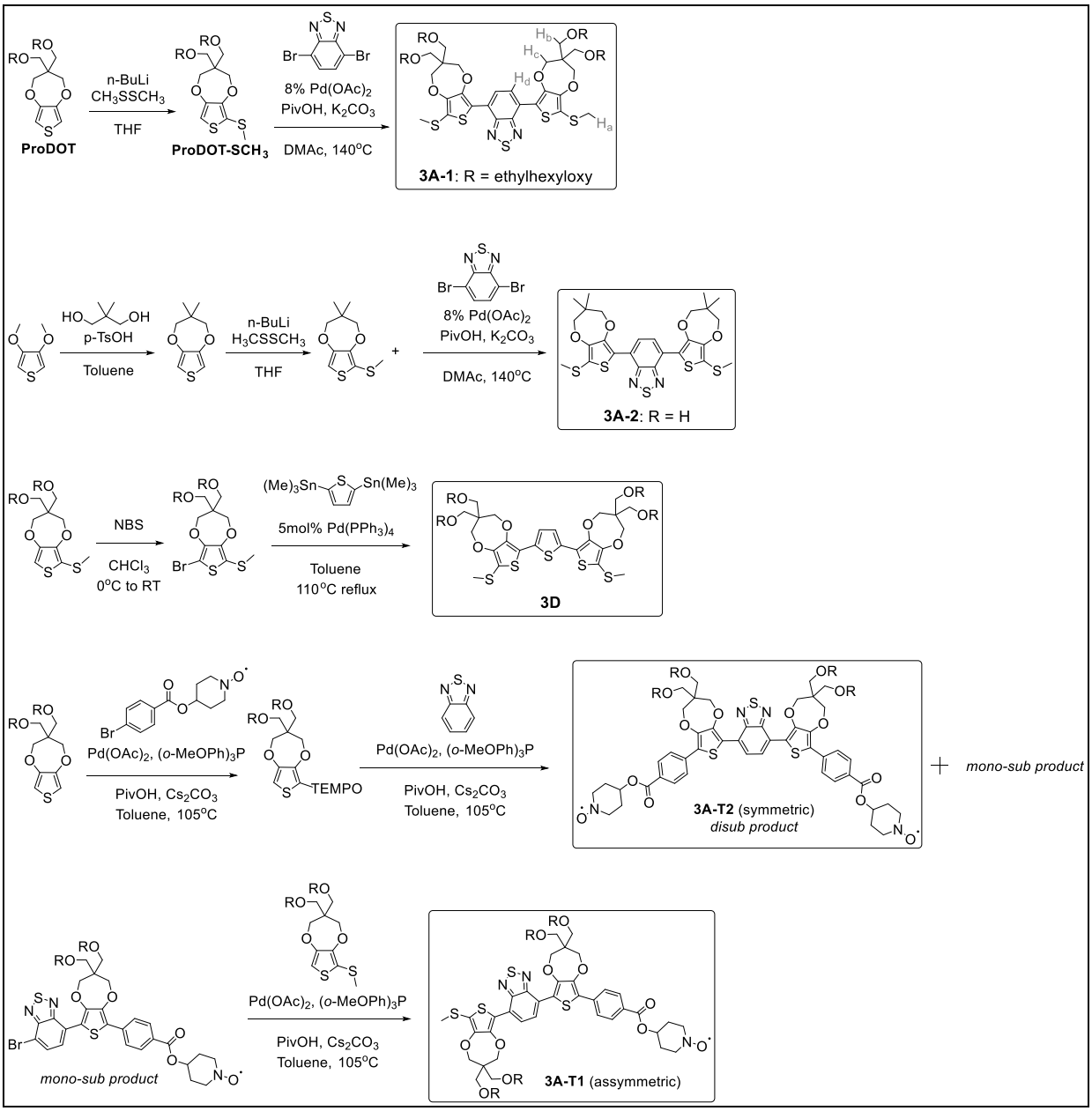

Scheme 3. Synthesis of n=3, PBP, derivatives labeled as 3A-1, 3A-2, 3D, 3A-T2, and 3A-T1. Hydrogen atom labels on 3A-1 correspond to the 1H NMR spectra in Figure 5. (Abbreviations: Pivalic Acid (PivOH), Dimethylacetamide (DMAc)).

Sequence Effect (D-A-D vs. D-D-D)-3D: To determine if the D-A-D structure was the cause of the low peak separation by voltammetry, a D-D-D oligomer composed of ProDOT-Thiophene-ProDOT and sulfide endcapping groups was synthesized by Stille coupling, as shown in scheme 3. The D-D-D control oligomer oxidized at a lower voltage, as expected for an electron rich molecule. However, this compound showed a greater peak-to-peak separation, indicating two things a) non-faradaic processes were not to blame in the previous electrochemical analysis of 1 and b) that the mid-thiophene unit induced greater planarity and conjugation between the ProDOT units, thereby inducing a higher Coulombic repulsion between two charges in the dication state. This experiment revealed that the PB repeat unit experiences a higher twist angle between monomer units in comparison to ProDOT-Thiophene. Therefore, its lower peak-to-peak separation implies the dication state of the PBP oligomer is not as conjugated or planar as the ProDOT-Thiophene-ProDOT oligomer, albeit both oligomers experience an increase in planarization upon oxidation and transition from an aromatic to a quinoidal backbone.

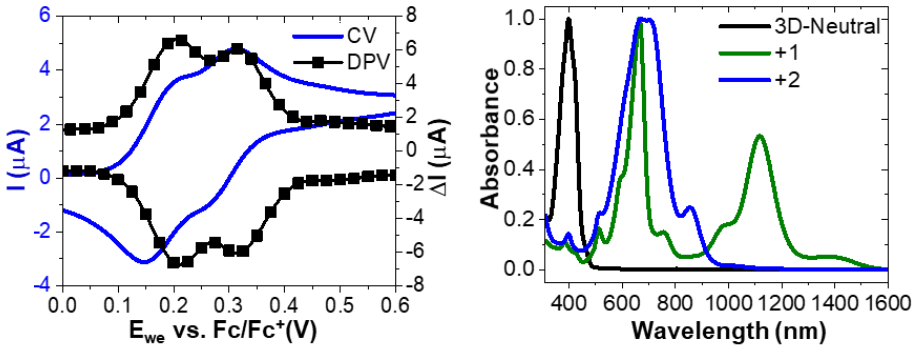

Figure S5. Voltammetric and optical properties of of 3D.

End-Group Effect: 3A-T2 and 3A-T1: The impact of the endcapping group was explored by replacement of the methyl thio endcapping groups with TEMPO moieties.

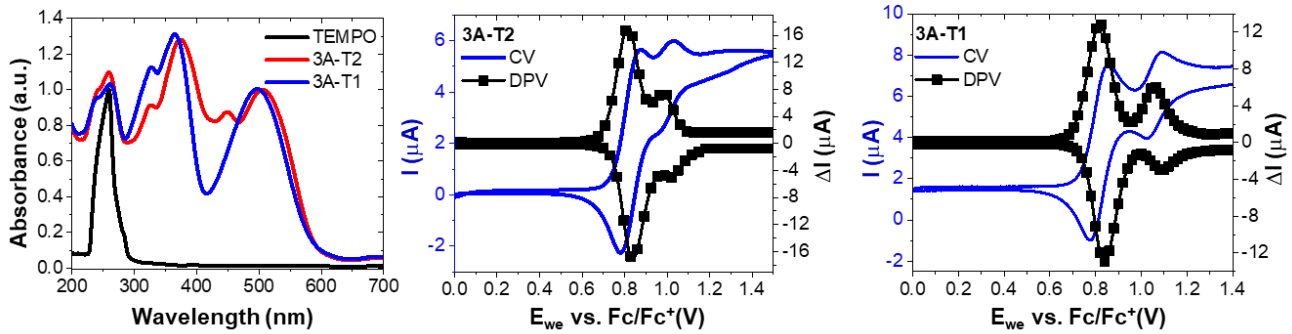

Figure S6. Voltammetry and optical properties of 3A-T2 and 3A-T1.

Table S1. Summary of Voltametric Properties

	$E½^1$ (V)	$E½^2$ (V)	ΔE^1-E^2(mV)	IP (eV)	π-π* λ_{max} (nm)	D-A λ_{max} (nm)
3A-1	0.317	0.376	59	-5.417	329	491
3A-2	0.318	0.37	52	-5.418	328	485
3D	0.207	0.312	105	-5.307	398	--
3A-T2	0.316	0.498	182	-5.416	366	498
3A-T1	0.318	0.562	244	-5.418	375	507
[a] All values referenced to ferrocene E½ = 0.51 V vs. Ag/Ag^+ in CH_2Cl_2 [b] Values reported relative to vacuum (-5.1 eV)						

E. Cyclic Voltammetry (CV)

Solution CV of molecule 3A-1 was conducted under a nitrogen atmosphere at 1 mM in 0.2 M $TBAPF_6$/ CH_2Cl_2 on a platinum button electrode and a platinum wire counter electrode. An Ag/AgCl wire was used as the pseudoreference electrode which was calibrated against a ferrocene/ ferrocenium as an internal standard ($E_{1/2}$ = 0.51 V). The voltage was scanned from -0.2 to 0.6 V vs. Fc^+/Fc, at a 5 mV/s scan rate. The second cycle is reported in the main text figure.

F. Differential Pulse Voltammetry (DPV)

After CV, the same solution of neutral molecule 3A-1 was used to conduct DPV. The voltage was scanned from -0.2 V to 0.6 V vs. Fc^+/Fc, at a 200 mV/sec scan rate. A 5 mV pulse height, 10 ms pulse width, 5.0 mV step height, and 25 ms step time were used.

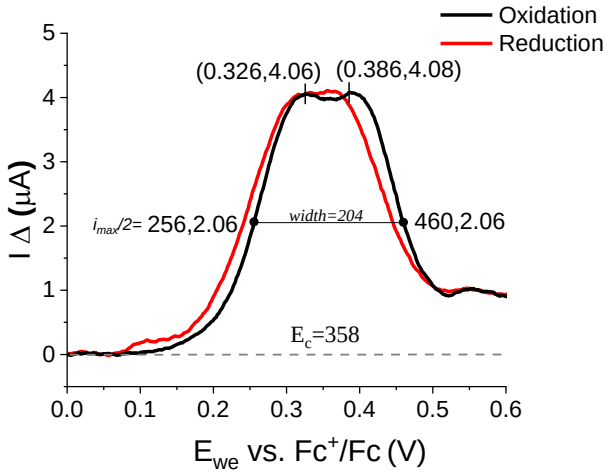

Figure S7: Differential Pulse Voltammetry (200 mV/s) of a 1 mM solution of molecule 3A-1 in 0.2 M $TBAPF_6/CH_2Cl_2$ at a platinum button working electrode vs. Fc^+/Fc as an internal standard ($E_{1/2}$ = 0.51V vs. Ag/AgCl).

$$E_{1/2}^{1} = E_C + \frac{\Delta E_{1/2} + E_{pul}}{2}$$

$$E_{pul} = pulse\ amplitude = 10\ mV$$

$$E_{1/2}^{2} = 358 + \left(\frac{117 + 10}{2}\right) = 422\ mV$$

$$E_{1/2}^{1} = 422 - 117 = 305\ mV$$

$$K_c = \exp\left[\frac{(E_1^o - E_2^o)n_1 n_2 F}{RT}\right] = \exp\left[\frac{(117)}{25.69}\right] = 95.04$$

G. Spectroelectrochemistry

Solution spectroelectrochemistry of molecule 3A-1 was done in a three electrode honeycomb electrochemical cell supplied by Pine Research. A 12.5 x 12.5 x 45.0 mm^3 quartz cuvette with a 1.7 mm path length was used as the cell, equipped with a polished platinum honeycomb electrode (working and counter) and Ag/AgCl pseudoreference electrode calibrated against a ferrocene/ferrocenium standard for which the $E_{1/2}$ is taken to be 0.51 V vs. Ag/AgCl. A homemade teflon cap was specially designed to keep the cell sealed from solvent evaporation and air contamination. In a nitrogen filled glove box, 4 $x10^{-4}$ M solution of PBP was prepared with 0.2 M $TBAPF_6$ in anhydrous DCM and transferred and sealed in the electrochemical quartz cell and sealed with teflon tape. During electrochemical oxidation, the voltage is increased from 0 to 1.2 V in 50 mV increments by linear scan voltammetry (LSV) at a 25 mV/s scan rate. The internal resistance was compensated for before every LSV reading by the EC-Lab software program. After the experiment was completed, a reduction potential of -0.1 V was applied to retrieve the neutral species. The time constant between each absorption spectrum measurement is 170 s; potential is applied for 10 seconds and the UV-vis-NIR absorption is taken immediately after from 250 to 1600 nm at a rate of 10 nm/sec (160 s).

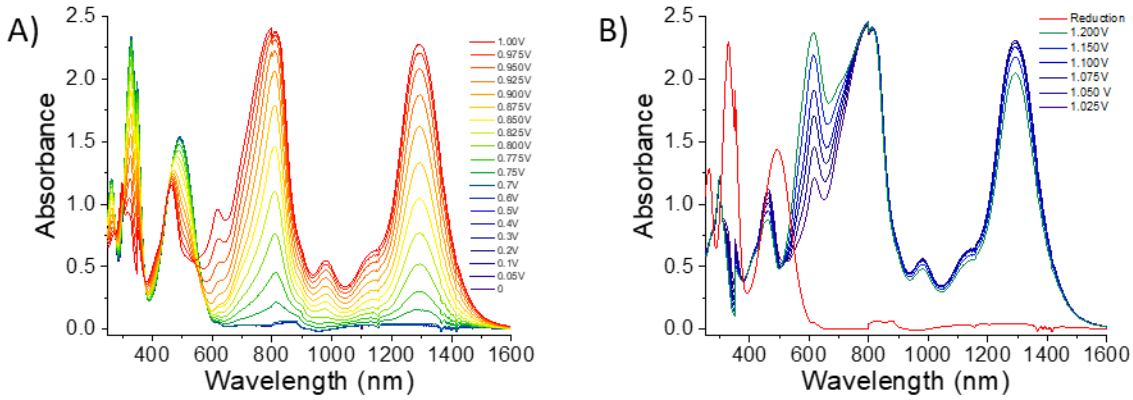

Figure S8: Spectroelectrochemistry of a 2.0 mM solution of molecule 3A-1 in 0.2 M $TBAPF_6/CH_2Cl_2$ in an optically transparent thin layer quartz cuvette equipped with a platinum honeycomb electrode vs. Ag/AgCl. The spectra is divided into A) oxidation potential from 0 to 1.00 V and B) 1.025 to 1.200 V and reduction back to neutral.

H. Comproportionation Reaction of 3A-1 and 3A-1

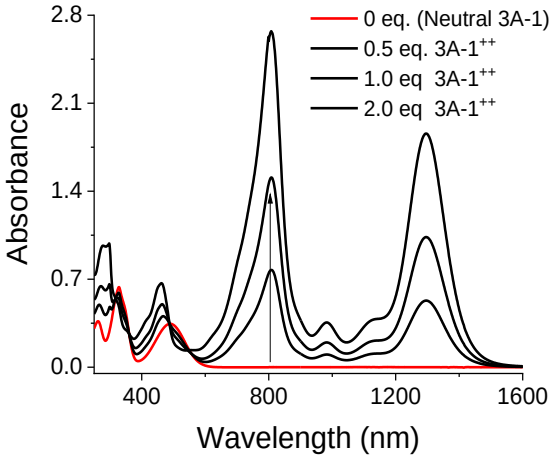

Figure S9: Absorption spectra tracking the addition of 3A-1 into a solution of 3A-1. This is a comproportionation reaction ($X + X \rightarrow X^{\bullet+}$) of 3A-1 and isolated 3A-1$(SbCl_6)_2$ to generate 3A-$1^{\bullet+}$. This experiment proves that the dication state should not be stable in the presence of the neutral state. For Cl-2^+, this is not the case, as this two-electron oxidized chlorine adduct is stable in the presence of neutral 3A-1.

I. Stability Measurement of Chlorine Adduct (Cl-2^+) in Reaction Solution

A 3.1×10^{-3} solution of molecule 3A-1 in CH_2Cl_2 was treated with 1.5 equivalent of 1.0 M $SbCl_5$ under an inert atmosphere. To measure the absorbance of the Cl-2^+ adduct (dication) at 620 nm as a function of time, aliquots of the reaction solution were taken at specific time intervals and diluted to 3.1×10^{-5} M to allow measurements in a 10 mm pathlength cuvette. The purpose of this analysis is to show that Cl-2^+ is stable in solution for several hours, even after dilution of the reaction

solution from 3.1×10^{-3} M to 3.1×10^{-5} M. The mass spectroscopy experiment (Figure S11) that was conducted to detect Cl-2^{+} took about 30 minutes under ambient conditions and required a 100× dilution of the reaction mixture due to signal saturation. Since this type of adduct is expected to be extremely sensitive to moisture content or concentration, this stability experiment was used to confirm that dilution nor time was a problem in the timeframe used to detect Cl-2^{+}.

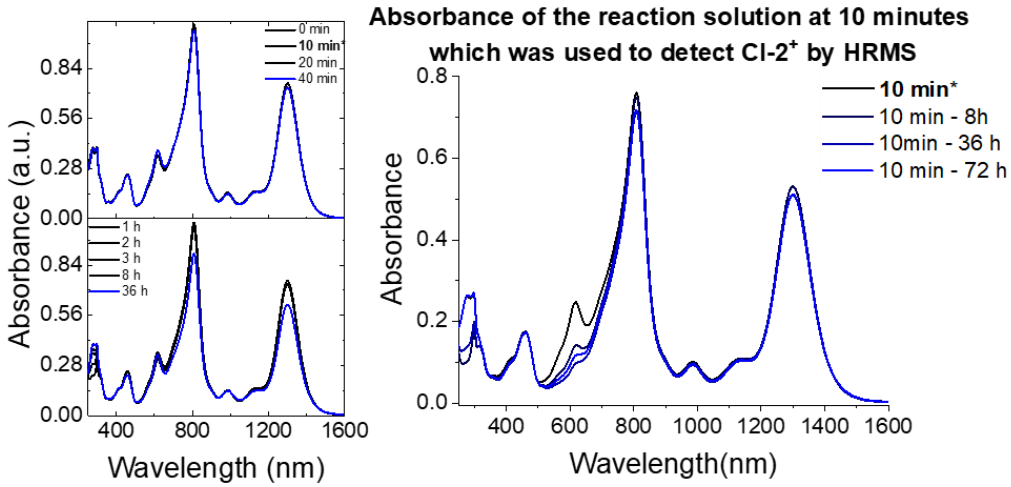

Figure S10. A) Absorption spectra depicting the consistency of the Chlorine adduct (Cl-2^{+}) absorbance peak at 620 nm over the course of several hours to show its stability over several hours after dilution from 10^{-3} to 10^{-5} M. B) Absorption spectra of the reaction solution aliquot taken at 10 min* to run the mass spectroscopy experiment (shown in Figure S11) and its stability after several hours.

J. High Resolution Mass Spectroscopy (HR-MS) by Atmospheric Pressure Chemical Ionization (APCI)

A 0.0032 M solution of molecule 3A-2 was prepared by dissolving 4.7 mg of 2 in 2.5 mL of anhydrous CH_2Cl_2 in a N_2 filled glove box. Chemical oxidation by 1.5 equivalent of $SbCl_5$ (0.012 mmol, 24 μL, 0.5 M) was added to the solution and ~25 μL of the reaction solution was analyzed by APCI. The chloro-sulfonium cation was successfully detected by observation of the chlorine 35 and 37 isotope peaks of $2^{\bullet+}$(Cl) at 627 and 629 m/z, with a difference of 1.4 ppm compared to theoretical calculations.

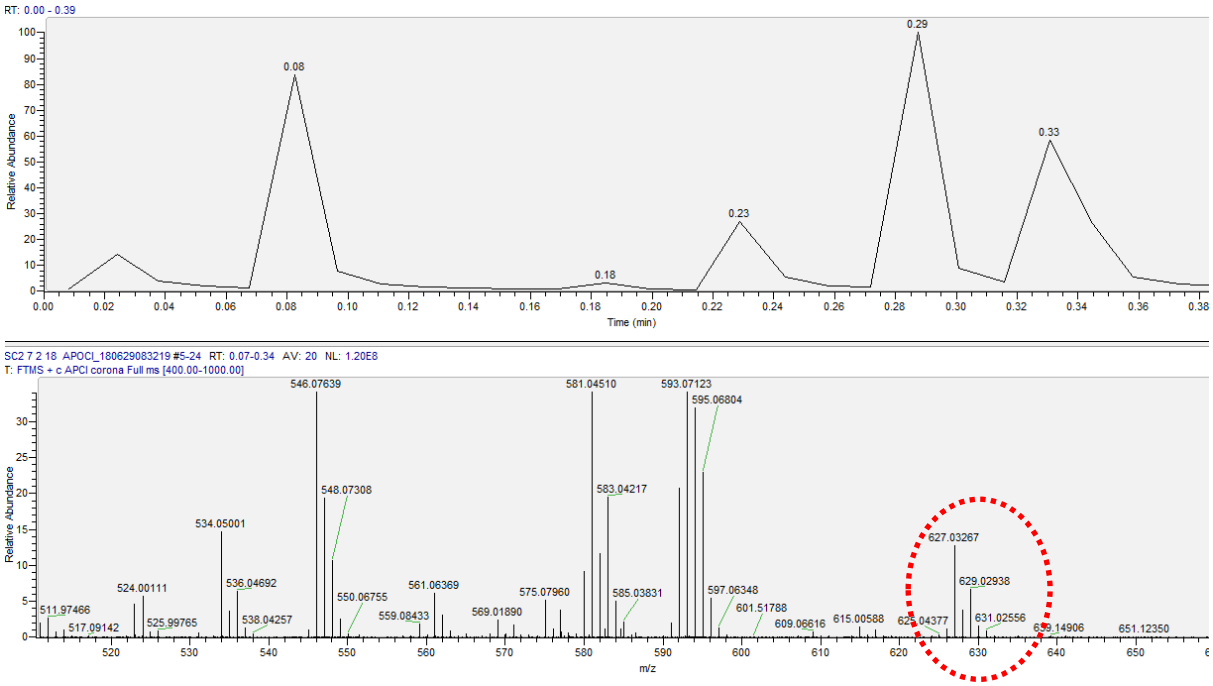

Figure S11: HR-APCI of a reaction solution of molecule 3A-2 with $SbCl_5$ showing the chlorine isotope peaks of Cl-2^+ at 627 and 629 m/z.

K. Electrochemical and Chemical Oxidation of Molecule 3A-2

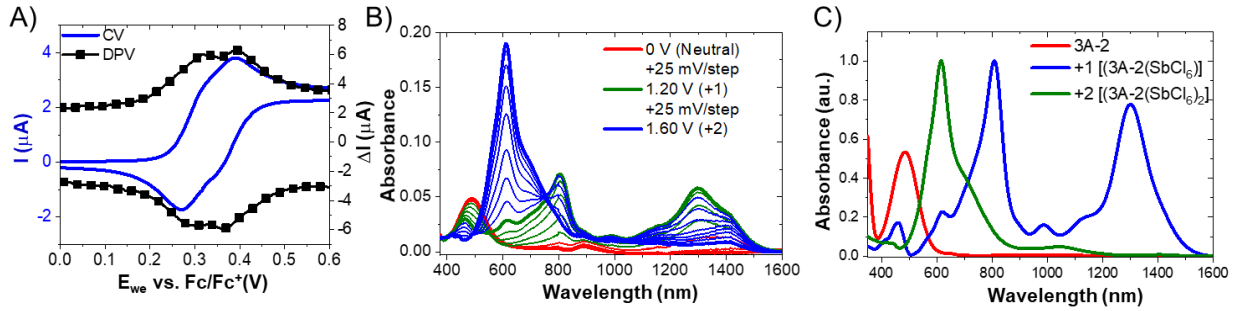

Figure S12: A) Cyclic voltammogram (scan rate: 5 mV/s) and differential pulse voltammogram (scan rate: 200 mV/s) of a 1 mM solution of molecule 3A-2 in 0.2 M $TBAPF_6/CH_2Cl_2$ at a platinum button working electrode vs. Fc^+/Fc as an internal standard ($E_{1/2}$ = 0.51V vs. Ag/AgCl). B) Spectroelectrochemistry of a 20 μM solution of molecule 3A-2 in 0.2 M $TBAPF_6/CH_2Cl_2$ in an optically transparent thin layer quartz cuvette equipped with a platinum honeycomb electrode vs. Ag/AgCl. C) 3A-2 in the neutral, radical cation, and dication states as isolated $SbCl_6$ salts redissolved in anhydrous CH_2Cl_2.

L. X-Ray Crystallography

The radical cation, 3A-$2^{\bullet+}[SbCl_6]$ was synthesized by $SbCl_5$ oxidation of 3A-2. After isolation of the radical cation salt, 10mg/ml solution of 3A-$2^{\bullet+}$ was prepared in o-dichlorobenzene (o-DCB),

carefully layered with 1:1 mixture of o-DCB:n-hexane, and a final layer of n-hexane in an NMR tube under air at RT. Slow diffusion for one week led to the formation of two black crystal with distinct morphologies. Manual separation and single crystal analysis of the two morphologies revealed the formation of rod-shaped crystals of 3A-2$^{\bullet+}$ and a block-shaped crystal of a decomposition product with one ketone terminal group (2$^{'}$).

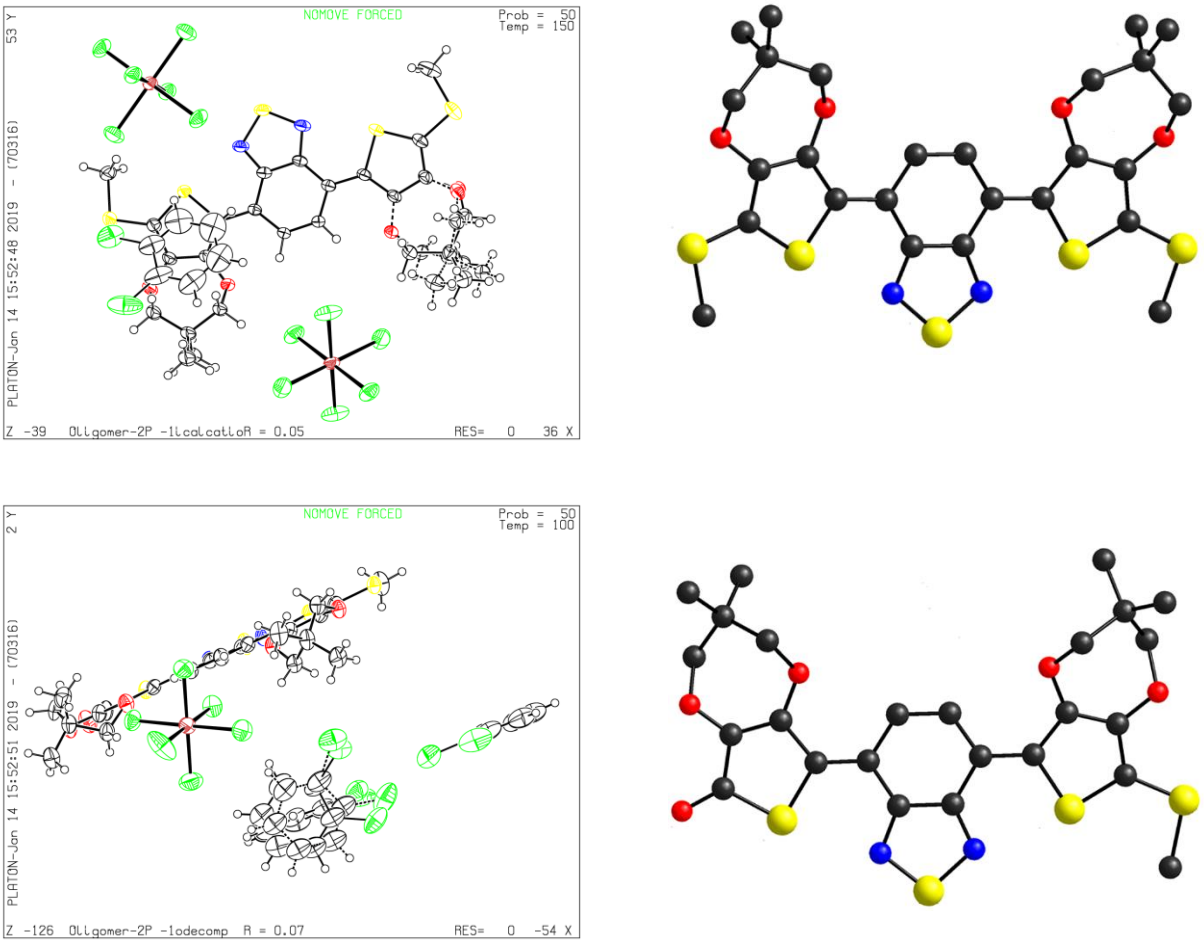

Figure S13. Perspective drawings from the x-ray crystal structure determination of A) 3A-2$^{\bullet+}$ and B) 2' depicting all counter anions and solvent molecules.

Bond #	3A-2 Bond Length (Å)	3A-2$^{\bullet+}$ Bond Length (Å)	3A-2 Bond Length (Å)	2' Bond Length (Å)
1	(1.831)	1.804(5)/ (1.819)	(1.819)	*C=O
2	(1.758)	1.698(3)/ (1.730)	(1.700)	1.241(7)/ (1.208)
3	(1.375)	1.394(4)/ (1.390)	(1.410)	1.440(8)/ (1.470)
4	(1.437)	1.394(4)/ (1.409)	(1.390)	1.367(7)/ (1.365)
5	(1.385)	1.413(4)/ (1.419)	(1.453)	1.464(8)/ (1.466)
6	(1.747)	1.755(3)/ (1.767)	(1.779)	1.759(5)/ (1.766)
7	(1.737)	1.726(3)/ (1.735)	(1.734)	1.784(6)/ (1.812)
8	(1.462)	1.419(4)/ (1.417)	(1.378)	1.380(7)/ (1.385)
9	(1.383)	1.415(4)/ (1.416)	(1.450)	1.447(7)/ (1.443)
10	(1.420)	1.381(4)/ (1.387)	(1.356)	1.381(7)/ (1.368)
11	(1.383)	1.414(4)/ (1.416)	(1.450)	1.403(8)/ (1.436)
12	(1.438)	1.444(4)/ (1.448)	(1.460)	1.457(7)/ (1.457)
13	(1.450)	1.432(4)/ (1.443)	(1.434)	1.435(7)/ (1.440)
14	(1.438)	1.439(4)/ (1.448)	(1.460)	1.441(8)/ (1.457)
15	(1.462)	1.412(4)/ (1.417)	(1.378)	1.402(7)/ (1.395)
16	(1.385)	1.413(4)/ (1.419)	(1.454)	1.436(7)/ (1.435)
17	(1.437)	1.395(4)/ (1.409)	(1.390)	1.380(8)/ (1.402)
18	(1.375)	1.391(4)/ (1.390)	(1.410)	1.399(8)/ (1.396)
19	(1.737)	1.718(3)/ (1.735)	(1.734)	1.719(5)/ (1.730)
20	(1.747)	1.754(3)/ (1.767)	(1.779)	1.753(6)/ (1.775)
21	(1.758)	1.707(3)/ (1.730)	(1.700)	1.693(6) (1.720)
22	(1.831)	1.793(4)/ (1.819)	(1.818)	1.808(6)/ (1.818)

Table S2. Select geometric parameters extracted from the x-ray crystal structures (w/ esd) and, in parentheses, from DFT calculations at the OT-ωB97X-D/6-31+G(d,p) level of theory.

M. DFT-derived Bond Lengths and Atomic Charges

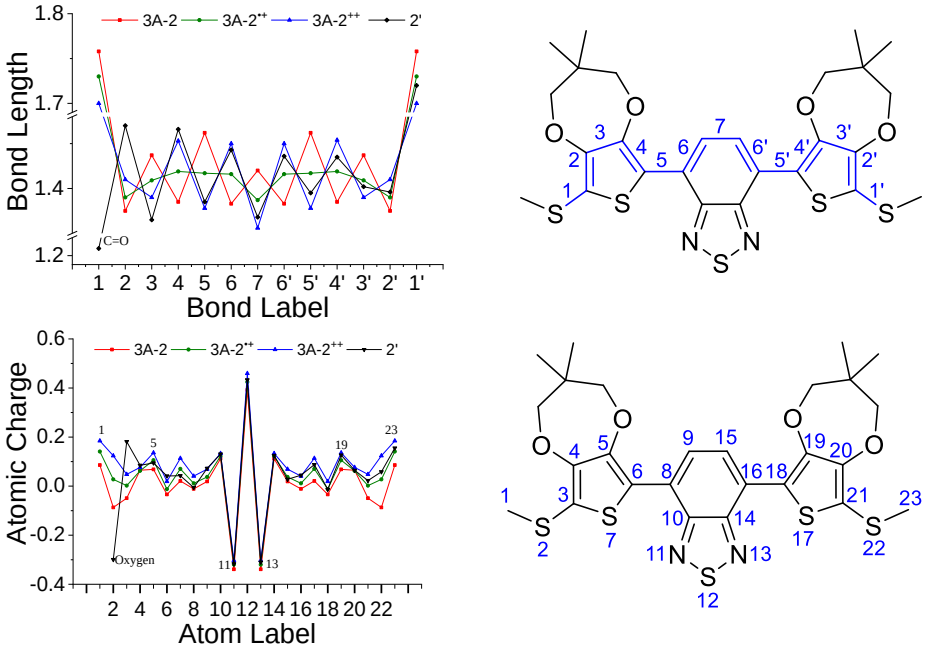

Figure S14. A) Select π-backbone bond lengths for 3A-2, 3A-2$^{\bullet+}$, 3A-2, and 2' with corresponding bond label scheme, and B) atomic charge distribution of 3A-2, 3A-2$^{\bullet+}$, 3A-2, and 2' with corresponding atom label scheme as determined at the OT-ωB97X-D/6-31+G(d,p) level of theory.

N. X-Ray Crystallography of (3A-2$^{\bullet+}$)$_2$ π-Dimer

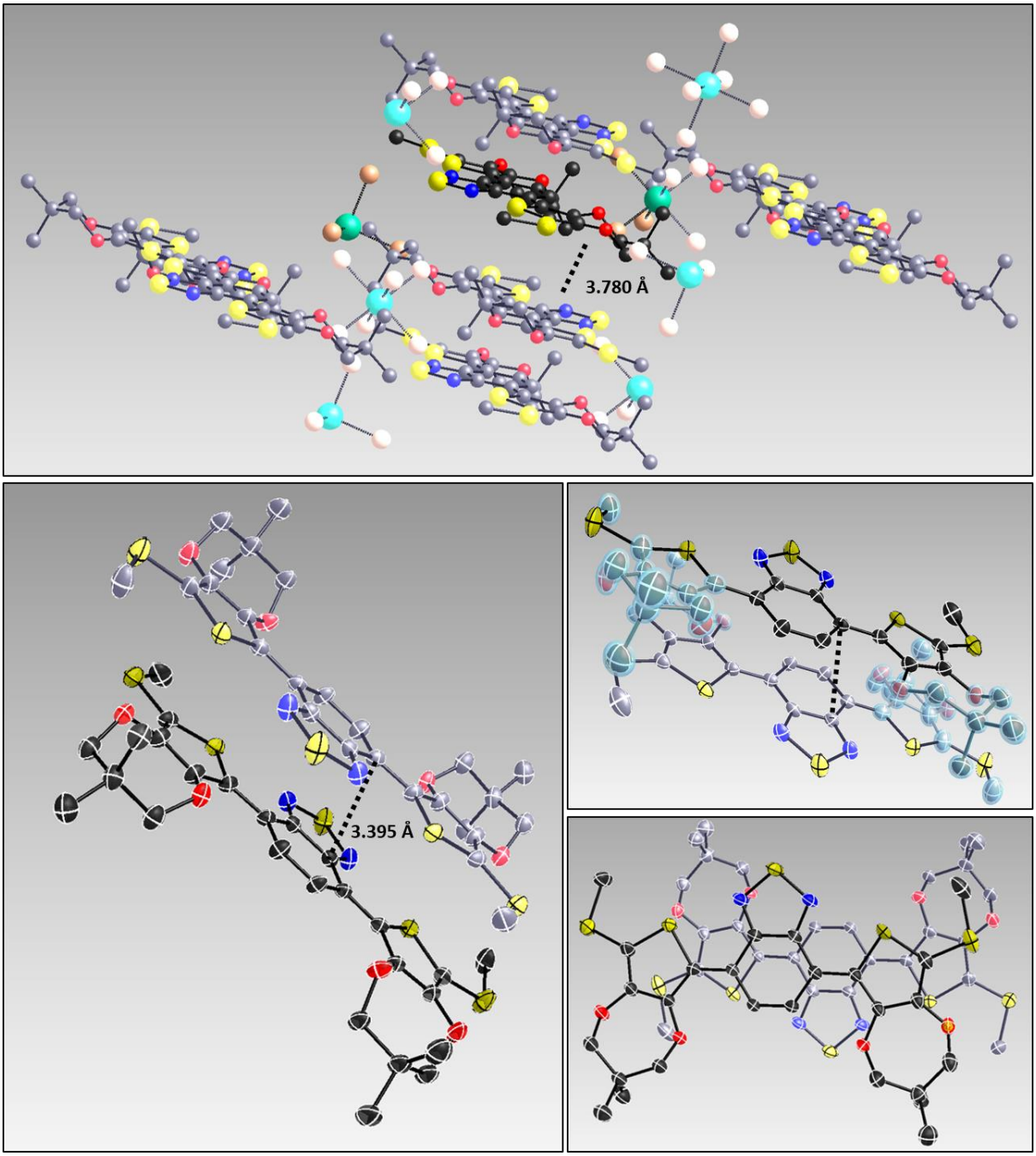

Figure S15: Perspective drawings from the X-ray crystal structure determination of 3A-2$^{\bullet+}$ that highlight a π-π stacking distance of 3.395 Å between two radical molecules and a 3.780 Å distance between two π-dimers.

O. Low Temperature UV-vis-NIR Spectroscopy

Table S2. Low Temperature UV-vis-NIR and NMR spectroscopy of Molecule 3A-1.

	UV-vis-NIR (nm)		^{1}H NMR (ppm, proton)	
	RT	~200 K	RT	~200 K
3A-**1**	328, 490	328, 490	A: 2.45, 6H C: 4.15, 4H and 4.21, 4H D: 8.33, 2H	A: 2.33 , 6H C: 4.07 , 4H and 4.16, 4H D: 8.18 , 2H
3A-**1**$^{\bullet+}$ [(a)]	808, 1295	624, 938[(a)], 1458[(c)]	Alkyl side chain peaks at 0.5-1.5 and 3.0-3.6[(b)]	A: 2.50, 3H and 2.89, 3H C: 4.03 – 4.57, 8 H D: 6.81-6.99, 2H
3A-**1**	620	620	Alkyl side chain peaks at 0.5-1.5 and 3.0-3.6[(b)]	A: 3.14, 6H C: 4.34 – 4.60, 8H D: 8.69, 2H

a – radical cation π-dimerization at 200 K in solution
b – paramagnetic line broadening effect
c – retrieved from solid state thin film

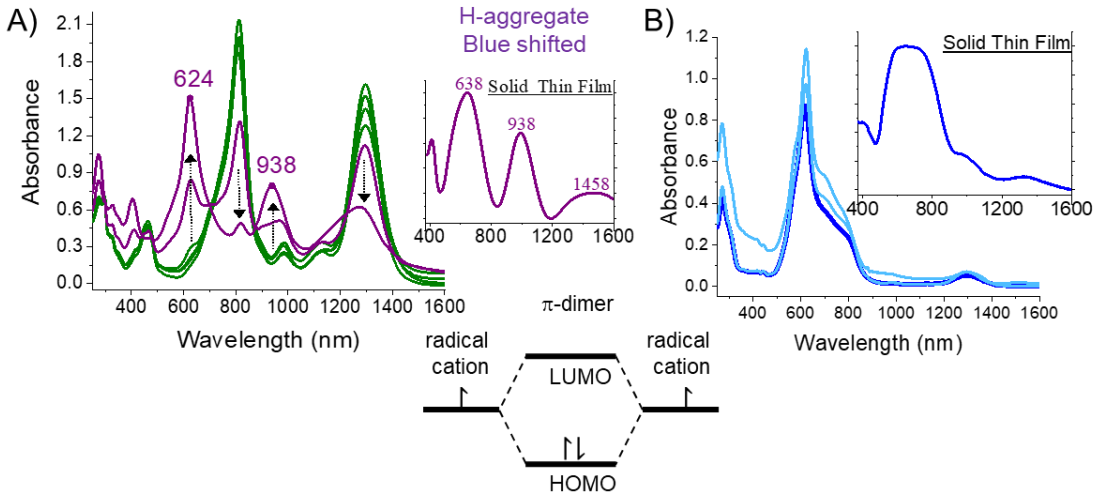

Figure S16. Temperature-modulated spectral change of the solution of A) 3A-1$^{\bullet+}$ and B) 3A-1 (20 μM in CH_2Cl_2). Temperature from (K): 290, 273, 243, 223, 203, 177. Inset: Solid thin-film spectra of isoalted 3A-1$^{\bullet+}$ and 3A-1.

P. Low Temperature Electron Paramagnetic Resonance (EPR) Spectroscopy

EPR spectroscopy was performed at a microwave bridge frequency of 9.49 GHz, 10.02 mW power, 100 kHz modulation frequency, 1.00 G modulation amplitude, and 2000 receiver gain. Solutions were prepared in a nitrogen filled glove box at a 300 μM in anhydrous CH_2Cl_2 for room temperature measurements. Oven tried EPR tubes were transferred into the glove box and 0.3 ml of each sample was transferred into the tube and sealed. Low temperature EPR measurements were conducted in an anhydrous solution of 1:1 CH_2Cl_2:$CHCl_3$, with a sample volume of 0.3 ml. Measurements were taken at 290 K, decreased to 170 K and raised in increments of 20 K back to 290 K. At each temperature, the sample was allowed to equilibrate for ~5 minutes before taking measurement.

Q. Low Temperature Nuclear Magnetic Resonance (NMR) Spectroscopy

Low temperature NMR spectroscopy was performed on molecule 3A-1, $3A1^{\bullet+}$ and $3A\text{-}2^{++}$. In a nitrogen filled glove box, 30 mg of each sample is dissolved in 0.75 ml anhydrous CD_2Cl_2 and transferred into a valved NMR tube via needle and syringe. ^1H measurements were taken at 290 K, decreased to ~200 K and raised in increments of ~20 K back to 290 K.

R. ^{1}H- and ^{13}C-NMR Spectra

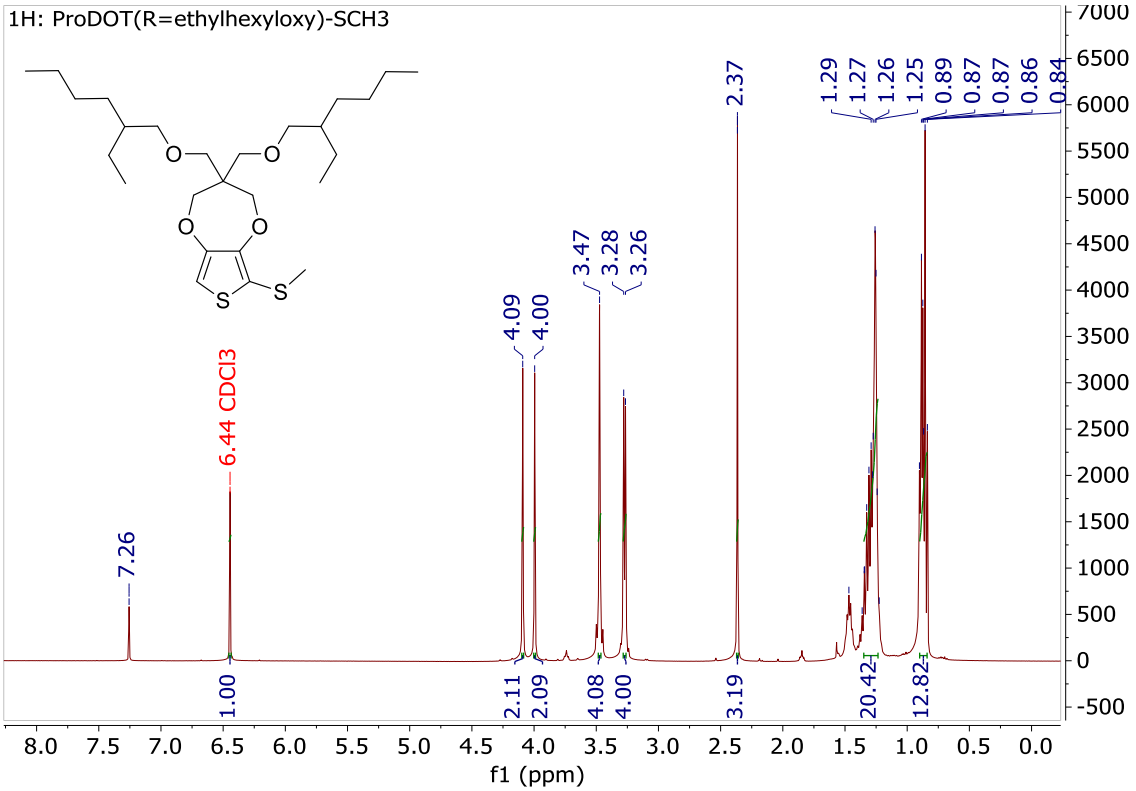

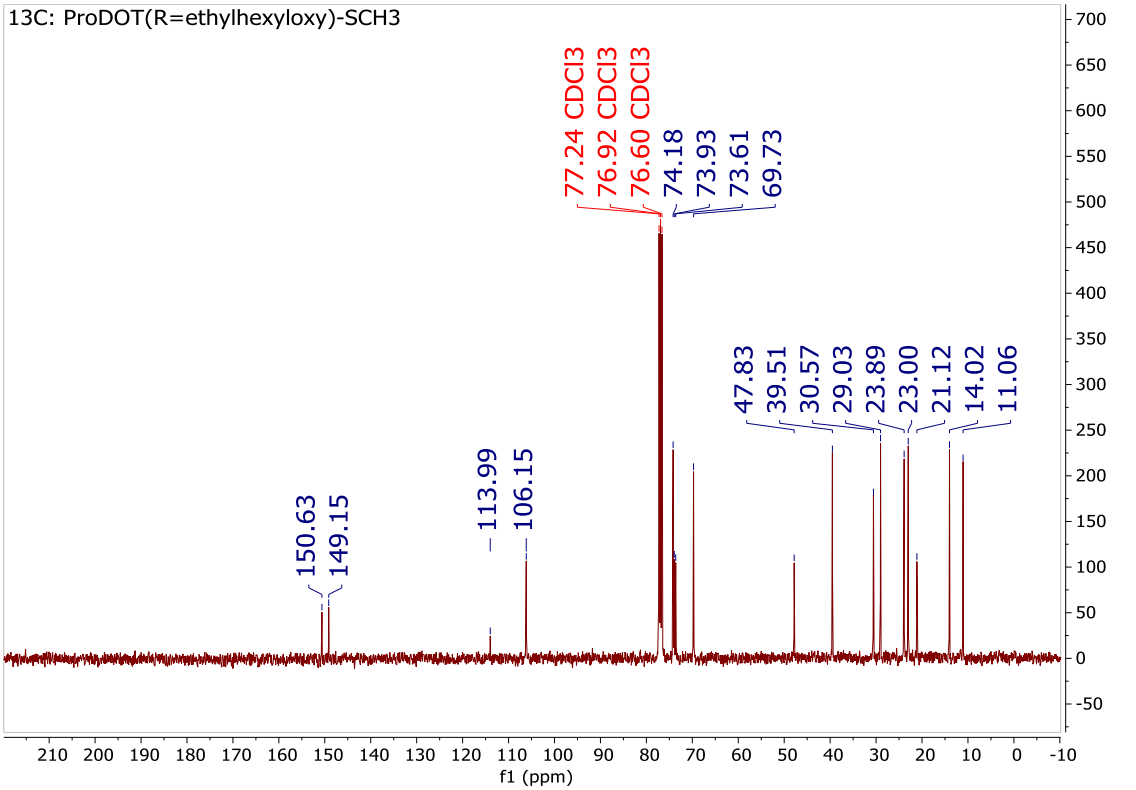

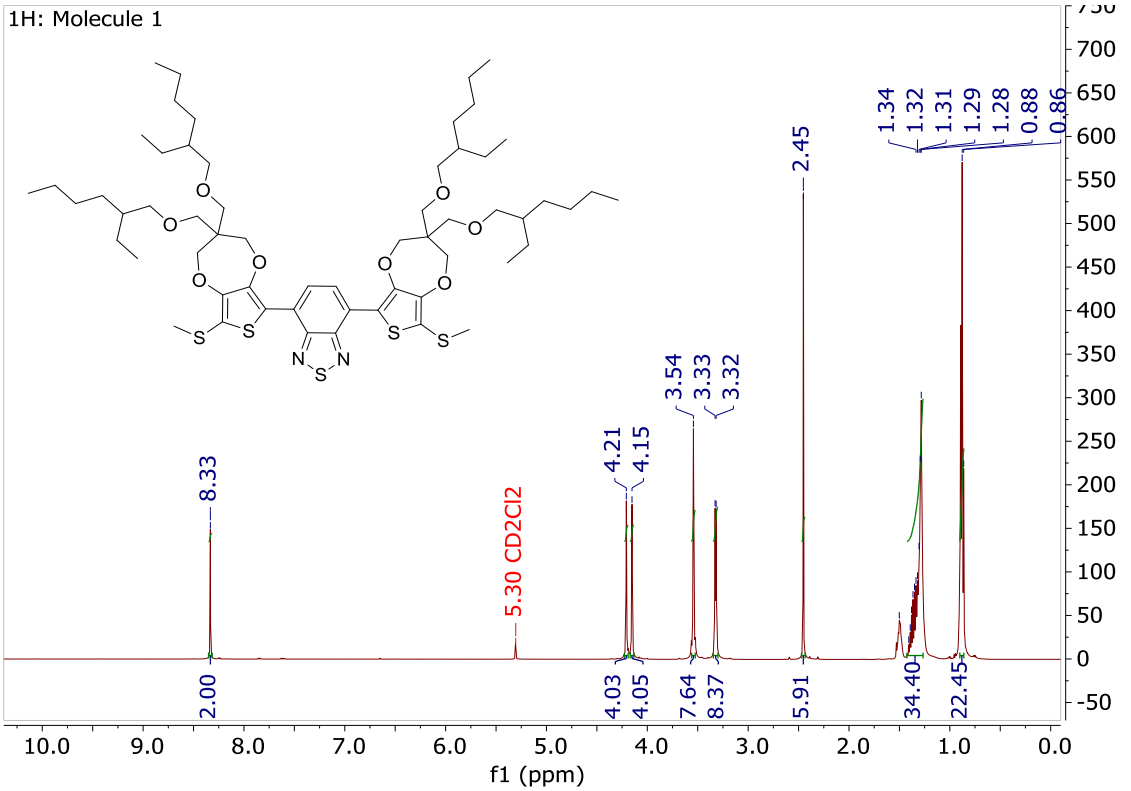
1H: Molecule 1
8.33
5.30 CD2Cl2
4.21
4.15
3.54
3.33
3.32
2.45
1.34
1.32
1.31
1.29
1.28
0.88
0.86
2.00
4.03
4.05
7.64
8.37
5.91
34.40
22.45
f1 (ppm)

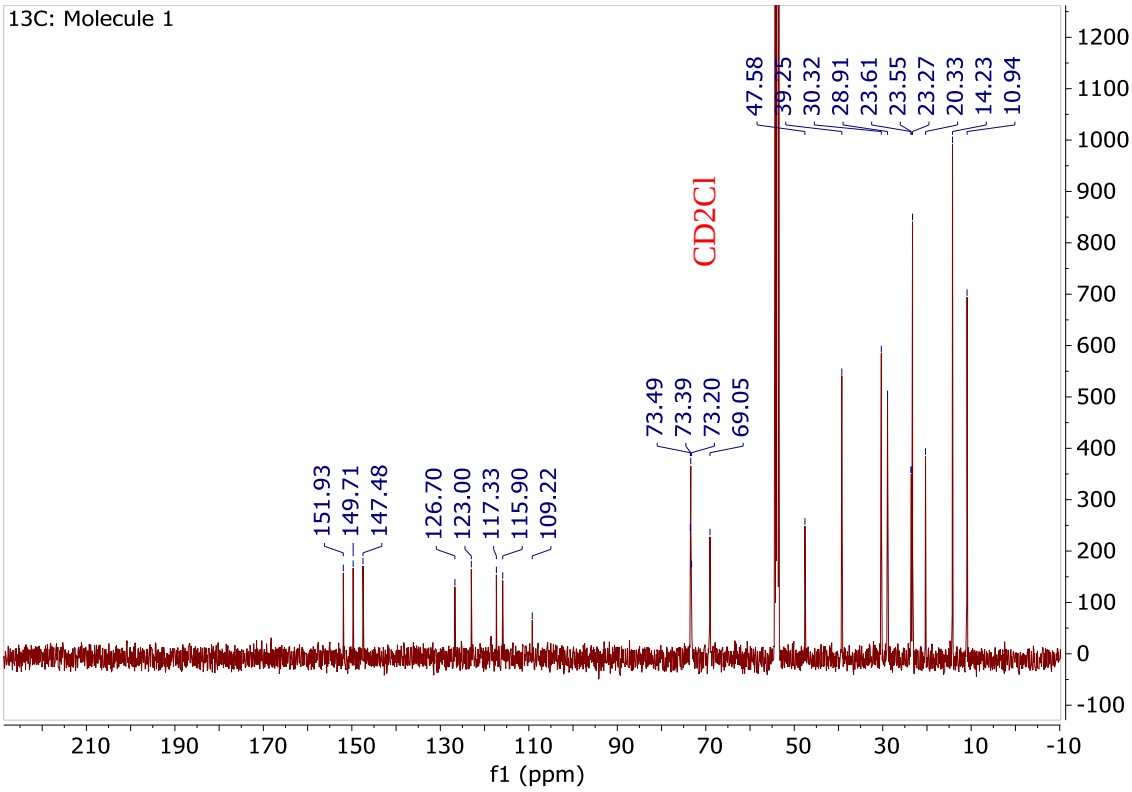
13C: Molecule 1
CD2Cl
47.58
39.25
30.32
28.91
23.61
23.55
23.27
20.33
14.23
10.94
73.49
73.39
73.20
69.05
151.93
149.71
147.48
126.70
123.00
117.33
115.90
109.22
f1 (ppm)

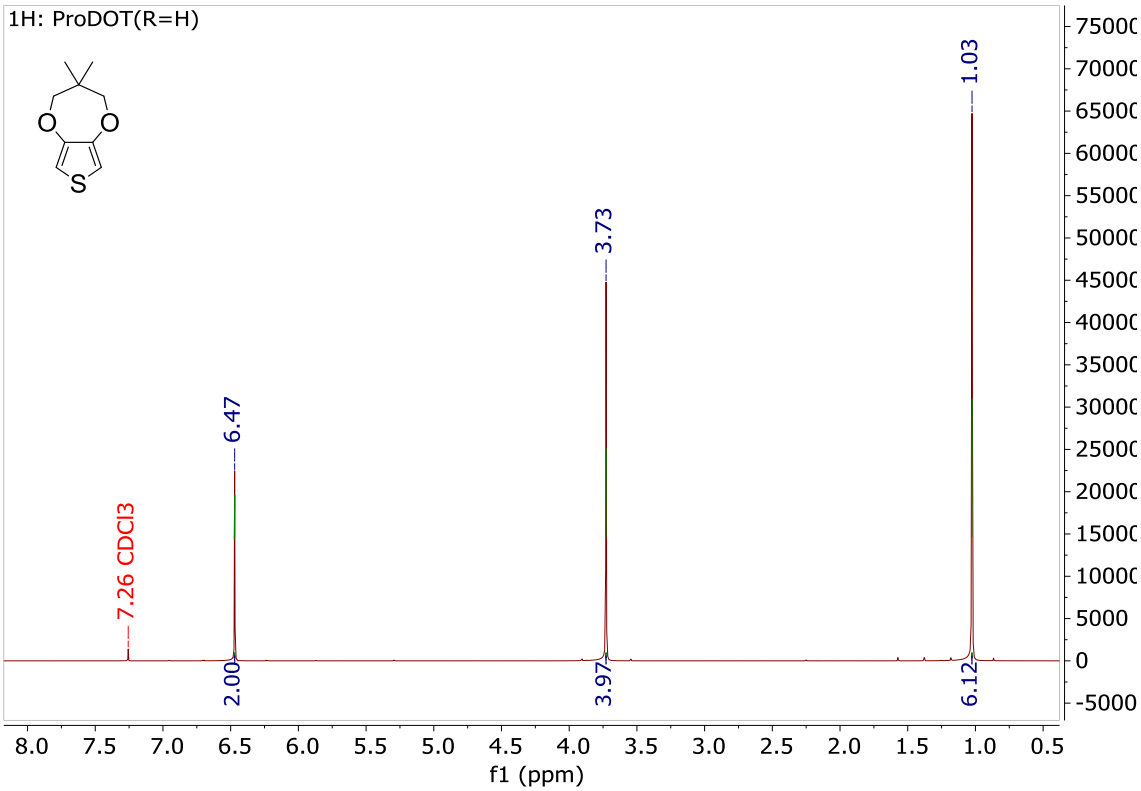
1H: ProDOT(R=H)
O
O
S
7.26 CDCl3
6.47
3.73
1.03
2.00
3.97
6.12
f1 (ppm)

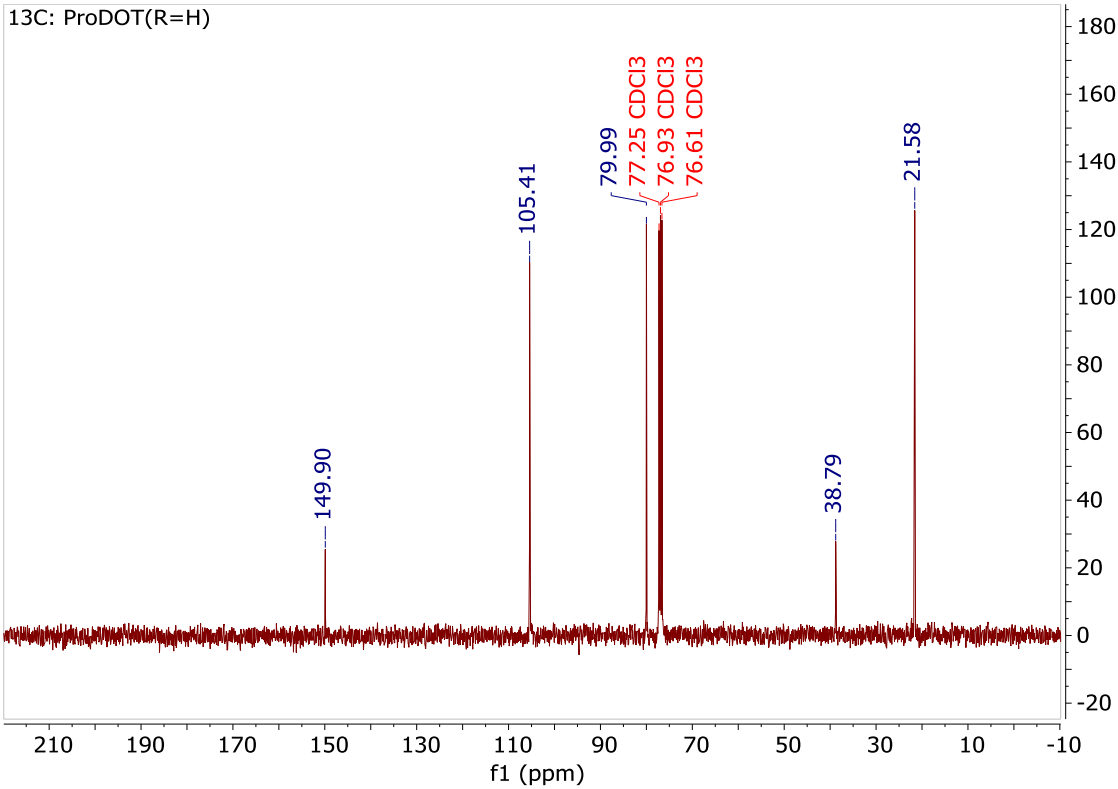
13C: ProDOT(R=H)
149.90
105.41
79.99
77.25 CDCl3
76.93 CDCl3
76.61 CDCl3
38.79
21.58
f1 (ppm)

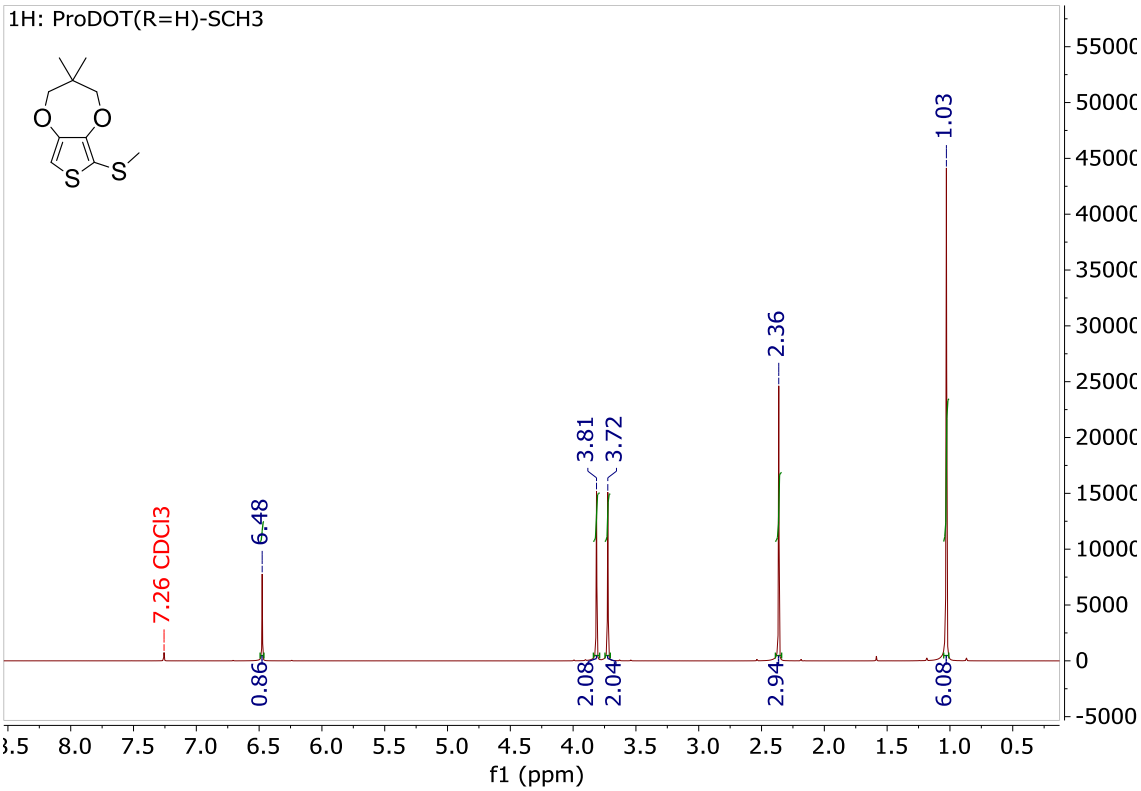
1H: ProDOT(R=H)-SCH3
7.26 CDCl3
6.48
3.81
3.72
2.36
1.03
0.86
2.08
2.04
2.94
6.08
f1 (ppm)

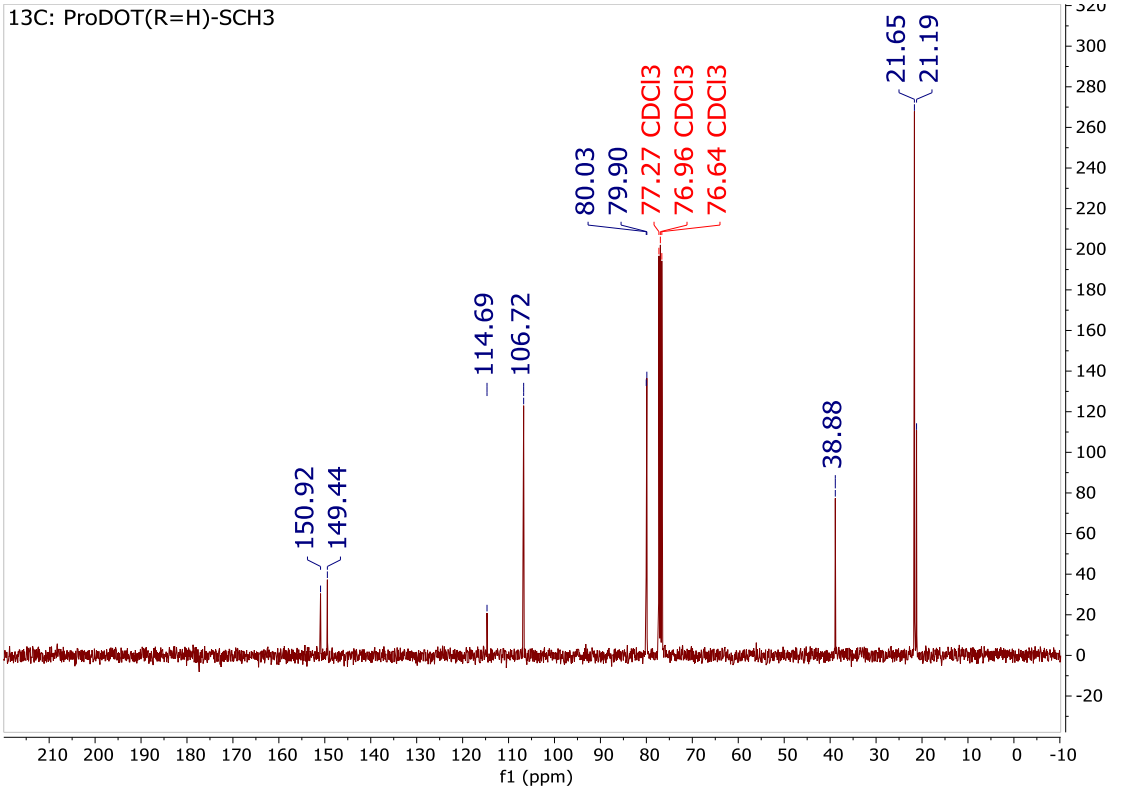
13C: ProDOT(R=H)-SCH3
150.92
149.44
114.69
106.72
80.03
79.90
77.27 CDCl3
76.96 CDCl3
76.64 CDCl3
38.88
21.65
21.19
f1 (ppm)

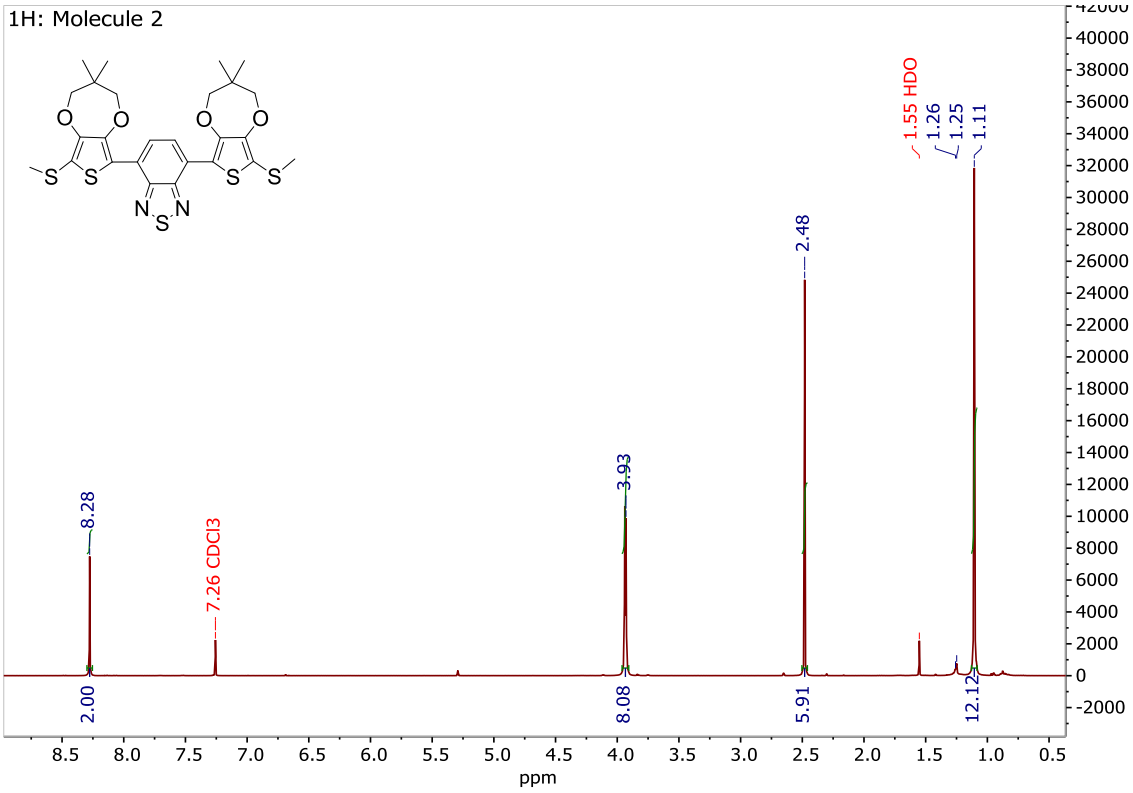
1H: Molecule 2
8.28
7.26 CDCl3
3.93
2.48
1.55 HDO
1.26
1.25
1.11
2.00
8.08
5.91
12.12
ppm

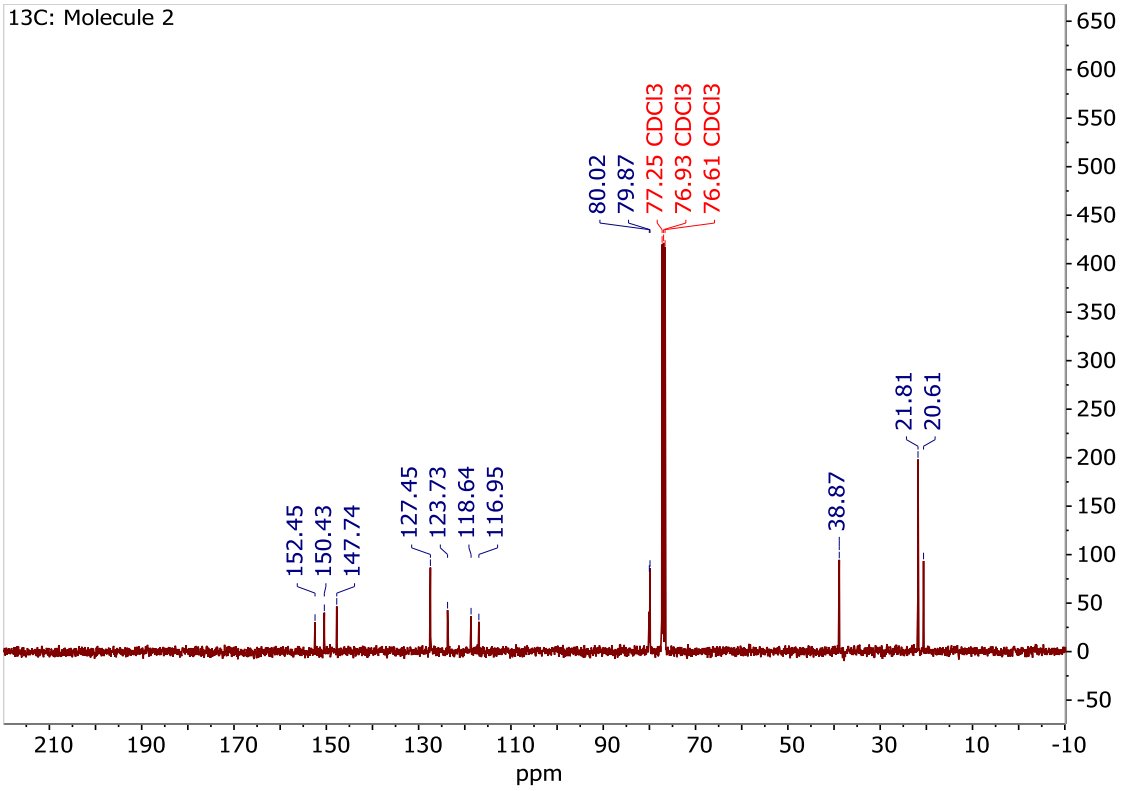
13C: Molecule 2
80.02
79.87
77.25 CDCl3
76.93 CDCl3
76.61 CDCl3
152.45
150.43
147.74
127.45
123.73
118.64
116.95
38.87
21.81
20.61
ppm

S. Low Temperature NMR Spectra

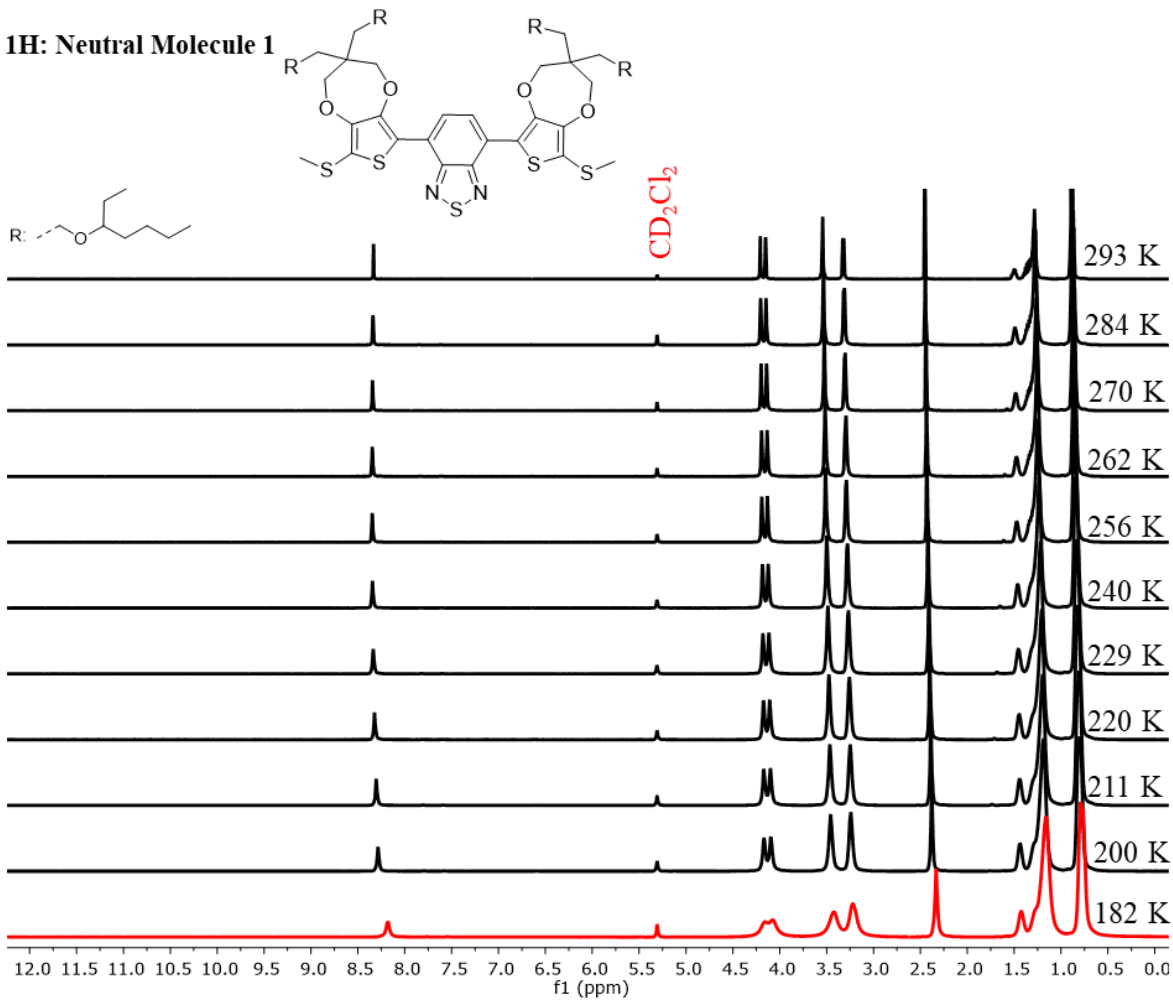

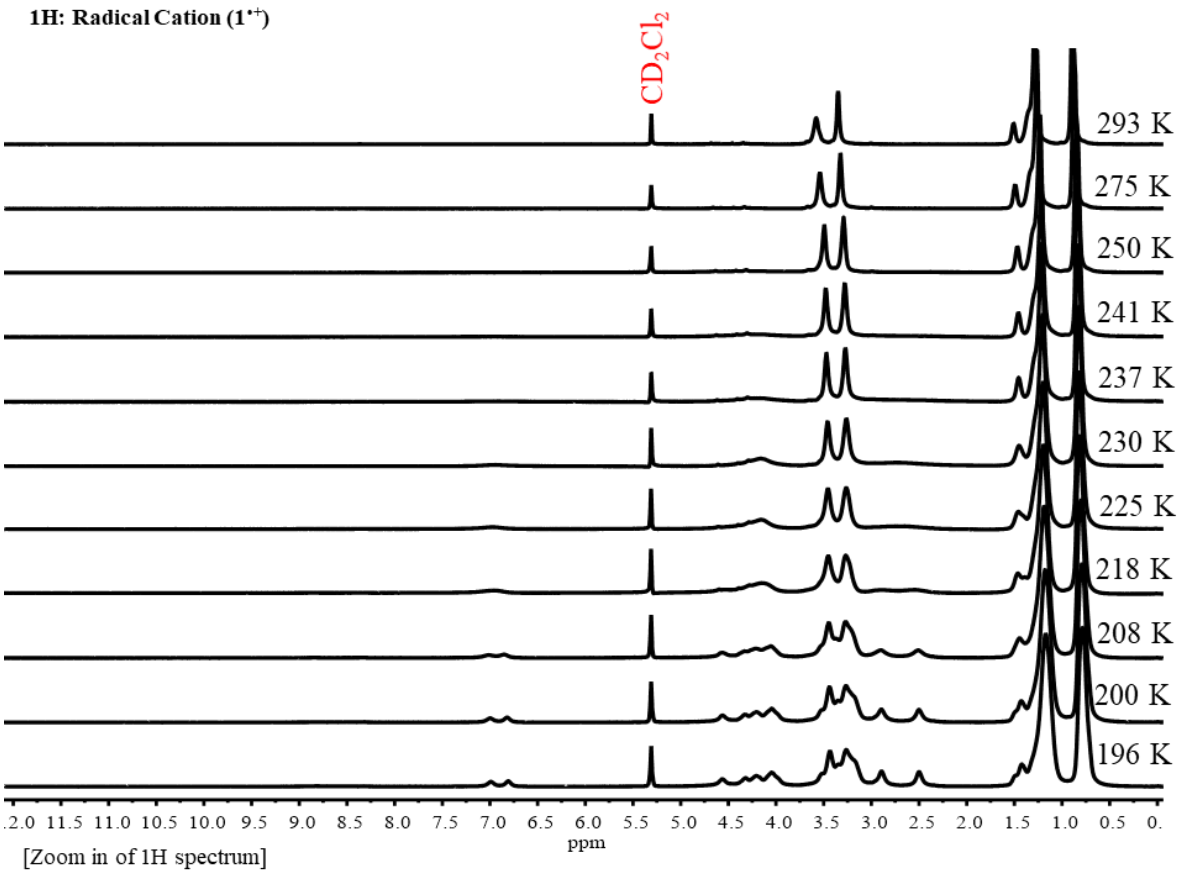
1H: Radical Cation (1•+)
CD2Cl2
293 K
275 K
250 K
241 K
237 K
230 K
225 K
218 K
208 K
200 K
196 K
.2.0 11.5 11.0 10.5 10.0 9.5 9.0 8.5 8.0 7.5 7.0 6.5 6.0 5.5 5.0 4.5 4.0 3.5 3.0 2.5 2.0 1.5 1.0 0.5 0.
ppm
[Zoom in of 1H spectrum]
293 K
275 K
250 K
241 K
237 K
230 K
225 K
218 K
208 K
200 K
196 K
7.4 7.2 7.0 6.8 6.6 6.4 6.2 6.0 5.8 5.6 5.4 5.2 5.0 4.8 4.6 4.4 4.2 4.0 3.8 3.6 3.4 3.2 3.0 2.8 2.6 2.4 2.2
ppm

1H: Dication (1^{++})

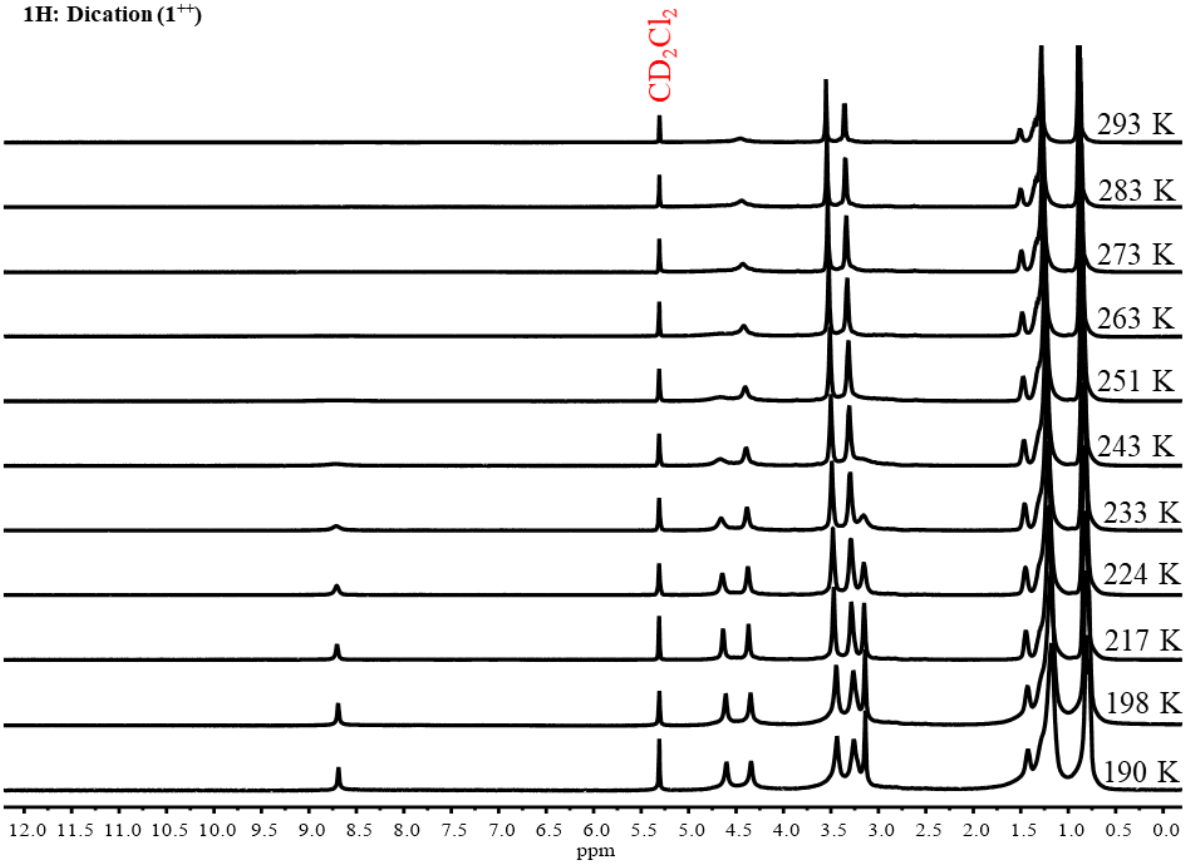

[Zoom in of 1H spectrum]

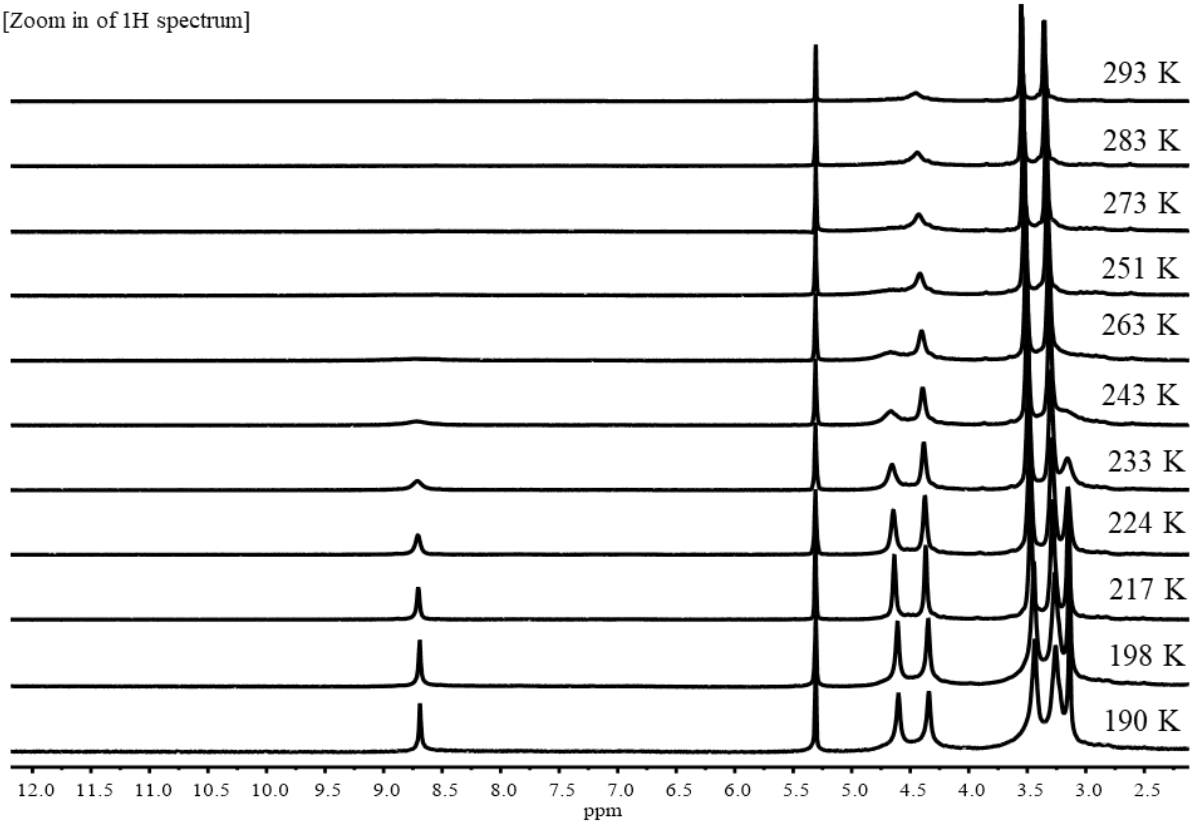

APPENDIX B: SUPPORTING INFORMATION FOR CHAPTER 3

A. General Information

All manipulations were carried out using standard Schlenk or glovebox techniques under an atmosphere of N_2. Solvents were dried and degassed by passing through a column of activated alumina, sparging with N_2 gas, and, storing over dry 3 Å molecular sieves for at least 72 h before use. Deuterated was purchased from Cambridge Isotope Laboratories, Inc. All reagents and starting materials were purchased from commercial vendors and used without further purification unless otherwise noted.

Physical Methods. ^{1}H NMR spectra were collected at room temperature on Bruker 400 MHz, 500 MHz, or 800 MHz spectrometers. ^{1}H and ^{13}C{^{1}H} NMR spectra are reported in parts per million relative to tetramethylsilane, using the residual solvent resonances as an internal standard. High resolution mass data were obtained using an Agilent 6320 LC-MS/MS for HR-APCI and an Applied Biosystems Voyager System 6270 for MALDI. Sample dispersity and polymer molecular weights were obtained using a TOSOH GPC with THF solvent vs. polystyrene standards at 40^{o}C. UV-vis-NIR measurements were acquired on an Agilent Technologies Cary 6000i spectrophotometer (350-2850 nm) using a 1-cm two-window quartz cuvette. Electrochemistry was performed using a BioLogic SΠ-150 and CHI-660 in

Abbreviations. 3,4-propylenedioxythiophene (ProDOT), benzothiadiazole (BTD), dichloromethane (DCM), tetrahydrofuran (THF).

B. Synthesis

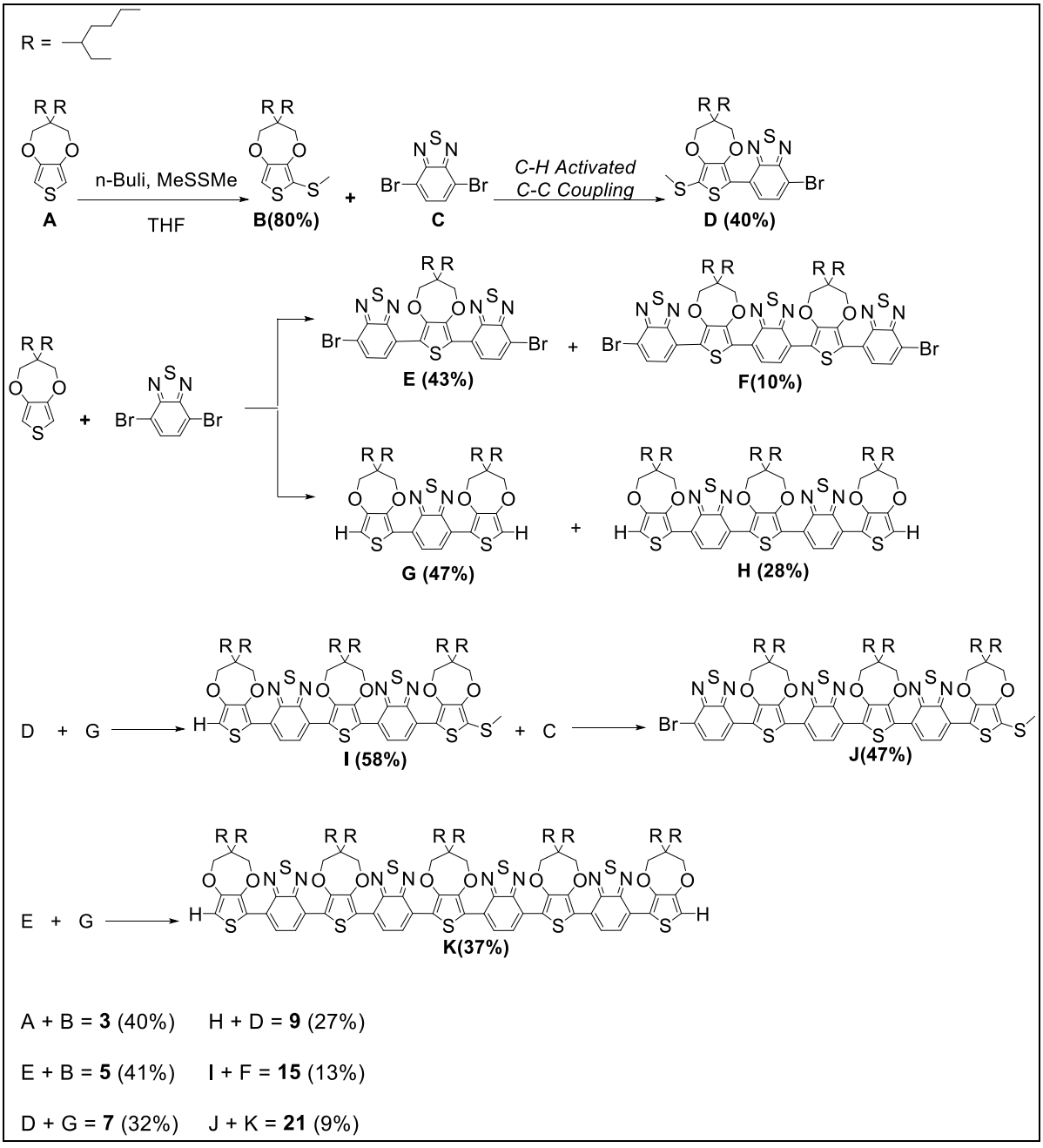

Scheme S1. Synthesis of the nPB oligomers. a) n-BuLi, CH_3SSCH_3, b) C-H Activation Conditions: $Pd(OAc)_2$, $(o\text{-}MeOPh)_3P$, pivalic acid, Cs_2CO_3.

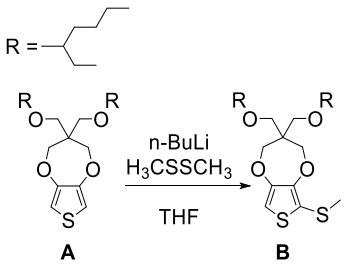

Compound B

To a THF solution (75 mL) of A (9.90 g, 22.5 mmol, 1.0 equiv) was added 9.88 ml of n-butyllithium (2.5 M, 24.7 mmol,1.1 equiv) in hexane at -78°C under N_2. After stirring for 120 min at 0°C, dimethyldisulfide (2.22 ml, 24.7 mmol, 1.1 equiv) was added dropwise to the reaction mixture and then allowed to warm to room temperature. After stirring overnight, the reaction mixture was quenched with water, extracted with hexane, and dried over Na_2SO_4. The crude product was concentrated under vacuum and passed through a short alumina column using hexanes:ethyl acetate (75:1). After solvent evaporation, the residue was separated by preparative HPLC (polystyrene/divinylbenzene stationary phase) with $CHCl_3$ to give B as a light-yellow oil (8.76 g, 80% yield).

- ^{1}H NMR (300 MHz, $CDCl_3$, ppm) δ: 6.44 (s, 1H), 4.09 (s, 2H), 4.00 (s, 2H), 3.47 (s, 4H), 3.27 (d, J = 5.7 Hz, 4H), 2.37(s, 3H), 1.35 – 1.23 (m, 20H), 0.90 – 0.84 (m, 13H).
- ^{13}C NMR (101 MHz, $CDCl_3$, ppm) δ 150.63, 149.15, 106.15, 74.18, 73.93, 73.61, 69.73, 47.83, 39.51, 30.57, 29.03, 23.89, 23.00, 21.12, 14.02, 11.06.
- HRMS (ESI), [M+H]+ m/z calcd. for $C_{26}H_{47}O_4S_2$: 487.2910; found 487.2902.

General C-H Activation Conditions

In a 25 mL Schlenk tube, $Pd(OAc)_2$ (4-8 mol %), $(o\text{-}MeOPh)_3P$ (8-16 mol %), pivalic acid (0.5 per C-H monomer equivalence) and Cs_2CO_3 (1.5 per C-H monomer equivalence) were added, vacuumed for 30 minutes, and then subjected to N_2 purge cycles three times. Anhydrous toluene (0.1 M–0.5 M) was added via needle and syringe. The reaction was heated at 110°C in an oil bath, or until the limiting reagent was consumed per TLC analysis. Upon completion, the reaction mixture was quenched with water and extracted with dichloromethane. The organic layer was washed with water twice, then once with brine. The organic layer was separated and dried over $MgSO_4$ or Na_2SO_4, then filtered and concentrated under reduced pressure. The crude product was purified by SiO_2 column chromatography concentrated, and further purified by recycling preparative HPLC (polystyrene/divinylbenzene stationary phase) with $CHCl_3$. In cases where an excess of a compound is used, the unreacted portion is retrieved during column chromatography as its rf value is generally higher than the generated product.

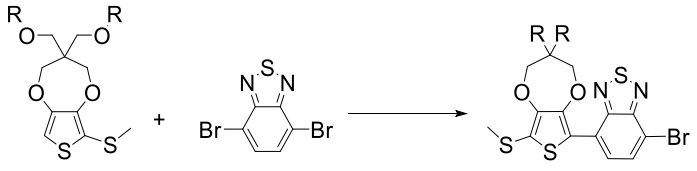

B **C** **D**

Compound D

The reaction was conducted according to the general procedure without modification using compound B (3.0 g, 6.16 mmol, 1.0 equiv) , compound C (5.44 g, 18.49 mmol, 3.0 equiv) $Pd(OAc)_2$ (4 mol %, 55.3 mg), $(o\text{-}MeOPh)_3P$ (8 mol %, 173.6 mg), pivalic acid (314.6 mg, 3.08 mmol, 0.5 equiv) and Cs_2CO_3 (3.01 g, 9.24 mmol, 1.5 equiv) in 35 mL of anhydrous toluene. The product was filtered by column chromatography (CH_2Cl_2:hexanes, gradient of 1:1 to 2:1) and purified by preparative HPLC to provide compound D (1.72 g, 40% yield) as an orange oil. Unreacted compound C and oligomer 3 was recovered in ~20% yield.

- ^1H NMR (400 MHz, $CDCl_3$) δ 8.11 (d, J = 7.9 Hz, 1H), 7.79 (d, J = 7.9 Hz, 1H), 4.18 (d, J = 6.8 Hz, 4H), 3.54 (s, 4H), 3.30 (d, J = 5.7 Hz, 4H), 2.47 (s, 3H), 1.48 (dt, J = 11.6, 5.7 Hz, 2H), 1.41 – 1.23 (m, 18H), 0.90 – 0.84 (m, 13H).
- ^{13}C NMR (101 MHz, $CDCl_3$) δ 147.79, 132.40, 127.07, 125.25, 111.26, 74.21, 74.18, 73.95, 73.77, 69.84, 47.81, 39.53, 30.59, 30.56, 29.03, 23.92, 23.00, 20.33, 14.03, 11.08.
- HRMS (APCI), [M+H]+ m/z calcd. for $C_{32}H_{48}BrN_2O_4S_3$: 699.1954; found 699.1944.

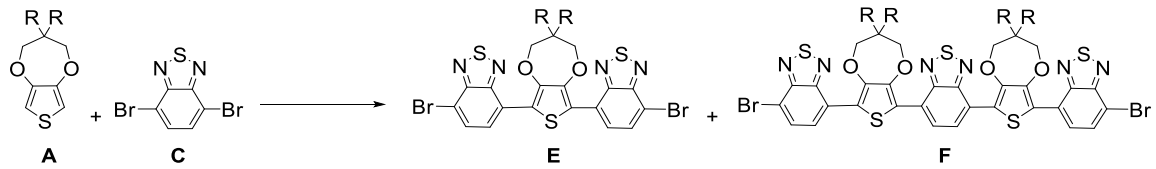

Compounds E and F

The reaction was conducted according to the general procedure using compound A (2.0 g, 4.55 mmol, 1.0 equiv), compound C (6.67 g, 22.7 mmol, 5.0 equiv) $Pd(OAc)_2$ (4 mol %, 40.77 mg), $(o\text{-}MeOPh)_3P$ (8 mol %, 127.98 mg), pivalic acid (927.34 mg, 9.08 mmol, 2.0 equiv) and Cs_2CO_3 (4.59 g, 14.07 mmol, 3.1 equiv) in 130 ml anhydrous toluene. After work-up, the crude material was dissolved in hexane to precipitate out and recover excess compound C from the mixture and the filtrate was concentrated. The two products were purified by column chromatography (CH_2Cl_2:hexanes, gradient of 1:1 to 3:1) to sequentially provide compound E as a dark red solid (1.69 g, 43% yield) and compound F as a dark purple solid (624 mg, 10% yield).

Compound E

- ^{1}H NMR (400 MHz, $CDCl_3$) δ 8.19 (d, *J* = 7.8 Hz, 2H), 7.85 (d, *J* = 7.9 Hz, 2H), 4.28 (s, 4H), 3.60 (s, 4H), 3.34 (d, *J* = 5.7 Hz, 4H), 1.56 – 1.46 (m, 1H), 1.44 – 1.22 (m, 17H), 0.93 – 0.84 (m, 12H).
- ^{13}C NMR (101 MHz, $CDCl_3$) δ 153.42, 152.03, 148.14, 132.37, 127.77, 125.47, 118.54, 111.85, 74.24, 73.88, 69.94, 47.78, 39.53, 30.57, 29.03, 23.92, 23.02, 14.04, 11.08.
- HRMS (APCI), $[M+H]^+$ *m/z* calcd. for $C_{37}H_{47}Br_2N_2O_4S_3$: 865.1121; found 865.1186.

Compound F

- ^{1}H NMR (400 MHz, $CDCl_3$) δ 8.43 (s, 2H), 8.21 (d, *J* = 7.9 Hz, 2H), 7.87 (d, *J* = 7.9 Hz, 2H), 4.31 (d, *J* = 7.7 Hz, 8H), 3.62 (s, 8H), 3.35 (d, *J* = 5.7 Hz, 8H), 1.53 (dt, *J* = 12.0, 5.6 Hz, 6H), 1.42 – 1.24 (m, 38H), 0.93 – 0.87 (m, 24H).
- ^{13}C NMR (101 MHz, $CDCl_3$) δ 153.46, 152.51, 152.13, 148.25, 132.40, 127.77, 127.65, 124.10, 119.74, 111.56, 74.24, 73.87, 69.99, 47.79, 39.56, 30.58, 29.60, 29.04, 23.95, 23.03, 14.05, 11.10.
- HRMS (APCI), $[M+H]^+$ *m/z* calcd. for $C_{68}H_{91}Br_2N_6O_8S_5$: 1437.3863; found 1437.3866.

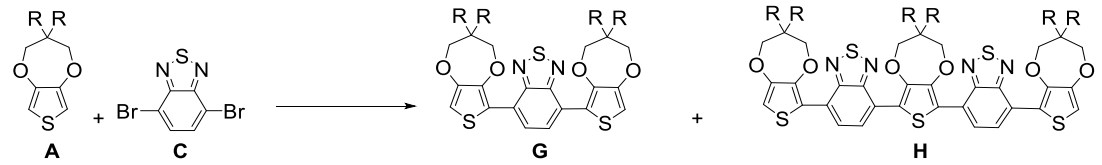

Compound G and H

The reaction was conducted according to the general procedure without modification using compound A (10.3 g, 23.46 mmol, 6.0 equiv) , compound C (1.15 g, 3.91 mmol, 1.0 equiv), $Pd(OAc)_2$ (2 mol %, 17.56 mg), $(o\text{-}MeOPh)_3P$ (4 mol %, 55.1 mg), pivalic acid (400 mg, 3.91 mmol, 1.0 equiv), and Cs_2CO_3 (3.7 g, 11.73 mmol, 3.0 equiv) in 75 ml anhydrous toluene. The two products were purified by column chromatography (CH_2Cl_2:hexanes, gradient of 1:2 to 2:1) to sequentially provide compound G as an orange oil (1.86 g, 47% yield) and compound H as a sticky, magenta solid (1.74 g, 28% yield).

Compound G

- ^{1}H NMR (400 MHz, $CDCl_3$) δ 8.29 (s, 2H), 6.66 (s, 2H), 4.20 (s, 4H), 4.10 (s, 4H), 3.54 (s, 8H), 3.31 (d, J = 5.5 Hz, 8H), 1.56 – 1.45 (m, 7H), 1.40 – 1.23 (m, 42H), 0.95 – 0.84 (m, 30H).
- ^{13}C NMR (101 MHz, $CDCl_3$) δ 152.56, 149.66, 147.75, 127.47, 124.11, 117.49, 106.38, 74.23, 73.74, 69.87, 47.81, 39.54, 30.57, 29.03, 23.92, 23.01, 14.02, 11.07.
- HRMS (APCI), $[M+H]^+$ *m/z* calcd. for $C_{56}H_{88}N_2O_8S_3$: 1013.5776; found 1013.5771.

Compound H

- ^{1}H NMR (400 MHz, $CDCl_3$) δ 8.32 (q, *J* = 8.0 Hz, 4H), 6.64 (s, 2H), 4.38 – 4.03 (m, 12H), 3.59 (d, *J* = 40.8 Hz, 12H), 3.35 (dd, *J* = 21.8, 5.6 Hz, 12H), 1.53 (tq, *J* = 14.5, 8.5, 7.0 Hz, 7H), 1.47 – 1.24 (m, 51H), 1.00 – 0.83 (m, 38H).
- ^{13}C NMR (101 MHz, $CDCl_3$) δ 152.45, 152.41, 149.57, 147.89, 147.74, 127.27, 127.10, 124.00, 123.95, 119.20, 117.63, 106.53, 77.28, 74.19, 74.13, 73.59, 69.97, 69.81, 47.80, 39.64, 39.60, 30.65, 29.08, 24.05, 24.00, 23.10, 23.07, 14.10, 11.17, 11.13.
- HRMS (APCI), $[M+H]^+$ *m/z* calcd. for $C_{87}H_{132}N_4O_{12}S_5$: 1585.8518; found 1585.8509.

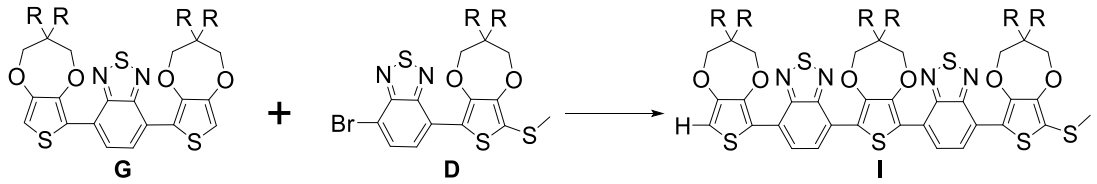

Compound I

The reaction was conducted according to the general procedure without modification using compound G (761.3 mg, 0.75 mmol, 2.7 equiv) , compound D (194.7 mg, 0.28 mmol, 1.0 equiv), $Pd(OAc)_2$ (8 mol %, 5.0 mg), $(o\text{-}MeOPh)_3P$ (16 mol %, 15.7 mg), pivalic acid (14.3 mg, 0.14 mmol, 0.5 equiv), and Cs_2CO_3 (135.9 mg, 0.42 mmol, 1.5 equiv) in 7 ml anhydrous toluene. The product was purified by column chromatography (CH_2Cl_2:hexanes, gradient of 1:3 to 1:1) to provide compound I as a sticky, magenta solid (265 mg, 58% yield).

- ^{1}H NMR (400 MHz, $CDCl_3$) δ 8.40 – 8.31 (m, 4H), 6.66 (s, 1H), 4.32 (s, 5H), 4.27 – 4.17 (m, 6H), 4.10 (s, 2H), 3.69 – 3.51 (m, 13H), 3.35 (dd, J = 16.2, 5.7 Hz, 13H), 2.49 (s, 3H), 1.52 (dt, J = 11.7, 5.9 Hz, 7H), 1.46 – 1.22 (m, 56H), 0.91 (m, 40H).
- ^{13}C NMR (101 MHz, $CDCl_3$) δ 152.47, 150.00, 149.63, 148.00, 147.94, 147.80, 147.46, 127.52, 127.26, 127.16, 124.16, 124.03, 123.96, 123.57, 119.21, 119.06, 118.27, 117.58, 116.42, 106.55, 74.22, 74.16, 73.94, 73.68, 70.00, 69.85, 47.82, 39.59, 30.62, 29.06, 23.98, 23.05, 20.51, 14.07, 11.13.
- HRMS (APCI), $[M+H]^+$ *m/z* calcd. for $C_{88}H_{135}N_4O_{12}S_6$: 1631.8395; found 1631.8355.

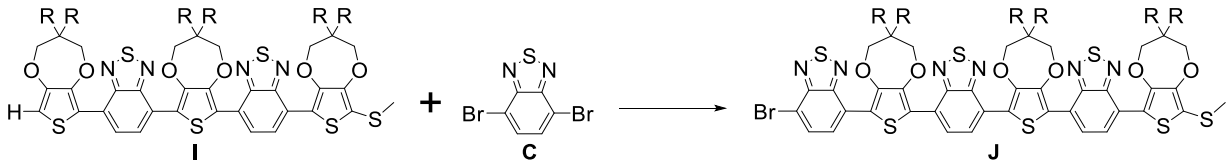

Compound J

The reaction was conducted according to the general procedure using compound I (177.1 mg, 0.108 mmol, 1.0 equiv), compound C (127.5 mg, 0.434 mmol, 4.0 equiv) $Pd(OAc)_2$ (8 mol %, 2 mg), $(o\text{-}MeOPh)_3P$ (16 mol %, 6.1 mg), pivalic acid (5.5 mg, 0.054 mmol, 0.5 equiv), and Cs_2CO_3 (54.6 mg, 0.173 mmol, 1.6 equiv) in 3 ml anhydrous toluene. After work-up, the crude material was dissolved in hexane to precipitate out and recover excess compound C from the mixture and the filtrate was concentrated. The product was purified by column chromatography (CH_2Cl_2:hexanes, gradient of 1:1 to 3:1) to provide compound J as a dark purple solid (93.9 mg, 47% yield).

- ^{1}H NMR (400 MHz, $CDCl_3$) δ 8.43 – 8.31 (m, 4H), 8.18 (d, J = 7.9 Hz, 1H), 7.83 (d, J = 7.9 Hz, 1H), 4.38 – 4.25 (m, 8H), 4.21 (d, J = 13.5 Hz, 4H), 3.69 – 3.51 (m, 12H), 3.42 – 3.28 (m, 12H), 2.49 (s, 3H), 1.57 – 1.47 (m, 7H), 1.43 – 1.24 (m, 57H), 0.96 – 0.84 (m, 39H).
- ^{13}C NMR (101 MHz, $CDCl_3$) δ 153.51, 152.58, 152.51, 152.19, 150.08, 148.30, 148.17, 148.06, 147.98, 147.55, 132.44, 127.91, 127.81, 127.69, 127.28, 125.81, 124.45, 124.05, 123.89, 123.79, 119.90, 119.30, 118.25, 117.95, 116.51, 111.57, 74.28, 74.23, 74.03, 73.90, 73.80, 70.06, 69.94, 53.34, 47.87, 47.84, 39.62, 39.60, 30.62, 29.64, 29.07, 23.98, 23.96, 23.06, 20.57, 14.08, 11.13.
- HRMS (APCI), $[M+H]^+$ *m/z* calcd. for $C_{94}H_{136}BrN_6O_{12}S_7$: 1843.7439; found 1843.7404.

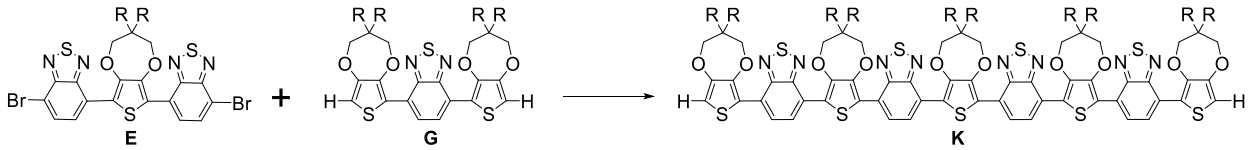

Compound K

The reaction was conducted according to the general procedure using compound E (950.6 mg, 0.938 mmol, 4.0 equiv), compound G (203.2 mg, 0.234 mmol, 1.0 equiv) $Pd(OAc)_2$ (8 mol %, 4.2 mg), $(o\text{-}MeOPh)_3P$ (16 mol %, 13.2 mg), pivalic acid (24 mg, 0.234 mmol, 1.0 equiv) and Cs_2CO_3 (229.1 mg, 0.725 mmol, 3.1 equiv) in 3 ml anhydrous toluene. The product was purified by column chromatography (CH_2Cl_2:hexanes, gradient of 1:2 to 2:1) to provide compound K as a dark blue solid (233 mg, 37% yield).

- ^1H NMR (500 MHz, $CDCl_3$, ppm) δ 8.48 (s, 4H), 8.45 (d, J = 7.9 Hz, 2H), 8.40 (d, J = 7.9 Hz, 2H), 6.74 (s, 2H), 4.40 (d, J = 3.9 Hz, 13H), 4.28 (s, 4H), 4.17 (s, 4H), 3.71 (s, 13H), 3.61 (s, 9H), 3.43 (d, J = 5.7 Hz, 12H), 3.38 (d, J = 5.6 Hz, 8H), 1.60 (dt, J = 19.2, 6.0 Hz, 12H), 1.53 – 1.29 (m, 91H), 1.04 – 0.91 (m, 67H).
- ^{13}C NMR (126 MHz, $CDCl_3$, ppm) δ 152.74, 152.70, 149.81, 148.19, 148.14, 147.95, 127.74, 127.67, 127.49, 124.32, 124.30, 124.23, 119.45, 119.38, 119.34, 117.76, 106.65, 74.40, 74.34, 73.94, 73.85, 70.17, 69.99, 47.96, 39.76, 39.72, 30.77, 30.74, 29.21, 24.15, 24.10, 23.20, 23.18, 14.22, 14.19, 11.28, 11.24.
- HRMS (APCI), $[M+H]^+$ *m/z* calcd. for $C_{149}H_{221}N_8O_{20}S_9$: 2730.4003; found 2730.3894.

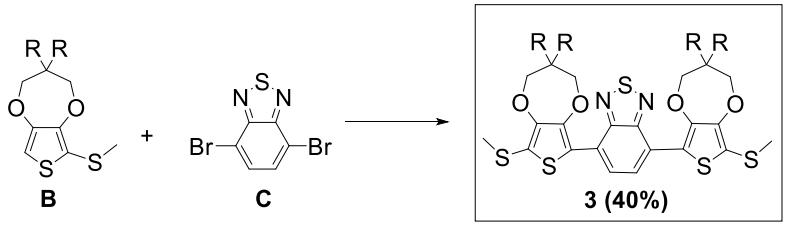

Oligomer n=3

The reaction was conducted according to the general procedure without modification using compound B (1.95 g, 4.01 mmol, 2.1 equiv) and compound C (560.8 mg, 1.907 mmol, 1.0 equiv), $Pd(OAc)_2$ (5 mol %, 5.0 mg), $(o\text{-}MeOPh)_3P$ (10 mol %, 67.2 mg), pivalic acid (97.4 mg, 0.95 mmol, 0.5 equiv) and Cs_2CO_3 (932 mg, 2.86 mmol, 1.5 equiv) in 5 ml anhydrous toluene. The product was purified by column chromatography (CH_2Cl_2:hexanes, 1:3) and further purified by preparative HPLC to provide oligomer n=3 as an orange viscous oil (886 mg, 42% yield).

- ^1H NMR (500 MHz, CD_2Cl_2, ppm) δ 8.33 (s, 2H), 4.21 (s, 4H), 4.15 (s, 4H), 3.54 (s, 8H), 3.32 (dd, J = 5.0 Hz, 8H), 2.45 (s, 6H), 1.43 – 1.27 (m, 34H), 0.87 (m, 22H).
- ^{13}C NMR (126 MHz, CD_2Cl_2, ppm) δ 151.92, 149.69, 147.47, 126.69, 122.98, 117.32, 115.89, 109.21, 73.48, 73.38, 73.20, 69.04, 54.33, 54.11, 53.89, 53.68, 53.46, 47.58, 39.24, 30.32, 28.91, 23.60, 23.55, 23.26, 20.32, 14.23, 10.94.
- HRMS (ESI), [M+H]+ m/z calcd. for $C_{58}H_{92}N_2O_8S_5$: 1104.5458; found 1104.5441.

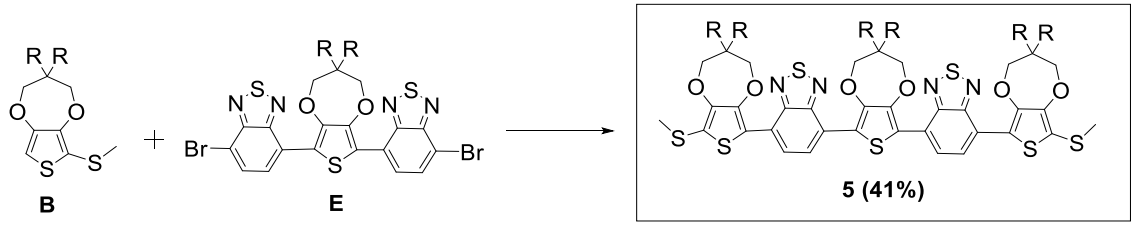

Oligomer n=5

The reaction was conducted according to the general procedure without modification using compound B (288 mg, 0.592 mmol, 2.2 equiv) and compound E (233.2 mg, 0.269 mmol, 1.0 equiv), Pd(OAc)2 (8 mol %, 6.3 mg), $(o\text{-MeOPh})_3P$ (16 mol %, 15.2 mg), pivalic acid (13.7 mg, 0.135 mmol, 0.5 equiv), and Cs_2CO_3 (131.5 mg, 0.404 mmol, 1.5 equiv) in 2 ml anhydrous toluene. The product was purified by column chromatography (CH_2Cl_2:hexanes, 1:1) and further purified by preparative HPLC to provide oligomer n=5 as a magenta wax-like solid (185 mg, 41% yield).

- ^{1}H NMR (400 MHz, $CDCl_3$, ppm) δ 8.37 (q, J = 8.0 Hz, 4H), 4.31 (s, 4H), 4.21 (d, J = 12.6 Hz, 8H), 3.63 (s, 4H), 3.57 (d, J = 2.4 Hz, 9H), 3.34 (dd, J = 11.8, 5.6 Hz, 12H), 2.49 (s, 6H), 1.58 – 1.46 (m, 7H), 1.46 – 1.37 (m, 5H), 1.37 – 1.32 (m, 13H), 1.32 – 1.23 (m, 36H), 0.90 (dd, J = 7.3, 4.9 Hz, 39H).
- ^{13}C NMR (101 MHz, $CDCl_3$, ppm) δ 150.04, 148.01, 147.49, 127.70, 127.23, 123.69, 119.09, 74.23, 73.99, 73.74, 70.01, 69.89, 47.83, 39.57, 30.59, 29.04, 23.95, 23.03, 20.54, 14.05, 11.11.
- HRMS (APCI), $[M+H]^+$ *m/z* calcd. for $C_{89}H_{137}N_4O_{12}S_7$: 1677.8272; found 1677.8253.

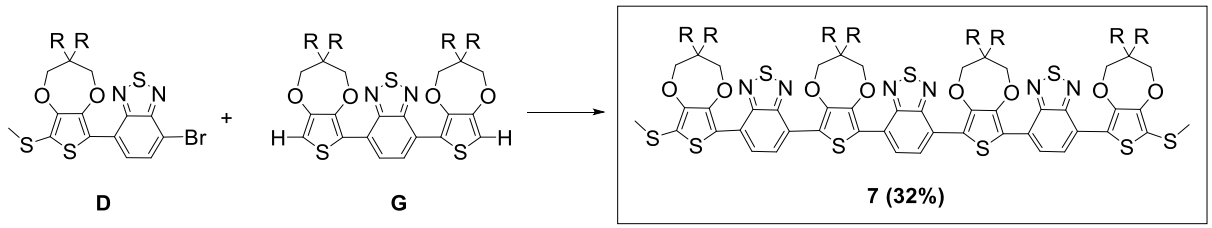

Oligomer n=7

The reaction was conducted according to the general procedure without modification using compound D (445.9 mg, 0.637 mmol, 2.7 equiv) and compound G (239.2 mg, 0.236 mmol, 1.0 equiv), Pd(OAc)2 (4 mol %, 2.7 mg), (o-MeOPh)$_3$P (8 mol %, 6.7 mg), pivalic acid (24.1 mg, 0.236 mmol, 1.0 equiv) and Cs_2CO_3 (238.4 mg, 0.732 mmol, 3.1 equiv) in 3 ml anhydrous toluene. The product was purified by column chromatography (CH_2Cl_2:hexanes, gradient of 1:1 to 2:1) and further purified by preparative HPLC to provide oligomer 7-A as a purple solid (170 mg, 32 % yield).

- ^{1}H NMR (500 MHz, $CDCl_3$, ppm) δ 8.40 (s, 3H), 8.40 – 8.32 (m, 4H), 4.33 (s, 8H), 4.21 (d, *J* = 17.4 Hz, 8H), 3.57 (s, 8H), 3.37 (d, *J* = 5.7 Hz, 8H), 3.32 (d, *J* = 5.8 Hz, 8H), 2.50 (s, 6H), 1.53 (s, 8H), 1.42 – 1.27 (m, 67H), 0.95 – 0.87 (m, 52H).
- ^{13}C NMR (201 MHz, $CDCl_3$, ppm) δ 152.47, 152.43, 150.04, 148.05, 148.01, 147.46, 127.21, 124.12, 124.01, 123.49, 119.39, 119.17, 118.32, 116.35, 74.25, 74.18, 73.89, 73.71, 69.97, 69.77, 47.85, 47.82, 39.66, 39.62, 30.66, 30.64, 29.10, 24.05, 24.01, 23.99, 23.11, 23.08, 20.56, 14.14, 14.11, 11.19, 11.16.
- HRMS (APCI), $[M+H]^+$ *m/z* calcd. for $C_{120}H_{181}N_6O_{16}S_9$: 2250.1015; found 2250.1029.

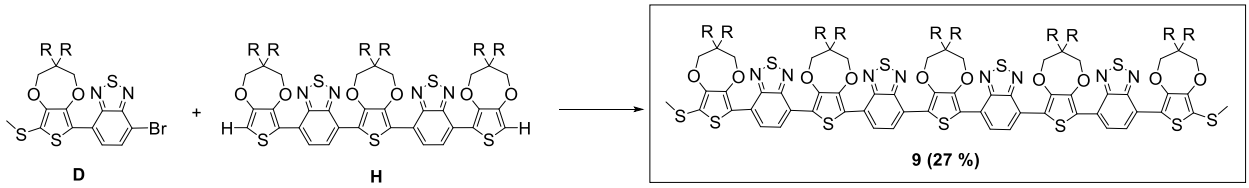

Oligomer n=9

The reaction was conducted according to the general procedure without modification using compound D (135 mg, 0.277 mmol, 2.2 equiv) and compound H (200 mg, 0.126 mmol, 1.0 equiv), $Pd(OAc)_2$ (8 mol %, 3.0 mg), $(o\text{-}MeOPh)_3P$ (16 mol %, 7.1 mg), pivalic acid (12.9 mg, 0.158 mmol, 1.0 equiv) and Cs_2CO_3 (127.4 mg, 0.391 mmol, 3.1 equiv) in 2 ml anhydrous toluene. The product was purified by column chromatography (CH_2Cl_2:hexanes, gradient of 2:1 to 4:1) to provide oligomer n=9 as a blue solid (96 mg, 27 % yield).

- ^{1}H NMR (800 MHz, $CDCl_3$, ppm) δ 8.45 – 8.39 (m, 6H), 8.36 (d, *J* = 7.7 Hz, 2H), 4.35 (s, 10H), 4.24 (s, 4H), 4.21 (s, 4H), 3.67 (s, 11H), 3.58 (s, 8H), 3.39 (s, 12H), 3.34 (s, 8H), 2.52 (s, 6H), 1.55 (dd, *J* = 38.4, 5.9 Hz, 12H), 1.33 (d, *J* = 20.7 Hz, 88H), 0.97 – 0.89 (m, 70H).
- ^{13}C NMR (201 MHz, $CDCl_3$, ppm)δ 152.59, 152.53, 152.48, 150.07, 148.08, 148.05, 147.49, 127.53, 127.26, 124.18, 124.14, 124.07, 123.61, 119.37, 119.34, 119.17, 118.32, 116.40, 74.26, 74.21, 73.96, 73.81, 73.70, 70.03, 69.98, 69.86, 47.86, 47.83, 39.65, 39.61, 34.61, 31.53, 30.65, 30.63, 29.10, 25.22, 24.03, 24.00, 23.98, 23.10, 23.07, 22.60, 20.57, 14.12, 14.09, 14.06, 11.17, 11.14.
- HRMS (APCI), $[M+H]^+$ *m/z* calcd. for $C_{151}H_{225}N_8O_{20}S_{11}$: 2822.3757; found 2822.3812.

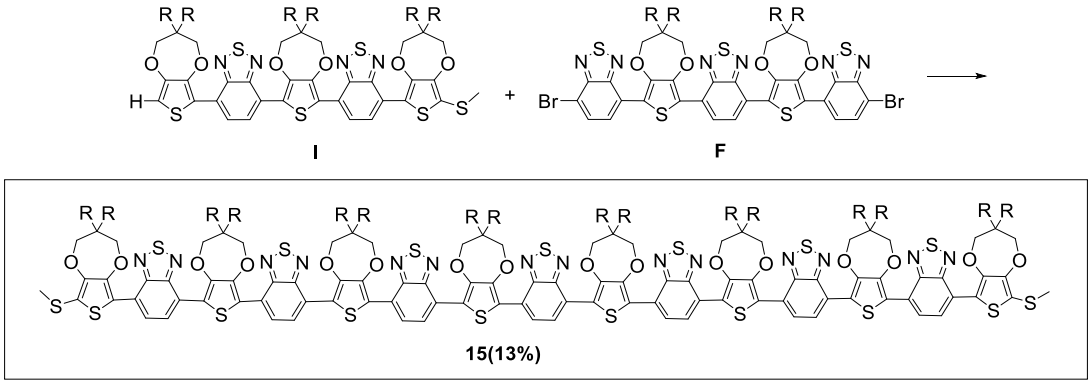

Oligomer n=15

The reaction was conducted according to the general procedure without modification using compound I (264.9 mg, 0.162 mmol, 2.3 equiv) and compound F (101.5 mg, 0.071 mmol, 1.0 equiv), $Pd(OAc)_2$ (20 mol %, 4.2 mg), $(o\text{-}MeOPh)_3P$ (40 mol %, 10 mg), pivalic acid (8.0 mg, 0.078 mmol, 1.1 equiv), and Cs_2CO_3 (71.7 mg, 0.220 mmol, 3.1 equiv) in 3 ml anhydrous toluene. The product was purified by column chromatography (CH_2Cl_2:hexanes, gradient of 1:1 to 5:1) and further purified by preparative HPLC to provide oligomer n=15 as a blue solid (42 mg, 13% yield).

- ^{1}H NMR (800 MHz, $CDCl_3$, ppm) δ 8.47 (d, *J* = 8.6 Hz, 10H), 8.43 – 8.36 (m, 4H), 4.36 (t, *J* = 8.0 Hz, 24H), 4.25 (s, 4H), 4.22 (s, 4H), 3.67 (d, *J* = 10.4 Hz, 24H), 3.60 (s, 8H), 3.40 – 3.38 (m, 24H), 3.34 (d, *J* = 5.6 Hz, 8H), 2.51 (s, 6H), 1.59 – 1.51 (m, 20H), 1.45 – 1.28 (m, 160H), 0.96 – 0.89 (m, 118H).
- ^{13}C NMR (201 MHz, $CDCl_3$, ppm) δ 152.66, 152.58, 152.51, 150.08, 148.11, 148.08, 147.51, 127.68, 127.30, 124.21, 124.13, 123.71, 119.35, 119.31, 119.14, 118.30, 116.43, 74.28, 74.23, 74.03, 73.89, 73.78, 70.08, 69.93, 47.88, 47.85, 39.63, 39.60, 30.64, 29.09, 24.01, 23.97, 23.09, 23.06, 20.59, 14.11, 14.08, 11.16, 11.13.
- MS (MALDI+), [M+H] *m/z* calcd. for $C_{244}H_{356}N_{14}O_{32}S_{17}$: 4541.20; found 4536.57.

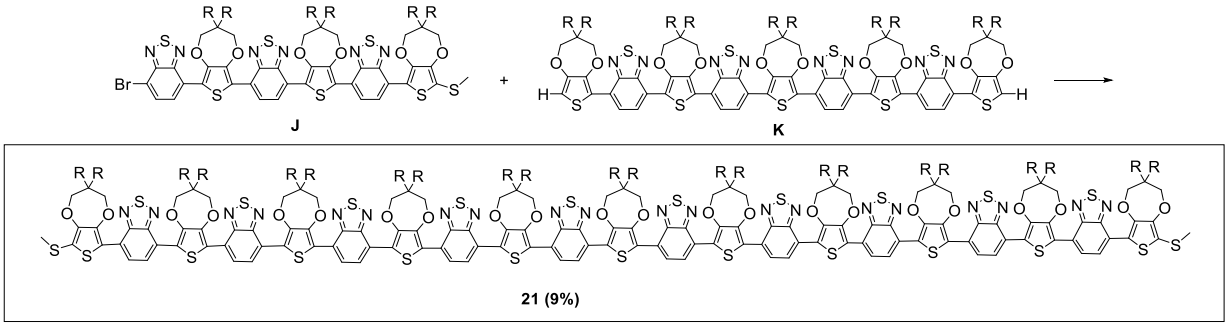

Oligomer n=21

The reaction was conducted according to the general procedure without modification using compound 10 (93.9 mg, 0.051 mmol, 2.2 equiv) and compound 11 (63.2 mg, 0.023 mmol, 1.0 equiv), $Pd(OAc)_2$ (40 mol %, 2.7 mg), $(o\text{-}MeOPh)_3P$ (80 mol %, 6.5 mg), pivalic acid (2.3 mg, 0.023 mmol, 1.0 equiv) and Cs_2CO_3 (23.4 mg, 0.072 mmol, 3.1 equiv) in 2 ml anhydrous toluene. The product was purified by column chromatography (CH_2Cl_2:hexanes, gradient of 1:1 to 5:1) and further purified by preparative HPLC to provide oligomer 21-A as a blue solid (37 mg, 26% yield).

- ^{1}H NMR (800 MHz, $CDCl_3$) δ 8.47 (s, 16H), 8.42 – 8.35 (m, 4H), 4.39 (s, 46H), 4.24 (d, *J* = 25.9 Hz, 8H), 3.70 (s, 48H), 3.60 (s, 14H), 3.41 (s, 52H), 3.35 (s, 16H), 2.51 (d, *J* = 7.5 Hz, 6H), 1.56 (d, *J* = 42.1 Hz, 39H), 1.35 (s, 309H), 0.94 (d, *J* = 8.0 Hz, 229H).
- ^{13}C NMR (201 MHz, $CDCl_3$) δ 152.57, 150.03, 148.02, 147.45, 127.56, 124.12, 119.36, 119.12, 118.30, 116.42, 74.27, 74.23, 73.90, 70.14, 69.94, 47.83, 39.65, 39.61, 30.65, 29.64, 29.10, 24.03, 23.99, 23.97, 23.10, 23.07, 20.58, 14.11, 14.09, 11.16, 11.13.
- MS (MALDI+), [M+H] *m/z* calcd. for $C_{337}H_{488}N_{20}O_{44}S_{23}$: 6261.09; found 6260.57.

General Polymerization Condition

To a Schlenk tube charged with a stir bar, compound A (1.0 equiv), compound B (0.05 equiv.), compound C (1.0 equiv), $Pd(OAc)_2$ (2 mol %), $(o\text{-}MeOPh)_3P$ (4 mol %), pivalic acid (1.1 equiv) and Cs_2CO_3 (3.1 equiv) were added, vacuumed for 30 minutes, and then subjected to N_2 purge cycles three times. Anhydrous toluene (3 ml) was added via needle and syringe. The reaction was heated at 110°C in an oil bath until completion. After polymerization was complete, the mixture was precipitated into methanol. The solids were collected by a Soxhlet thimble and purified by Soxhlet extraction successively with methanol, acetone, hexane, dichloromethane and chloroform. 3 separate reaction were carried out with variations in heating time; 24 h (P1, extracted from DCM fraction), 48 h (P2, extracted form chloroform extract), and 72 h (P3, extracted from chloroform extract). The fractions were concentrated and precipitated into methanol. The polymer was collected and further purified by recycling HPLC.

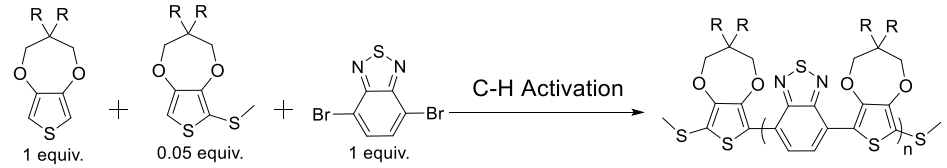

Polymer	Reaction Time	Yield	GPC Mn (Da)	PDI
P1	24 h	112 mg	9,396	1.37
P2	48 h	82 mg	14,470	1.34
P3	72 h	157 mg	15,892	1.26

C. Recycling Preparative HPLC Chromatograms for Polymers

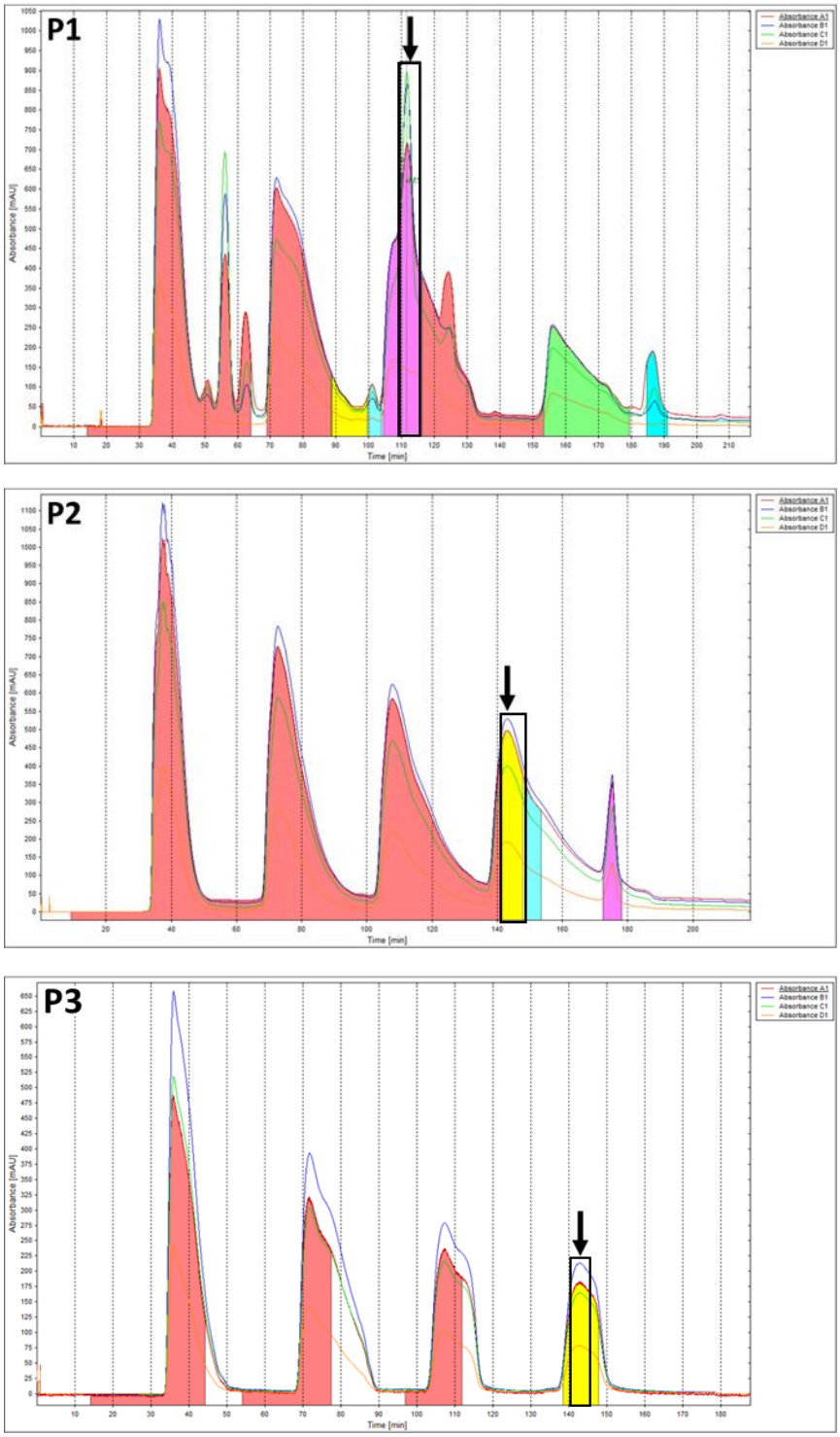

Figure S1. Preparative HPLC chromatograms of P1, P2, and P3.

D. Gel Permeation Chromatography (GPC)

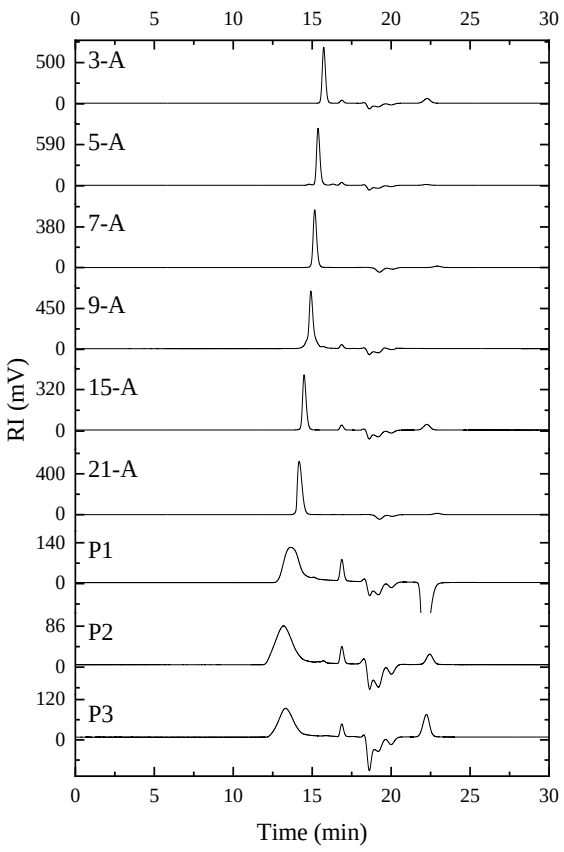

Figure S2. Raw GPC chromatogram for nPB series.

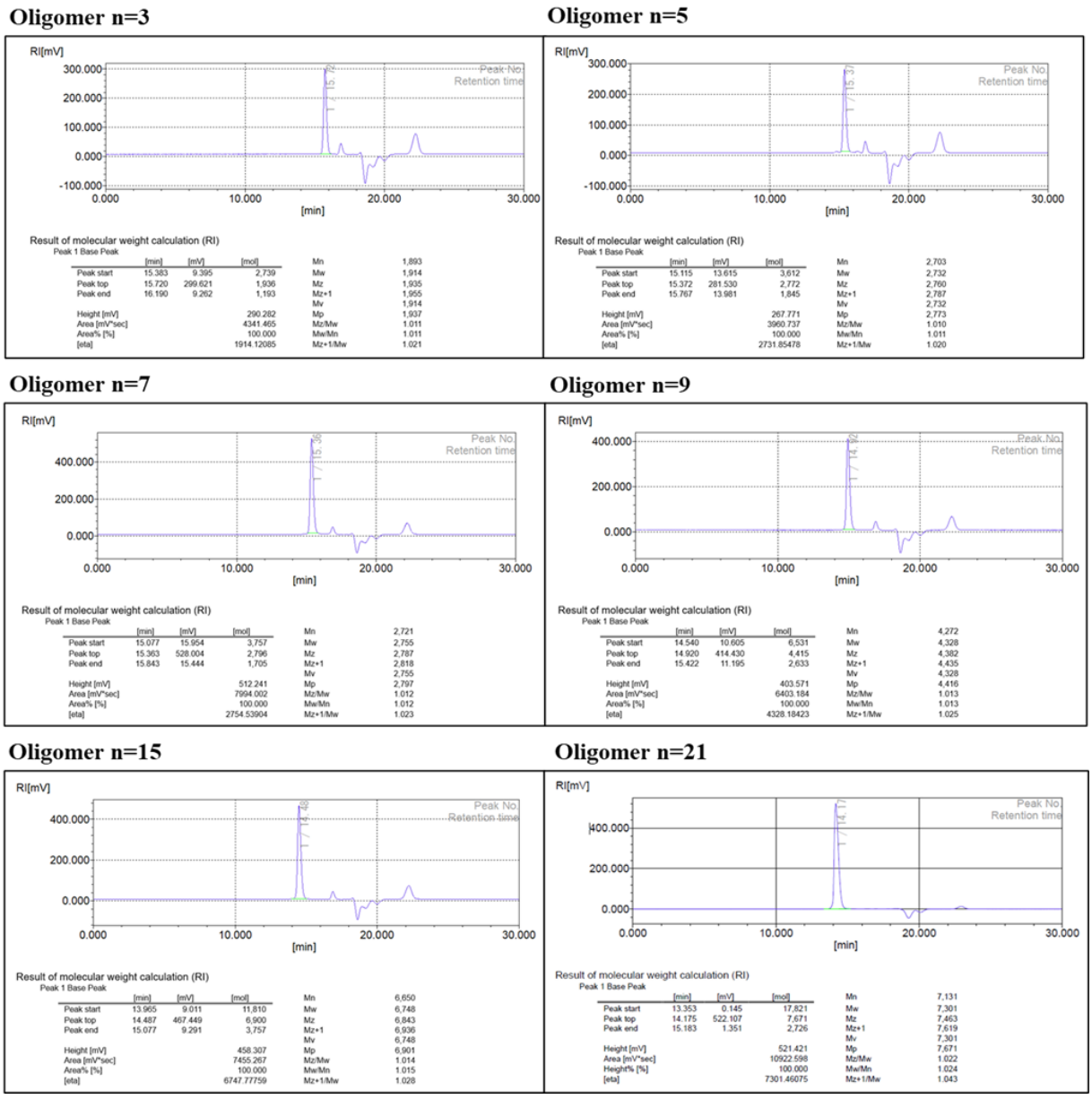

Figure S3.1. Raw GPC chromatograms for nPB Oligomers.

P1

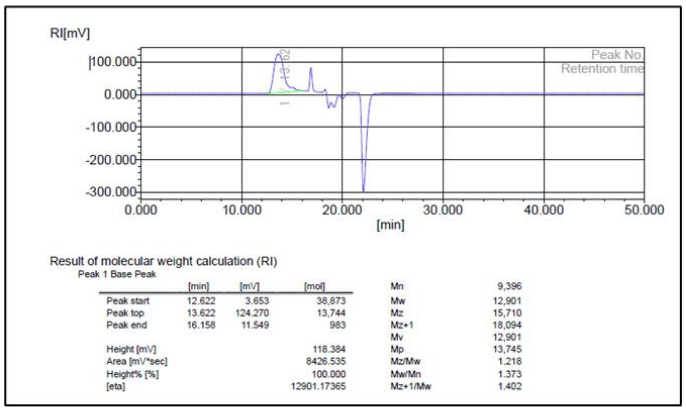

P2

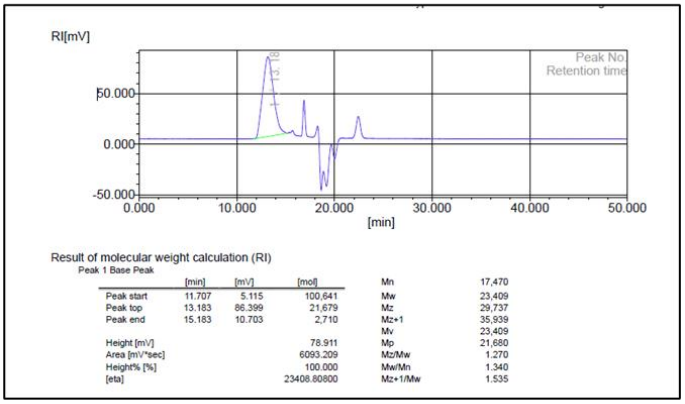

P3

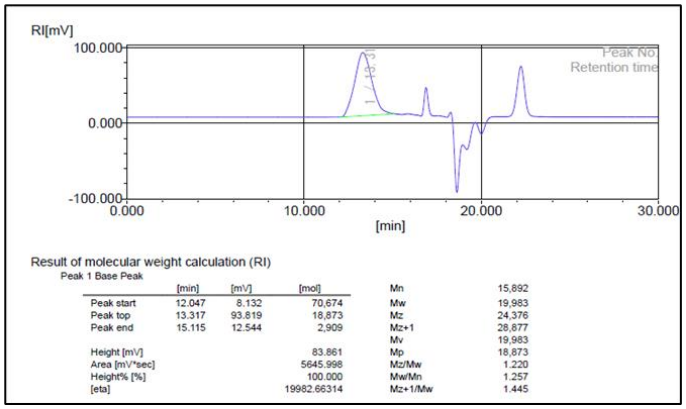

Figure S3.2. Raw GPC chromatograms for *n*PB polymers.

E. Small Angle Neutron Scattering (SANS)

Dilute solutions of oligomers and polymers were prepared (5 mg/mL) in chlorobenzene-d5. Chlorobenzene-d5 (D > 99%) and was purchased from Cambridge Isotopes (Tewksbury, MA) and used as received. SANS measurements were carried out using the Extended Q-Range Small-

Angle Neutron Scattering Diffractometer (EQ-SANS) at the Spallation Neutron Source (SNS), ORNL. The scattering wavevector q ranged from 0.003 to 0.8 Å-1, by using two different configurations (4m 12 Å and 2.5m 2.5 Å). The samples were contained in Hellma quartz cells with a 2 mm path length. Measurements were performed at 75 °C. The absolute intensity was obtained through data reduction and correction. Reduced data was later fitted to a flexible cylinder model in SasView.24.

F. Electrochemistry

Solution CV and DPV of the oligomer series dissolved at ~1 mM in 0.2 M $TBAPF_6$/ CH_2Cl_2 was conducted under a nitrogen atmosphere on a ultramicroelectrode (25 mm) platinum button electrode and a platinum wire counter electrode. An Ag/AgCl wire was used as the pseudoreference electrode which was calibrated against a ferrocene/ ferrocenium as an internal standard ($E_{1/2}$ = 0.51 V). The voltage was scanned from 0 to 2.0 V vs. Fc+/Fc, at a 10 mV/s scan rate. The second cycle is reported in the main text figure.

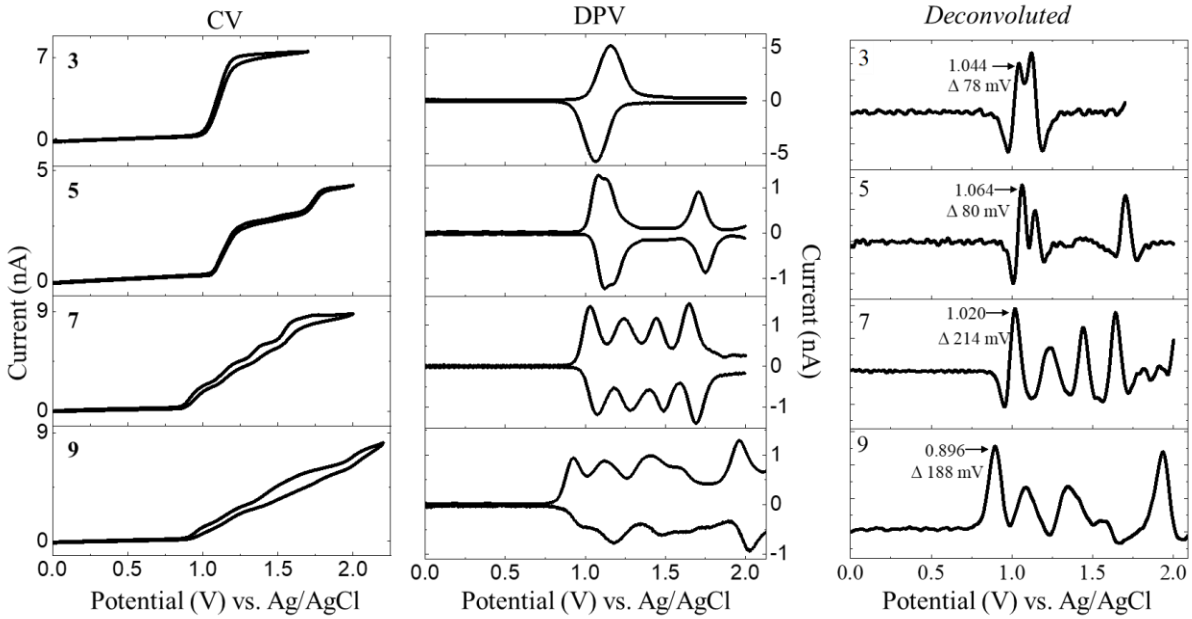

Figure S4. Raw and deconvoluted CV and DPV voltammograms for n=3, 5, 7, and 9.

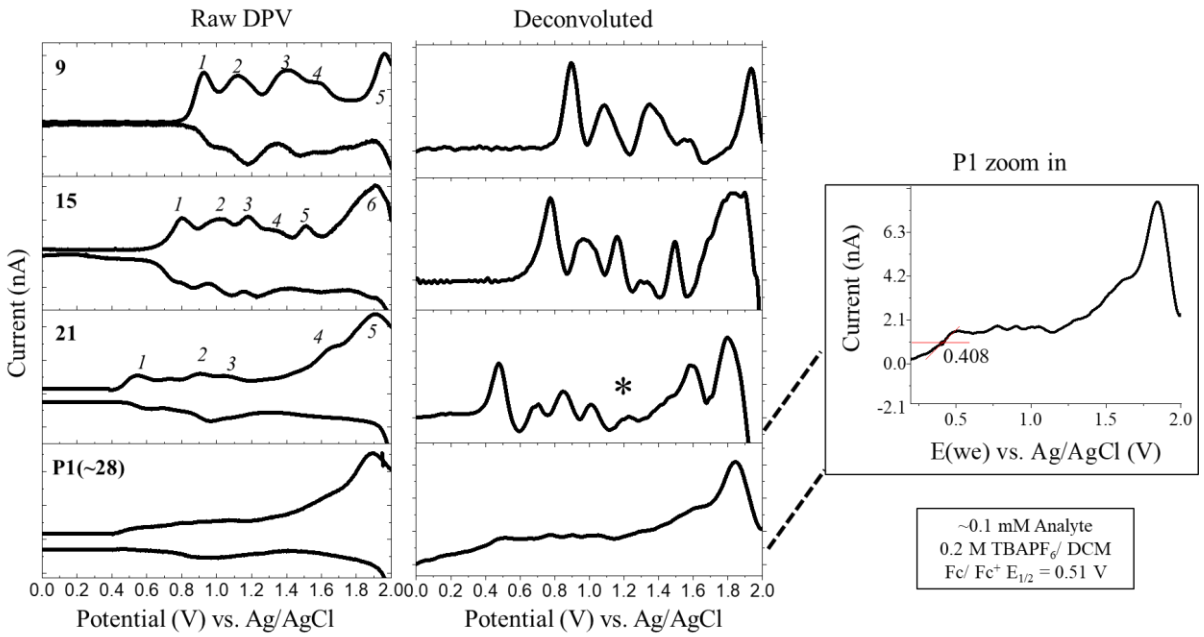

Figure S5. Raw and deconvoluted DPV voltammograms for n=9, 15, 21, and P1.

G. ^{1}H- and ^{13}C-NMR Spectra

^{1}H NMR: Compound D

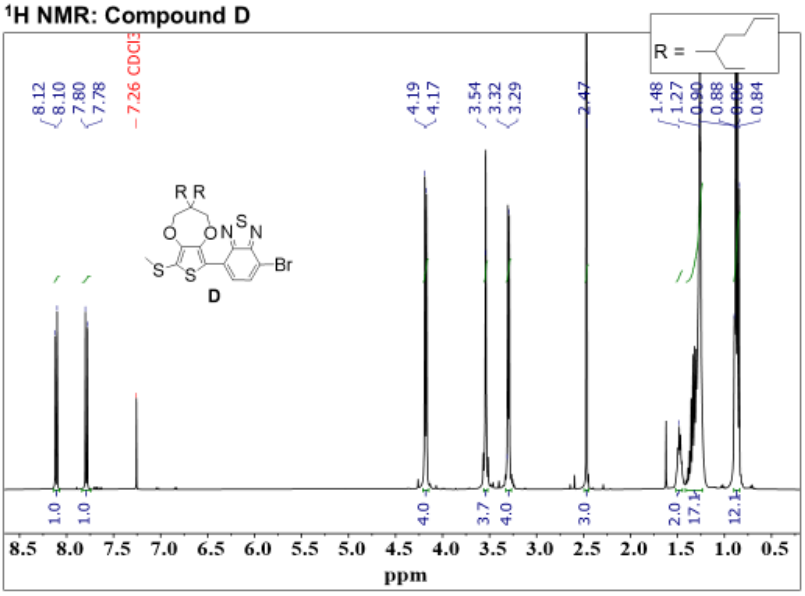

^{13}C NMR: Compound D

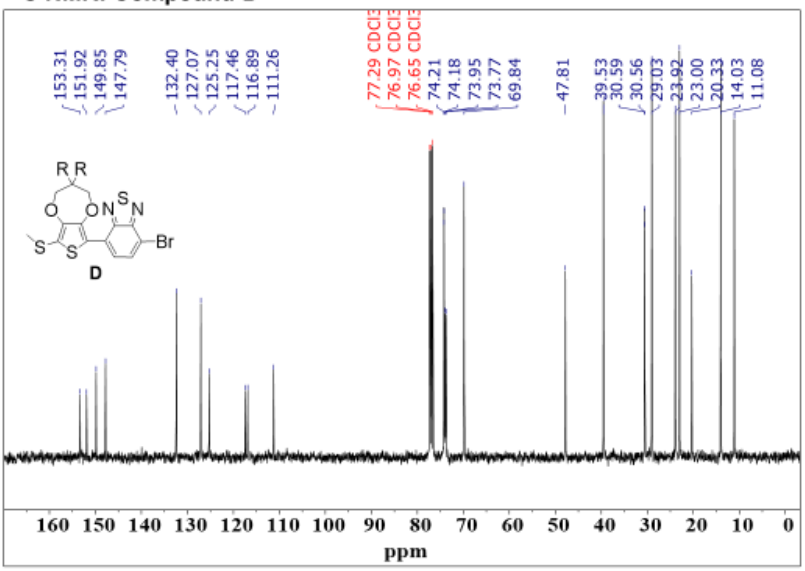

^{1}H NMR: Compound E

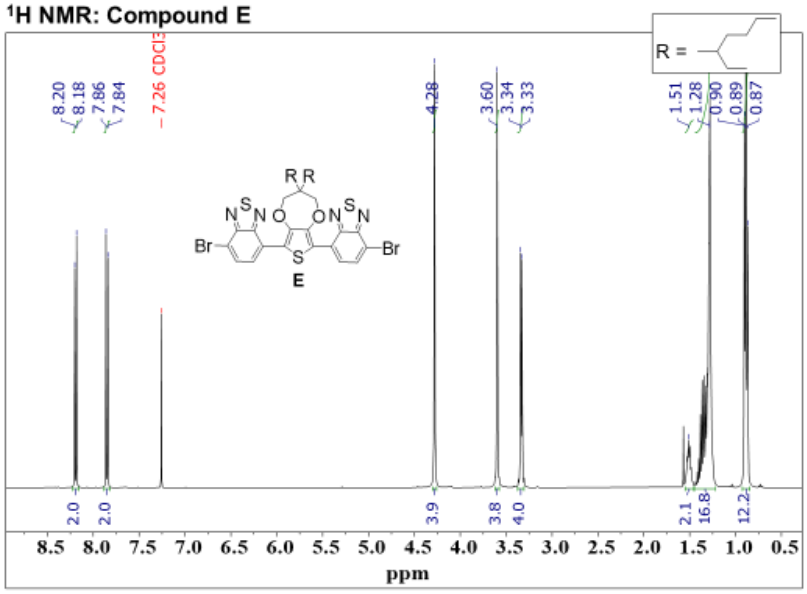

^{13}C NMR: Compound E

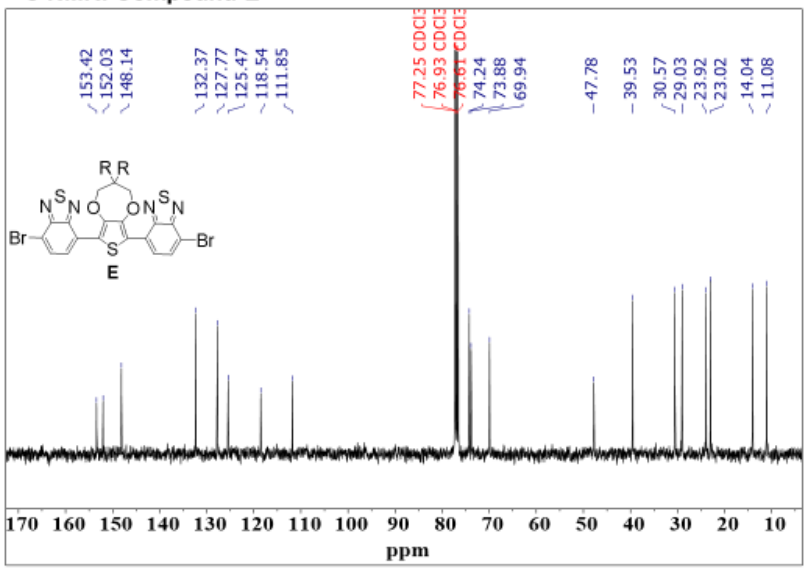

^{1}H NMR: Compound F

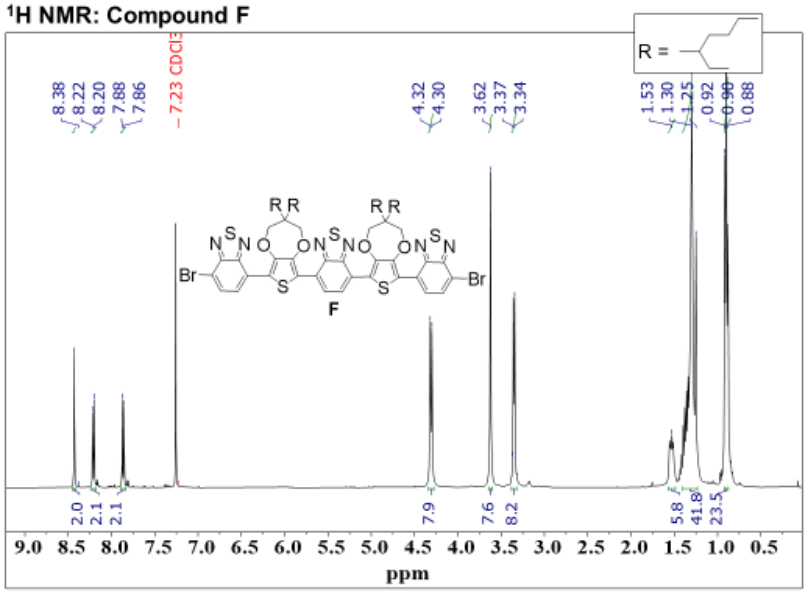

^{13}C NMR: Compound F

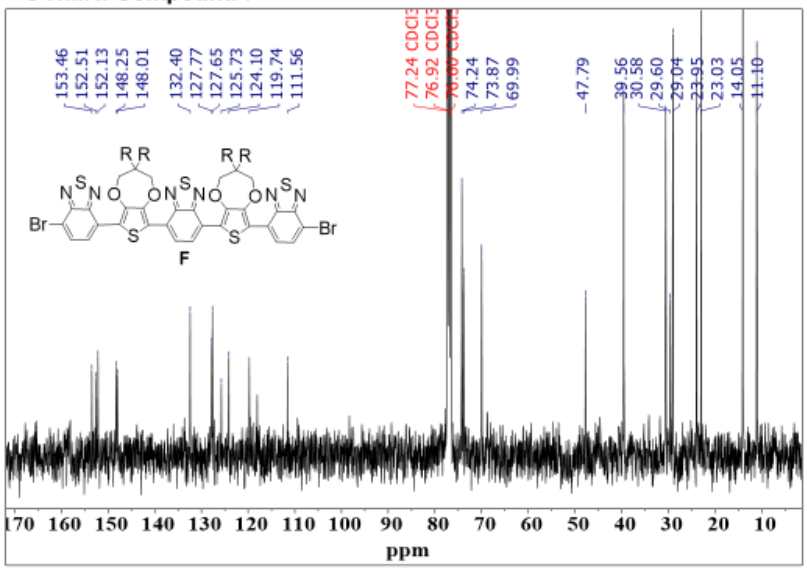

^{1}H NMR: Compound G

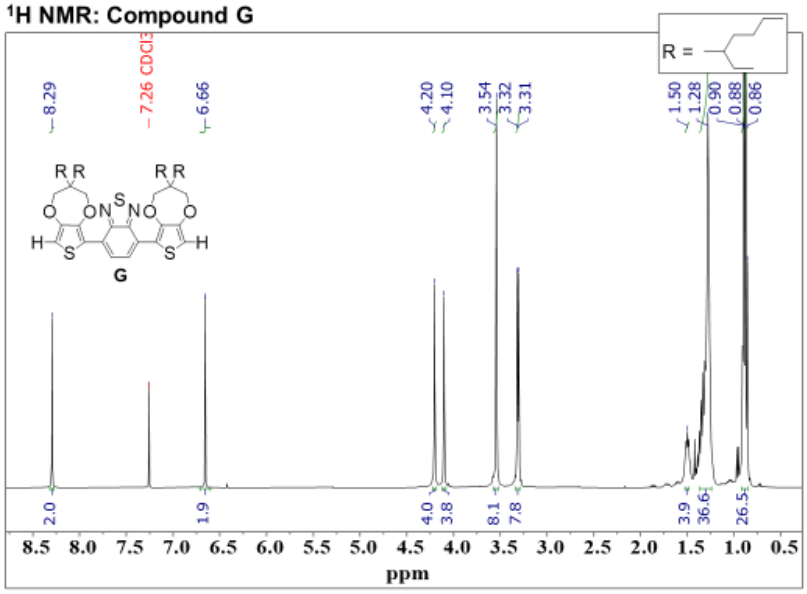

^{13}C NMR: Compound G

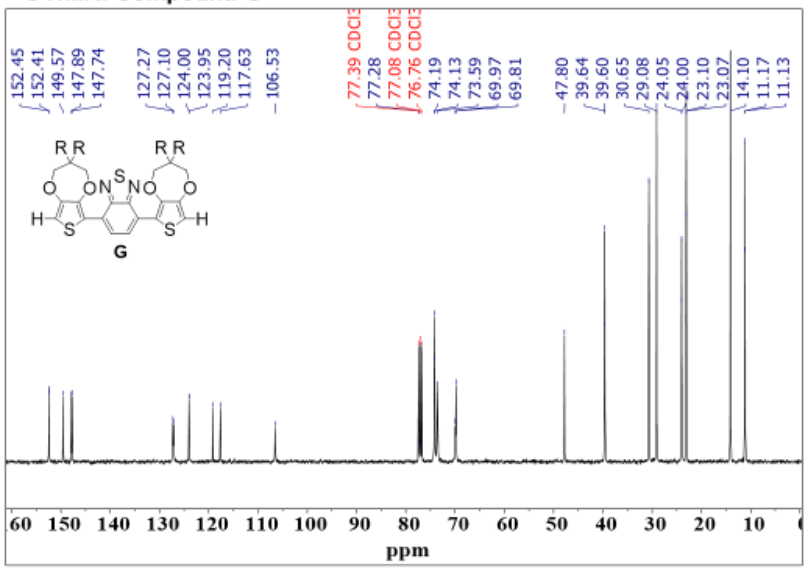

^{1}H NMR: Compound H

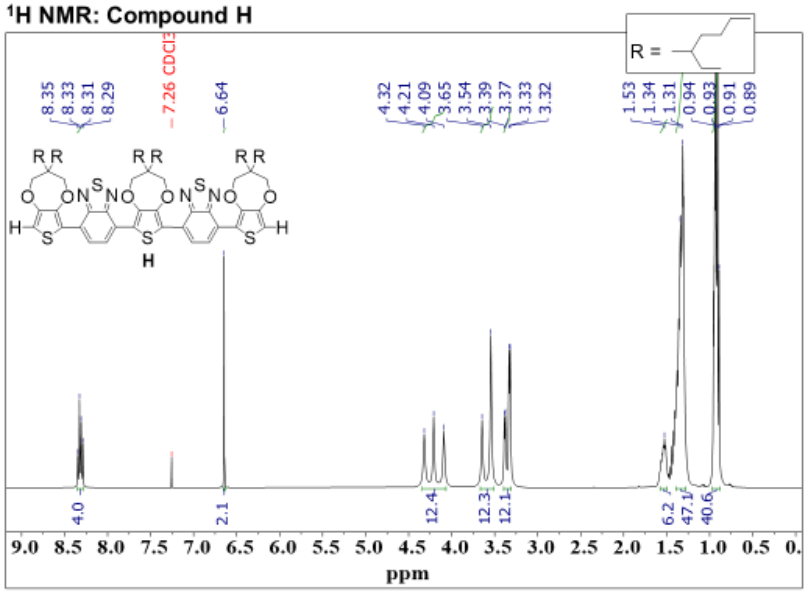

^{13}C NMR: Compound H

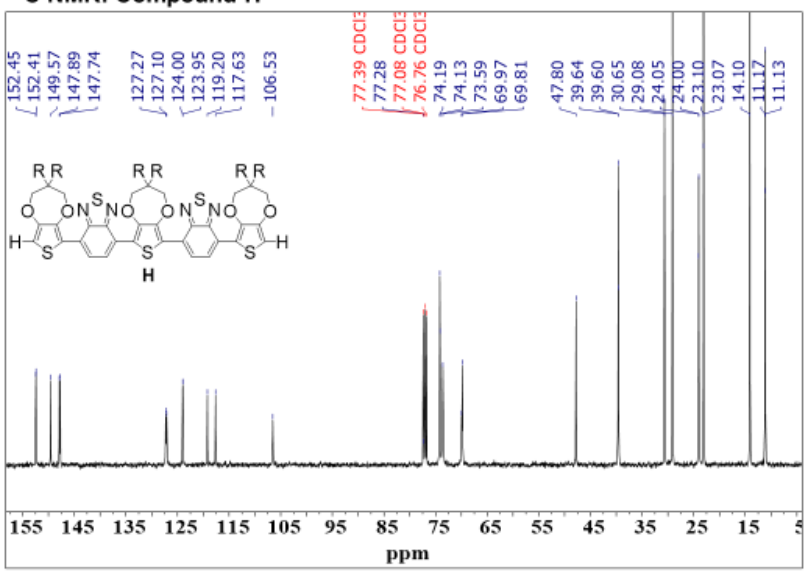

^{1}H NMR: Compound J

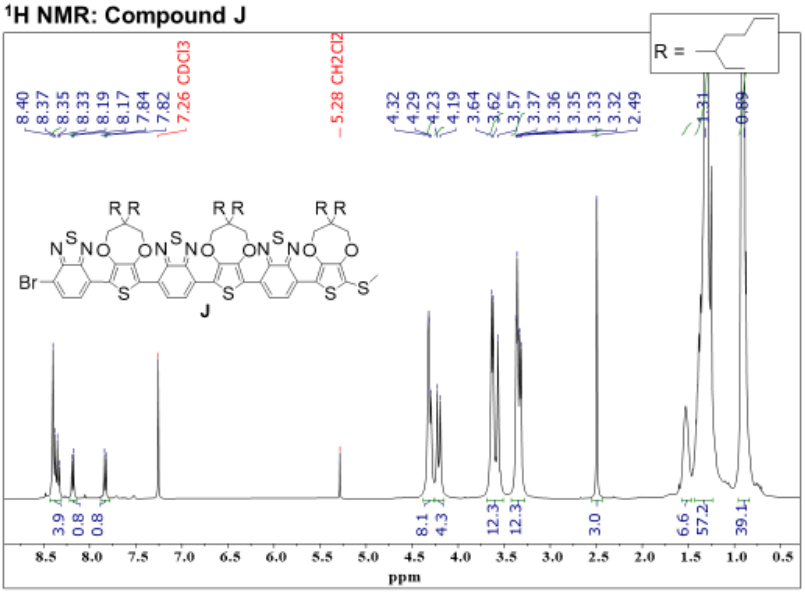

^{13}C NMR: Compound J

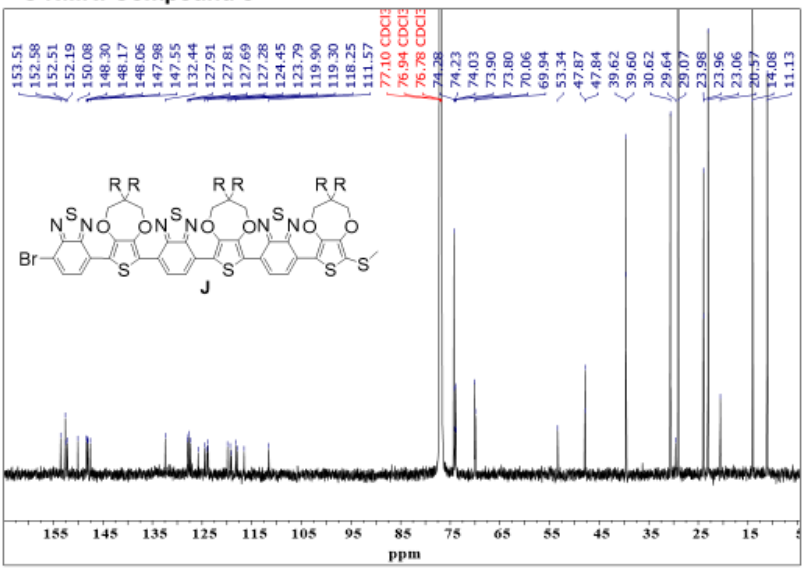

^{1}H NMR: Compound K

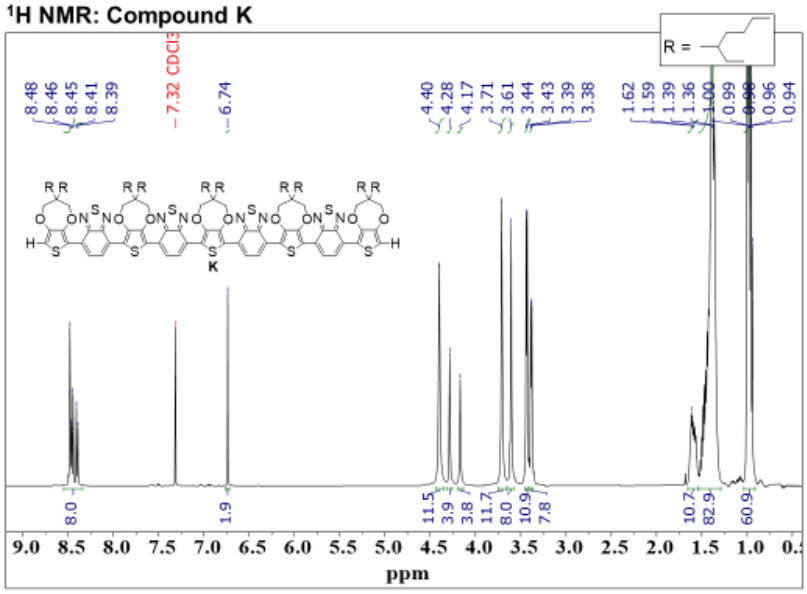

^{13}C NMR: Compound K

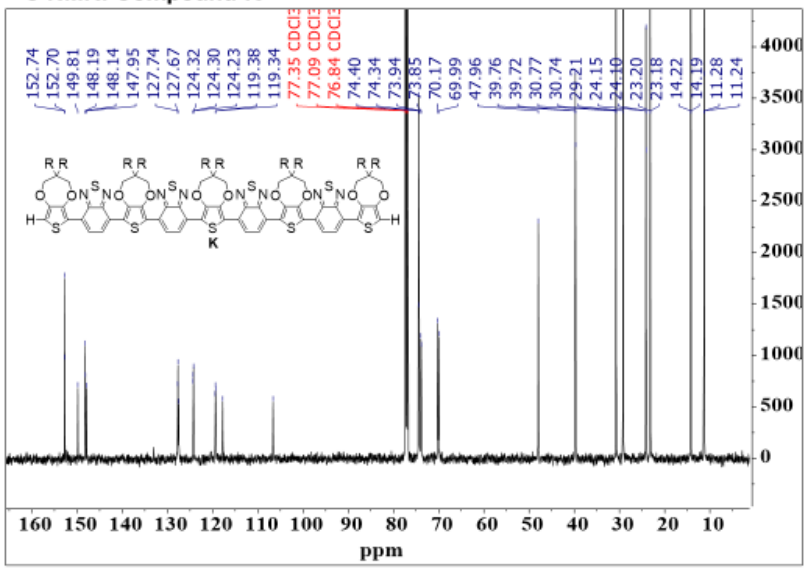

^{1}H NMR: n=3

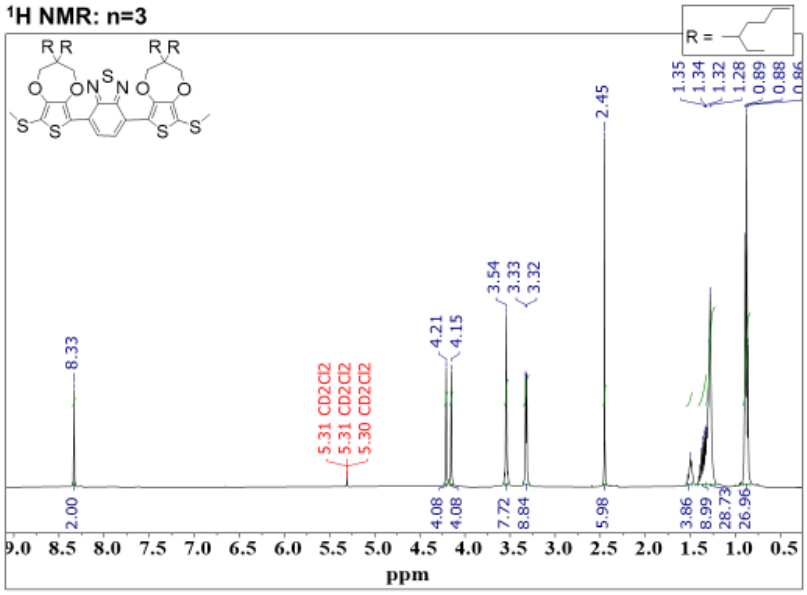

^{13}C NMR: n=3

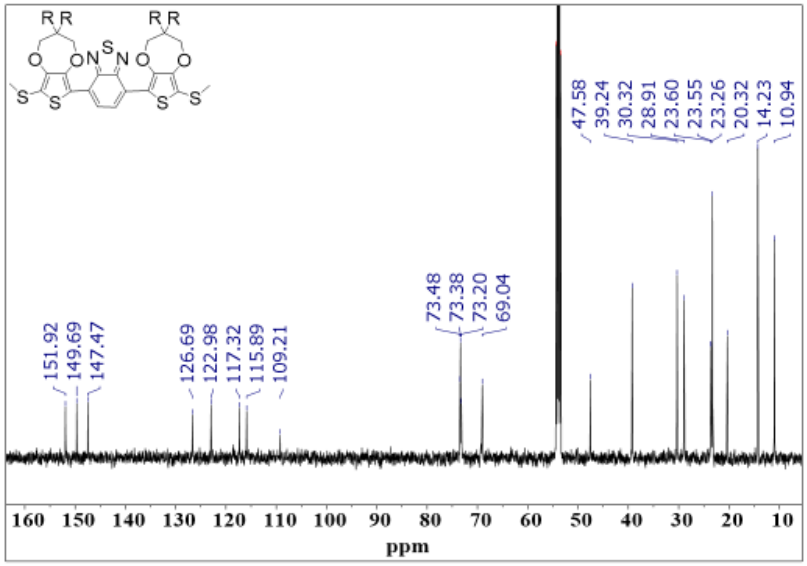

^{13}C NMR: n=3

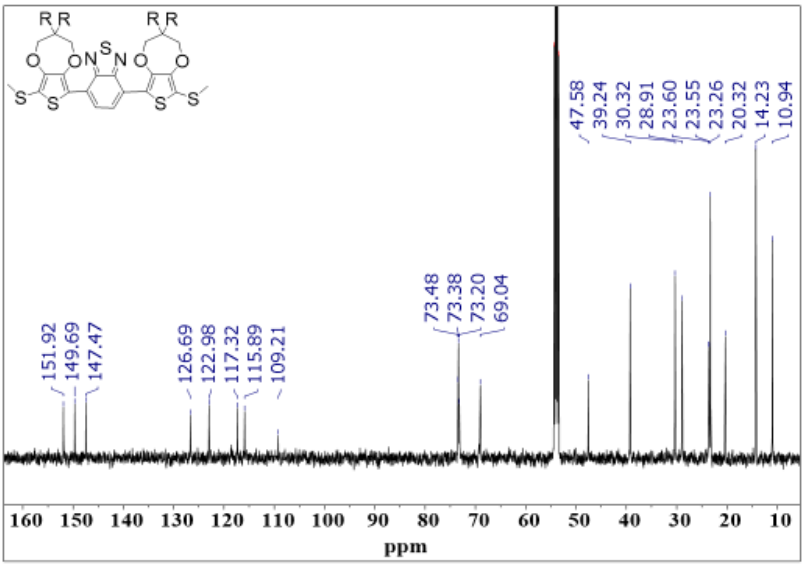

^{13}C NMR: n=5

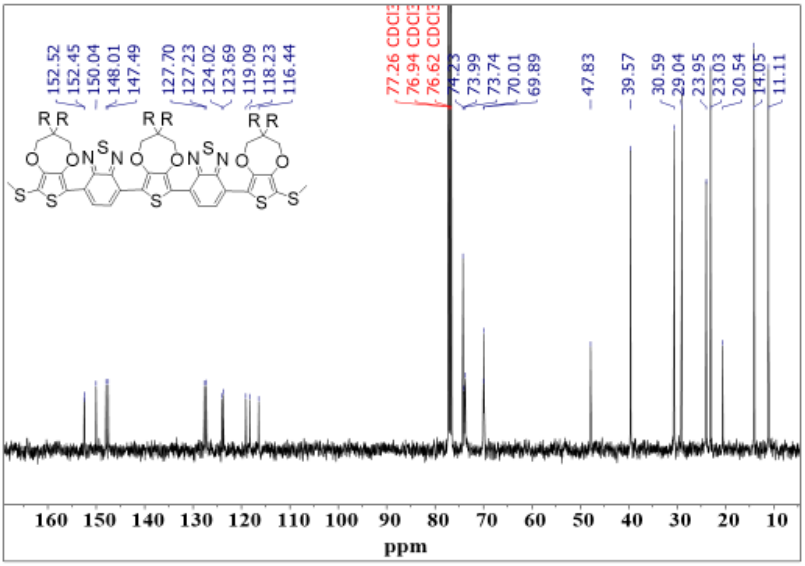

^{1}H NMR: n=7

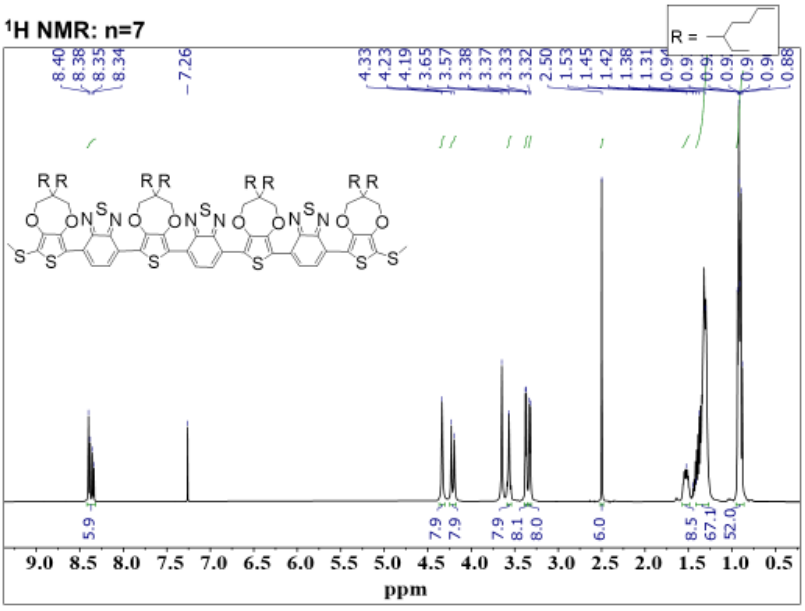

^{13}C NMR: n=7

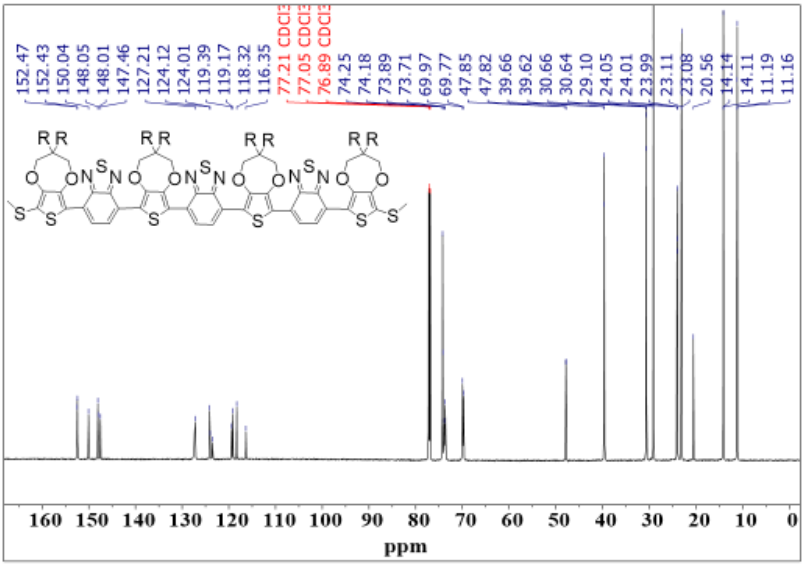

^{1}H NMR: n=9

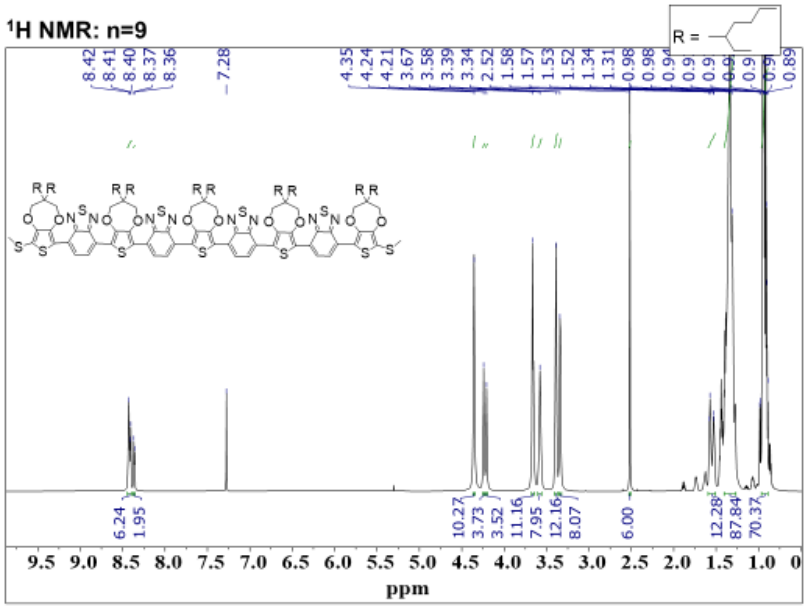

^{13}C NMR: n=9

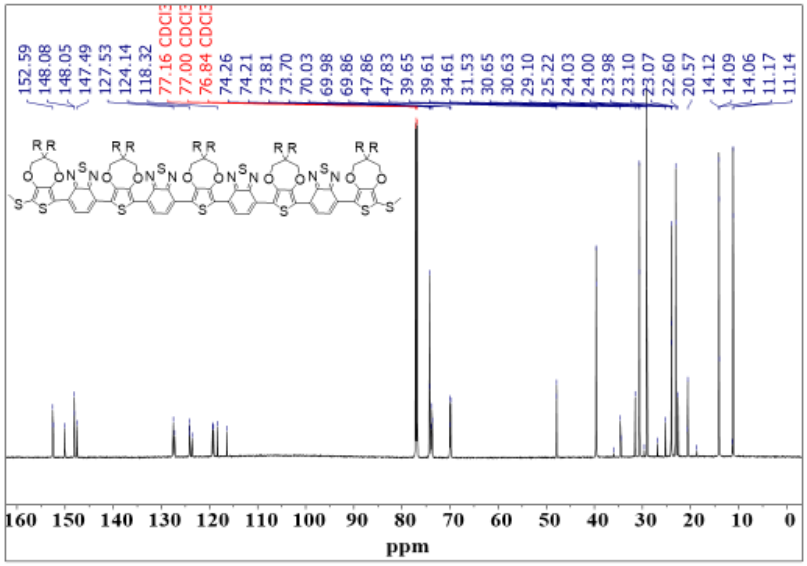

^{1}H NMR: n=15

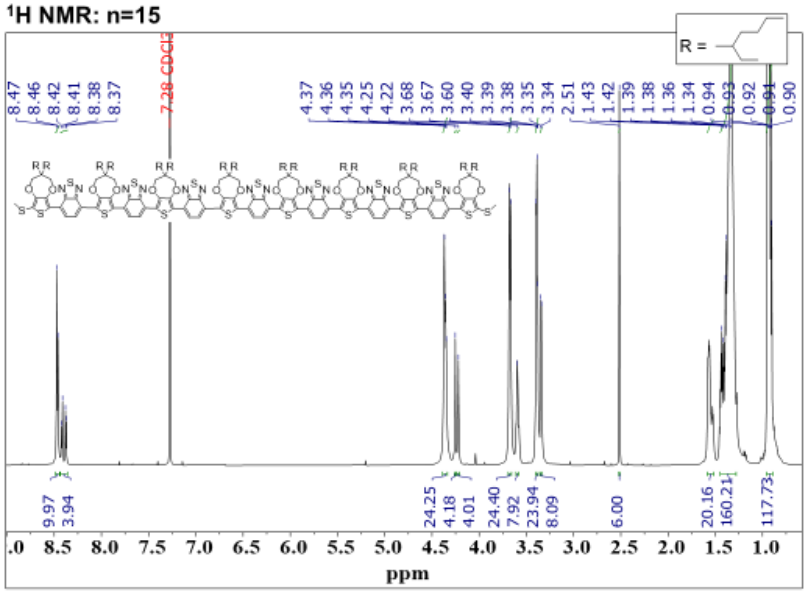

^{13}C NMR: n=15

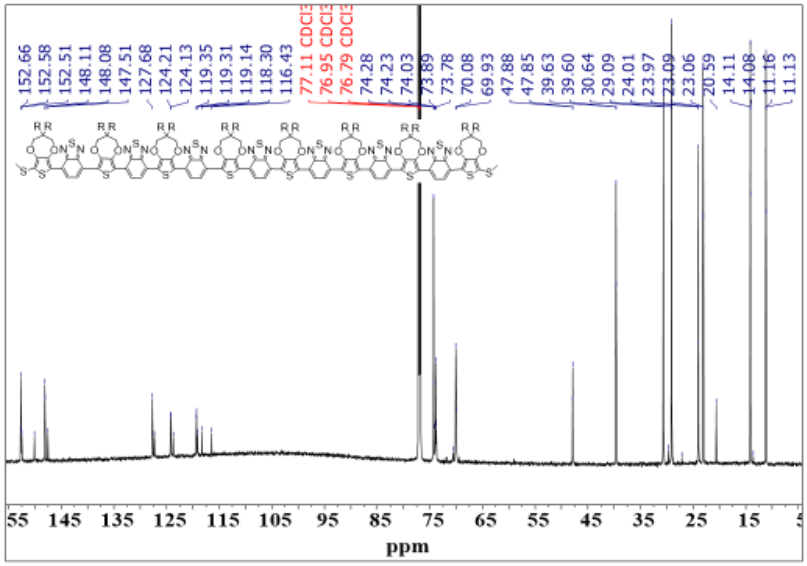

^{1}H NMR: n=21

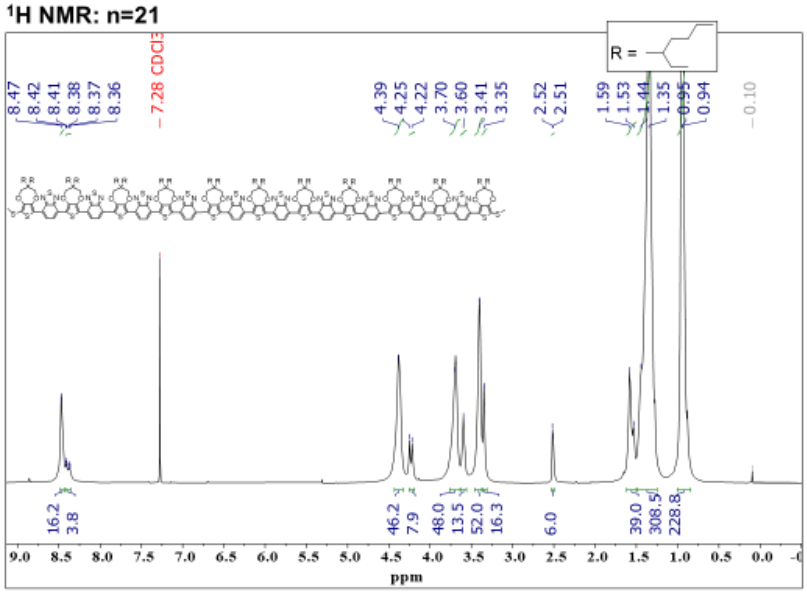

^{13}C NMR: n=21

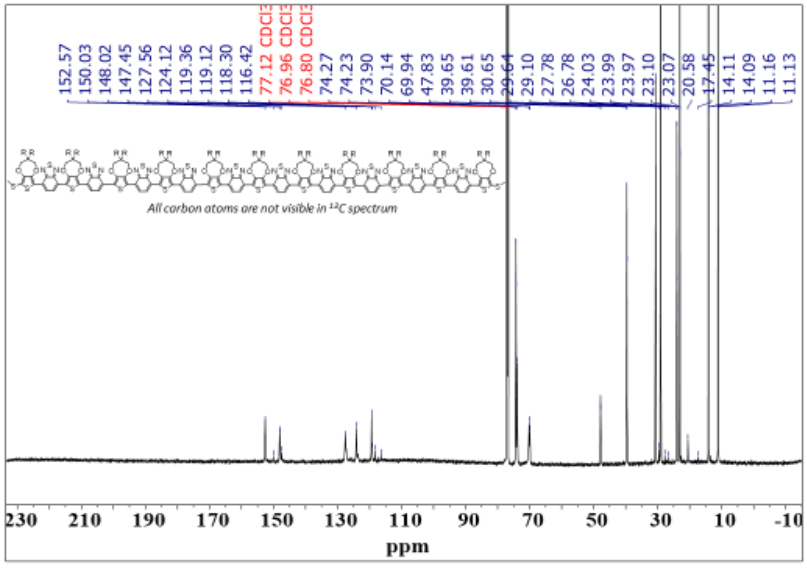

^{1}H NMR: P1–Raw

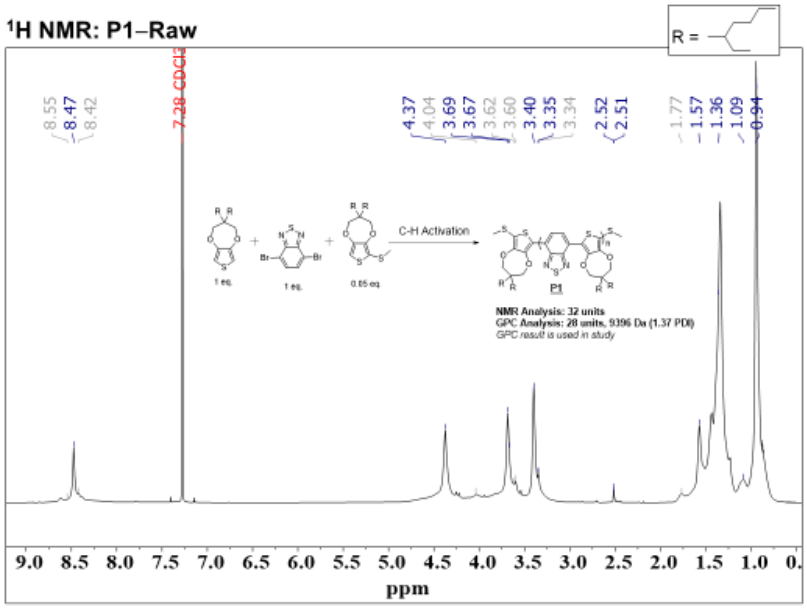

^{1}H NMR: P1–Peak Fitting

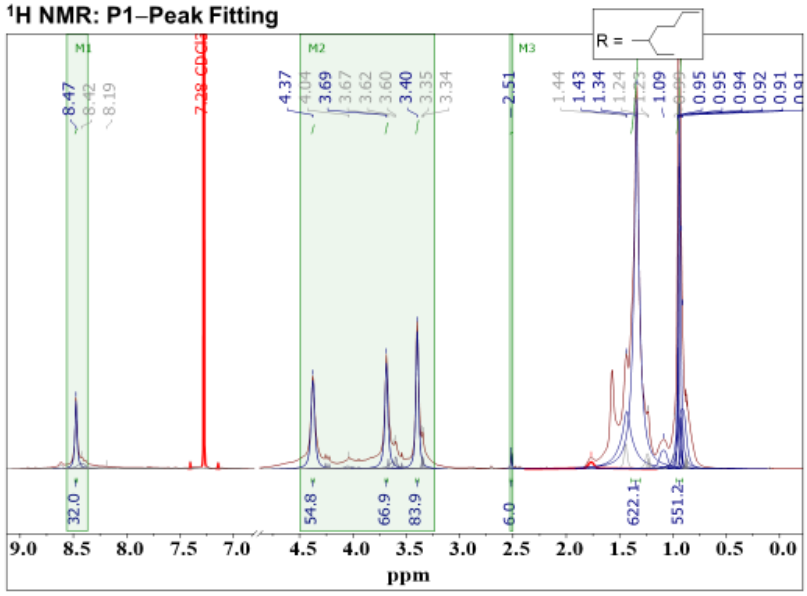

^{1}H NMR: P2–Raw

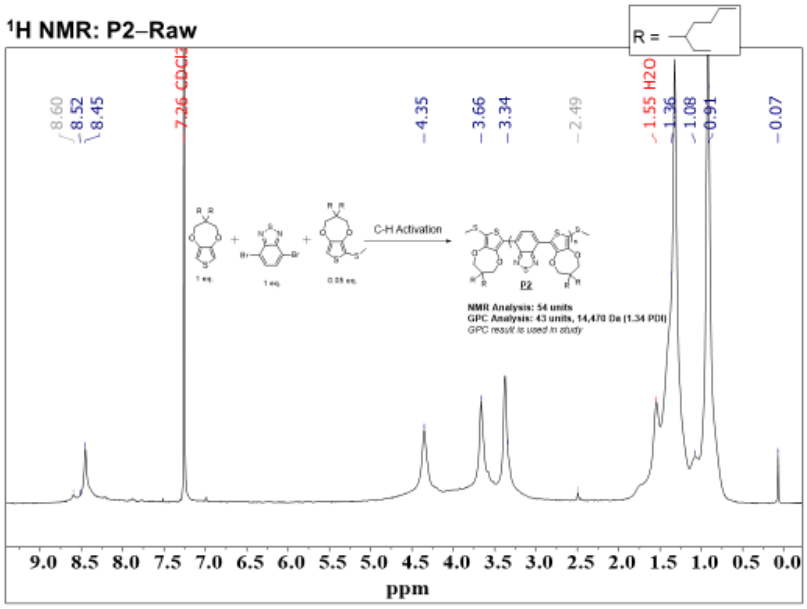

^{1}H NMR: P2–Peak Fitting

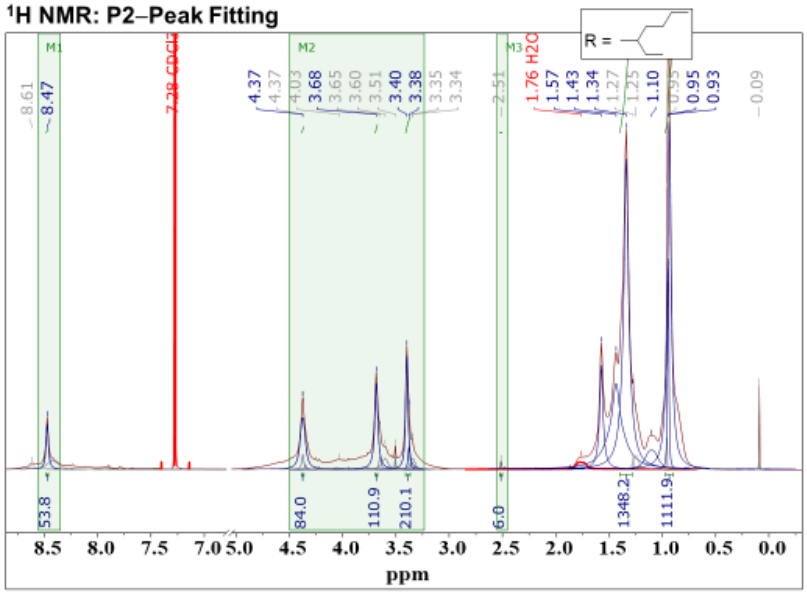

^{1}H NMR: P3–Raw

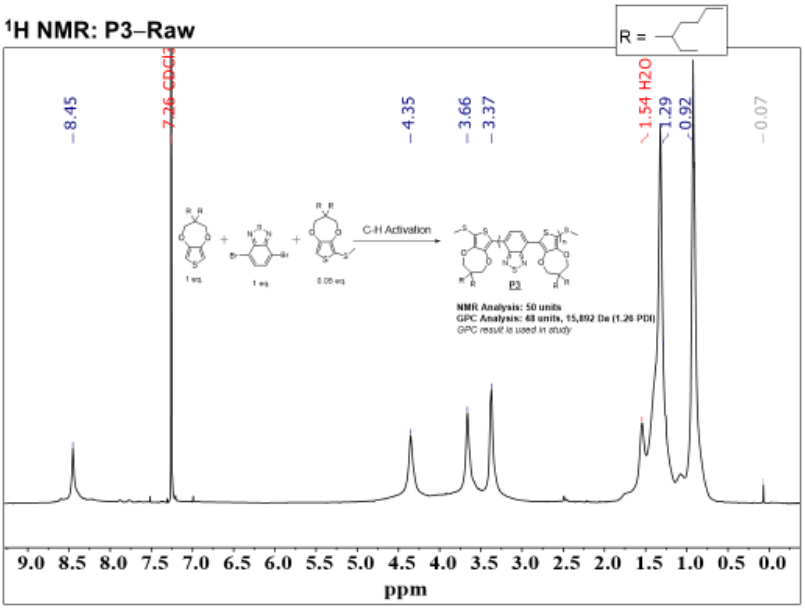

^{1}H NMR: P3–Peak Fitting

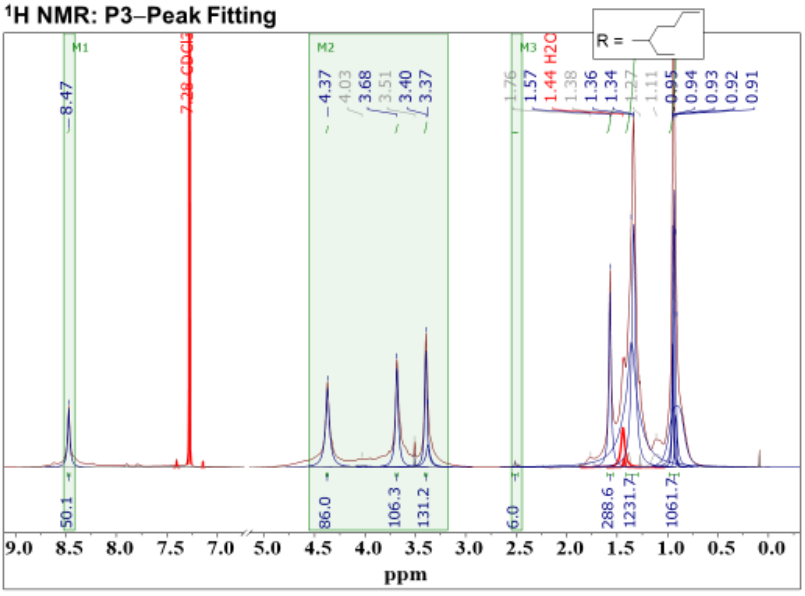

APPENDIX C: SUPPORTING INFORMATION FOR CHAPTER 4

A. Synthesis of Non-Alternating Oligomer Series

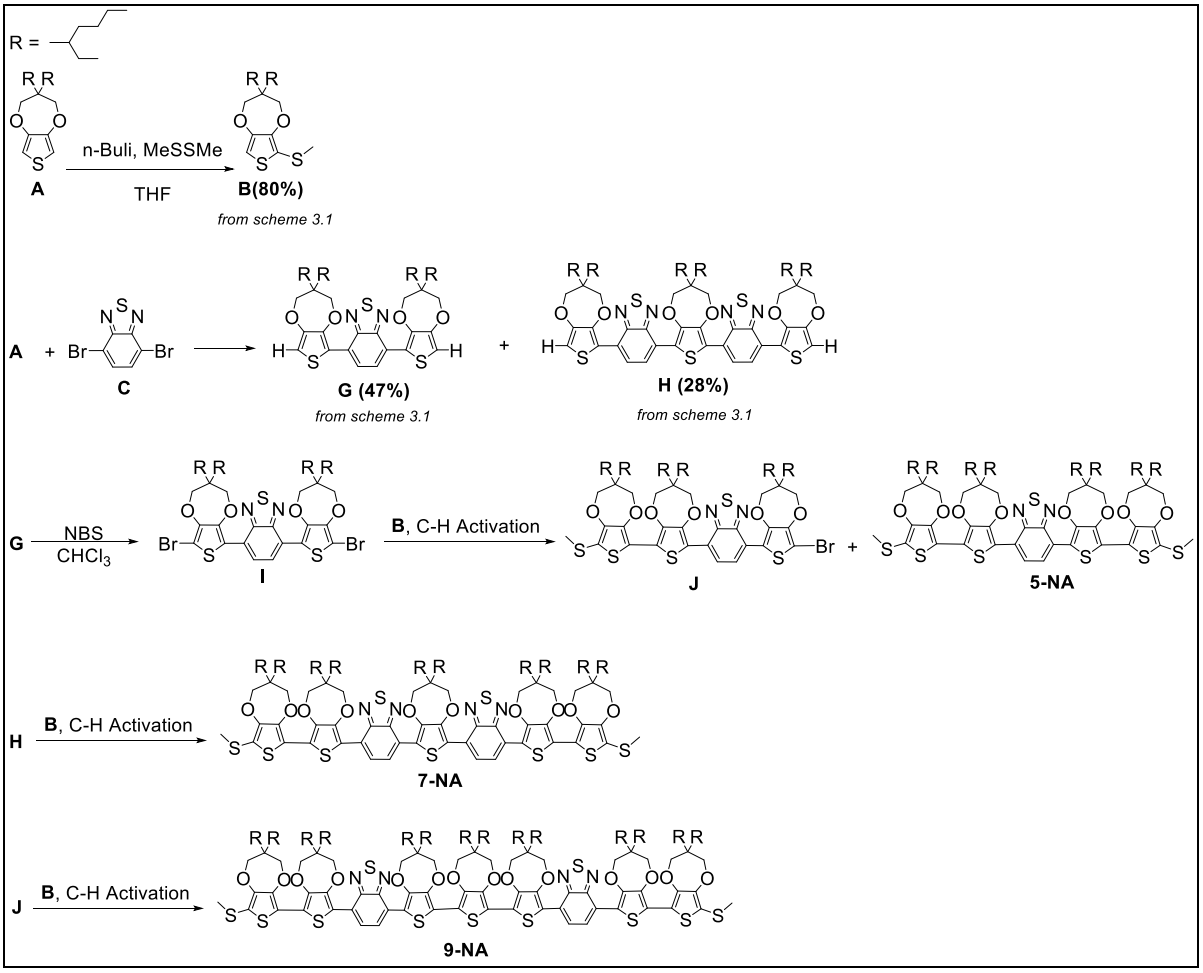

Scheme 1. Synthesis of the non-alternating nPB oligomers. a) n-BuLi, CH_3SSCH_3, b) C-H Activation Conditions: $Pd(OAc)_2$, $(o\text{-}MeOPh)_3P$, pivalic acid, Cs_2CO_3.

General C-H Activation Conditions

In a 25 mL Schlenk tube, $Pd(OAc)_2$ (4-8 mol %), $(o\text{-}MeOPh)_3P$ (8-16 mol %), pivalic acid (0.5 per C-H monomer equivalence) and Cs_2CO_3 (1.5 per C-H monomer equivalence) were added, vacuumed for 30 minutes, and then subjected to N_2 purge cycles three times. Anhydrous toluene (0.1 M–0.5 M) was added via needle and syringe. The reaction was heated at 110°C in an oil bath, or until the limiting reagent was consumed per TLC analysis. Upon completion, the reaction mixture was quenched with water and extracted with dichloromethane. The organic layer was

washed with water twice, then once with brine. The organic layer was separated and dried over $MgSO_4$ or Na_2SO_4, then filtered and concentrated under reduced pressure. The crude product was purified by SiO_2 column chromatography concentrated, and further purified by recycling preparative HPLC (polystyrene/divinylbenzene stationary phase) with $CHCl_3$. In cases where an excess of a compound is used, the unreacted portion is retrieved during column chromatography as its rf value is generally higher than the generated product.

Compound I

(G) (2.77 mmol, 2.80 g) was dissolved in 100 ml of chloroform and cooled to 0^{o}C in an ice bath. 2.30 eq. of N-bromosuccinimide (6.37 mmol, 1.13 g) was added in three portions. The reaction mixture was protected from light with aluminum foil, put under N2, and al-lowed to stir overnight at RT. Upon completion, the reaction mixture was quenched with 100 ml of 1M Na2SO4 and washed with water twice. The organic layer was separated and concentrated under vacuum. The crude material was purified by column chromatography, eluting DCM:Hexane (2:3) to give a yield of 69.9 % (2.26 g) as a highly viscous, dark orange oil.

Compound J and Oligomer 5-NA

Synthesis of (J) and (5-NA) follows the standard conditions stated in the 1st round of C-H activation with the following differences: a 1:1.5 ratio of (5, (0.91 mmol, 1.06 g)) to (8) was used; the reaction was ran overnight; the desired products (9) and (5-mer) were purified sequentially via column chromatography eluting with a DCM:Hexane gradient from 1:5 to 1:3. (9) was collected in 26.7% yield (383.2 mg) as a sticky purple-blue film and (5-mer) was collected in 20.55 % yield (370.8 mg) as a sticky magenta film.

- ^{1}H NMR (400 MHz, $CDCl_3$) δ 8.30 (s, 2H), 4.25 – 4.18 (m, 12H), 4.15 (s, 4H), 3.58 (d, *J* = 8.2 Hz, 16H), 3.32 (t, *J* = 5.4 Hz, 16H), 2.42 (s, 6H), 1.29 (s, 41H), 0.93 – 0.84 (m, 53H).
- (MALDI $[M+H]^+$) m/z calculated: 1983.0, found: 1982.8

Oligomer 7-NA

(H) (1.42 mmol, 2.26 g) was dissolved in 50 ml of chloroform and cooled to 0oC in an ice bath. 2.30 eq. of N-bromosuccinimide (3.26 mmol, 581.3 mg) was added in three portions. The reaction mixture was protected from light with aluminum foil, put under N2, and allowed to stir overnight at RT. Upon completion, the reaction mixture was quenched with 75 ml of 1M Na2SO4 and washed with water twice. The organic layer was separated and concentrated under vacuum. The crude material was purified by column chromatography, eluting DCM:Hexane (2:3) to give a yield of 71.0 % (1.75 g) as a sticky, magenta solid. Brominated (4) was subjected to C-H activation with a 1:3 ratio of brominated (4) (0.25 mmol, 430 mg)) to (8); the reaction was ran overnight; the desired product (7-mer) was puri-fied via column chromatography eluting with a DCM:Hexane gradient from 1:3 to 1:1. (7-mer) was collected in 3.4% yield (21.7 mg) as a sticky purple-blue film.

- ^{1}H NMR (400 MHz, $CDCl_3$) δ 8.43 – 8.34 (m, 4H), 4.24 (dd, *J* = 39.8, 24.3 Hz, 24H), 3.66 – 3.55 (m, 24H), 3.34 (q, *J* = 7.5, 6.3 Hz, 24H), 2.42 (s, 6H), 1.31 (s, 49H), 0.90 (dd, *J* = 7.1, 4.5 Hz, 68H).
- (MALDI $[M+H]^+$) m/z calculated: 2555.8, found: 2554.9

Oligomer 9-NA

Synthesis of (9-mer) follows the standard conditions stated in the 1st round of C-H activation with the following differences: a 2.5:1 ratio of (9) (0.22 mmol, 383.5 mg)) to (1) was used; the reaction was ran overnight; the desired product was purified via column chromatog-raphy eluting with a DCM:Hexane gradient from 1:5 to 1:1. (9-mer) was collected in 33.2 % yield (277.8 mg) as a sticky blue film.

- ^{1}H NMR (400 MHz, $CDCl_3$) δ 8.36 – 8.29 (m, 4H), 4.31 – 4.14 (m, 29H), 3.67 – 3.56 (m, 28H), 3.34 (d, *J* = 5.9 Hz, 28H), 2.42 (s, 6H), 1.37 (d, *J* = 5.4 Hz, 31H), 1.30 (s, 68H), 0.90 (d, *J* = 7.1 Hz, 79H).
- (MALDI $[M+H]^+$) m/z calculated: 3433.2, found: 3431.7

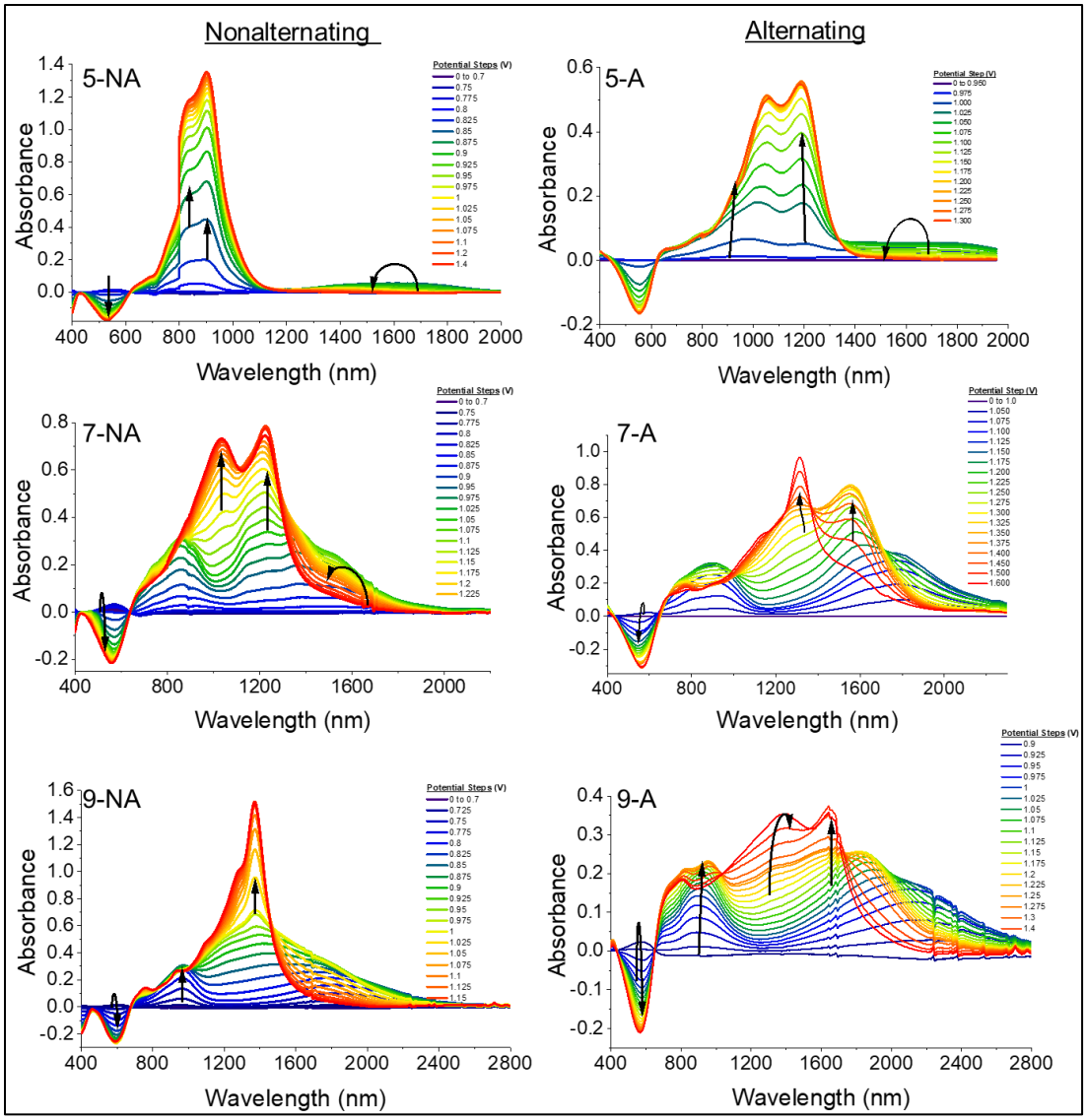

FigureS1. Spectroelectrochemistry of nonalternating and alternating series.

REFERENCES

(1) George Carlin: Jammin' in New York (1992) - George Carlin as Self - IMDb https://www.imdb.com/title/tt0246643/characters/nm0137506 (accessed Apr 10, 2021).

(2) Thompson, R. C.; Swan, S. H.; Moore, C. J.; Vom Saal, F. S. Our Plastic Age. https://doi.org/10.1098/rstb.2009.0054.

(3) *100+ Years of Plastics. Leo Baekeland and Beyond*; Strom, E. T., Rasmussen, S. C., Eds.; ACS Symposium Series; American Chemical Society: Washington, DC, 2011; Vol. 1080. https://doi.org/10.1021/bk-2011-1080.

(4) Chiang, C. K.; Fincher, C. R.; Park, Y. W.; Heeger, A. J.; Shirakawa, H.; Louis, E. J.; Gau, S. C.; MacDiarmid, A. G. Electrical Conductivity in Doped Polyacetylene. *Phys. Rev. Lett.* **1977**, *39* (17), 1098–1101. https://doi.org/10.1103/PhysRevLett.39.1098.

(5) Pankow, R. M.; Thompson, B. C. The Development of Conjugated Polymers as the Cornerstone of Organic Electronics. *Polymer (Guildf).* **2020**, *207*, 122874. https://doi.org/10.1016/j.polymer.2020.122874.

(6) Rasmussen, S. C. Conjugated and Conducting Organic Polymers: The First 150 Years. *Chempluschem* **2020**, *85* (7), 1412–1429. https://doi.org/10.1002/cplu.202000325.

(7) Skotheim, T. A.; Reynolds, J. *Conjugated Polymers*, 3rd ed.; CRC Press, 2006. https://doi.org/10.1201/9781420043594.

(8) Elschner, A.; Kirchmeyer, S.; Lövenich, W.; Merker, U.; Reuter, K. *PEDOT: Principles and Applications of an Intrinsically Conductive Polyme*; CRC Press, 2010. https://doi.org/10.1201/b10318.

(9) Kar, P. Introduction to Doping in Conjugated Polymer. *Doping Conjug. Polym.* **2013**, 1–18. https://doi.org/10.1002/9781118816639.ch1.

(10) Kar, P. Doping Techniques for the Conjugated Polymer. *Doping Conjug. Polym.* **2013**, 47–62. https://doi.org/10.1002/9781118816639.ch3.

(11) Teran, N. B.; Reynolds, J. R. Discrete Donor-Acceptor Conjugated Systems in Neutral and Oxidized States: Implications toward Molecular Design for High Contrast Electrochromics. *Chem. Mater.* **2017**, *29* (3), 1290–1301. https://doi.org/10.1021/acs.chemmater.6b04725.

(12) Shi, P.; Amb, C. M.; Knott, E. P.; Thompson, E. J.; Liu, D. Y.; Mei, J.; Dyer, A. L.; Reynolds, J. R. Broadly Absorbing Black to Transmissive Switching Electrochromic Polymers. *Adv. Mater.* **2010**, *22* (44), 4949–4953. https://doi.org/10.1002/adma.201002234.

(13) Lin, C.; Endo, T.; Takase, M.; Iyoda, M.; Nishinaga, T. Structural, Optical, and Electronic Properties of a Series of 3,4-Propylenedioxythiophene Oligomers in Neutral and Various Oxidation States. *J. Am. Chem. Soc.* **2011**, *133* (29), 11339–11350. https://doi.org/10.1021/ja2035442.

(14) Groenendaal, L.; Zotti, G.; Aubert, P.-H.; Waybright, S. M.; Reynolds, J. R. Electrochemistry of Poly(3,4-Alkylenedioxythiophene) Derivatives. *Adv. Mater.* **2003**, *15* (11), 855–879. https://doi.org/10.1002/adma.200300376.

(15) Groenendaal, L.; Jonas, F.; Freitag, D.; Pielartzik, H.; Reynolds, J. R. Poly(3,4-Ethylenedioxythiophene) and Its Derivatives: Past, Present, and Future. *Adv. Mater.* **2000**, *12* (7), 481–494. https://doi.org/10.1002/(SICI)1521-4095(200004)12:7<481::AID-ADMA481>3.0.CO;2-C.

(16) and, J. C.; Curtis*, M. D. Polarons, Bipolarons, and π-Dimers of Bis(3,4-Ethylene-Dioxythiophene)-(4,4‘-Dialkyl-2,2‘-Bithiazole)- Co-Oligomers. Direct Measure of the Intermolecular Exciton Transfer Interaction. **2003**. https://doi.org/10.1021/CM034484K.

(17) Polander, L. E.; Pandey, L.; Barlow, S.; Tiwari, S. P.; Risko, C.; Kippelen, B.; Brédas, J. L.; Marder, S. R. Benzothiadiazole-Dithienopyrrole Donor-Acceptor-Donor and Acceptor-Donor-Acceptor Triads: Synthesis and Optical, Electrochemical, and Charge-Transport Properties. *J. Phys. Chem. C* **2011**, *115* (46), 23149–23163. https://doi.org/10.1021/jp208643k.

(18) Karsten, B. P.; Bijleveld, J. C.; Viani, L.; Cornil, J.; Gierschner, J.; Janssen, R. A. J. Electronic Structure of Small Band Gap Oligomers Based on Cyclopentadithiophenes and Acceptor Units. *J. Mater. Chem.* **2009**, *19* (30), 5343–5350. https://doi.org/10.1039/b901374a.

(19) Welsh, D. M.; Kumar, A.; Meijer, E. W.; Reynolds, J. R. Enhanced Contrast Ratios and Rapid Switching in Electrochromics Based on Poly(3,4-Propylenedioxythiophene) Derivatives. *Adv. Mater.* **1999**, *11* (16), 1379–1382. https://doi.org/10.1002/(SICI)1521-4095(199911)11:16<1379::AID-ADMA1379>3.0.CO;2-Q.

(20) Groenendaal, L.; Zotti, G.; Aubert, P. H.; Waybright, S. M.; Reynolds, J. R. Electrochemistry of Poly(3,4-Alkylenedioxythiophene) Derivatives. *Advanced Materials*. June 5, 2003, pp 855–879. https://doi.org/10.1002/adma.200300376.

(21) Hapiot, P.; Kispert, L. D.; Konovalov, V. V.; Savéant, J. M. Single Two-Electron Transfers vs Successive One-Electron Transfers in Polyconjugated Systems Illustrated by the Electrochemical Oxidation and Reduction of Carotenoids. *J. Am. Chem. Soc.* **2001**, *123* (27), 6669–6677. https://doi.org/10.1021/ja0106063.

(22) Evans, D. H. One-Electron and Two-Electron Transfers in Electrochemistry and Homogeneous Solution Reactions. *Chem. Rev.* **2008**, *108* (7), 2113–2144. https://doi.org/10.1021/cr068066l.

(23) Qi, H.; Chang, J.; Abdelwahed, S. H.; Thakur, K.; Rathore, R.; Bard, A. J. Electrochemistry and Electrogenerated Chemiluminescence of π-Stacked Poly(Fluorenemethylene) Oligomers. Multiple, Interacting Electron Transfers. *J. Am. Chem. Soc.* **2012**, *134* (39), 16265–16274. https://doi.org/10.1021/ja3057997.

(24) Kaim, W.; Fiedler, J. Spectroelectrochemistry: The Best of Two Worlds. *Chem. Soc. Rev.* **2009**, *38* (12), 3373–3382. https://doi.org/10.1039/b504286k.

(25) Connelly, N. G.; Geiger, W. E. Chemical Redox Agents for Organometallic Chemistry. *Chem. Rev.* **1996**, *96* (2), 877–910. https://doi.org/10.1021/cr940053x.

(26) Rathore, R.; Hecht, J.; Kochi, J. K. Isolation and X-Ray Structure of Chloroarenium Cations as Wheland Intermediates in Electrophilic Aromatic Chlorination [16]. *Journal of the American Chemical Society*. American Chemical Society December 23, 1998, pp 13278–13279. https://doi.org/10.1021/ja983314j.

(27) Shekarchi, M.; Behbahani, F. K. Antimony(V) Chloride, SbCl5 as a Labile Reagent in Organic Transformations. *Catal. Letters* **2017**, *147* (12), 2950–2961. https://doi.org/10.1007/s10562-017-2194-2.

(28) Rathore, R.; Kumar, A. S.; Lindeman, S. V.; Kochi, J. K. Preparation and Structures of Crystalline Aromatic Cation-Radical Salts. Triethyloxonium Hexachloroantimonate as a Novel (One-Electron) Oxidant. *J. Org. Chem.* **1998**, *63* (17), 5847–5856. https://doi.org/10.1021/jo980407a.

(29) Rathore, R.; Burns, C. L.; Deselnicu, M. I. Multiple-Electron Transfer in a Single Step. Design and Synthesis of Highly Charged Cation-Radical Salts. *Org. Lett.* **2001**, *3* (18), 2887–2890. https://doi.org/10.1021/ol0163474.

(30) Meerwein, H.; Battenberg, E.; Gold, H. Über Tertiäre Oxoniumsalze, II. *J. für Prakt. Chemie* **1939**, *154* (3–5), 83–156. https://doi.org/10.1002/prac.19391540305.

(31) Bell, F. A.; Ledwith, A.; Sherrington, D. C. Cation-Radicals: Tris-(p-Bromophenyl) Amminium Perchlorate and Hexachloroantimonate. *J. Chem. Soc. C Org.* **1969**, *77* (20), 2719–2720. https://doi.org/10.1039/j39690002719.

(32) Cowell, G. W.; Ledwith, A.; White, A. C.; Woods, H. J. Electron-Transfer Oxidation of Organic Compounds with Hexachloroantimonate [SbcCl6]- Ion. *J. Chem. Soc. B Phys. Org.* **1970**, *43* (2), 227–231. https://doi.org/10.1039/j29700000227.

(33) Kovacic, P.; Sparks, A. K. Chlorination of Aromatic Compounds by Antimony Pentachloride. *J. Am. Chem. Soc.* **1960**, *82* (21), 5740–5743. https://doi.org/10.1021/ja01506a044.

(34) Todres, Z. *Ion-Radical Organic Chemistry: Principles and Applications*; 2008.

(35) Cotton, F. A.; Wilkinson, G.; Universitaria, C.; Rica, C.; Bochmann, M. Sixth Edition ADVANCED INORGANIC CHEMISTRY. *Adv. Inorg. Chemestry* **1999**, *6th ed*.

(36) Meerwein, H.; Zenner, K. -F; Gipp, R. Über Chlor-dimethyl-sulfoniumsalze. *Justus Liebigs Ann. Chem.* **1965**, *688* (1), 67–77. https://doi.org/10.1002/jlac.19656880109.

(37) Partridge, R. H. Electroluminescence from Polyvinylcarbazole Films: 1. Carbazole Cations. *Polymer (Guildf).* **1983**, *24* (6), 733–738. https://doi.org/10.1016/0032-3861(83)90012-5.

(38) Shouji, E.; Yamamoto, K.; Tsuchida, E. Synthesis of Poly(Arylene Sulfide) via Poly(Sulfonium Cation) through Electrophilic Substitution Reaction of Methyl Phenyl Sulfide with Antimony Pentachloride. *Chem. Lett.* **1993**, *22* (11), 1927–1930. https://doi.org/10.1246/cl.1993.1927.

(39) Kumar, A.; Welsh, D. M.; Morvant, M. C.; Piroux, F.; Abboud, K. A.; Reynolds, J. R. Conducting Poly(3,4-Alkylenedioxythiophene) Derivatives as Fast Electrochromics with High-Contrast Ratios. *Chem. Mater.* **1998**, *10* (3), 896–902. https://doi.org/10.1021/cm9706614.

(40) Gonschorek, W. Molekül- Und Kristallstrukturen Des Dibrom- Und Dijodmaleinsäurethioanhydrids. *Zeitschrift fur Naturforsch. - Sect. A J. Phys. Sci.* **1980**, *35* (1), 14–17. https://doi.org/10.1515/zna-1980-0104.

(41) Aitken, R. A.; Harper, A. D.; Slawin, A. M. Z. Synthesis, Structure, and Unusual Reactivity of a Stable 3-(Oxazolidin-2-Ylidene)Thiophen-2-One. *J. Org. Chem.* **2016**, *81* (21), 10527–10531. https://doi.org/10.1021/acs.joc.6b01309.

(42) Ravindranathan, T.; Chavan, S. P.; Awachat, M. M.; Kelkar, S. V. A Facile and Efficient Method for Deprotection of Thioketones. *Tetrahedron Lett.* **1995**, *36* (13), 2277–2280. https://doi.org/10.1016/0040-4039(95)00189-J.

(43) Corsaro, A.; Pistarà, V. Conversion of the Thiocarbonyl Group into the Carbonyl Group. *Tetrahedron*. Elsevier Ltd December 10, 1998, pp 15027–15062. https://doi.org/10.1016/S0040-4020(98)00880-1.

(44) Francl, M. M.; Pietro, W. J.; Hehre, W. J.; Binkley, J. S.; Gordon, M. S.; DeFrees, D. J.; Pople, J. A. Self-Consistent Molecular Orbital Methods. XXIII. A Polarization-Type Basis Set for Second-Row Elements. *J. Chem. Phys.* **1982**, *77* (7), 3654–3665. https://doi.org/10.1063/1.444267.

(45) Chai, J. Da; Head-Gordon, M. Long-Range Corrected Hybrid Density Functionals with Damped Atom-Atom Dispersion Corrections. *Phys. Chem. Chem. Phys.* **2008**, *10* (44), 6615–6620. https://doi.org/10.1039/b810189b.

(46) Hariharan, P. C.; Pople, J. A. The Influence of Polarization Functions on Molecular Orbital Hydrogenation Energies. *Theor. Chim. Acta* **1973**, *28* (3), 213–222. https://doi.org/10.1007/BF00533485.

(47) Stein, T.; Kronik, L.; Baer, R. Prediction of Charge-Transfer Excitations in Coumarin-Based Dyes Using a Range-Separated Functional Tuned from First Principles. *J. Chem. Phys.* **2009**, *131* (24). https://doi.org/10.1063/1.3269029.

(48) Stein, T.; Kronik, L.; Baer, R. Reliable Prediction of Charge Transfer Excitations in Molecular Complexesusing Time-Dependent Density Functional Theory. *J. Am. Chem. Soc.* **2009**, *131* (8), 2818–2820. https://doi.org/10.1021/ja8087482.

(49) Refaely-Abramson, S.; Baer, R.; Kronik, L. Fundamental and Excitation Gaps in Molecules of Relevance for Organic Photovoltaics from an Optimally Tuned Range-Separated Hybrid Functional. *Phys. Rev. B - Condens. Matter Mater. Phys.* **2011**, *84* (7). https://doi.org/10.1103/PhysRevB.84.075144.

(50) Stein, T.; Eisenberg, H.; Kronik, L.; Baer, R. Fundamental Gaps in Finite Systems from Eigenvalues of a Generalized Kohn-Sham Method. *Phys. Rev. Lett.* **2010**, *105* (26). https://doi.org/10.1103/PhysRevLett.105.266802.

(51) Sutton, C.; Körzdörfer, T.; Coropceanu, V.; Brédas, J. L. Toward a Robust Quantum-Chemical Description of Organic Mixed-Valence Systems. *J. Phys. Chem. C* **2014**, *118* (8), 3925–3934. https://doi.org/10.1021/jp410461v.

(52) Frisch, M. J. .; Trucks, G. W. .; Schlegel, H. B. .; Scuseria, G. E. .; Robb, M. A. .; Cheeseman, J. R. .; Scalmani, G. .; Barone, V. .; Mennucci, B. .; Petersson, G. A. .; et al. Gaussian 09 Citation | Gaussian.Com, 2009.

(53) Lewis, I. C.; Singer, L. S. Electron Spin Resonance of Radical Cations Produced by the Oxidation of Aromatic Hydrocarbons with SbCl5. *J. Chem. Phys.* **1965**, *43* (8), 2712–2727. https://doi.org/10.1063/1.1697200.

(54) Hill, M. G.; Penneau, J. F.; Zinger, B.; Mann, K. R.; Miller, L. L. Oligothiophene Cation Radicals. π-Dimers as Alternatives to Bipolarons in Oxidized Polythiophenes. *Chem. Mater.* **1992**, *4* (5), 1106–1113. https://doi.org/10.1021/cm00023a032.

(55) Graf, D. D.; Duan, R. G.; Campbell, J. P.; Miller, L. L.; Mann, K. R. From Monomers to π-Stacks. A Comprehensive Study of the Structure and Properties of Monomeric, π-Dimerized, and π-Stacked Forms of the Cation Radical of 3', 4 "-Dibuty 1- 2,5 -Diphenyl- 2,2": 5',2'-Terthiophene. *J. Am. Chem. Soc.* **1997**, *119* (25), 5888–5899. https://doi.org/10.1021/ja964345m.

(56) Nishinaga, T.; Sotome, Y. Stable Radical Cations and Their π-Dimers Prepared from Ethylene- and Propylene-3,4-Dioxythiophene Co-Oligomers: Combined Experimental and Theoretical Investigations. *J. Org. Chem.* **2017**, *82* (14), 7245–7253. https://doi.org/10.1021/acs.joc.7b00816.

(57) Hestand, N. J.; Spano, F. C. Interference between Coulombic and CT-Mediated Couplings in Molecular Aggregates: H- to J-Aggregate Transformation in Perylene-Based π-Stacks. *J. Chem. Phys.* **2015**, *143* (24). https://doi.org/10.1063/1.4938012.

(58) Köhler, F. H. Paramagnetic Complexes in Solution: The NMR Approach. In *Encyclopedia of Magnetic Resonance*; John Wiley & Sons, Ltd: Chichester, UK, 2011. https://doi.org/10.1002/9780470034590.emrstm1229.

(59) Kuei, B.; Gomez, E. D. Chain Conformations and Phase Behavior of Conjugated Polymers. *Soft Matter* **2017**, *13* (1), 49–67. https://doi.org/10.1039/C6SM00979D.

(60) Noriega, R.; Salleo, A.; Spakowitz, A. J. Chain Conformations Dictate Multiscale Charge Transport Phenomena in Disordered Semiconducting Polymers. *Proc. Natl. Acad. Sci. U. S. A.* **2013**, *110* (41), 16315–16320. https://doi.org/10.1073/pnas.1307158110.

(61) Carraher, C. E. Polymer Models. *J. Chem. Educ.* **1970**, *47* (8), 581–582. https://doi.org/10.1021/ed047p581.

(62) Müller, M.; Schmidt, M.; Wegner, G. A Single-chain Rod-to-coil Transition of a Conjugated Polymer in Solution? Caveat Emptor. *Die Makromol. Chemie, Rapid Commun.* **1984**, *5* (2), 83–88. https://doi.org/10.1002/marc.1984.030050205.

(63) Spakowitz, A. J.; Wang, Z. G. Semiflexible Polymer Solutions. I. Phase Behavior and Single-Chain Statistics. *J. Chem. Phys.* **2003**, *119* (24), 13113–13128. https://doi.org/10.1063/1.1628669.

(64) Lim, K. C.; Fincher, C. R.; Heeger, A. J. Rod-to-Coil Transition of a Conjugated Polymer in Solution. *Phys. Rev. Lett.* **1983**, *50* (24), 1934–1937. https://doi.org/10.1103/PhysRevLett.50.1934.

(65) Lee, F. L.; Barati Farimani, A.; Gu, K. L.; Yan, H.; Toney, M. F.; Bao, Z.; Pande, V. S. Solution-Phase Conformation and Dynamics of Conjugated Isoindigo-Based Donor-Acceptor Polymer Single Chains. *J. Phys. Chem. Lett.* **2017**, *8* (22), 5479–5486. https://doi.org/10.1021/acs.jpclett.7b02360.

(66) Lu, Y.; Weers, B.; Stellwagen, N. C. DNA Persistence Length Revisited. *Biopolymers 61* (4), 261–275. https://doi.org/10.1002/bip.10151.

(67) Bura, T.; Blaskovits, J. T.; Leclerc, M. Direct (Hetero)Arylation Polymerization: Trends and Perspectives. *J. Am. Chem. Soc.* **2016**, *138* (32), 10056–10071. https://doi.org/10.1021/jacs.6b06237.

(68) Facchetti, A.; Vaccaro, L.; Marrocchi, A. Semiconducting Polymers Prepared by Direct Arylation Polycondensation. *Angew. Chemie - Int. Ed.* **2012**, *51* (15), 3520–3523. https://doi.org/10.1002/anie.201200199.

(69) Segawa, Y.; Maekawa, T.; Itami, K. Synthesis of Extended π-Systems through C-H Activation. *Angew. Chemie - Int. Ed.* **2015**, *54* (1), 66–81. https://doi.org/10.1002/anie.201403729.

(70) Suraru, S. L.; Lee, J. A.; Luscombe, C. K. C-H Arylation in the Synthesis of π-Conjugated Polymers. *ACS Macro Lett.* **2016**, *5* (6), 724–729. https://doi.org/10.1021/acsmacrolett.6b00279.

(71) Kuninobu, Y.; Sueki, S. C-H Bond Transformations Leading to the Synthesis of Organic Functional Materials. *Synth.* **2015**, *47* (24), 3823–3845. https://doi.org/10.1055/s-0035-1560346.

(72) Lapointe, D.; Fagnou, K. Overview of the Mechanistic Work on the Concerted Metallation-Deprotonation Pathway. *Chem. Lett.* **2010**, *39* (11), 1118–1126. https://doi.org/10.1246/cl.2010.1118.

(73) Mao, H.; Xu, B.; Holdcroft, S. Synthesis and Structure—Property Relationships of Regioirregular Poly(3-Hexylthiophenes). *Macromolecules* **1993**, *26* (5), 1163–1169. https://doi.org/10.1021/ma00057a041.

(74) You, A.; Be, M. A. Y.; In, I. A Planar – Nonplanar Conformational Transition in Conjugated Polymer Solutions. **2017**, *4387* (July 2008).

(75) Lupton, J. M. Chromophores in Conjugated Polymers - All Straight? *ChemPhysChem* **2012**, *13* (4), 901–907. https://doi.org/10.1002/cphc.201100770.

(76) Roux, C.; Leclerc, M. Rod-to-Coil Transition in Alkoxy-Substituted Polythiophenes. *Macromolecules* **1992**, *25* (8), 2141–2144. https://doi.org/10.1021/ma00034a012.

(77) Fauvell, T. J.; Zheng, T.; Jackson, N. E.; Ratner, M. A.; Yu, L.; Chen, L. X. Photophysical and Morphological Implications of Single-Strand Conjugated Polymer Folding in Solution. *Chem. Mater.* **2016**, *28* (8), 2814–2822. https://doi.org/10.1021/acs.chemmater.6b00734.

(78) Wang, Z. G. 50th Anniversary Perspective: Polymer Conformation - A Pedagogical Review. *Macromolecules* **2017**, *50* (23), 9073–9114. https://doi.org/10.1021/acs.macromol.7b01518.

(79) McCulloch, B.; Ho, V.; Hoarfrost, M.; Stanley, C.; Do, C.; Heller, W. T.; Segalman, R. A. Polymer Chain Shape of Poly(3-Alkylthiophenes) in Solution Using Small-Angle Neutron Scattering. *Macromolecules* **2013**, *46* (5), 1899–1907. https://doi.org/10.1021/ma302463d.

(80) Lüssem, B.; Keum, C. M.; Kasemann, D.; Naab, B.; Bao, Z.; Leo, K. Doped Organic Transistors. *Chem. Rev.* **2016**, *116* (22), 13714–13751. https://doi.org/10.1021/acs.chemrev.6b00329.

(81) Brédas, J. L.; Beljonne, D.; Coropceanu, V.; Cornil, J. Charge-Transfer and Energy-Transfer Processes in π-Conjugated Oligomers and Polymers: A Molecular Picture. *Chem. Rev.* **2004**, *104* (11), 4971–5003. https://doi.org/10.1021/cr040084k.

(82) *Electronic Materials: The Oligomer Approach*; Mllen, K., Wegner, G., Eds.; Wiley-VCH Verlag GmbH: Weinheim, Germany, 1998. https://doi.org/10.1002/9783527603220.

(83) Bredas, J. L.; Street, G. B. Polarons, Bipolarons, and Solitons in Conducting Polymers. *Acc. Chem. Res.* **1985**, *18* (10), 309–315. https://doi.org/10.1021/ar00118a005.

(84) Haare, J. A. E. H. van; Havinga, E. E.; Dongen, J. L. J. van; Janssen, R. A. J.; Cornil, J.; Brédas, J. Redox States of Long Oligothiophenes: Two Polarons on a Single Chain. *Chem. - A Eur. J.* **1998**, *4* (8), 1509–1522. https://doi.org/10.1002/(SICI)1521-3765(19980807)4:8<1509::AID-CHEM1509>3.0.CO;2-#.

(85) Lin, C.; Endo, T.; Takase, M.; Iyoda, M.; Nishinaga, T. Structural, Optical, and Electronic Properties of a Series of 3,4-Propylenedioxythiophene Oligomers in Neutral and Various Oxidation States. *J. Am. Chem. Soc.* **2011**, *133* (29), 11339–11350. https://doi.org/10.1021/ja2035442.

(86) Mao, H.; Xu, B.; Holdcroft, S. Synthesis and Structure—Property Relationships of Regioirregular Poly(3-Hexylthiophenes). *Macromolecules* **1993**, *26* (5), 1163–1169. https://doi.org/10.1021/ma00057a041.

(87) Chen, X.; Inganäs, O. Three-Step Redox in Polythiophenes: Evidence from Electrochemistry at an Ultramicroelectrode. *J. Phys. Chem.* **1996**, *100* (37), 15202–15206. https://doi.org/10.1021/jp9601779.

(88) Zotti, G.; Schiavon, G.; Berlin, A.; Pagani, G. Thiophene Oligomers as Polythiophene Models 3. Conductive... *Adv. Mater.* **1993**, *5*, 551–554.

(89) Zotti, G.; Schiavon, G.; Berlin, A.; Pagani, G. Thiophene Oligomers as Polythiophene Models. 2. Electrochemistry and in Situ ESR of End-Capped Oligothienyls in the Solid State. Evidence for π-Dimerization of Hexameric Polarons in Polythiophene. *Chem. Mater.* **1993**, *5* (5), 620–624. https://doi.org/10.1021/cm00029a008.

(90) Zotti, G.; Schiavon, G.; Berlin, A.; Pagani, G. Thiophene Oligomers as Polythiophene Models. 1. Anodic Coupling of Thiophene Oligomers to Dimers: A Kinetic Investigation. *Chem. Mater.* **1993**, *5* (4), 430–436. https://doi.org/10.1021/cm00028a006.

(91) Heinze, J.; Tschuncky, P. 9 Electrochemical Properties 9 . 2 Charge Storage Mechanism of Conjugated Oligomeric Systems. **1998**.

(92) Heinze, J.; Frontana-Uribe, B. A.; Ludwigs, S. Electrochemistry of Conducting Polymers-Persistent Models and New Concepts. *Chem. Rev.* **2010**, *110* (8), 4724–4771. https://doi.org/10.1021/cr900226k.

(93) Heinze, J.; Tschuncky, P.; Smie, A. The Oligomeric Approach - The Electrochemistry of Conducting Polymers in the Light of Recent Research. *J. Solid State Electrochem.* **1998**, *2* (2), 102–109. https://doi.org/10.1007/s100080050073.

(94) Stone, M. T.; Heemstra, J. M.; Moore, J. S. The Chain-Length Dependence Test. *Acc. Chem. Res.* **2006**, *39* (1), 11–20. https://doi.org/10.1021/ar0501267.

(95) Yu, H.; Li, S.; Schwieter, K. E.; Liu, Y.; Sun, B.; Moore, J. S.; Schroeder, C. M. Charge Transport in Sequence-Defined Conjugated Oligomers. *J. Am. Chem. Soc.* **2020**, *142* (10), 4852–4861. https://doi.org/10.1021/jacs.0c00043.

(96) Chai, J. Da; Head-Gordon, M. Long-Range Corrected Hybrid Density Functionals with Damped Atom-Atom Dispersion Corrections. *Phys. Chem. Chem. Phys.* **2008**, *10* (44), 6615–6620. https://doi.org/10.1039/b810189b.

(97) Francl, M. M.; Pietro, W. J.; Hehre, W. J.; Binkley, J. S.; Gordon, M. S.; DeFrees, D. J.; Pople, J. A. Self-Consistent Molecular Orbital Methods. XXIII. A Polarization-Type Basis Set for Second-Row Elements. *J. Chem. Phys.* **1982**, *77* (7), 3654–3665. https://doi.org/10.1063/1.444267.

(98) Hariharan, P. C.; Pople, J. A. The Influence of Polarization Functions on Molecular Orbital Hydrogenation Energies. *Theor. Chim. Acta* **1973**, *28* (3), 213–222. https://doi.org/10.1007/BF00533485.

(99) Stein, T.; Eisenberg, H.; Kronik, L.; Baer, R. Fundamental Gaps in Finite Systems from Eigenvalues of a Generalized Kohn-Sham Method. *Phys. Rev. Lett.* **2010**, *105* (26), 266802. https://doi.org/10.1103/PhysRevLett.105.266802.

(100) Refaely-Abramson, S.; Baer, R.; Kronik, L. Fundamental and Excitation Gaps in Molecules of Relevance for Organic Photovoltaics from an Optimally Tuned Range-Separated Hybrid Functional. *Phys. Rev. B - Condens. Matter Mater. Phys.* **2011**, *84* (7), 075144. https://doi.org/10.1103/PhysRevB.84.075144.

(101) Stein, T.; Kronik, L.; Baer, R. Reliable Prediction of Charge Transfer Excitations in Molecular Complexesusing Time-Dependent Density Functional Theory. *J. Am. Chem. Soc.* **2009**, *131* (8), 2818–2820. https://doi.org/10.1021/ja8087482.

(102) Risko, C.; McGehee, M. D.; Brédas, J. L. A Quantum-Chemical Perspective into Low Optical-Gap Polymers for Highly-Efficient Organic Solar Cells. *Chem. Sci.* **2011**, *2* (7), 1200–1218. https://doi.org/10.1039/c0sc00642d.

(103) Zade, S. S.; Zamoshchik, N.; Bendikov, M. From Short Conjugated Oligomers to Conjugated Polymers. Lessons from Studies on Long Conjugated Oligomers. *Acc. Chem. Res.* **2011**, *44* (1), 14–24. https://doi.org/10.1021/ar1000555.

(104) Gierschner, J.; Cornil, J.; Egelhaaf, H.-J. Optical Bandgaps of π-Conjugated Organic Materials at the Polymer Limit: Experiment and Theory. *Adv. Mater.* **2007**, *19* (2), 173–191. https://doi.org/10.1002/adma.200600277.

(105) Rg Rissler, J. Effective Conjugation Length of P-Conjugated Systems. **2004**. https://doi.org/10.1016/j.cplett.2004.07.058.

(106) Meier, H.; Stalmach, U.; Kolshorn, H. Effective Conjugation Length and UV/Vis Spectra of Oligomers. *Acta Polym.* **1997**, *48* (9), 379–384. https://doi.org/10.1002/actp.1997.010480905.

(107) Kuhn, H. A Quantum-Mechanical Theory of Light Absorption of Organic Dyes and Similar Compounds. *J. Chem. Phys.* **1949**, *17* (12), 1198–1212. https://doi.org/10.1063/1.1747143.

(108) Robin, M. B.; Day, P. Mixed Valence Chemistry-A Survey and Classification. *Adv. Inorg. Chem. Radiochem.* **1968**, *10* (C), 247–422. https://doi.org/10.1016/S0065-2792(08)60179-X.

(109) Aoki, K. Theory of Ultramicroelectrodes. *Electroanalysis* **1993**, *5* (8), 627–639. https://doi.org/10.1002/elan.1140050802.

(110) Heinze, J. Ultramicroelectrodes in Electrochemistry. *Angewandte Chemie International Edition in English*. John Wiley & Sons, Ltd September 1, 1993, pp 1268–1288. https://doi.org/10.1002/anie.199312681.

(111) Chaudhry, S.; Ryno, S. M.; Zeller, M.; McMillin, D. R.; Risko, C.; Mei, J. Oxidation Pathways Involving a Sulfide-Endcapped Donor-Acceptor-Donor π-Conjugated Molecule and Antimony(V) Chloride. *J. Phys. Chem. B* **2019**, *123* (17), 3866–3874. https://doi.org/10.1021/acs.jpcb.9b01389.

(112) Blanchard, P.; Malacrida, C.; Cabanetos, C.; Roncali, J.; Ludwigs, S. Triphenylamine and Some of Its Derivatives as Versatile Building Blocks for Organic Electronic Applications. *Polymer International*. John Wiley and Sons Ltd April 1, 2019, pp 589–606. https://doi.org/10.1002/pi.5695.

(113) Leli ege, A.; Blanchard, P.; eodulf Rousseau, T.; Roncali, J. Triphenylamine/Tetracyanobutadiene-Based D-A-D π-Conjugated Systems as Molecular Donors for Organic Solar Cells. *Org. Lett.* **2011**, *13* (12), 3098–3101. https://doi.org/10.1021/ol201002j.

VITA

Saadia Chaudhry was born in 1992 in Lahore, Pakistan. She immigrated with her family to the US at the age of 10, settling in Jersey City, NJ, where she graduated from Abraham Lincoln High School. She then pursued her Bachelor of Science in chemistry from William Paterson University of New Jersey. As an undergraduate student, she conducted three years of materials chemistry research in the laboratories of Dr. Bhanu Chauhan, on the synthesis and characterization of silane stabilized metal nanoparticles, and Dr. David Snyder, on NMR techniques for protein analysis. She then attended Purdue University in West Lafayette, Indiana to pursue her doctorate in organic chemistry in the laboratory of Prof. Jianguo Mei. In June 2021, Saadia will begin a postdoctoral research fellowship at Beckman Institute at the University of Illinois at Urbana-Champagne.

PUBLICATIONS

FIRST AUTHOR

(1) Saadia Chaudhry, Yukun Wu, Zhiqiang Cao, Shi Li, Jodie L. Canada, Xiaodan Gu, Chad Risko and Jianguo Mei. Chain Structure and Oxidation Chemistry of an Oligomeric Donor-Acceptor π-Conjugated Series. 2021, *preparing for submission.*

(2) Saadia Chaudhry, Sean M. Ryno, Matthias Zeller, David R. McMillin*, Chad Risko*, Jianguo Mei*. Oxidation Pathways Involving a Sulfide Endcapped Donor-Acceptor-Donor π-Conjugated Molecule and Antimony(V) Chloride. *J. Phys. Chem. B*, **2019**, DOI: 10.1021/acs.jpcb.9b01389.

COLLABORATIONS

(3) Liyan You, Saadia T. Chaudhry, Yan Zhao, Junchen Liu, Xikang Zhao, Jianguo Mei*. Direct Arylation Polymerization of Asymmetric Push-Pull Aryl Halides. *Polym. Chem.*, **2017**, 8, 2438 – 2441.

(4) Jiayingzi Wu, Liyan You, Lu Lan, Hyeon Jeong Lee, Saadia T. Chaudhry, Rui Li, Ji-Xin Cheng*, Jianguo Mei*. Semiconducting Polymer Nanoparticles for Centimeter-Deep Photoacoustic Imaging in the Second Near-Infrared Window. *Adv. Mater.*, **2017**, 29, 1703403.